題目(和文)	
Title(English)	Effect of Alloying Elements and Microstructure on the Steam Oxidation Behavior of 9Cr Ferritic Alloy at 923 K
著者(和文)	Lidyana Utami
Author(English)	Lidyana Utami
出典(和文)	学位:博士（工学）, 学位授与機関:東京工業大学, 報告番号:甲第12198号, 授与年月日:2022年9月22日, 学位の種別:課程博士, 審査員:上田 光敏,河村 憲一,木村 好里,多田 英司,小林 覚
Citation(English)	Degree:Doctor (Engineering), Conferring organization: Tokyo Institute of Technology, Report number:甲第12198号, Conferred date:2022/9/22, Degree Type:Course doctor, Examiner:,,,,
学位種別(和文)	博士論文
Type(English)	Doctoral Thesis

Doctoral Dissertation

Effect of Alloying Elements and Microstructure on the Steam Oxidation Behavior of 9Cr Ferritic Alloy at 923 K

Lidyana Utami

Supervised By

Assoc. Prof. Mitsutoshi Ueda

Assoc. Prof. Kenichi Kawamura

Department of Materials Science and Engineering

School of Materials and Chemical Technology

Tokyo Institute of Technology

September 2022

Table of Content

Chapter 4 The Effect of Tungsten and Niobium on the Cr Diffusivity in the Fe-9Cr Alloys with the Alloying Element..................... 119

Chapter 1 Introduction

1.1 Background

Global energy demand, including electricity, is increasing more than the capacity can be provided by renewable energy. It means that the fossil fuel power plant is still required to fill the energy supply gap for the following years. Since coal is the most reliable and affordable energy source for many countries, developing high-efficiency and low-emissions power plants is necessary. According to Paris Agreement, the new construction of conventional or typical power plants with an efficiency of around 37% should be limited. As a replacement, work is now focused on the development of an advanced ultra-supercritical (A-USC) power plant, which has an efficiency of more than 45%, and the technology of carbon capture and utilization or storage (CCUS) [1]. Efficiency improvement of newly constructed or existing coal power plants combined with CCUS may result in a lower cost of energy generation with a significant reduction of CO_2 emissions per unit of electricity produced.

The fossil fuel power plants burn fossil fuels (coal, natural gas, petroleum oil, etc.) to heat the flowing water into high-pressure and high-temperature steam, which will be flowed to the turbine to rotate the turbine blades. The schematic diagram of a typical coal-fired power plant is shown in figure 1.1 [2]. The movement of the blades rotates the generator shaft and converts it to produce electricity. The steam then flows into the condenser, transforms the steam into water, and repeats the cycles [2]. In the ideal conditions, the attained thermal efficiency of a heat engine, such as a fossil fuel power plant, often be determined by using the Carnot cycle, which is given by [3]:

$$\eta = \frac{T_{\max} - T_{\min}}{T_{\max}} \text{ x } 100(\%) \tag{1.1}$$

where $T_{\max}$ and $T_{\min}$ are the maximum temperature of the steam and minimum temperature of the heat sink, respectively. However, in reality, heat transfer loss may occur on gas inlet and outlet during the power plant operation. Therefore, in order to achieve higher power plant efficiency, several efforts are being considered to maximize the gap between

T_{max} and T_{min}, such as increasing the temperature and pressure of the steam and employing the cooling turbine and cooling boiler exhaust condensers [4]. From the options, increasing the temperature is more feasible because the limitation mostly comes from the maximum temperature performance of the components.

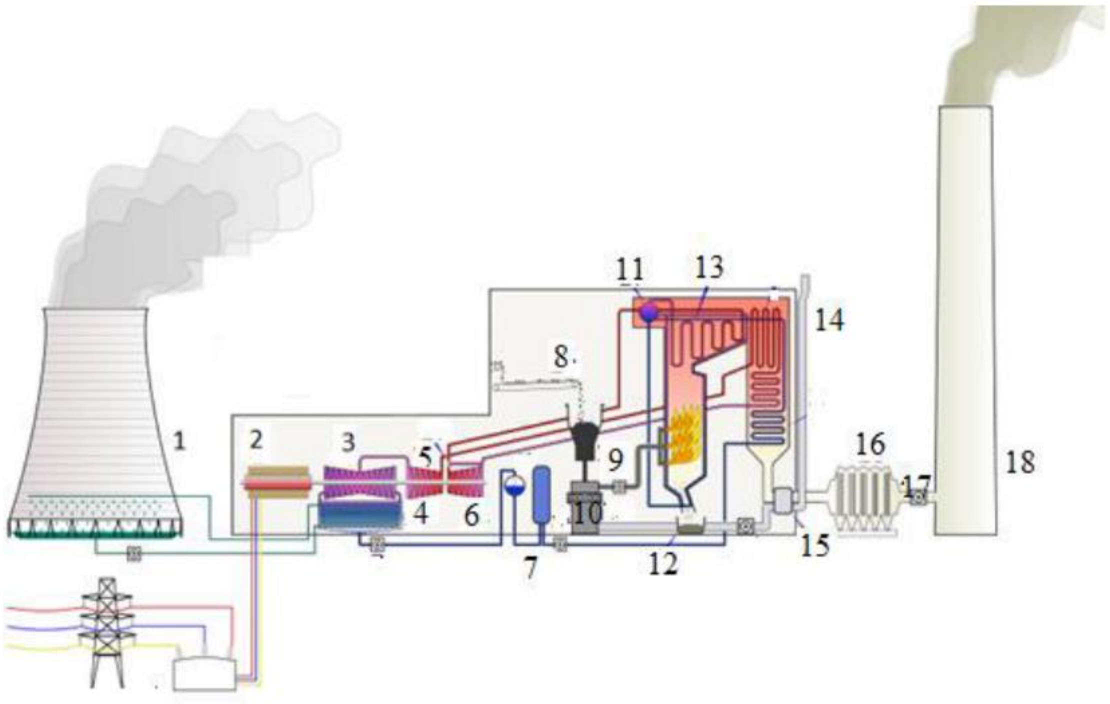

1	Colling tower	7	Deaerator	13	Superheater
2	Generator	8	Coal conveyor	14	Air Intake
3	Low pressure turbine	9	Coal hopper	15	Air preheater
4	Condenser	10	Pulverized fuel mill	16	Precipitator
5	Intermediate pressure turbine	11	Boiler drum	17	Induced draught fan
6	High pressure turbine	12	Ash hopper	18	Stack

Figure 1.1 Schematic illustration of typical coal fired power plant [2].

The power plants are classified based on the conditions in the main steam/hot reheat and plant efficiency. Table 1.1 [5] shows the classification of the coal power plants in the world. The development of higher operating conditions for higher efficiency of fossil fuel power plants has been started in many countries. The project of advanced ultra-super-critical (A-USC) technology in the US aims for the steam condition could reach 760^{o}C with a pressure of 35 MPa, while in Japan [6-8], Europe, China, and India [4,5], the steam temperature is projected to be 600^{o}C. Figure 1.2 [9] shows the development of power plants in Japan. By 2018, the highest steam condition of the power plant operated in Japan reached 600^{o}C/620^{o}C - 25 MPa with an efficiency of 45%. Since higher operating conditions are needed to achieve better efficiency, works on providing reliable material at elevated temperatures are highly developed.

Table 1.1 Classification of coal fired power plants [5].

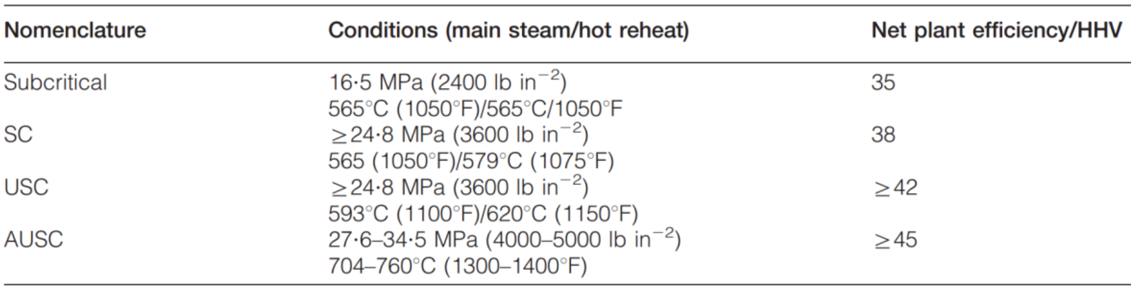

Nomenclature	**Conditions (main steam/hot reheat)**	**Net plant efficiency/HHV**
Subcritical	16·5 MPa (2400 lb in^{-2}) 565°C (1050°F)/565°C/1050°F	35
SC	≥24·8 MPa (3600 lb in^{-2}) 565 (1050°F)/579°C (1075°F)	38
USC	≥24·8 MPa (3600 lb in^{-2}) 593°C (1100°F)/620°C (1150°F)	≥42
AUSC	27·6–34·5 MPa (4000–5000 lb in^{-2}) 704–760°C (1300–1400°F)	≥45

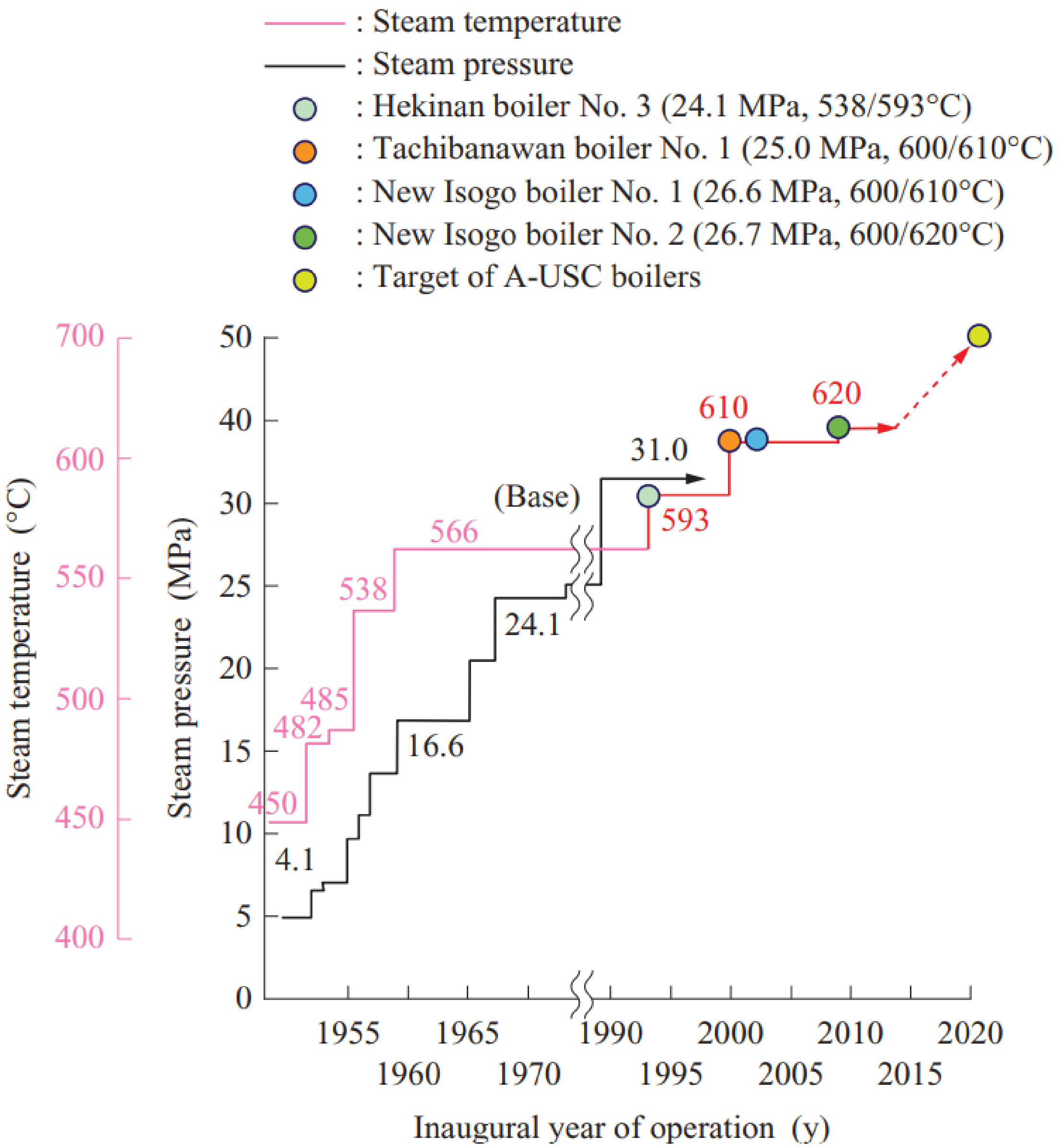

Figure 1.2 Development of steam condition in Japan [9].

The main issues for power plant components are the steam oxidation resistance and long-term creep rupture strength of base material and welded joints [10]. Furthermore, it is well known that the degradation processes such as atom mitigation, grain and precipitation coarsening, and high-temperature corrosion may occur in higher temperatures. Therefore, in such operating temperature and pressure of the main steam of the power plant, A-USC technology supposed to use Ni based alloy which offer excellent properties at the condition of A-USC power plant.

Other aspects should be considered when choosing the materials for components of power plant. One of them is the material's price. High Cr ferritic/martensitic steels are being developed for thick and large component of A-USC power plant operated at a lower temperature in order to minimize the requirement of Ni based alloys, which are more expensive. However, the steam temperature in the A-USC power plant reaches 650^{o}C, which is still higher than the allowed application temperature of typical high Cr ferritic/martensitic steels. Therefore, this maximum application of typical ferritic steels becomes a bottleneck for achieving a highly efficient power plant.

1.2 Ferritic steels as a power plant material

Ferritic steels offer a lower price compared to other materials developed for application in power plant components, such as austenitic steels and Ni based alloys. Due to its properties, ferritic steels have been proven reliable in application of power plant components for decades [7]. Ferritic steel has a BCC structure. It has a low thermal expansion coefficient, capable of resisting during sliding steam pressure operation [7]. Ferritic steel offers sufficient properties such as creep strength, long-term stability, good weldability, resistance towards steam oxidation, and applied cyclic load and variable load at temperature around 600°C [5]. Due to lower Cr content, ferritic steels show lower high-temperature strength and oxidation resistance levels than austenitic steels and Ni based alloys. However, due to its reliable properties (at 600°C) [5] and lower price, ferritic steel is preferred to be used in power plants, especially for heavy and thick-walled components such as headers or pipes.

Optimization works on this typical steel is mainly conducted by controlling the microstructure and adding or substituting amount of alloying elements such as molybdenum (Mo) with tungsten (W), or adding cobalt (Co), niobium (Nb), Nitrogen (N), and boron (B). Figure 1.3 [8] shows the development of ferritic steels containing 2, 9, and 12%Cr, which were applied for the USC coal power plant in the previous generation [6,8,10,11]. Figure 1.4 [11] shows the development of typical 9-12%Cr ferritic/martensitic steels for boiler and turbine materials in Japan. Among the commercial 9Cr steel, grade P91 has been used extensively as headers and steam pipes on USC plants with operating steam temperatures reaching 593°C [8]. The modification brings development grade P92 by substituting some Mo in P91 grade with W [8]. Further works lead to the upper limit for advanced typical 9-12%Cr ferritic/martensitic steels set to be applicable at 650°C.

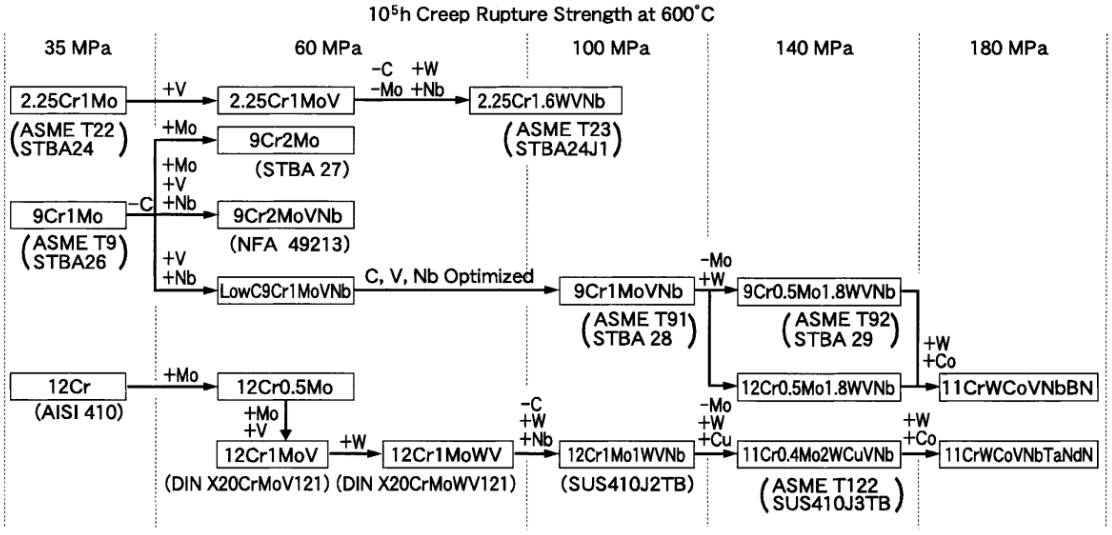

Figure 1.3 Development of ferritic steels for boiler material [8].

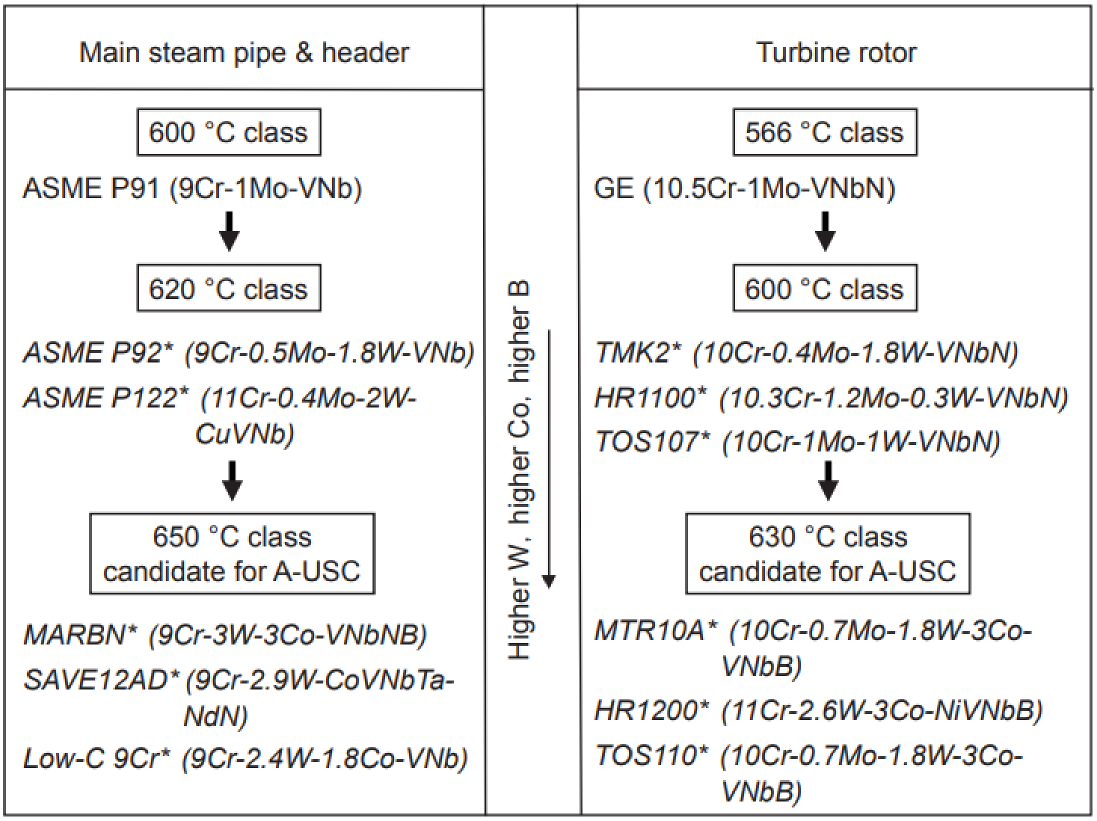

Figure 1.4 Development of 9-12%Cr steel for boiler and turbine materials [11].

The 9-12%Cr ferritic/martensitic steel is well known for having excellent creep strength, low thermal expansion, and good oxidation resistance up to 600°C [8]. This typical steel is widely used for thick or large diameter parts on USC power plants. The microstructure of this typical steel is commercially available as tempered martensite. Figure 1.5 [8] shows the representative microstructure of a typical 9-12%Cr heat resistance steel observed by TEM. The microstructure consists of a single phase of tempered martensite which decorated with precipitates. This microstructure was formed during normalizing and heat treatments. The carbides and Laves phase were found precipitated along the lath boundaries and prior-austenite grain boundaries. The fine MX carbonitrides precipitated coherently in the lath of ferrite matrix. In addition, the dislocation networks were found at the lath boundaries or sub-grain boundaries. The strengthening mechanism is provided by a single phase of tempered martensite, sub-grain hardening, and precipitation hardening [8,12,13].

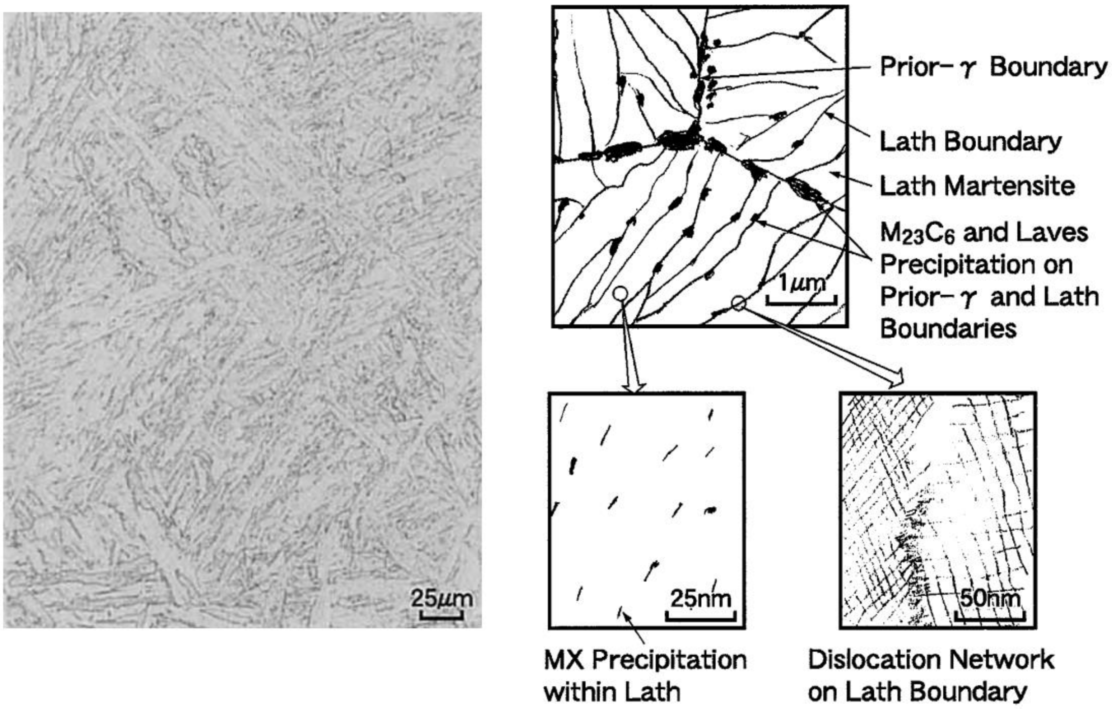

a) LOM b) TEM (Illustrated)

Figure 1.5 Typical microstructure of 9-12% Cr steel [8].

Most of the works to improve the mechanical properties and microstructural stability of 9-12%Cr steel are conducted by changing the chemical composition to utilize a solid solution and interaction between precipitate particles [12]. In addition, the chemical composition may change the transformation temperature, which influences the heat treatment and hot working conditions. For example, the alloy designed in grade P91 is mostly conducted by [5]: (1) precipitation hardening by adding W, Nb, Ti, C, and N; (2) solid solution strengthening by adding W and Mo, (3) dislocation hardening, and (4) boundaries strengthening. In addition, since it is crucial to transform all the austenite to tempered martensite, the heat treatments and working conditions also need to be optimized to achieve the desired structure. Another work on 9-12%Cr steel is to solve the issue of the microstructure instabilities during long-term creep exposure at the operating temperature of the USC power plant, around 600°C. This instability is also attributed to structure change from temper martensite to ferrite, precipitation of the Laves phase of $Fe_2(W, Mo)$ and Z phase.

For decades, the alloy design has been conducted by modifying the existing materials. Recently the new grade steel (ASME Code 2839, ASTM T93/P93) has been developed. This material is suggested to have better stability and creep than the traditional 9Cr ferritic/martensitic steel such as P91, P92, and modified 9Cr-1Mo martensitic steel at 650°C [14]. This type of steel contains 3W, 3Co, and B. A similar steel containing 9Cr-3W-Co with code G115 has been developed in China [15]. The presence of W in these steels is meant to give a better creep strength from solid solution strengthening [14,16]. The presence of Co is meant to suppress delta formation and reduce the coarsening rate of $M_{23}C_6$ [14,17]. In addition, B is added to stabilize $M_{23}C_6$ carbides and suppress the coarsening, which gives better microstructure stability of grain boundaries and a longer duration of transient creep [18,19]. This material can be used at 650°C in term of mechanical properties. However, the steam oxidation resistance at 650°C is not well investigated.

1.3 Application of alloying element on ferritic steel

As mentioned earlier, the alloying element can act as a solute atom and precipitate. In general, solute atoms are reported to improve the creep strain by forming a cluster around the dislocation. While precipitates help to pin the dislocation movement and retard the mitigation of sub-grain boundaries and improve the stability of sub-grain [13]. It is reported that there are seven groups of alloying elements usually added into typical 9-12%Cr steels, which were divided based on their properties and effects [8]: (1) Cr; (2) Mo, W, and Re; (3) V, Nb, Ti, and Ta; (4) C and N; (5) B; (6) Si and Mn; (7) Ni, Cu, and Co.

Cr is well known to give better oxidation and corrosion resistance in heat-resistant steels. Mo, W, and Re are reported to provide solid solution strengthening and improve creep strength [8,20]. However, W promotes the formation of δ-ferrite and the Laves phase if it exceeds a certain concentration limit. V, Nb, Ti, and Ta contribute to precipitation hardening by forming carbides, nitrides, and carbonitrides, which are coherent to the matrix of ferrite [8]. C and N give a solid solution and precipitation strengthening. As austenite-former elements, adding C and N inhibit the formation of δ-ferrite, which is promoted by adding ferrite-former elements. B improves hardenability and creep strength and affects the stability of carbides in the ferritic steel [8,21]. Si and Mn are not good in terms of creep strength. However, Si is well known to positively influence the oxidation property of ferritic steel in ambiance containing water vapor. Ni, Cu, and Co inhibit the δ-ferrite formation and affect the tempering temperature of the material [8].

One of the latest developments of 9Cr steel is the finding of new grade steel, which contains 3%W and 3%Co. This material is reported as the strongest creep-resistant ferritic steel for steam turbine applications up to 650°C for now [14]. As major alloying elements, there are many works to investigate the effect of W on mechanical properties. W additions are well known as a ferrite stabilizers, and the addition of W is meant to give solid solution strengthening and precipitation hardening [20]. W additions are reported to influence the kinetics in the steel, such as formation, dissolution, and coarsening processes of precipitates. Adding W into steel may help stabilize the microstructure that resists the martensite recovery by stabilizing the dislocation substructure. The W refines the prior austenite grain size for fine lath martensite during creep exposure [20]. The W in carbides is also reported to retard self-diffusion of iron which reduces the coarsening rate.

It is reported by Abe *et al.* [22] that the temperature where the Laves phase precipitate occurs is in the range of 550°C-700°C, and the nose is at about 650°C [16]. Figure 1.6 shows the phase diagram of the Fe-9Cr-W system estimated by Pandat 2020 software [23]. In the operating temperature of USC or A-USC power plants, W containing steel may precipitate the laves phase due to the enrichment of W during the formation or growth of carbide. Although it is reported that the fine Laves phase has proven to improve the mechanical properties such as creep strength at elevated temperatures in the primary transient creep region, the effect decreases drastically due to precipitate coarsening [24]. Therefore, 9Cr-3W-3Co containing B is suggested to offer the best combination for all mentioned aspects.

Another promising alloying element on 9Cr ferritic/martensitic steel is Nb. Since the solubility of Nb in the Fe matrix is narrow, the addition of Nb on 9-10% Cr steel is proposed to form stable, finely dispersed precipitates such as Nb-rich MX nitrides [16]. This precipitate shows a long-term creep behavior up to 100,000 hours at 600°C. Figure 1.7 shows the phase diagram of the Fe-9Cr-2Nb system [23]. It is reported that adding Nb to steel can increase the strength in many ways, such as solid solution elements, forming micro carbides, and intermetallic phase (Fe_2Nb Laves phase). Although adding Nb into 9Cr steel is meant to form Nb-rich MX nitrides, works are investigating the role of Fe_2Nb in ferritic stainless steel [25].

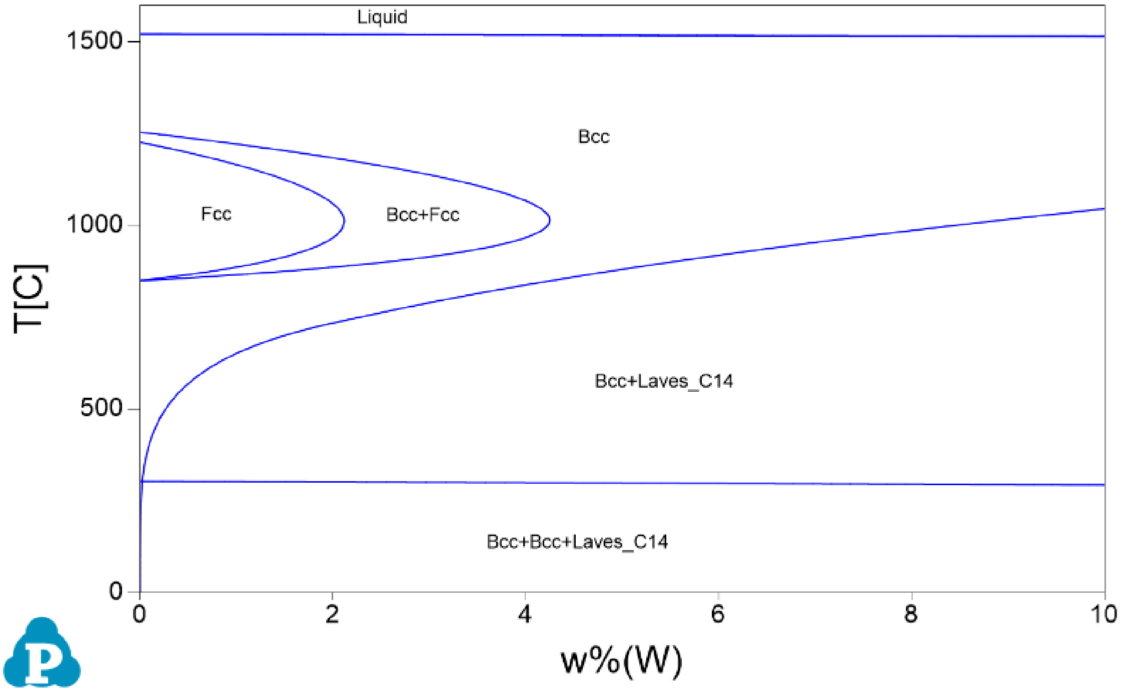

Figure 1.6 Phase diagram of Fe-9Cr-W system [23].

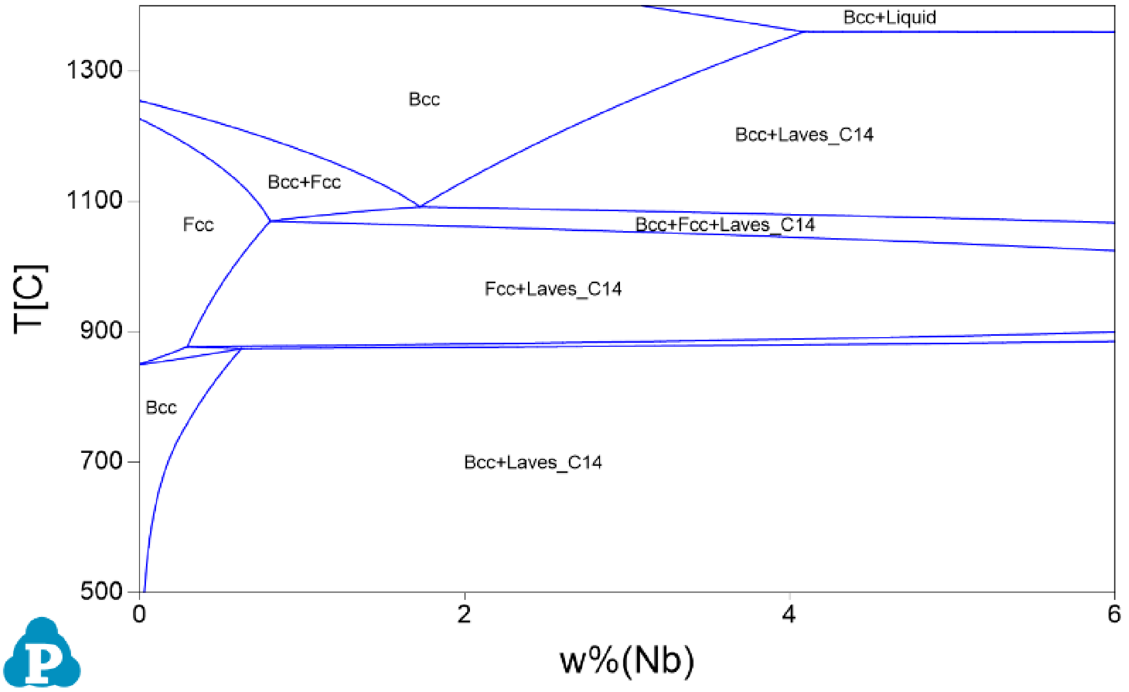

Figure 1.7 Phase diagram of Fe-9Cr-Nb system [23].

1.4 Steam oxidation behavior of Fe-Cr ferritic alloys

One of the crucial issues in operating a higher efficiency power plant is to control the corrosion protection of component material. It is well known that the power plant parts such as headers, pipes, and boilers are addressed to be exposed to the high temperature and high-pressure flowing steam during the power plant operation. Moreover, the fluctuating condition inside the power plant makes the oxide scale detach or exfoliate. This phenomenon will cause severe consequences, from steam flow blockage to material failure. Therefore, more profound knowledge of the oxidation behavior of materials, how to control the reaction, and how to modify the oxidation process in the materials are essential to achieve a longer lifetime of materials.

Considering the proposed minimum Cr required to develop and maintain a continuous external Cr_2O_3 layer by Wagner [26], 9Cr in Fe-Cr ferritic alloy is insufficient to develop an external Cr_2O_3 layer. Moreover, the presence of steam increases the minimum Cr requirement for developing an external layer of Cr_2O_3. Although higher Cr concentration is preferred, remembering that 9Cr concentration gives an optimum creep strength among 9-12%Cr ferritic/martensitic steels, much research is still concerned with optimizing the typical 9Cr steel. Therefore, a deeper knowledge of the effect of alloying elements is essential for improving the oxidation resistance at elevated temperatures. Especially, the Laves phase former elements, such as Mo, W, and Nb, are the major alloying elements that have been added into typical 9Cr ferritic/ martensitic steels.

The behavior of typical 9Cr steel in various atmospheres 600-700^{o}C has been studied extensively [27-29]. Figure 1.8 shows the cross-sectional area of grade P92 steel in flowing steam at 650^{o}C. It is well known that this steel will form a duplex scale consisting of an outer scale of iron oxides, an inner scale of Fe-Cr spinel, and a very thin Cr_2O_3 included layer at the IOZ front. Since the protective layer was not established, the oxygen kinetics follow a nearly parabolic manner with a rate-controlling step is the outward diffusion of Fe ions (Fe^{2+} and Fe^{3+}) through spinel lattice. Therefore, in terms of steam oxidation resistance, the 9Cr steel is believed insufficient to be performed at the operating temperature of the A-USC power plants.

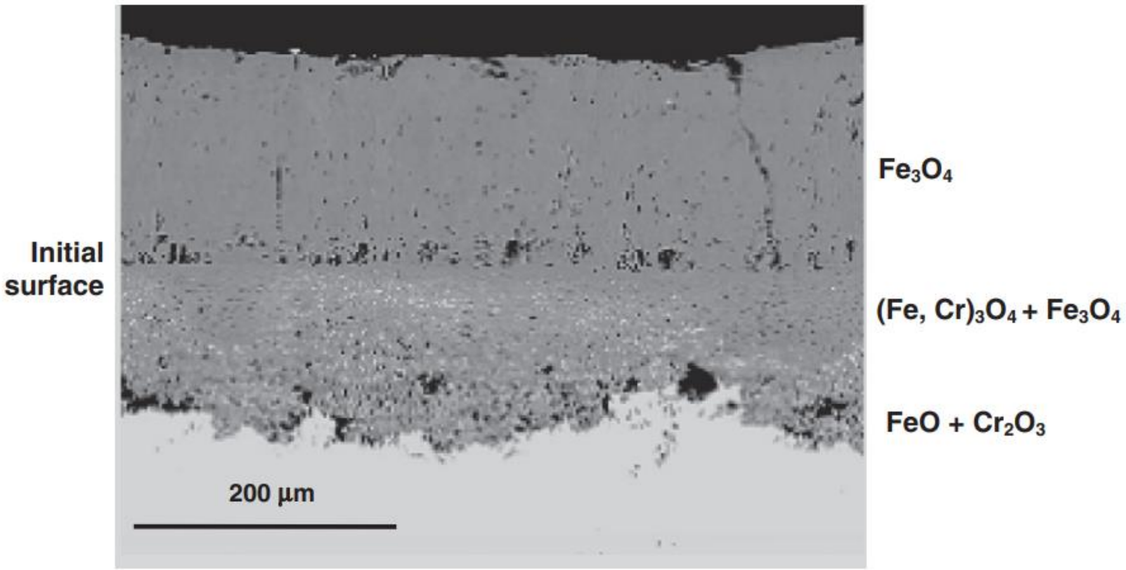

Figure 1.8 Cross-sectional area of P92 exposed to flowing steam at 650°C for 10,000 h [30].

Some effect of alloying elements on the oxidation behavior of typical 9Cr alloys was reported. However, still, limited studies elucidated the effect of laves former elements. It is reported that the 2.25 and 9% Cr steels containing 1% Mo (T22 and T91) show a lower corrosion rate in steam at 650°C than similar steel with lower Mo concentration (T23 and T92) [31]. Although Mo seems to improve the effect on oxidation resistance, there are still limited data concerning the role of Mo on oxidation behavior. Similar to Mo, there are limited data on the effect of W on the oxidation behavior of the steel. Although it is reported that W did not have any negative effect on the oxidation of 9Cr steel in water vapor at 650°C [32], it is still believed that 1.5-2 mass% of W has a detrimental impact on the oxidation resistance of typical 9-12%Cr steels in steam at 650°C [31].

The effect of Nb on oxidation behavior was reported in many studies. Adding Nb into a steel can improve the oxide scale adhesion, improve spallation resistance, reduce expansion crack during cyclic oxidation, and reduce voids and gaps in the scale and scale/metal interface. At high temperatures, the formation of Fe_2Nb Laves phase easily forms at scale/metal interface, which is rich in Nb. The precipitation of the Laves phase is easier than the formation of Nb_2O_5. It is reported that the nucleation of the Laves phase in the oxide/metal interface prevents the cation diffusion to the oxide scale. At the same time, the oxygen anion movement from the oxide scale to the metal becomes retarded, which improves the oxidation properties. The effect of Nb addition to alumina forming alloy was found to help reduce the critical Al required for forming an external alumina layer and decrease the solubility induced at 800°C [33,34].

In recent years, the strategy to use the Laves phase not only improves the mechanical properties but also improves oxidation resistance has been proposed. It is reported that in ferritic stainless steel with Cr concentration above 18%, adding a low amount of Laves phase former element (Nb and Mo) is found can improve both strengths and retarding the growth of the oxide film [25,35]. It was found that the oxidation rate decreases by forming a thin spinel layer near the surface, as shown in figure 1.9 [35]. Besides, Horita *et al.* proposed that precipitation of Fe_2Nb Laves phase along grain boundaries controls the outward diffusion of metal at grain boundaries, as shown in figure 1.10 [25]. Although there are studies that reported the benefit of Laves phase on improving oxidation resistance, the work is limited to typical 9Cr alloy. Therefore, a better understanding is needed, particularly on how to benefit from this intermetallic compound to improve mechanical properties and oxidation resistance.

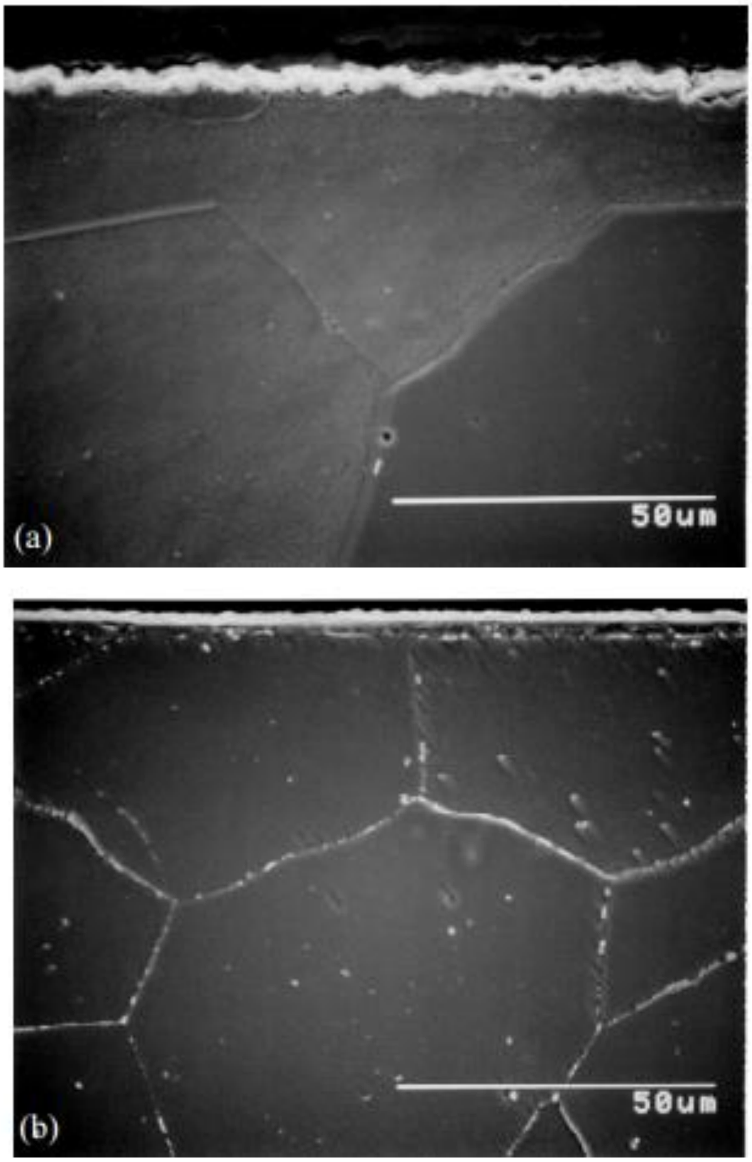

Figure 1.9 Cross section images of (a) 0%Nb steel and (b) 0.36%Nb steel oxidized for 720 ks at 1073 K [35].

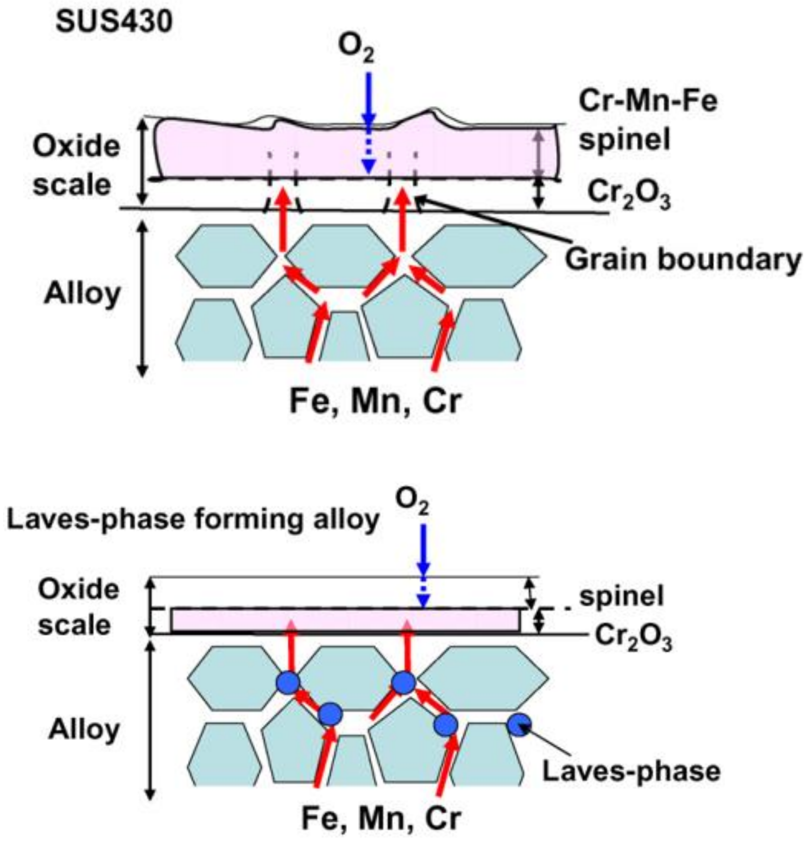

Figure 1.10 Schematic diagram of oxide scale growth for two different Fe-Cr alloys; SUS430 and Laves forming alloy [25].

1.5 Objective

The increasing energy demand pushed us to operate high-efficiency and low-emission power plants. Works on development on advanced ultra-supercritical (A-USC) power plant required materials components that are reliable at higher operating conditions. High Cr ferritic/martensitic steels are being developed for A-USC power plant components performed at a lower temperature to minimize the requirements of Ni based alloy. However, the steam temperature in the A-USC power plant reaches 650^{o}C (923 K), which is still higher than the allowed application temperature of typical high Cr ferritic/martensitic steels. Therefore, this maximum application of typical ferritic steels becomes a bottleneck for achieving a highly efficient power plant.

Development works on high Cr ferritic/martensitic steels are conducted by adding alloying elements and modifying the microstructure. This study aims to improve the steam oxidation behavior of 9Cr steel at 923 K by optimizing alloying elements. As mentioned earlier, tungsten is a major alloying element that contributes to solid solution strengthening and Laves phase strengthening in the typical 9-12%Cr ferritic steel. In comparison, niobium in ferritic steel contributes to better mechanical properties and oxidation resistance. Although Nb is not designed to form Fe_2Nb in typical 9Cr steel, the Fe_2Nb improved the oxidation resistance of ferritic stainless steel with Cr concentration above 18%. By investigating the effect of both Laves phase former elements as the way they are employed on improving mechanical properties, suggestions for further development on 9Cr steel with a better oxidation resistance can be concluded. In the present work, the effect of microstructure formed by different cooling rates was presented to give an insight into the microstructural effect, although in a simple system. In addition, the information on the effect of W and Nb on the Cr diffusivity in Fe and Fe-9Cr alloys can be used to clarify the role of precipitates on the Cr diffusivity and evaluate the feasibility of Wagner criteria [26] for forming an external layer of Cr_2O_3 is applicable or not in the W-added 9Cr and Nb-added 9Cr alloys.

1.6 Thesis layout

In this thesis, the work is separated into six chapters. The layout of this work is presented in figure 1.11.

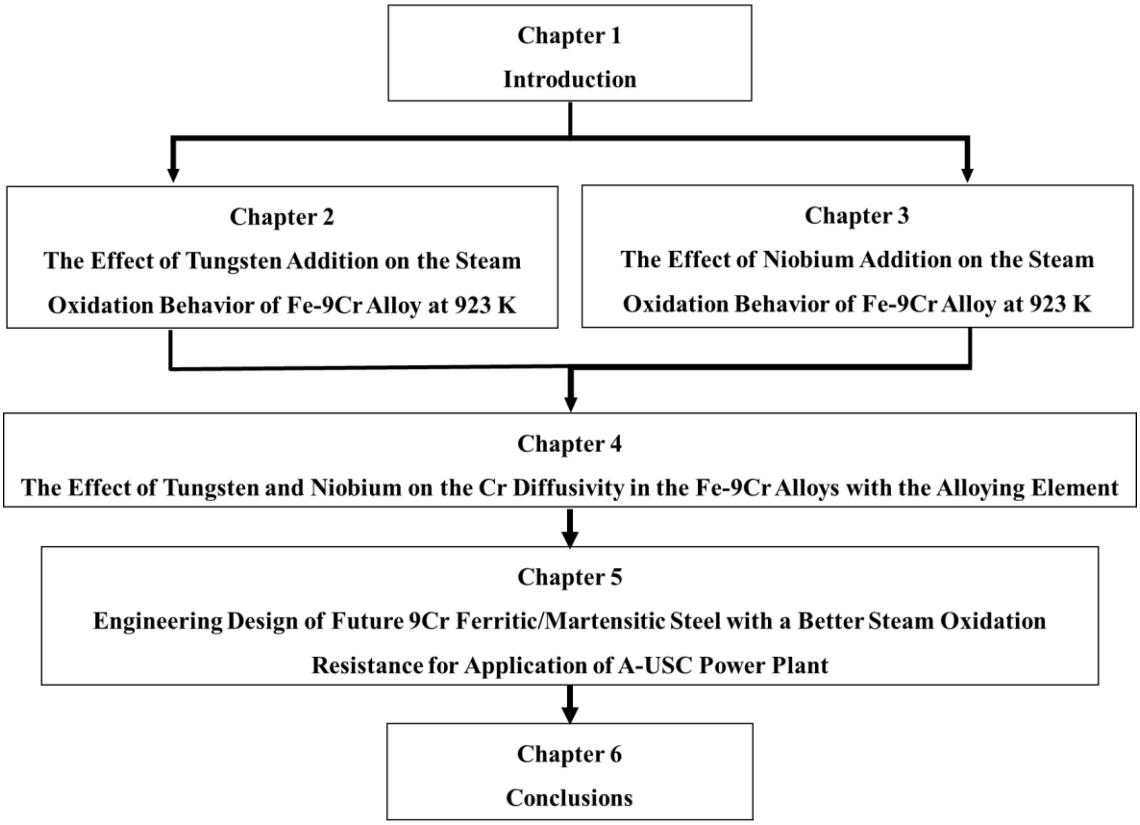

Figure 1.11 Layout of the thesis.

Chapter 1: Introduction

This chapter describes the background of this study: The energy demand and emission reduction issues that need to improve power plant efficiency. The literature review of typical 9-12% Cr steel properties is presented. Based on the research background, the objectives of this work are set.

Chapter 2: The Effect of Tungsten Addition on the Steam Oxidation Behavior of Fe-9Cr Alloy at 923 K

Fe-9Cr alloy and three different concentrations W added 9Cr alloys are compared to investigate the effect of tungsten as a dissolved element and precipitate in different volume fractions in the steam oxidation behavior of Fe-9Cr alloy at 923 K. The scale formation mechanism of W added Fe-9Cr alloy is clarified based on obtained data. In addition, the effect of microstructure due to different cooling rates is also presented in this chapter.

Chapter 3: The Effect of Niobium Addition on the Steam Oxidation Behavior of Fe-9Cr Alloy at 923 K

The steam oxidation behavior of base Fe-9Cr alloy and Nb added Fe-9Cr alloy at 923 K are compared. The oxidation mechanism of scale formation and the effect of Fe_2Nb in the ferritic matrix are clarified based on obtained data.

Chapter 4: The Effect of Tungsten and Niobium on the Cr Diffusivity in the Fe-9Cr Alloys with the Alloying Element

Cr diffusivity was determined by investigating the concentration profile from the diffusion couple sample. The tests were carried out at 1073 K in a vacuum ambiance. The effect of solute elements of W and Nb as well as precipitates on the Cr diffusivity are clarified based on the obtained data.

Chapter 5: Engineering Design of Future 9Cr Ferritic/Martensitic Steel with a Better Steam Oxidation Resistance for Application of A-USC Power Plant

Based on the obtained data from previous chapters, the suggestions are made for better knowledge to design typical 9Cr steel which precipitated Laves phase with a better oxidation resistance at elevated temperatures.

Chapter 6: Conclusions

The conclusions of each chapter are summarized in this chapter.

1.7 References

[1] SLOSS, *L. London, United Kingdom: IEA Clean Coal Center*, 2019.

[2] K.Shahzad Baig, M. Yousaf, J. *Earth Sci Clim. Change*, **8**(404), 2017, (2-10).

[3] Sarkar, Dipak. Thermal power plant: design and operation, *Elsevier*, 2015.

[4] NICOL, Kyle. *IEA Clean Coal Centre*, 2013.

[5] S. A. David, J. A. Siefert, and Z. Feng, *Sci. Technol. Weld. Join.*, **18(**8**)**, 2013, (631–651).

[6] Kiko Network, Tokyo, 2018.

[7] T. Sano, Journal of Power and Energy Systems, **5(**2**)**, 2011, (146–160).

[8] F. Masuyama, *ISIJ Int.*, **41(**6**)**, 2001, (612–625).

[9] K. Kubushiro, K. Nomura, T. Matsuoka, H. Nakagawa, And K. Muroki, *IHI Eng. Rev.*, **49(**6**)**, 2016, (34–43).

[10] F. Abe, *Engineering*, **1(**2**)**, 2015, (211–224).

[11] Viswanathan, R., Henry, J. F., Tanzosh, J., Stanko, G., Shingledecker, J., Vitalis, B., & Purgert, *Journal of materials engineering and performance*, **14(**3**)**, 2005, (281–292).

[12] J. Hald, *Int. J. Press. Vessel. Pip.*, **85(**1–2**)**, 2008, (30–37).

[13] W. Yan, W. Wang, Y. Y. Shan, and K. Yang, *Frontiers of Materials Science*, **7(**1**)**, 2013, (1–27).

[14] F. Abe, *Science and Technology of advanced materials*, **9(**1**)**, 2008, (013002).

[15] P. Yan and Z. Liu, *Mater. Sci. Eng. A*, **650**, 2016, (290–294).

[16] YAN, Wei, et al. 9-12Cr heat-resistant steels. *Springer*, 2015.

[17] V. Knezevic, G. Sauthoff, J. Vilk, G. Inden, A. Schneider, R. Agamennone, W. Blum, Y. Wang, A. Scholz, C. Berger, J. Ehlers and L. Singheiser, *ISIJ international*, **42**(12), 2002, (1505-1514).

[18] Fujio Abe. *International journal of materials research*, **99**(4), 2008, (387-394).

[19] Toshiaki Horiuchi, Masski Igarashi, and Fujio Abe, *ISIJ International*, **42**(Supplement), 2002, (S67–S71).

[20] V. T. Paul, V. D. Vijayanand, C. Sudha, and S. Saroja, *Metall. Mater. Trans. A*, **48(**1**)**, 2017, (425–438).

[21] S. K. Albert, M. Kondo, M. Tabuchi, F. Yin, K. Sawada, and F. Abe, *Metallurgical and Materials Transactions A*, **36(**2**)**, 2005, (333–343).

[22] F. Abe, H. Araki, and T. Noda, *Metallurgical Transactions A*, **22(**10**)**, 1991, (2225–2235).

[23] Pandat 2020 Software with PanFe.

[24] F. Abe, *A Phys. Metallurgical Transactions A.*, **36(**2**)**, 2005, (321–332).

[25] T. Horita *et al.*, *J. Power Sources*, **176(**1**)**, 2008, (54–61).

[26] C. Wagner, *Zeitschrift für Elektrochemie, Berichte der Bunsengesellschaft für Phys. Chemie*, **63(**7**)**, 1959, (772–782).

[27] E. Essuman, G. H. Meier, J. Żurek, M. Hänsel, and W. J. Quadakkers, *Oxid. Met.*, **69(**3–4**)**, 2008, (143–162).

[28] L. Tan, X. Ren, and T. R. Allen, *Corros. Sci.*, **52(**4**)**, 2010, (1520–1528).

[29] J. Yuan, X. Wu, W. Wang, S. Zhu, and F. Wang, *Materials*, **7(**4**)**, 2014, (2772–2783).

[30] A. Agüero, V. González, M. Gutiérrez, and R. Muelas, *Surf. Coat. Technol.*, **237**, 2013, (30–38).

[31] V. Lepingle, G. Louis, D. Allué, B. Lefebvre, and B. Vandenberghe, *Corros. Sci.*, **50(**4**)**, 2008, (1011–1019).

[32] M. Schütze, M. Schorr, D. P. Renusch, A. Donchev, and J. P. T. Vossen, **7(**1**)**, 2004, (111–123).

[33] M. P. Brady, I. G. Wright, and B. Gleeson, *Jom*, **52(**1**)**, 2000, (16–21).

[34] Y. Xu, J. Lu, X. Yang, J. Yan, and W. Li, *Corrosion Science*, **12**, 2017, (10–20).

[35] S. Ide, Y. Funakawa, Y. Kato, and O. Furukimi, in *Materials science forum*, 2007, **539**, (4887–4890).

Chapter 2 The Effect of Tungsten Addition on the Steam Oxidation Behavior of Fe-9Cr Alloy at 923 K

2.1 Introduction

The addition of alloying elements is one of the effective ways to improve mechanical properties and oxidation resistance. For many decades, researchers have been changing the chemical composition of ferritic steel by adding a low amount of Laves phase formation elements such as Nb, W, Mo, etc. This chapter investigated the effect of tungsten (W), as a laves phase former element, on the steam oxidation behavior of Fe-9Cr alloy at 923 K. Fe_2W or $(Fe,Cr)_2(Mo,W)$ Laves phase is well known to precipitate in the 9-12Cr ferritic/martensitic steel during long-term creep exposure at temperatures ranging 550°C-700°C [1]. The latest development of 9Cr steel is the finding grade P93, containing 3%W and 3%Co [2]. The presence of W in the steel provides both solid solutions strengthening and precipitation strengthening by the Fe_2W laves phase [3,4]. At the same time, Co, as an austenite stabilizer element, suppresses the formation of δ-ferrite [2,3]. Therefore, this material is expected to have better stability of lath martensite and better creep properties at 650°C [3,5].

The investigation of the oxidation behavior of this new grade is still limited. Tang *et al.* [6] reported the role of Co, Al, and Mn in forming an external Al_2O_3 in dry and wet at 650°C. Abe *et al.* [7] reported that using the pre-oxidation treatment on 9Cr-3W-3Co alloys developed Cr_2O_3-rich oxide in the steam at 650°C. However, further investigation on oxidation behavior by adding major alloying elements of this new grade steel is essential. Although W is a promising element for improving mechanical property, W is believed to harm steel in steam at 650°C, but still, no clear evidence has been found [8]. This chapter aims to investigate the effect of W addition, including the laves phase, on the oxidation behavior of the 9Cr alloy.

2.2 Experimental

2.2.1 Sample preparation

Fe-9Cr alloy and three different compositions of W added Fe-9Cr alloys were prepared to separate the effect of W as solute element and as precipitate on the steam oxidation behavior of Fe-9Cr alloy at 923 K. The composition was chosen by considering the ternary phase diagram of the Fe-Cr-W system at 873 K from the reference, as shown in figure 2.1 [9]. In addition, point analysis was taken on the matrix of pre-aged of supersaturated alloy (Fe-9Cr-6W alloy) to estimate the solubility limit of W in the matrix Fe. The point analysis found that the solubility limit of W in the matrix of the Fe-9Cr-6W alloy was around 2.7 mass% or 0.84 at.% after annealing for 864 ks at 923 K. Therefore, four ingots of Fe-9Cr (0W), Fe-9Cr-1.5W (1.5W), Fe-9Cr-3W (3W), and Fe-9Cr-6W (6W) (mass%) were made from Fe (purity 99.99%), Cr (99.999+%), and W (99.95%) by arc melting methods. The 0W represents the base alloy, 1.5W represents the W dissolved alloy, 3W represents W supersaturated alloy with small amount of precipitates, and 6W represents the precipitated alloy. The semiquantitative chemical composition obtained by X-Ray Fluorescence spectrometry (XRF) is presented in Table 2.1.

The heat treatment conditions of each ingot are listed in Table 2.2. Solution treatment was conducted in a certain condition. The ingots were then cut into around 1.5 mm thickness coupon and experienced cold rolling with a thickness reduction ± 30%. A hole was drilled into the sample. Recrystallization was conducted in a vacuum ampule in the same condition as solution treatment. Aging treatment was conducted on Fe-9Cr-3W and Fe-9Cr-6W alloys to precipitate laves phase. All heat treatments were conducted in a vacuum ampule to avoid surface degradation.

Two different cooling rates, water quenching (WQ) and furnace cooling (FC), were conducted to investigate the effect of microstructure produced by different cooling rates on the oxidation behavior of the alloys. In the case of the FC sample, the cooling rate was set to be 5 K/min inside the furnace to achieve a homogeneous ferrite structure, while the WQ was conducted to be comparable to the actual condition. Before the oxidation test, all the samples were grounded with abrasive paper (#600 ~ #5000) and polished using a series of diamond pastes (9 μm ~ 0.25 μm) to mirror finish, the thickness and circumference of the sample were measured, and the surface area of the sample was estimated using ‘Image J’ software. Before the oxidation test, the sample was cleaned with an ultrasonic cleaner in ethanol for 0.6 ks. Apart from the cooling rates, all sample experiences the same treatments.

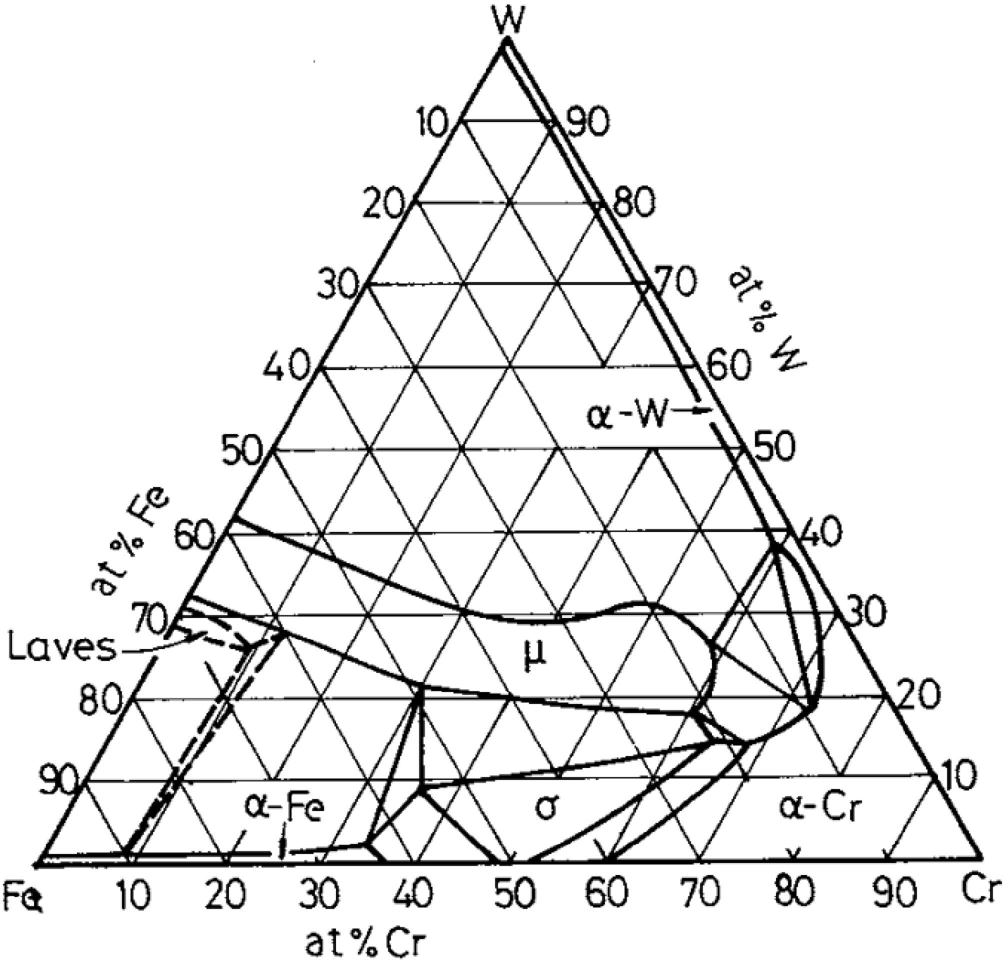

Figure 2.1 Fe-Cr-W ternary phase diagram at 873 K [9].

Table 2.1 Chemical composition of the alloys (mass%).

Alloy	Fe	Cr	W
FC 0W	Bal.	9.05	-
WQ 0W	Bal.	9.03	-
FC 1.5W	Bal.	9.13	1.35
FC 3W	Bal.	9.10	2.98
WQ 3W	Bal.	9.10	3.04
FC 6W	Bal.	8.97	6.10
WQ 6W	Bal.	9.16	6.14

Table 2.2 Heat treatment conditions of the alloys.

Alloy	Heat Treatment					
	Solution Treatment		Recrystallization		Aging Treatment	
	T / K	*t* / ks	*T* / K	*t* / ks	*T* / K	*t* / ks
0W	1273	86.4	1273	0.6	-	-
1.5W	1623	43.2	1623		-	-
3W					923	864
6W						

2.2.2 Experimental procedure

In this experiment, the steam oxidation test was carried out at 923 K in an Ar-15% H_2O gas mixture. The oxygen partial pressure inside the main furnace was maintained to be 1.3×10^{-11} Pa, which is in the stable region of magnetite at 923 K. The test was conducted in the apparatus, as illustrated in Figure 2.2. The argon gas was used to bring the water vapor to the ZrO_2 oxygen pump, which operated at 1173 K. The current was applied to eliminate impurity O_2 in the Ar gas and produce small amount of H_2 from H_2O. The gas mixture went through the evaporator and saturator, which operated at 338 K and 328 K, respectively, to produce a 15%H_2O gas mixture. The ribbon heater wrapped the glass pipes to prevent condensation of the gas mixture. The flow rate of the gas mixture was controlled by a mass flow controller to be 1.67×10^{-6} m^3/s (150 mL/min). During the test, the sample was placed in the soaking area of the main furnace, hanging in the Pt wire. The attached thermocouple continuously monitored the temperature of the vicinity of the sample. The oxygen partial pressure inside the furnace was monitored using a ZrO_2 oxygen sensor to measure the EMF in the vicinity of the sample.

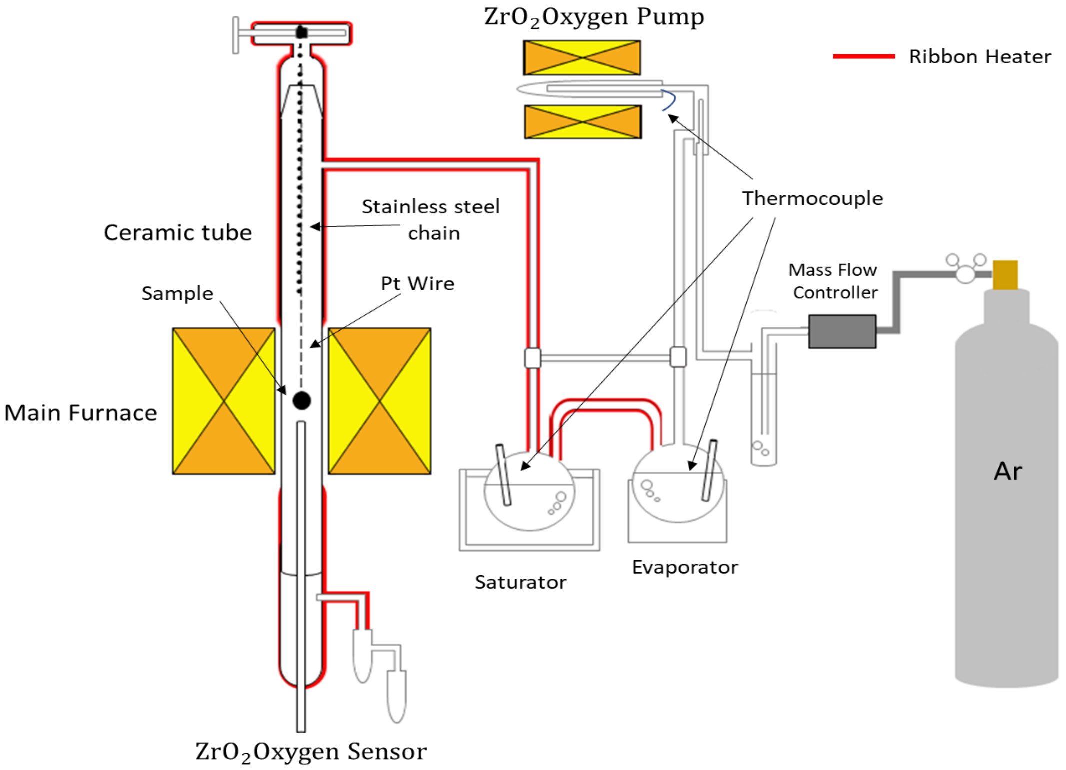

Figure 2.2 Experimental Apparatus.

2.2.3 Analytical method

The mass of samples before and after the oxidation test was measured by an electronic scale to evaluate the oxidation rate. The sample photographs before and after oxidation tests were taken by digital camera. After the test, the X-Ray Diffraction (XRD) analysis was employed to identify the oxide scales formed on the sample surface after the oxidation test. A Field Emission Scanning Electron Microscope (FE-SEM) equipped with an energy dispersive spectroscopy (EDS) was used to observe the microstructure of the sample before the oxidation test and the surface and cross-sectional morphology of the oxidized sample. The thickness of the oxide scale was measured from the obtained images from 10 points to evaluate the growth rate of the oxide scale, as shown in Figure 2.3. The element and point mapping were taken on the cross-sectional of the sample by EDS. This characterization was employed to analyze the elemental distribution as well as to analyze a point in quantitative measurement.

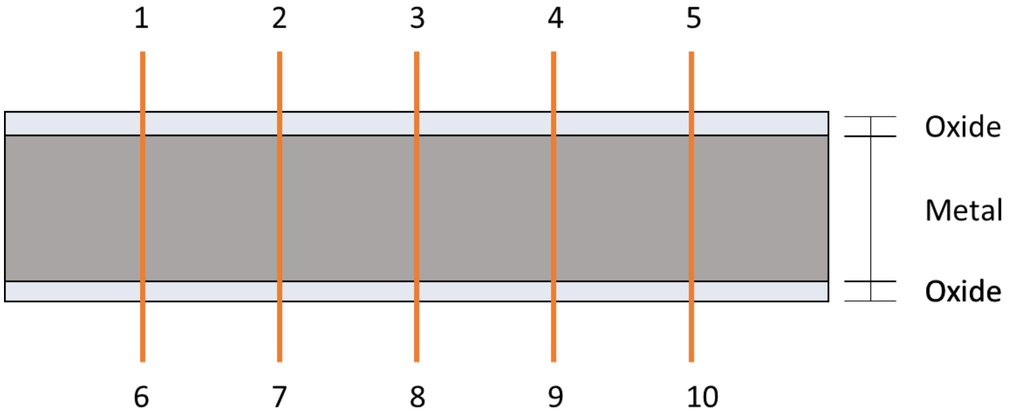

Figure 2.3 Points for cross-sectional observation.

2.3 Results

2.3.1 Microstructure and phases of samples before oxidation

Figure 2.4 shows the XRD pattern for all alloys before the test. All samples showed peaks of matrix ferrite. Figure 2.5 presents the BE images of the microstructural of each sample before the oxidation test observed by FE-SEM. The dark grey represents the matrix in the BE images, and the white particle is Laves phase. Large ferrite grain was observed on all FC samples. The Laves phase was not observed on the FC 1.5W due to the W content being below the solubility limit of W in the Fe-9Cr alloy, which was checked previously by point analysis was about 2.7 mass%. The FC 3W, which has a composition near the solubility limit and W fully solute in the substrate, precipitated laves phase along grain boundaries, while in the FC 6W, the laves phase was also found to decorate the grain boundaries and grain interior of the ferrite matrix.

Due to rapid cooling, different microstructure was observed on WQ samples. The formation of massive ferrite was observed on the WQ 0W. The WQ 3W showed a dual-phase microstructure of ferrite and martensite. The laves phase was precipitated along grain boundaries and lath boundaries, and a small amount in the grain interior of ferrite grain. The formation of a dual phase on WQ 3W becomes possible if, during the cooling process, the alloy enters the BCC + FCC region at a lower temperature than the solution treatment before rapidly cooling down to room temperature. The WQ 6W formed a large ferrite grain with laves phase precipitated homogeneously in the matrix. Etching was conducted only for binary alloys. From the obtained figures, the grain size of each sample was estimated using the mean linear intercept method and listed in Table 2.3.

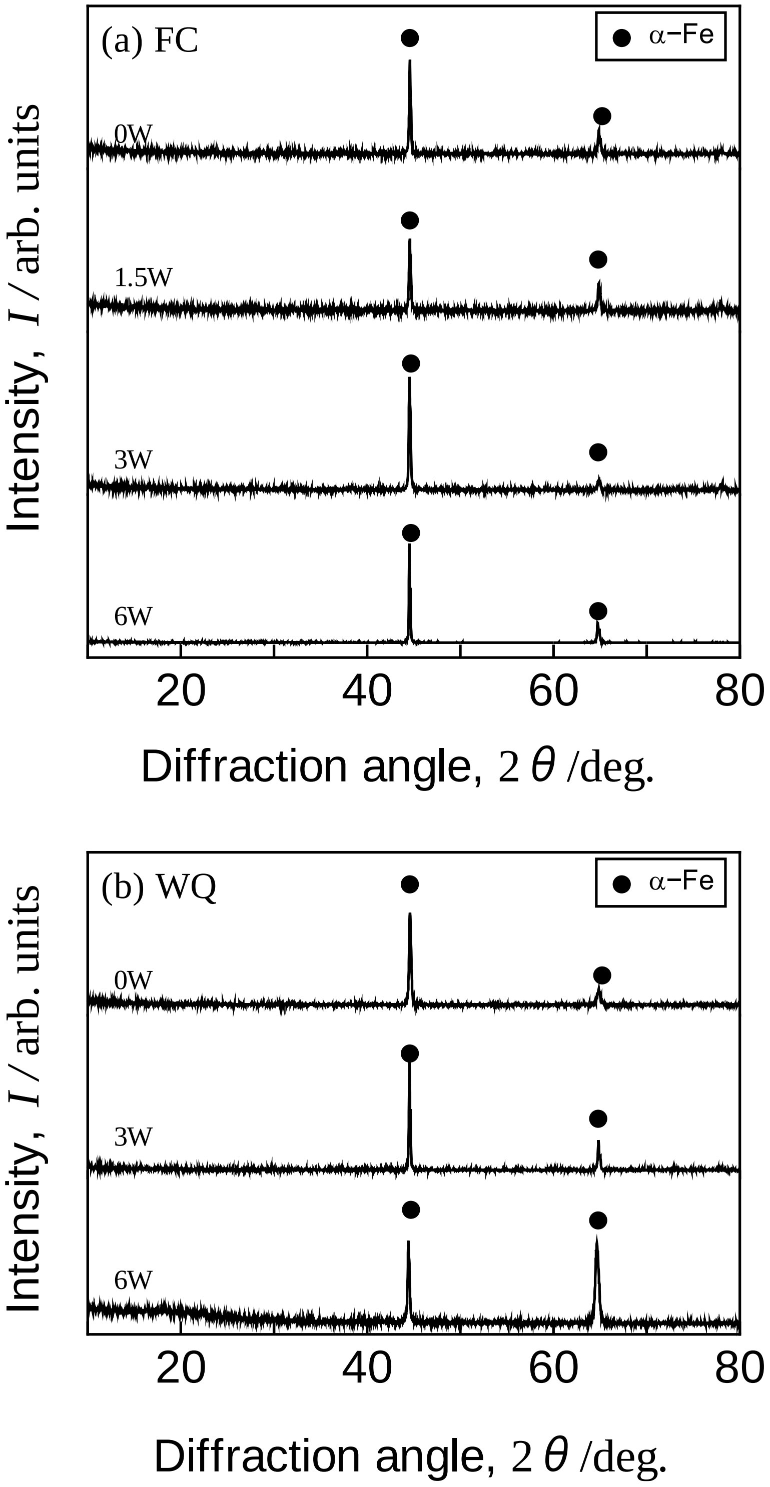

Figure 2.4 XRD patterns of all alloys before oxidation test. (a) Furnace cooling and (b) water quenching.

Alloy	FC	WQ
0W	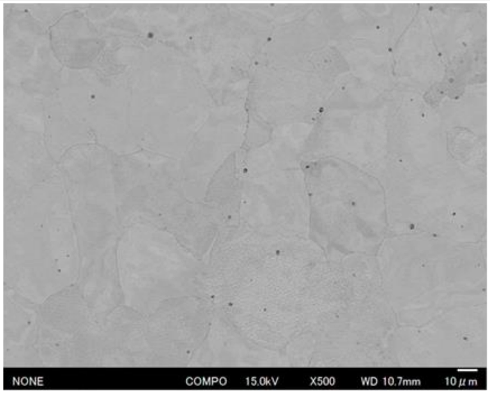	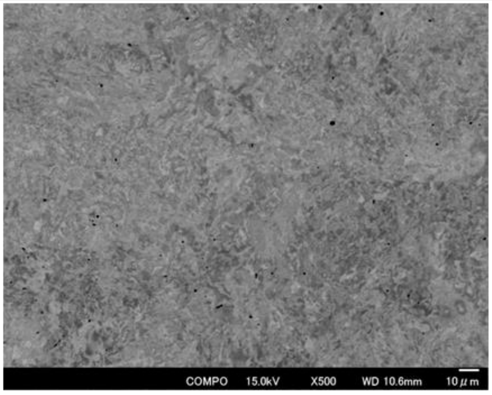
1.5W	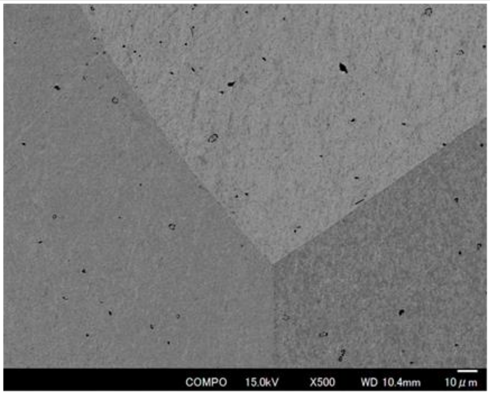	
3W	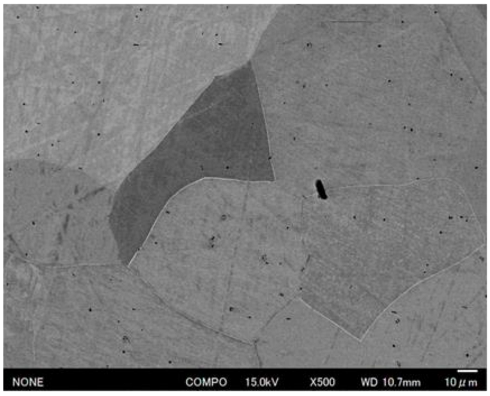	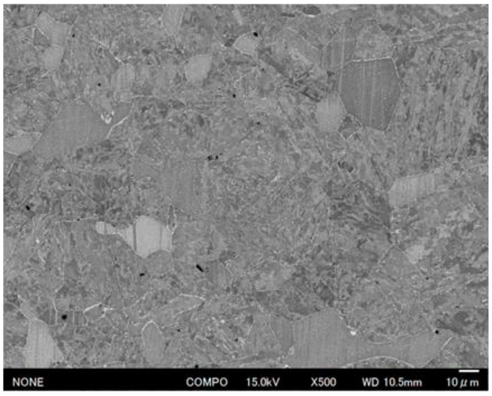
6W	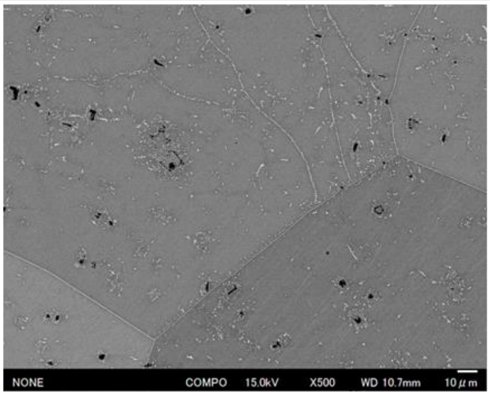	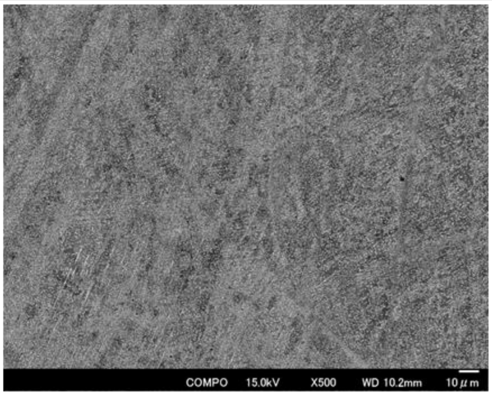

Figure 2.5 BE images of the surface morphology of all sample before the test.

Table 2.3 Estimated grain size of the alloy before oxidation

Alloy	Grain size (μm)
FC 0W	30
FC 1.5W	388
FC 3W	112
FC 6W	240
WQ 0W	-
WQ 3W	20
WQ 6W	244

2.3.2 Mass change of the sample after oxidation test

Figures 2.6 and 2.7 show mass change of the FC and WQ samples after the oxidation test at 923 K up to 345.6 ks. No exfoliation was found on all samples. The mass change value was not significant on both cooling rates alloys, indicating the effect of microstructure due to rapid cooling was minor. In all samples, the oxide growth could be seen gradually decrease after 21.6 ks. As all W added alloys showed a lower mass change to 0W alloys, adding W into 9Cr alloys could improve the oxidation resistance. Drastic improvement was observed from 0W to 3W alloys, which indicates that adding saturated W gave significant improvement to retard the oxidation rate. While an improvement on the mass change by adding more W from 3 mass% to 6 mass% to add volume fraction of Laves phase did not improve the oxidation properties as much as the effect of saturated W gave into the alloy. In comparison, the mass change trend was scattered in the case of low W alloy (FC 1.5W).

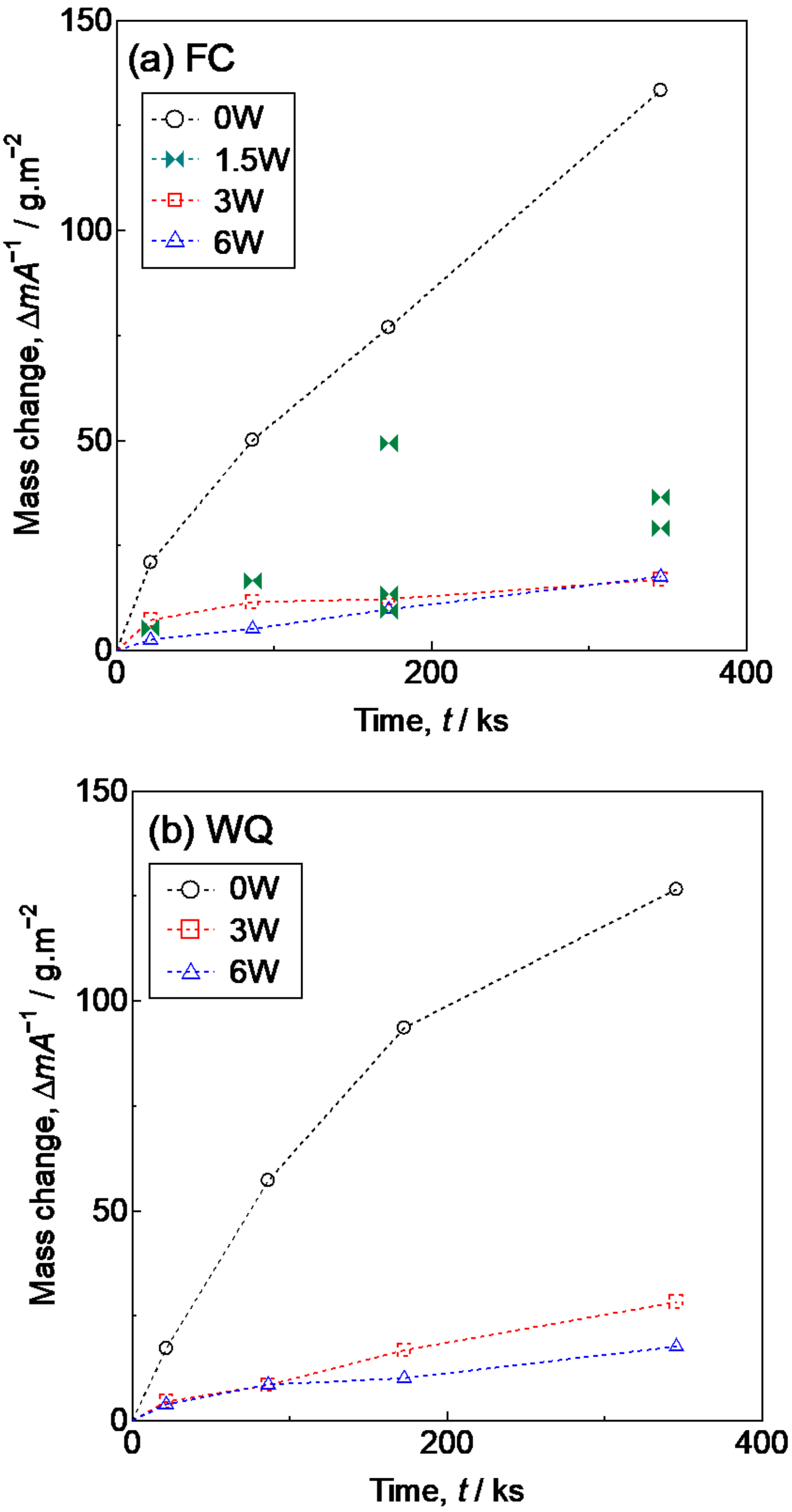

Figure 2.6 Mass change of (a) furnace cooling and (b) water quenching alloys after oxidation test up to 345.6 ks.

2.3.3 Identification of the oxide scale

Figures 2.7 - 2.10 shows the XRD pattern from all samples after the oxidation test up to 345.6 ks. As shown in Fig. 2.7, the oxide formed on both FC 0W and WQ 0W was dominated by FeO in the early stage of the oxidation test and then dominated by Fe_3O_4 after oxidization for 84.6 ks. Figure 2.8 shows the data from samples with lower mass change on FC 1.5W. The peaks of α-Fe were still detected on the sample oxidized for 345.6 ks. In comparison, the data from samples with higher mass change, which was not shown in the figure, the sample oxidized for 172.8 ks showed only peaks of Fe_3O_4, and the sample oxidized for 345.6 ks only showed FeO peaks. Different behavior was found on oxide formed on FC 3W, FC 6W, and WQ 6W, which was found to be dominated mainly by FeO. The WQ 3W showed a mixture of the α-Fe, FeO, and Fe_3O_4 for all samples.

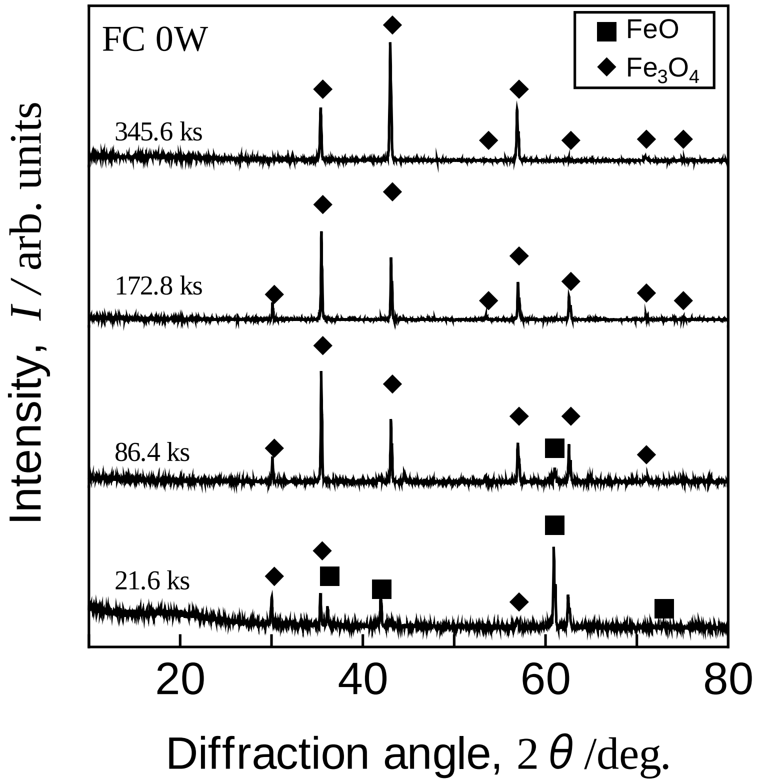

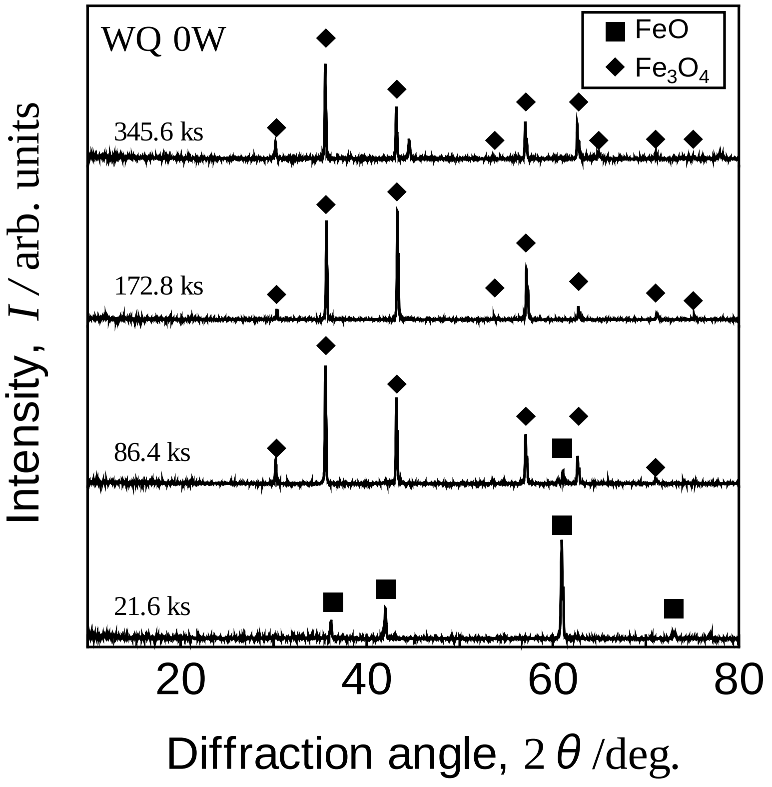

Figure 2.7 XRD patterns of 0W alloys after oxidation test up to 345.6 ks.

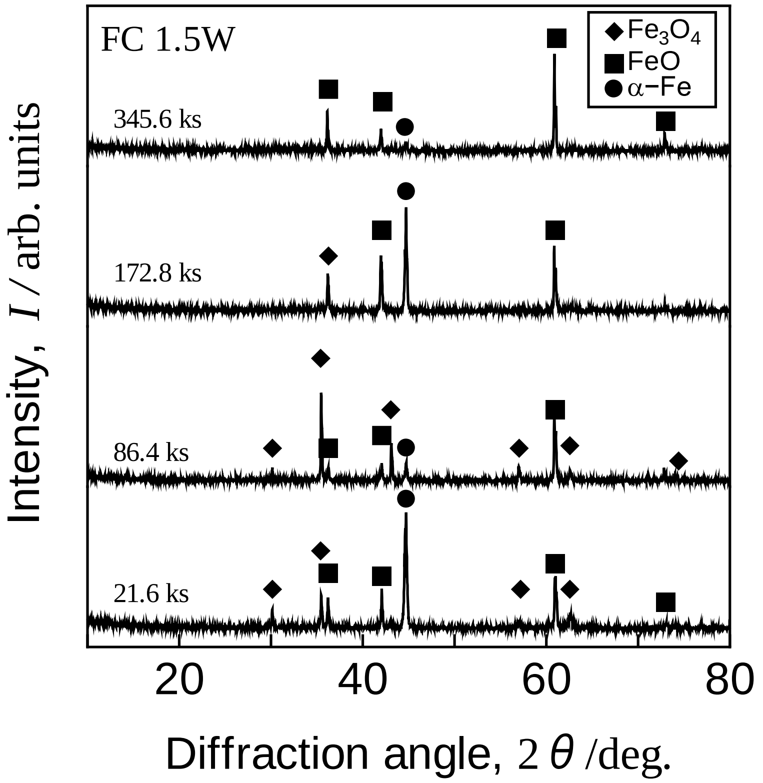

Figure 2.8 XRD patterns of FC 1.5W alloys after oxidation test up to 345.6 ks.

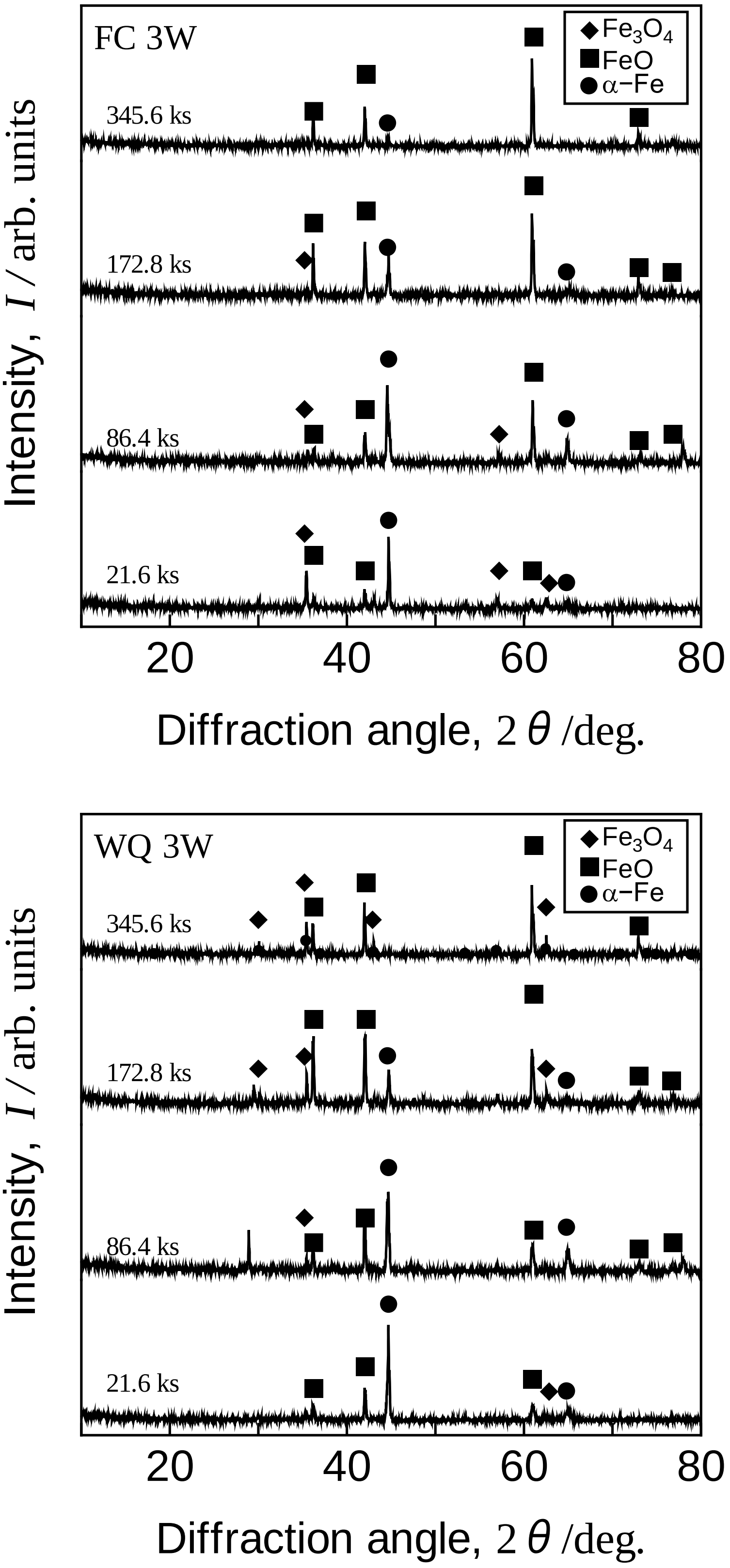

Figure 2.9 XRD patterns of 3W alloys after oxidation test up to 345.6 ks.

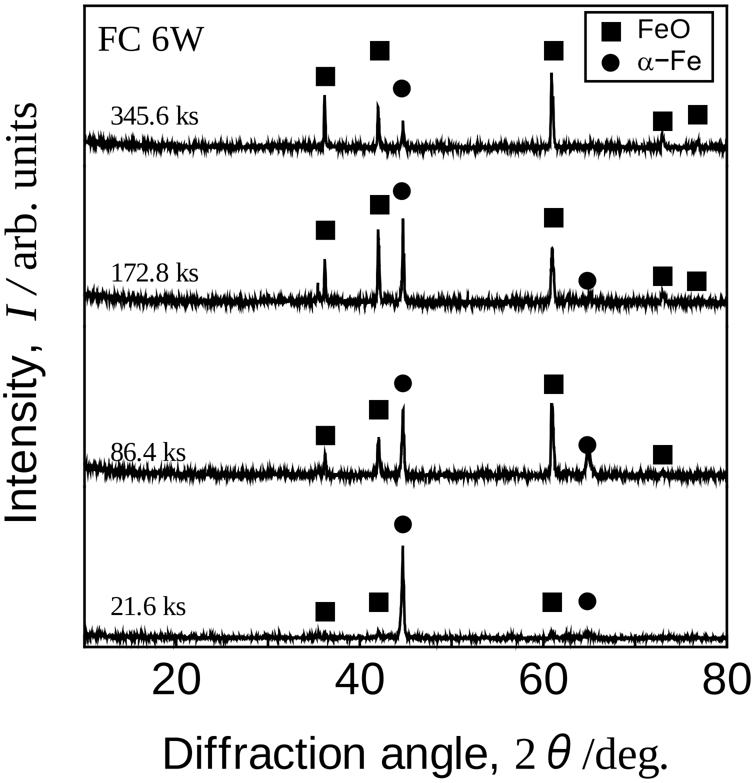

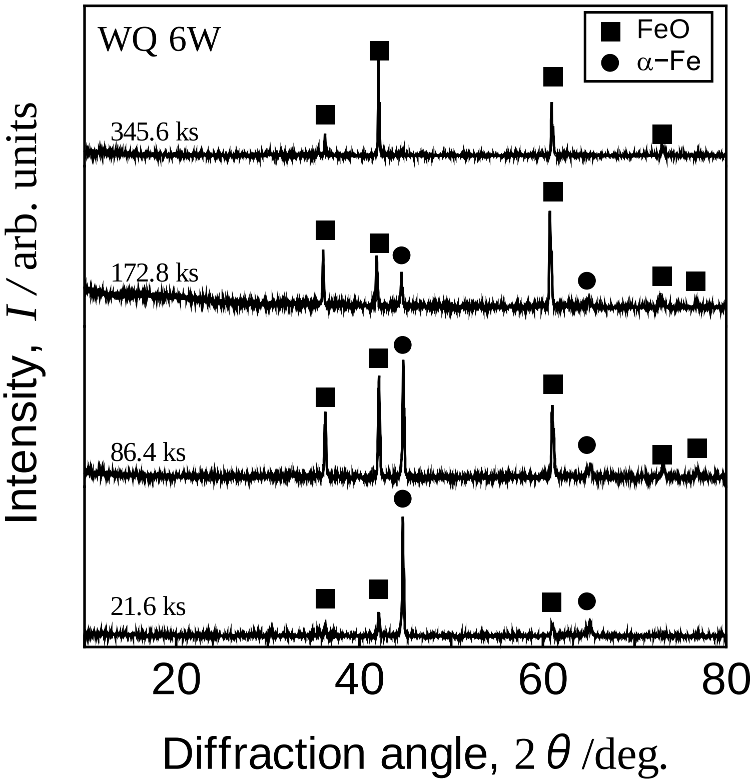

Figure 2.10 XRD patterns of 6W alloys after oxidation test up to 345.6 ks.

2.3.4 Surface morphology after oxidation

Figures 2.11-2.14 show scale morphology from each sample after the oxidation test up to 345.6 ks observed by FE-SEM. The oxide morphology observed on binary and ternary alloys was different. As shown in Fig. 2.11, bigger oxide grain was observed on both FC 0W and WQ 0W. From the XRD analysis, the outermost scale morphology formed on all FC 0W was expected as Fe_3O_4 while on the WQ 0W oxidized for 21.6 ks was FeO, then developed a Fe_3O_4.

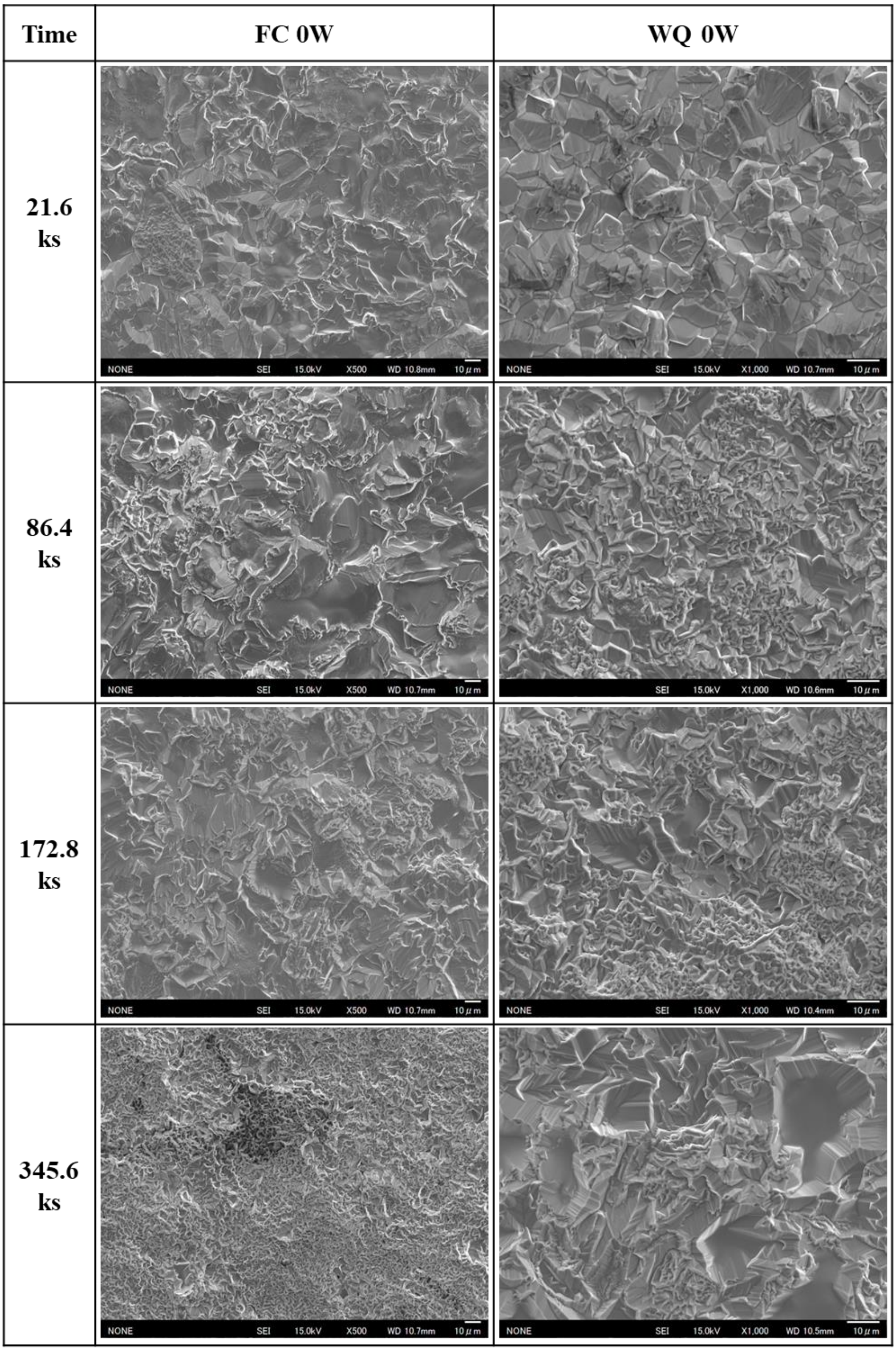

Figure 2.11 SE images of the surface morphology of FC 0W and WQ 0W after the oxidation test up to 345.6 ks.

Compared to binary alloys (Fig. 2.11), the W-added alloys showed a flatter surface with the formation of spike-like and or granule-shaped oxide grain on the top of the sample. (Figs. 2.12-2.14). Since that shape was not observed on the binary samples, the morphologies were suggested to be formed due to the presence of W in the alloy. The growth of spike-like and granule-shaped oxide was observed more in the WQ samples. The WQ 3W formed more granule-shaped oxide at the beginning of the oxidation test, then grew more fractions of spike-like oxide grain on the top of the granule-shape oxide.

The WQ 6W formed longer spike-like oxide on the granule-shaped oxide grain. All W-added FC samples formed non-uniform morphology on the whole sample's surfaces even after being oxidized for 345.6 ks. This non-uniform was found more on FC 1.5W, then more homogeneous with W addition. XRD identified the oxide as FeO on FC 3W and FC 6W. In addition, point analysis was taken of the FC 6W sample after the oxidation test for 345.6 ks. The result shows that Fe and O dominate the surface. The spike-like oxide grain consisted of Fe and W, the granule-shaped oxide grain contained a low concentration of W, and a small amount of Cr was presented on the sample's surface.

Time	FC 1.5W
21.6 ks	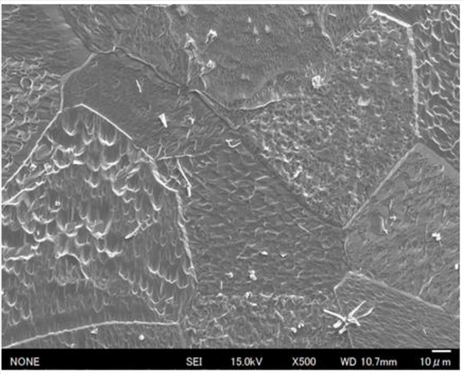
86.4 ks	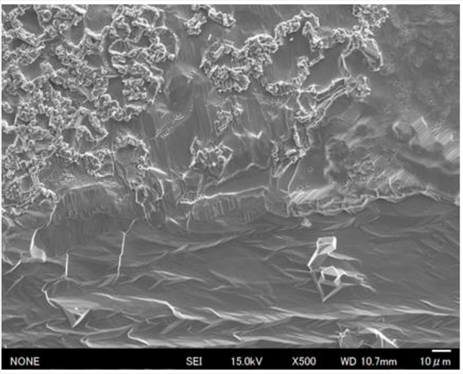
172.8 ks	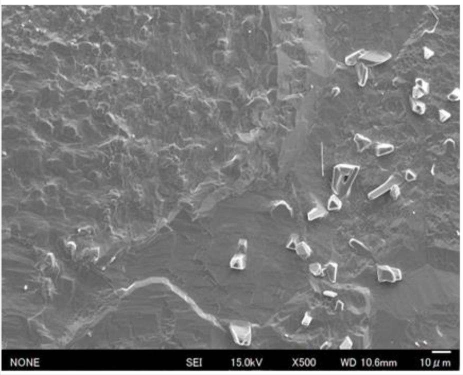
345.6 ks	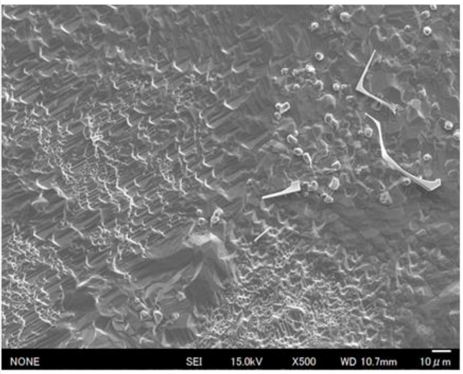

Figure 2.12 SE images of the surface morphology of FC 1.5W after the oxidation test up to 345.6 ks.

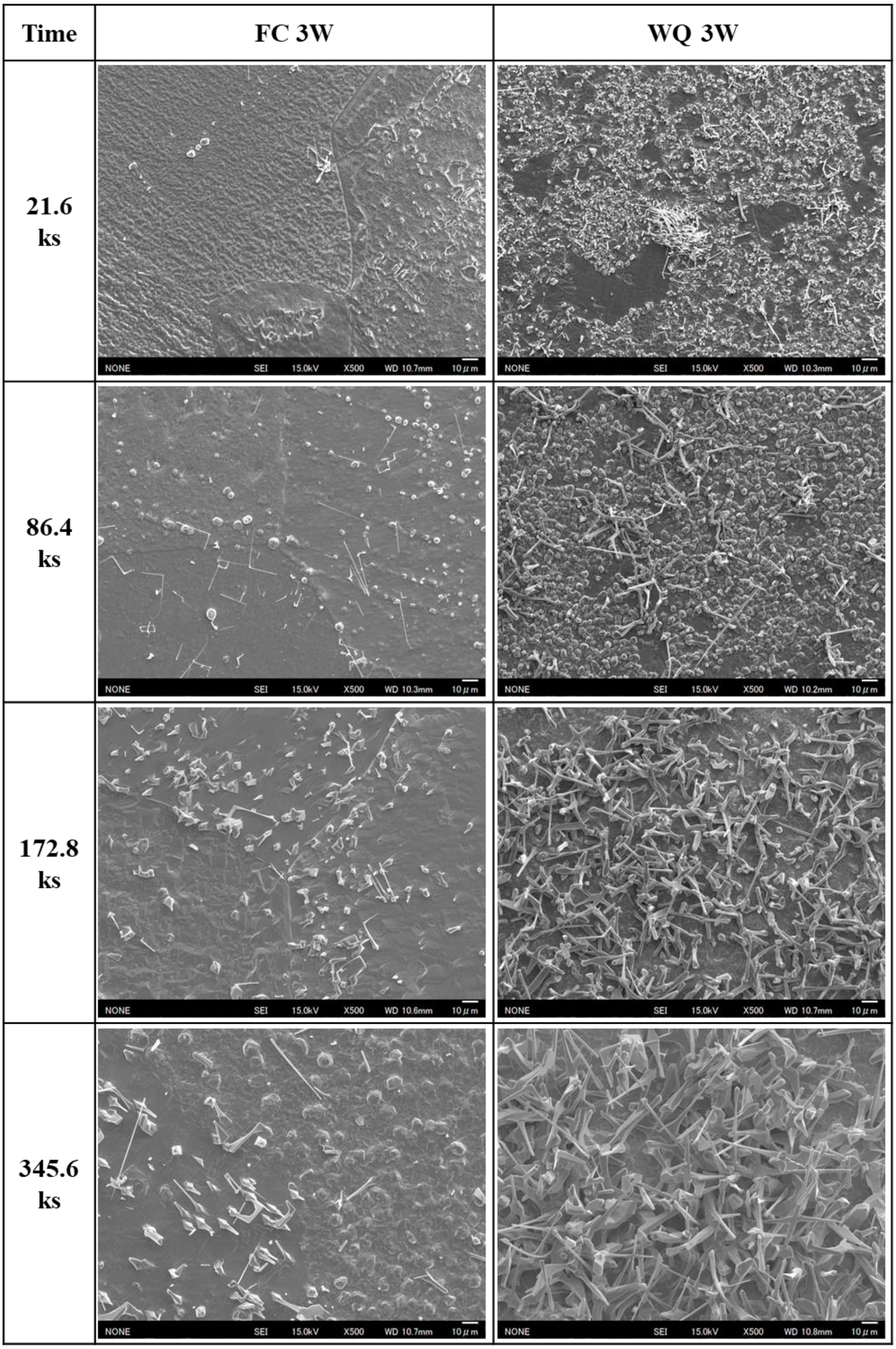

Figure 2.13 SE images of the surface morphology of FC 3W and WQ 3W after the oxidation test up to 345.6 ks.

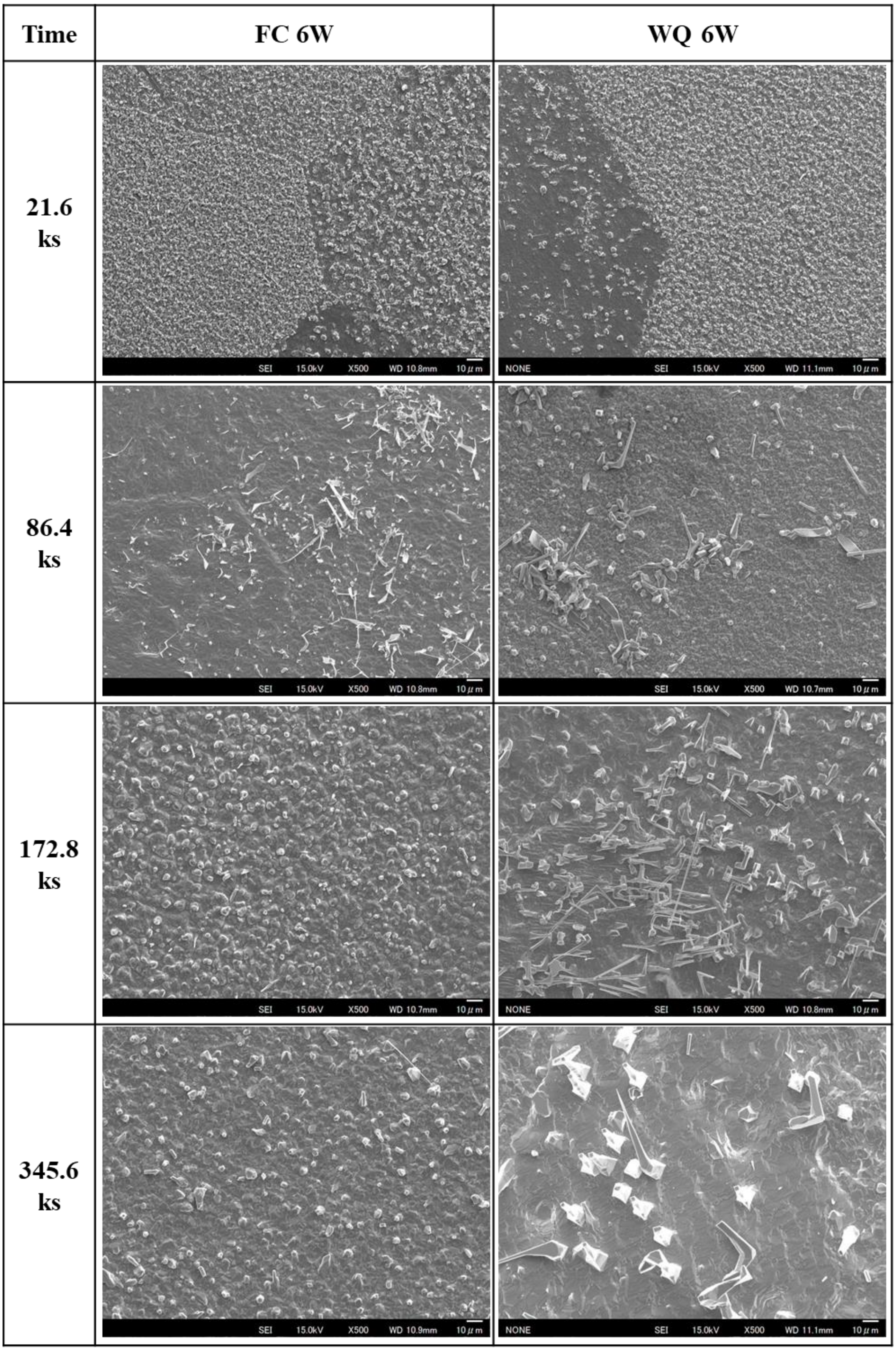

Figure 2.14 SE images of the surface morphology of FC 6W and WQ 6W after the oxidation test up to 345.6 ks.

2.3.5 Cross-sectional images of the oxide scale after the oxidation

Figure 2.15 shows the BE images of the cross-sectional area of FC 0W and WQ 0W oxidized up to 345.6 ks. The binary alloys exhibited a duplex scale from the beginning. Two layers could be distinguished on the outer and inner parts from the BE images. From the XRD, the outer part consisted of FeO on the bottom part and Fe_3O_4 on the outer part. The inner part was divided into the inner scale and internal oxidation zone (IOZ). The growth on the duplex scale on both FC and WQ 0W alloys formed a defect (pores) in the outer/inner scale interface.

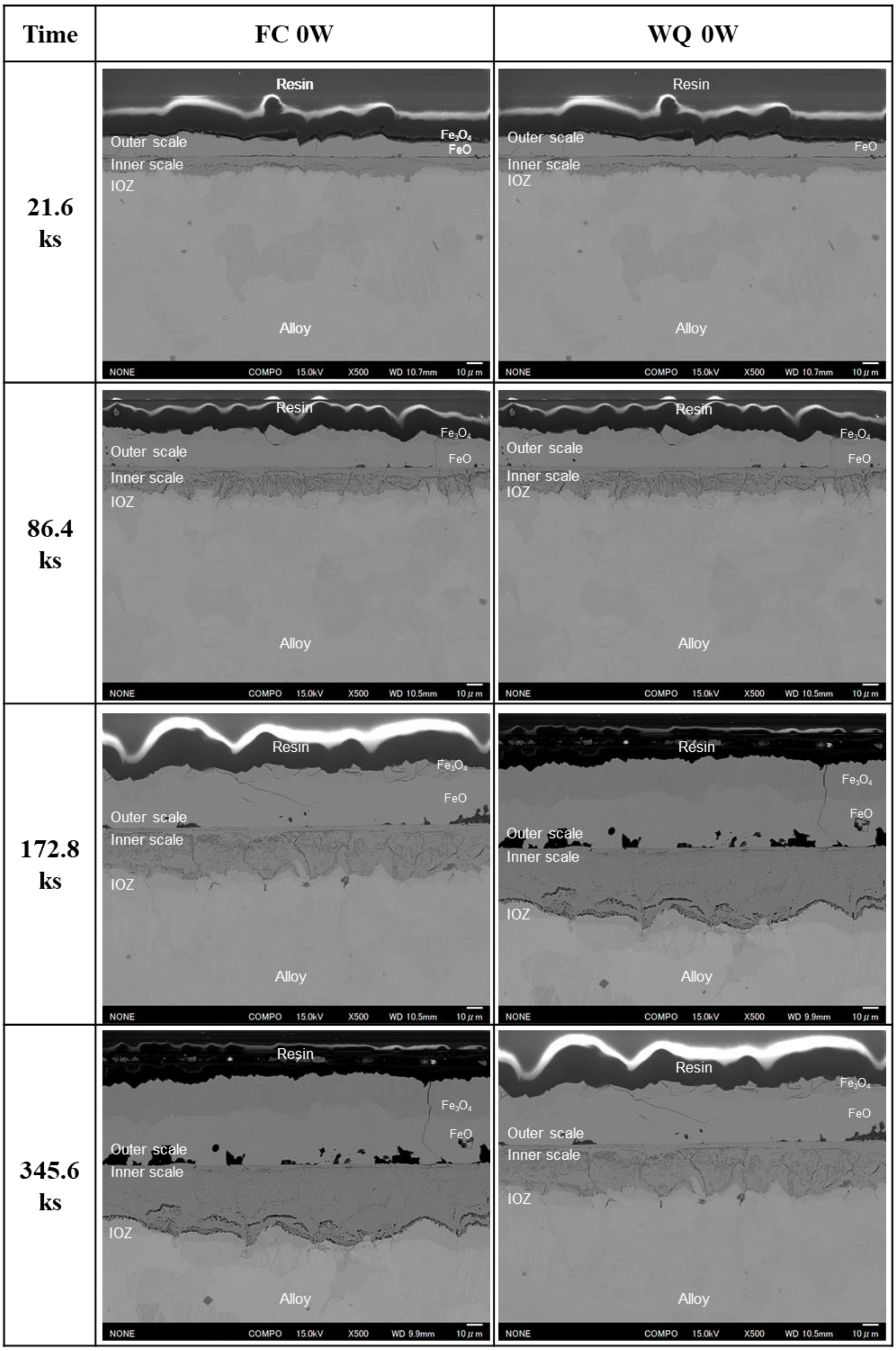

Figure 2.15 BE images of the surface morphology of FC 0W and WQ 0W after the oxidation test up to 345.6 ks.

Figure 2.16 shows the high magnification of the BE images on the sample after the oxidation test for 345.6 ks. It could be seen that severe oxidation attacked the grain boundaries. The difference between FC and WQ 0W alloys could be seen from the orientation of the internal oxidation in the IOZ. The internal oxidation that appeared on the FC sample was dominated by one direction, spike-like, from the oxide to metal direction. As a comparison, the internal oxide particle formed on WQ 0W was more random. In addition, the average thickness of the total scale after oxidation for 345.6 ks was 107 μm and 109 μm for FC 0W and WQ 0W, respectively. Besides, the inner part (inner scale and IOZ) was found even on the WQ 0W.

Figures 2.17 and 2.18 show the elemental mapping from the cross-sectional FC and WQ 0W samples after the oxidation test for 172.8 ks. Due to the different oxide thicknesses, higher magnification images were presented, which were focused on the IOZ side. From the figures, both samples show two layers of iron oxide on the outer scale, and the inner scale consists of $(Fe,Cr)_3O_4$ oxide. The Cr enrichment could be observed along with the darker band and former grain boundaries. This enrichment was more noticeable in the inner part of WQ 0W.

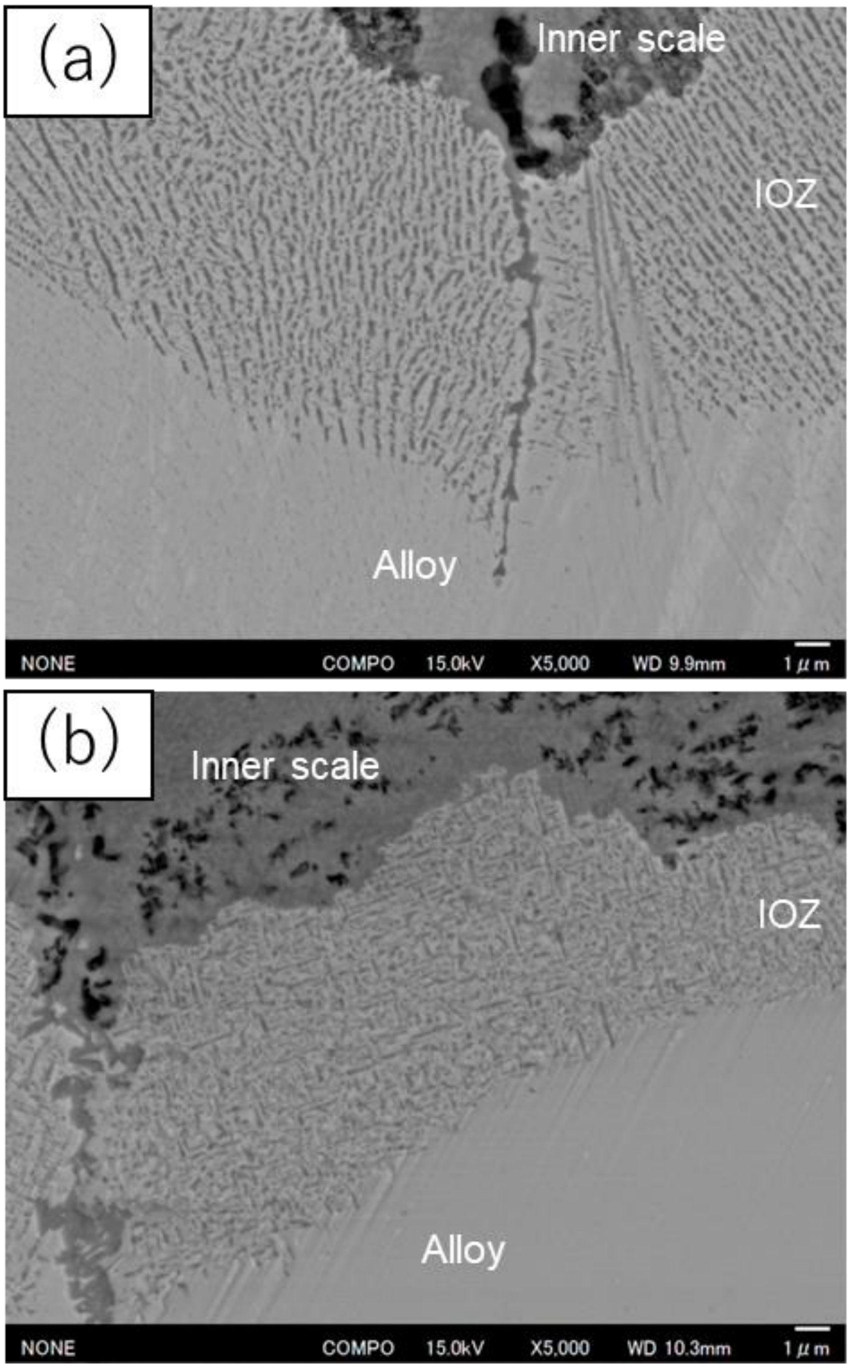

Figure 2.16 High magnification BE images of the cross-sectional of (a) FC 0W and (b) WQ 0W after the oxidation test for 345.6 ks.

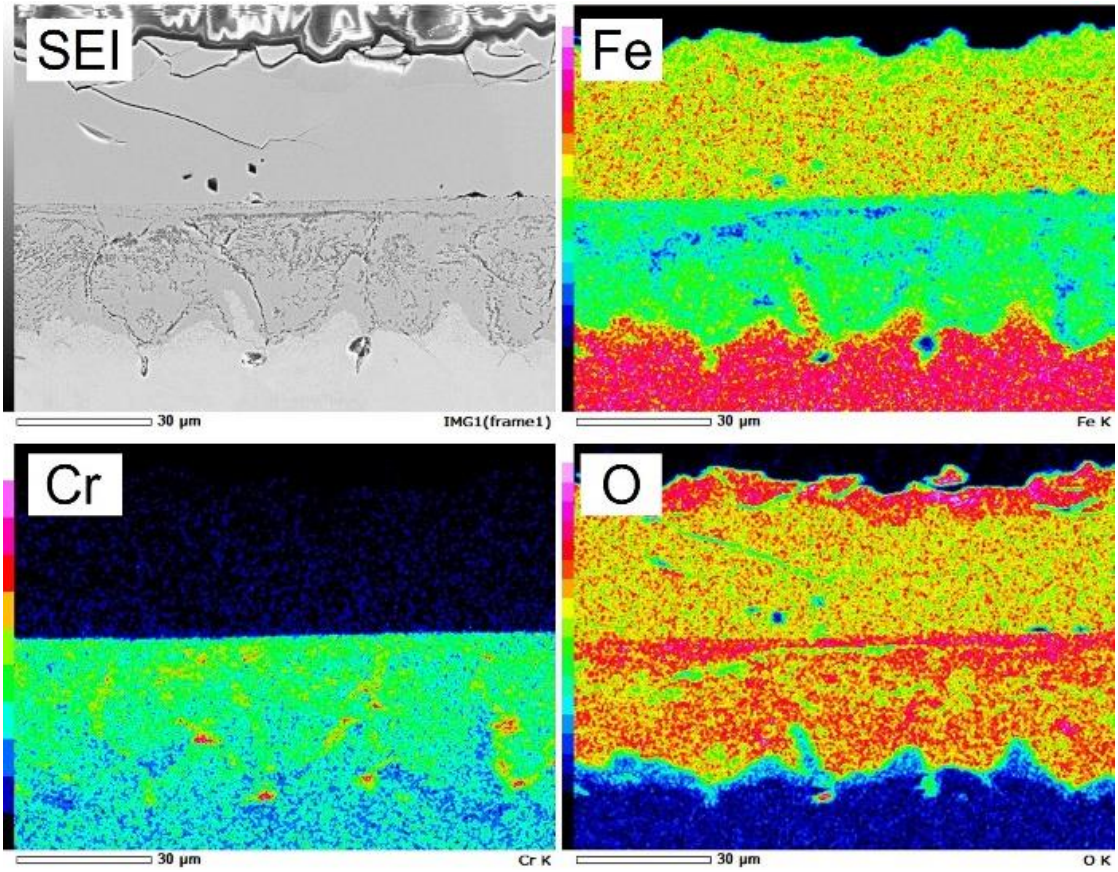

Figure 2.17 Elemental mapping of the cross-sectional of FC 0W after the oxidation test for 172.8 ks.

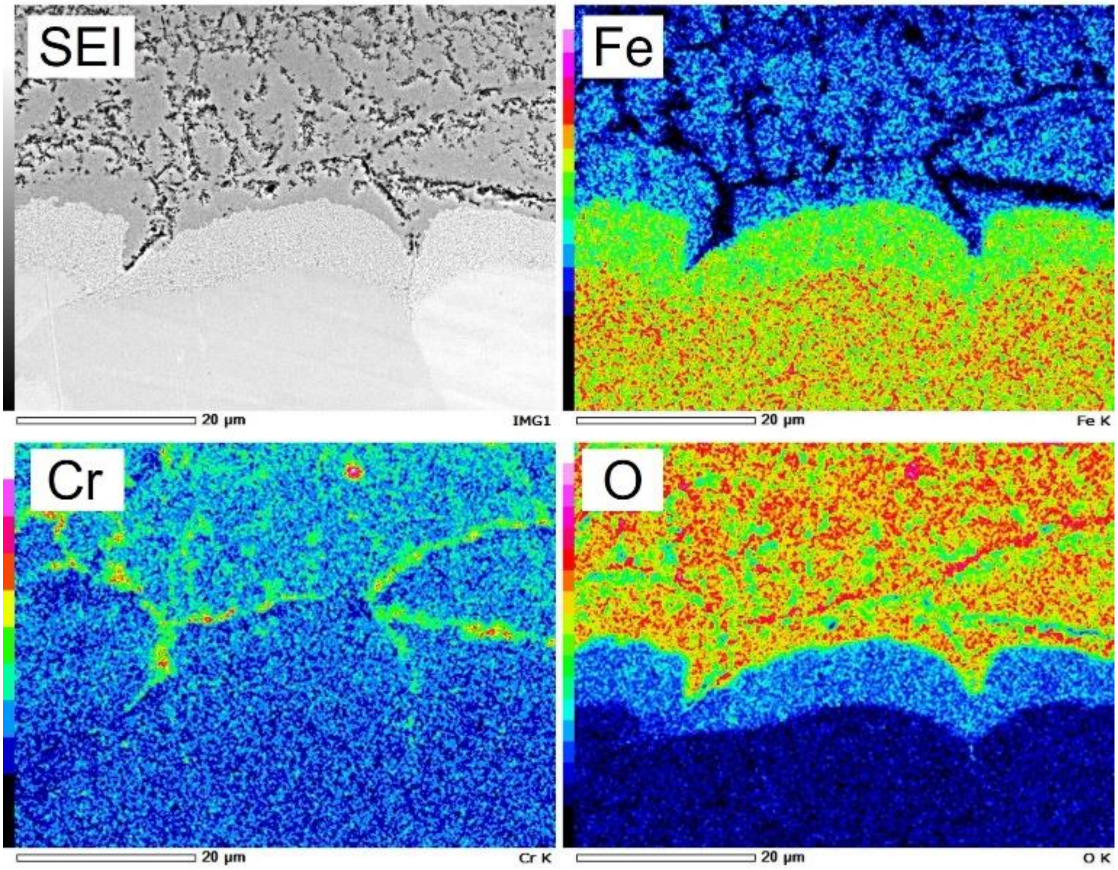

Figure 2.18 Elemental mapping of the cross-sectional of WQ 0W after the oxidation test for 172.8 ks.

Figure 2.19 shows the cross-sectional images from the cross-section of FC 1.5W alloy after the oxidation test up to 345.6 ks. Two different structures with significant thickness differences were observed in one sample of FC 1.5W from the beginning. Figure 2.20 shows the high magnification BE images from the sample oxidized for 345.6 ks. Formation of the duplex scale (thicker area) was observed on almost 70% of the sample. Compared to the duplex scale formed on FC 0W after oxidation for 345.6 ks (107 μ m), the duplex scale formed on FC 1.5W was thinner (39 μ m). In addition, the darker band was observed to be more noticeable in the interface of the inner scale/IOZ. Compared to the duplex scale formed on FC 0W, the ratio of inner scale to IOZ was smaller on FC 1.5 W. The IOZ of FC 0W can occupies more than 80% of inner part, while the IOZ of FC 1.5W only occupy less than 80% inner part. However, it should be noted that the mass change was scattered on the FC 1.5W. The presented data of the sample oxidized for 345.6 ks had thinner overall oxide scale than the sample oxidized for 172.8 ks.

The rest of the cross-section of FC 1.5W appeared as thin oxide without forming an inner scale. The thickness of IOZ on both thinner and thicker parts was about the same. The IOZ of the thinner part showed two different oxide grain sizes with the appearance of a small fraction of white particles at the upper part of IOZ, which was suggested as Laves phase. The outer part of the thinner part consisted of two layers but had a different layer than the outer part of the thicker part (duplex scale). As shown in Fig. 2.8, XRD analysis detected the whole surface was mixed with α-Fe, FeO, and Fe_3O_4.

Figures 2.21 and 2.22 show the elemental mapping for the thicker and thinner area on cross-sectional observed on one FC 1.5W sample oxidized for 345.6 ks. It could be seen that the inner scale of the thicker area was rich in Cr and W. While the IOZ on both the thicker area and thinner area was slightly rich in Cr.

Time	FC 1.5W (thick)	FC 1.5W (thin)
21.6 ks	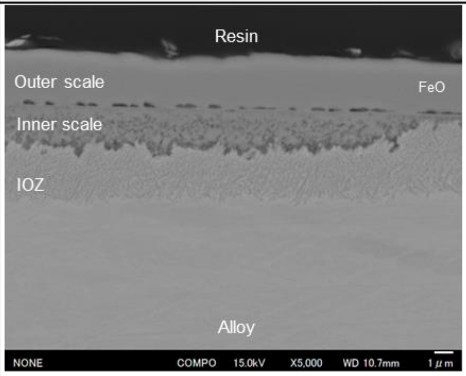	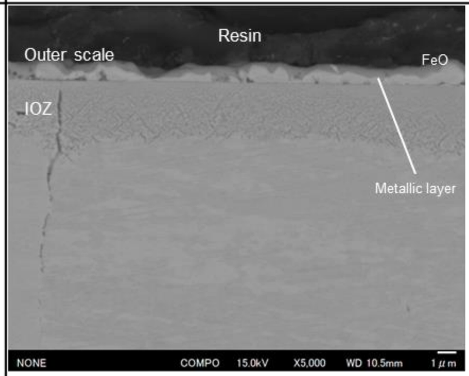
86.4 ks	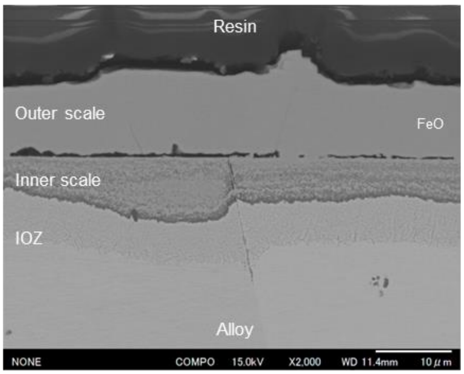	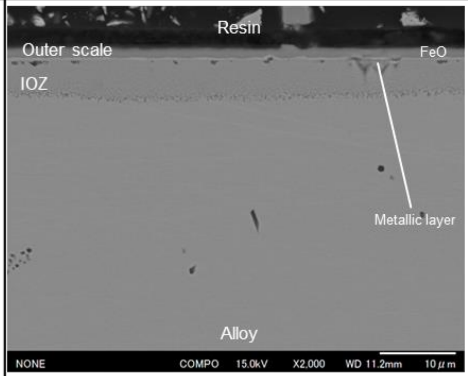
172.8 ks	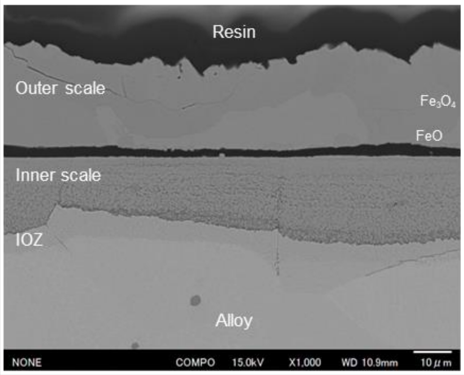	**No thin oxide**
345.6 ks	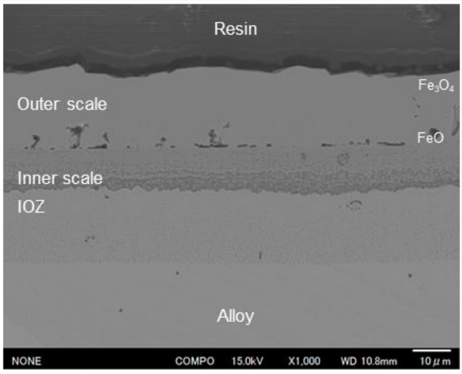	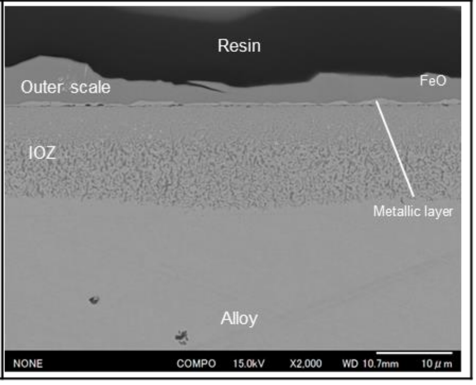

Figure 2.19 BE images of the cross-sectional of FC 1.5W after the oxidation test up to 345.6 ks.

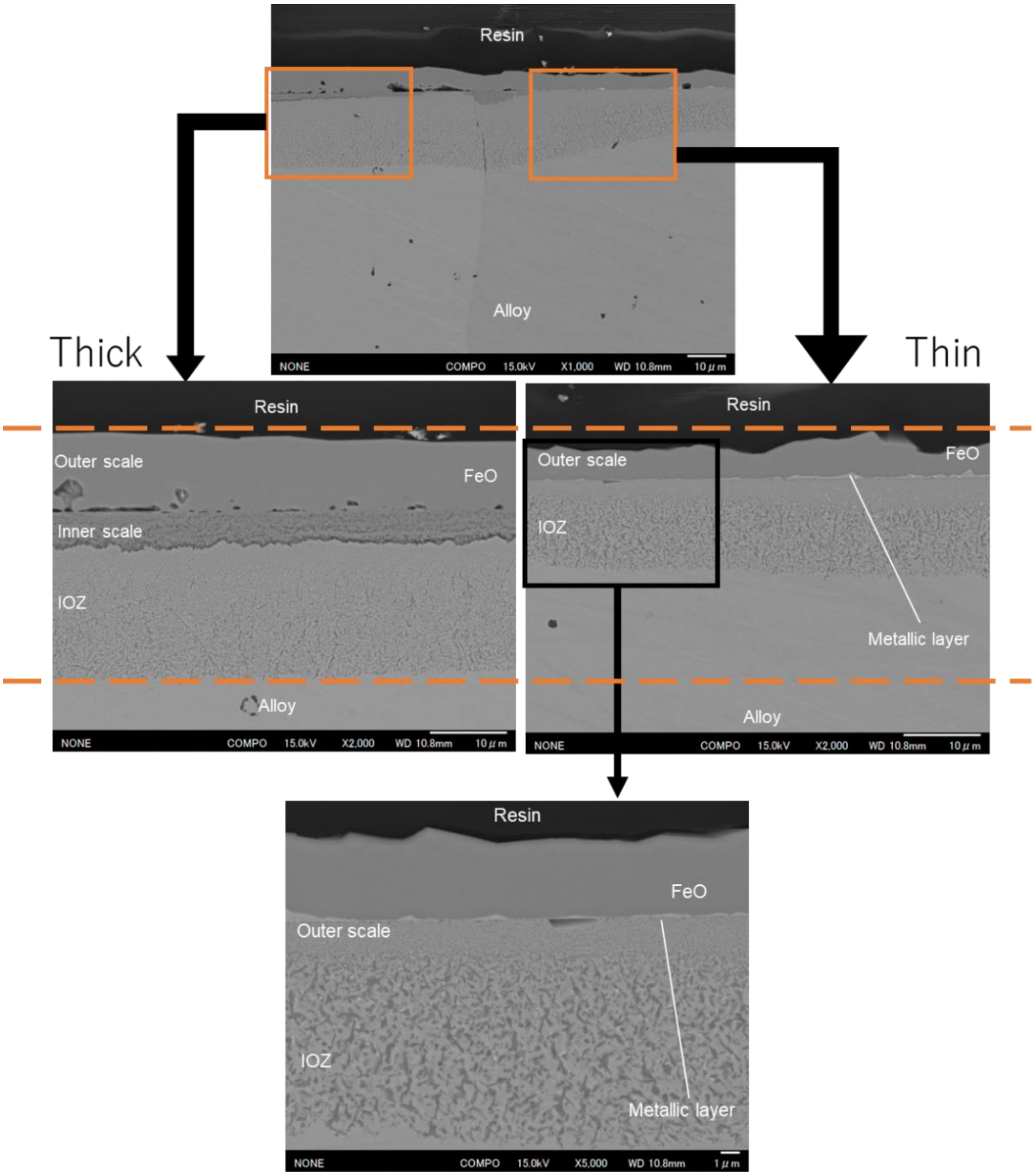

Figure 2.20 High magnification BE images of the cross-sectional of FC 1.5W after oxidation test for 345.6 ks.

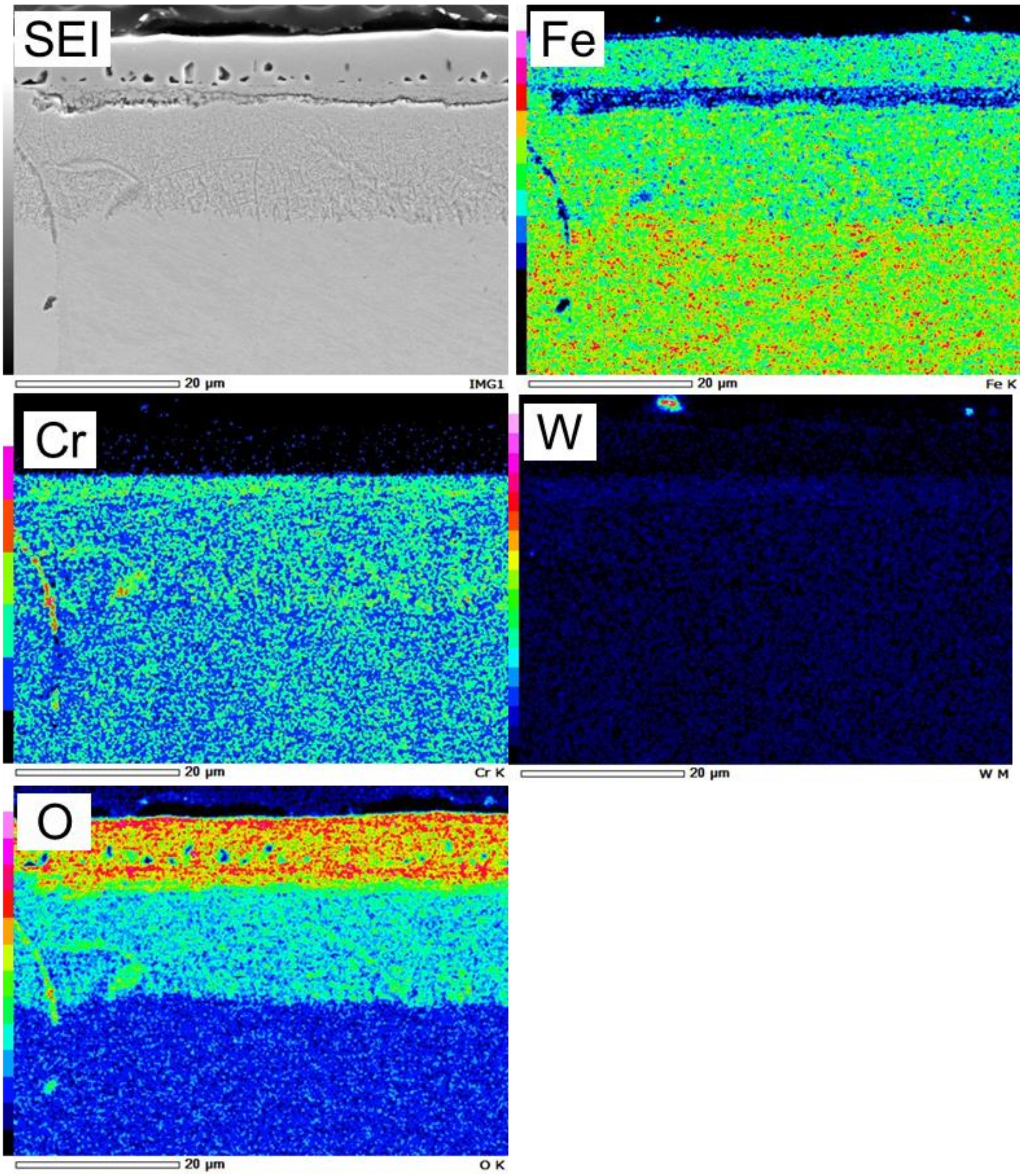

Figure 2.21 Elemental mapping of the cross-sectional of thicker part of FC 1.5W after the oxidation test for 345.6 ks.

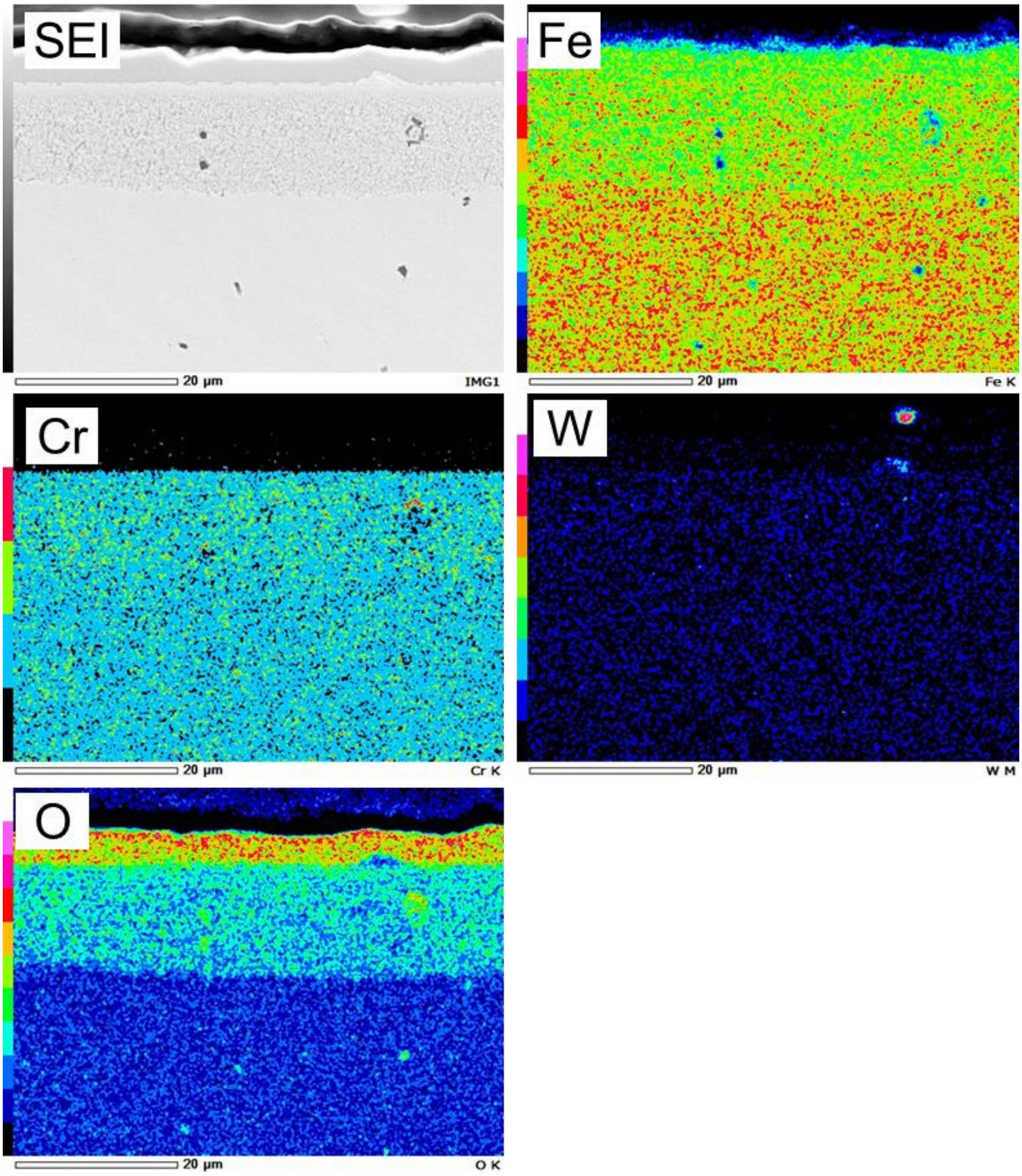

Figure 2.22 Elemental mapping of the cross-sectional of thinner part of FC 1.5W after the oxidation test for 345.6 ks.

Figure 2.23 shows the BE images of the cross-sectional images from FC 3W after the oxidation test up to 345.6 ks. Similar to the FC 1.5W alloys, the FC 3W formed two different thicker and thinner oxide structures. The ratio of the thicker part (duplex scale) to the thinner part was about 1:1, which is less than FC 1.5W. As shown in Fig. 2.9, XRD analysis showed that the oxide on FC 3W up to 345.6 ks was dominated by FeO, while FC 1.5 W showed a mix of FeO and Fe_3O_4.

Figure 2.24 shows BE images of the cross-sectional images from WQ 3W after the oxidation test up to 345.6 ks. Unlike FC 1.5W and FC 3W, the WQ 3W performed a uniform thin oxide structure on the whole of the sample. However, the mixed structure was found on the 345.6 ks sample with the disappearance of the lath boundaries phenomenon. In this sample, the formation of an inner scale was observed.

Figure 2.25 shows the high magnification of the cross-sectional area of FC 3W and WQ 3W oxidized for 172.8 ks. The size of internal oxidation grain on all samples was found bigger and darker near the alloy substrate (IOZ front). The former grain boundaries (lath boundaries) experienced more severe oxidation than the grain interior and appeared as a darker band. In addition, this darker band was more noticeable along the interface of the inner scale and IOZ on the thicker oxide structure.

Time	FC 3W (thick)	FC 3W (thin)
21.6 ks	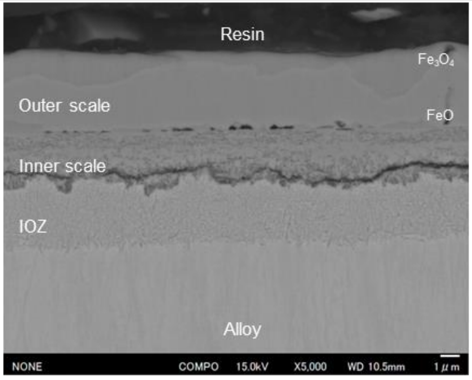	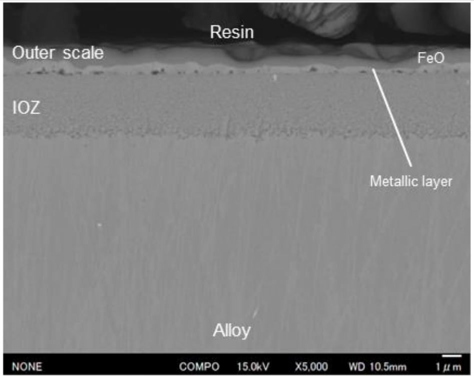
86.4 ks	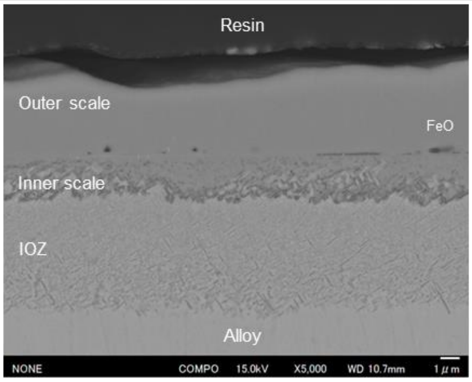	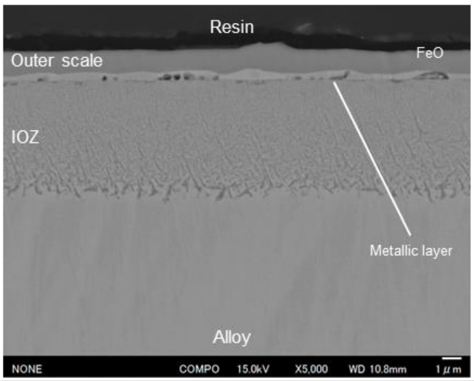
172.8 ks	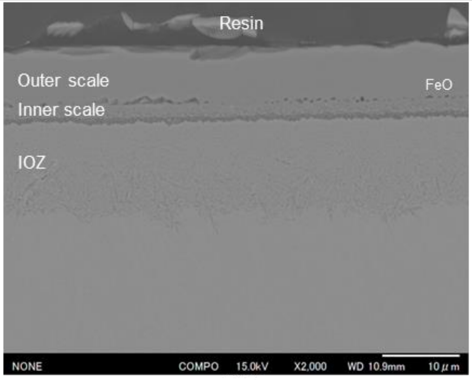	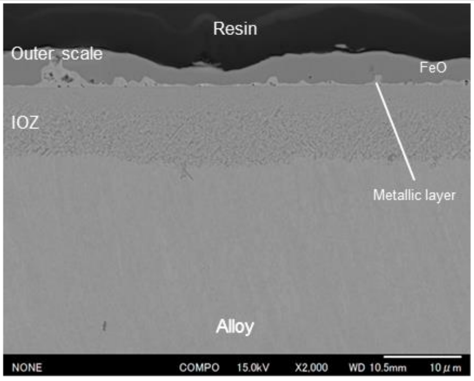
345.6 ks	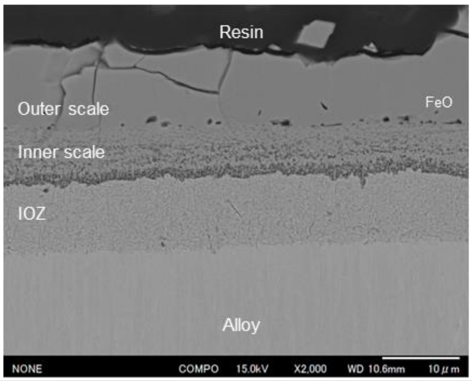	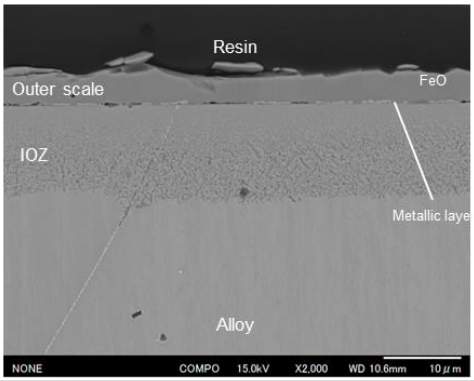

Figure 2.23 BE images of the cross-sectional of FC 3W after the oxidation test up to 345.6 ks.

Time	WQ 3W (thick)	WQ 3W (thin)
21.6 ks	**No thick oxide**	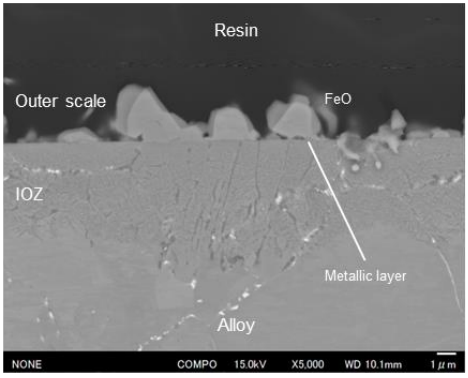
86.4 ks	**No thick oxide**	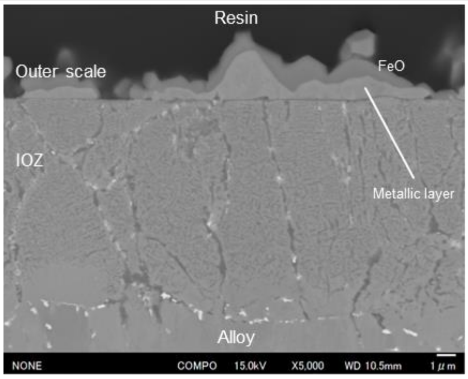
172.8 ks	**No thick oxide**	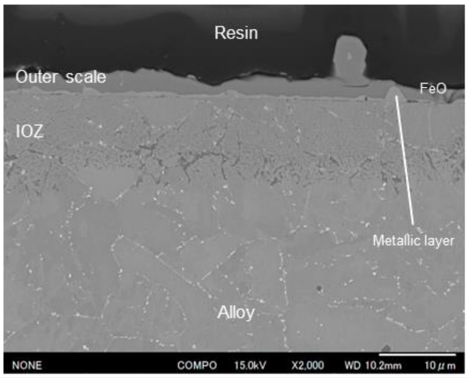
345.6 ks	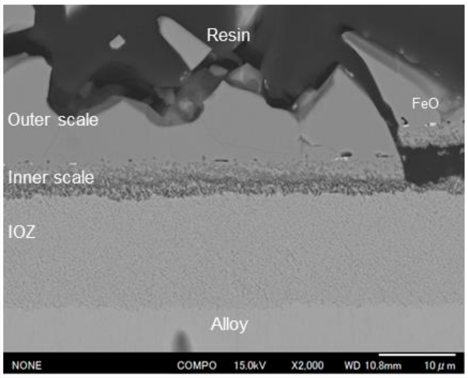	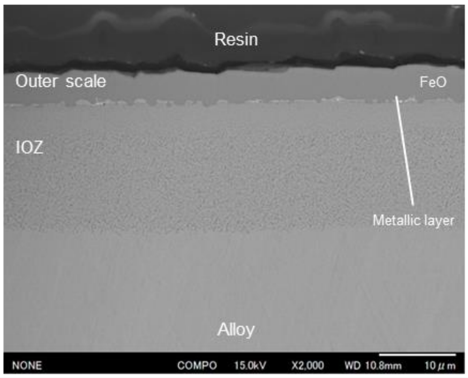

Figure 2.24 BE images of the cross-sectional of WQ 3W after the oxidation test up to 345.6 ks.

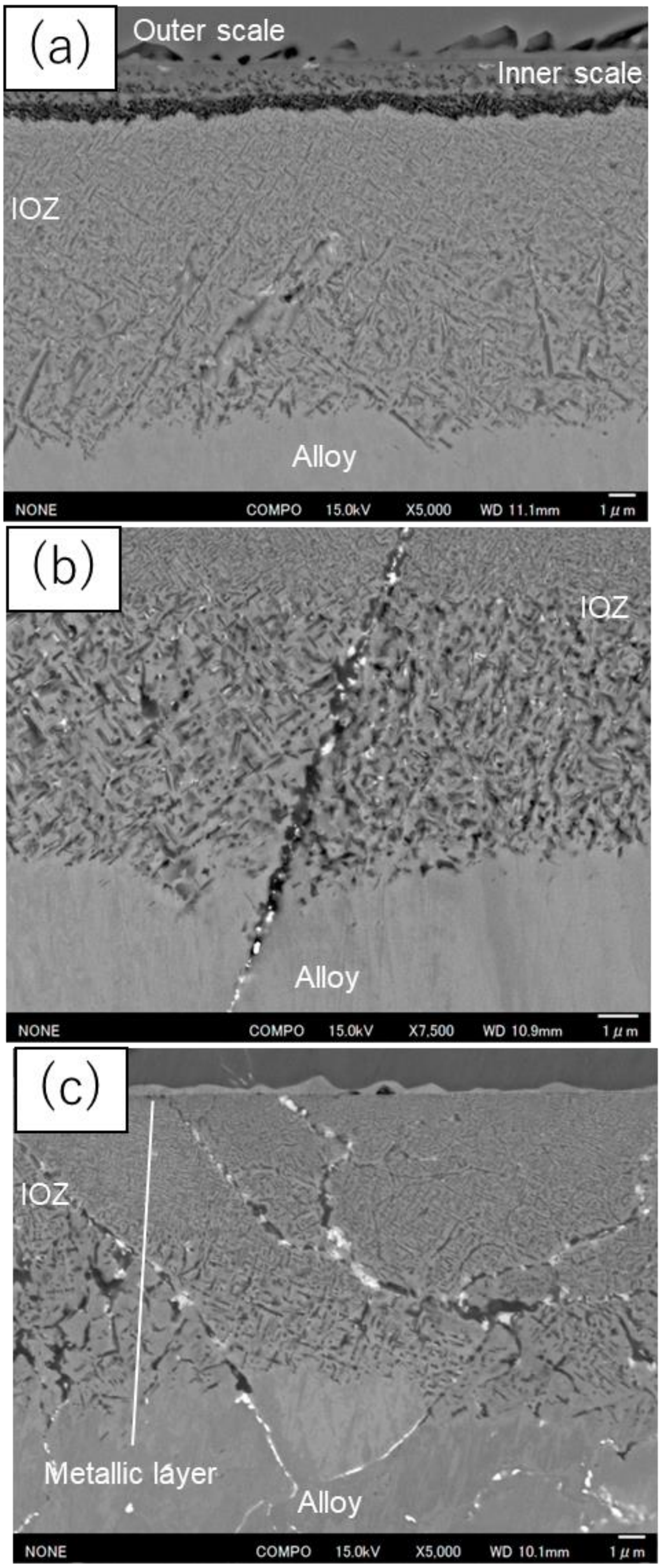

Figure2.25 High magnification BE images of the cross-sectional of (a) FC 3W thicker part, (b) FC 3W thinner part, and (c) WQ 3W after the oxidation test for 172.8 ks.

Figures 2.26 and 2.27 show the elemental mapping for the thicker and thinner area on cross-sectional observed on one FC 3W sample. Compared with FC 1.5W (Figs. 2.21 and 2.22), a distinct Cr-rich layer was found at the bottom part of the inner scale. W was found higher in concentration in this layer than in the matrix. Cr enrichment was also found in the grain boundaries of the thinner area. The elemental mapping confirmed the deposit of metal (mostly Fe).

Figure 2.28 shows the elemental mapping of the cross-sectional area observed on WQ 3W. It could be seen that the darker parts: IOZ front, former grain boundaries, and along the interface of inner scale and IOZ; were rich in Cr. It was observed that precipitation of a small fraction of newly Laves phase precipitated in both inner scale and IOZ. At the same time, former Laves are still not fully oxidized and still decorate the oxidized former grain boundaries. Furthermore, the IOZ was found slightly deeper in the matrix near grain boundaries.

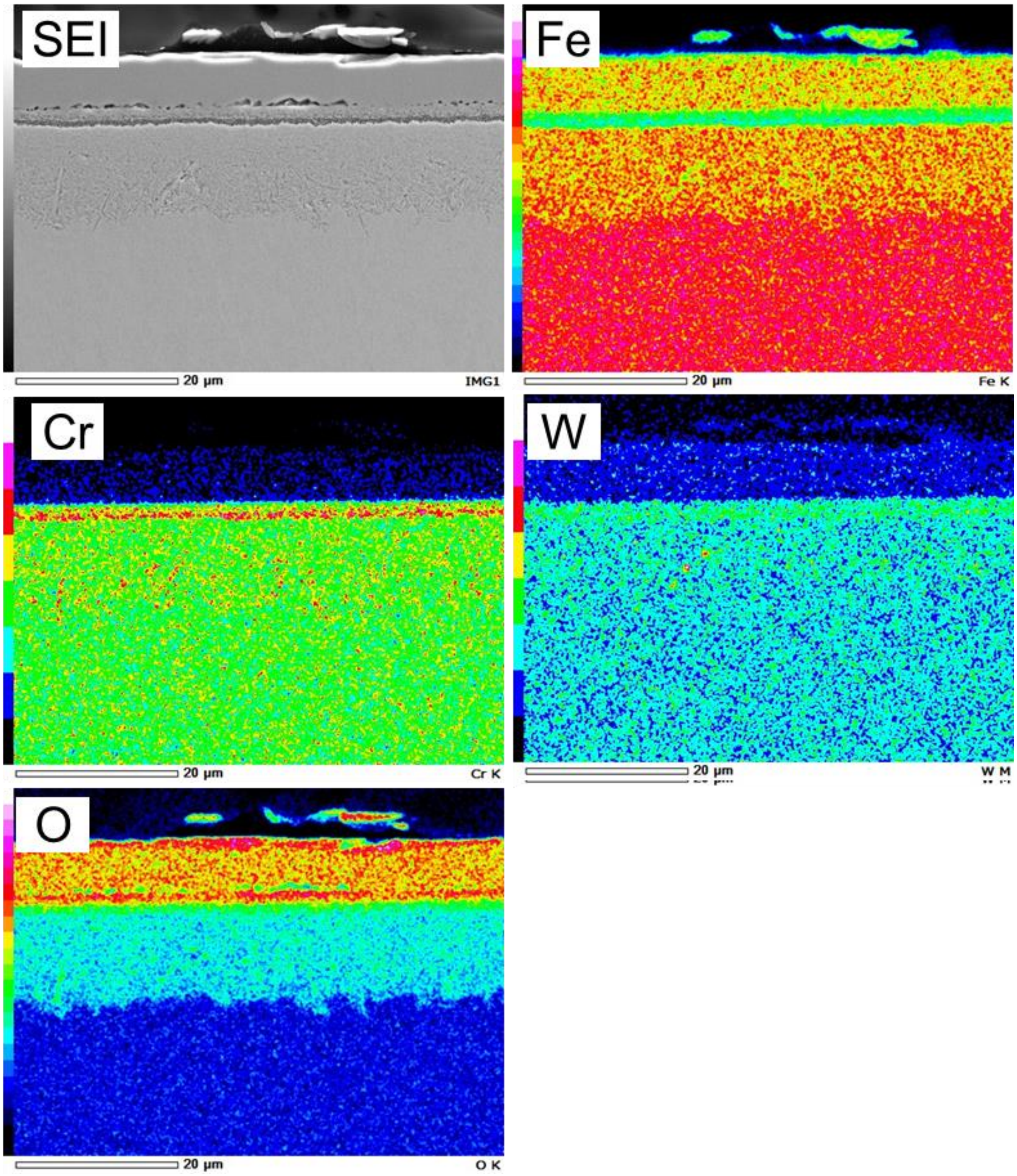

Figure 2.26 Elemental mapping of the cross-sectional of thicker part of FC 3W after the oxidation test for 172.8 ks.

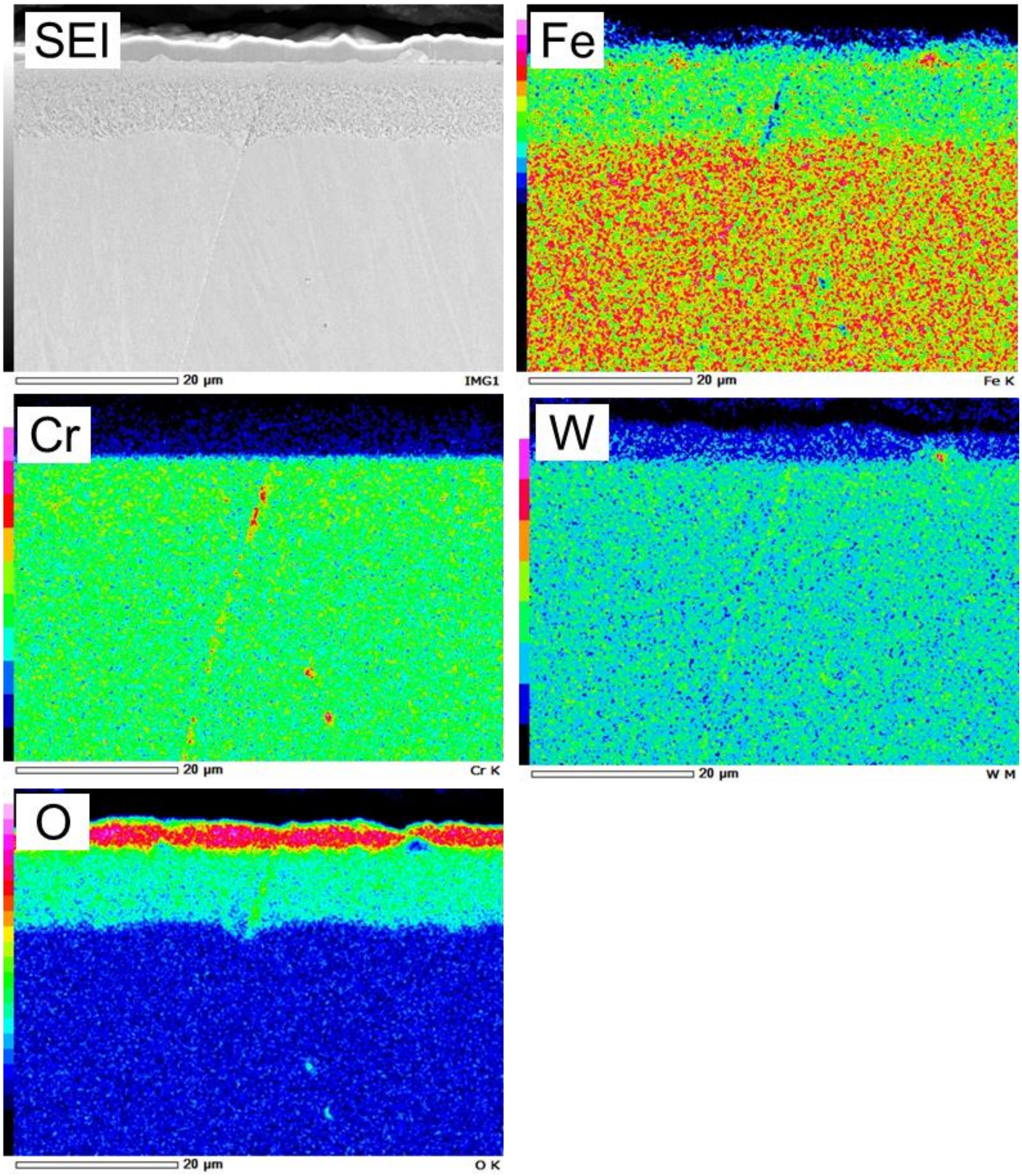

Figure 2.27 Elemental mapping of the cross-sectional of thinner part of FC 3W after the oxidation test for 172.8 ks.

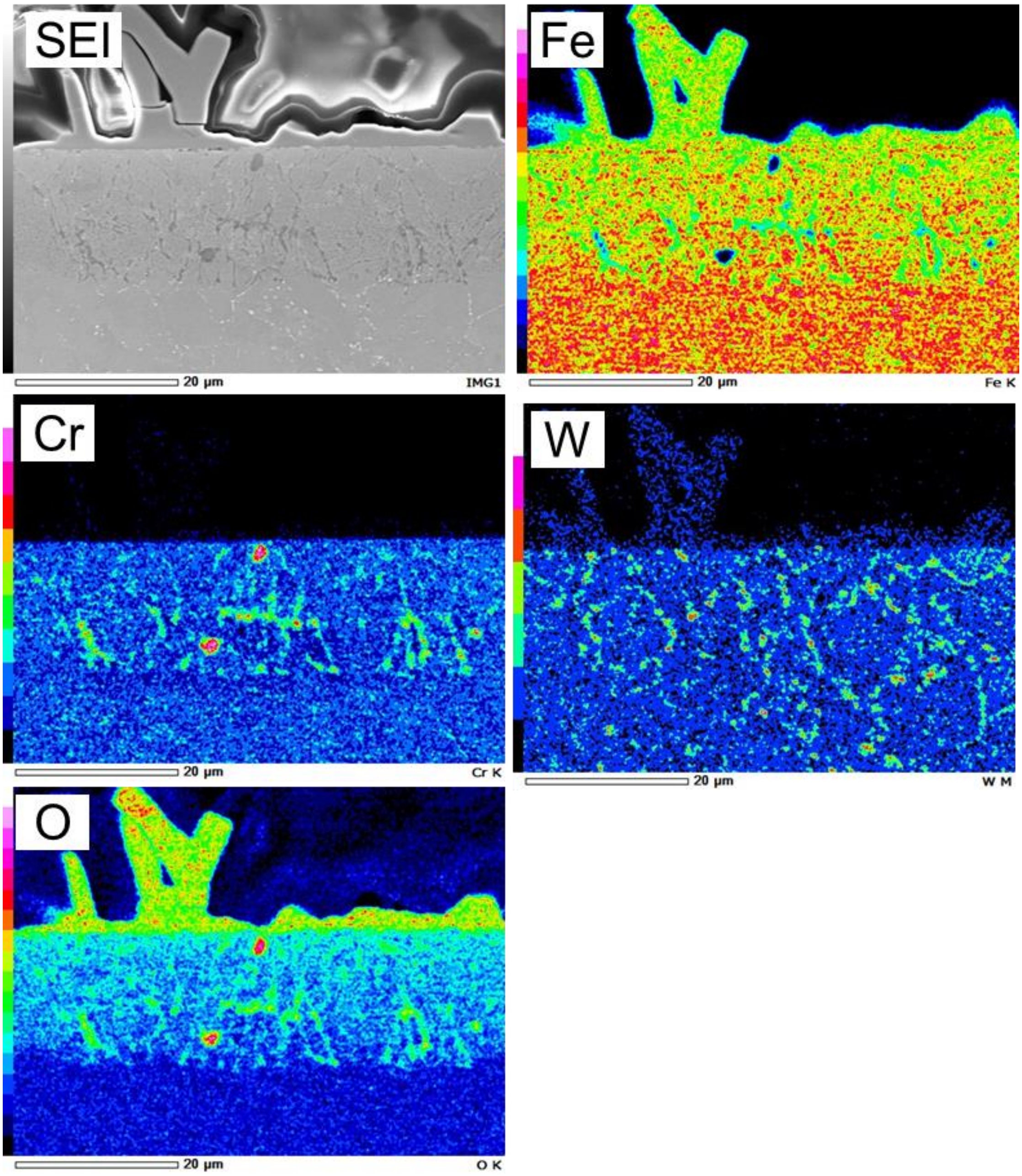

Figure 2.28 Elemental mapping of the cross-sectional of thicker part of WQ 3W after the oxidation test for 172.8 ks.

Figure 2.29 shows the BE images of the cross-section from FC 6W and WQ 6W after oxidation tests up to 345.6 ks. Unlike fewer W alloys, the 6W offers the stability of the thin oxide structure. The scale thickness was about the same on both FC and WQ 6W alloy, although the Laves phase precipitated finer and homogeneously in WQ alloy. In addition, the formation of a darker band in the IOZ/metal interface was found in the WQ 6W before it started to annihilate by more extended oxidation time. Furthermore, it was found that IOZ od FC 6W grew by the oxidation time, but in the WQ 6W, the growth of IOZ was found to be almost the same after 86.4 ks.

Figure 2.30 shows the high magnification from the inner part of the samples. The figure shows the formation of the new fine Laves phase in the IOZ in FC 6W alloy. In contrast, the precipitation of the newly Laves phase in the WQ 6W, which precipitated a higher volume fraction of the fine Laves phase, was harder to distinguish from the former Laves phase.

Time	FC 6W	WQ 6W
21.6 ks	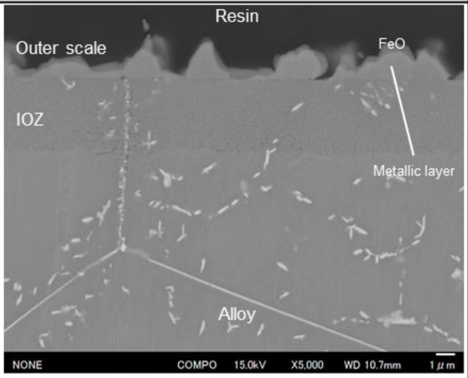	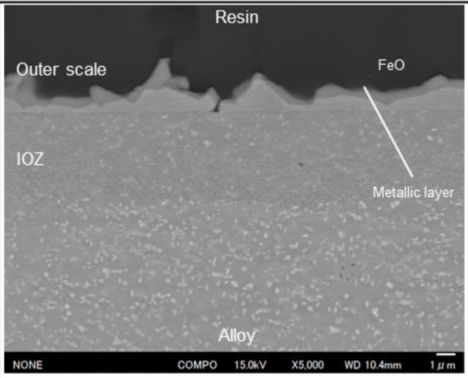
86.4 ks	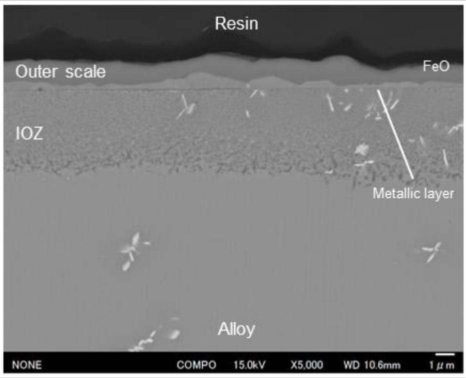	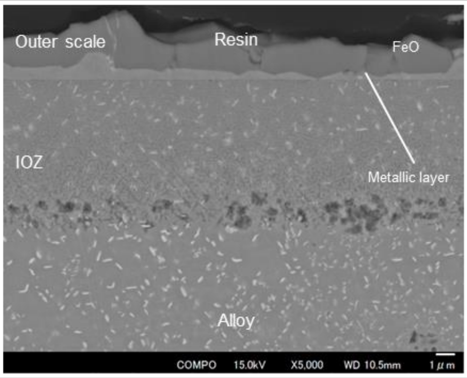
172.8 ks	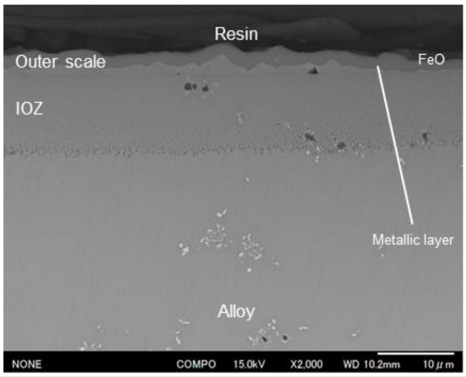	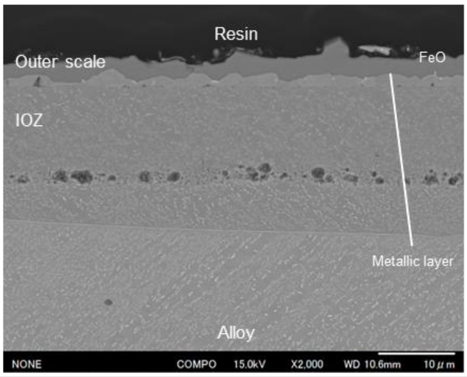
345.6 ks	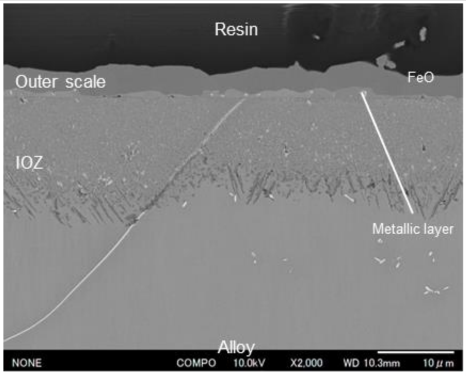	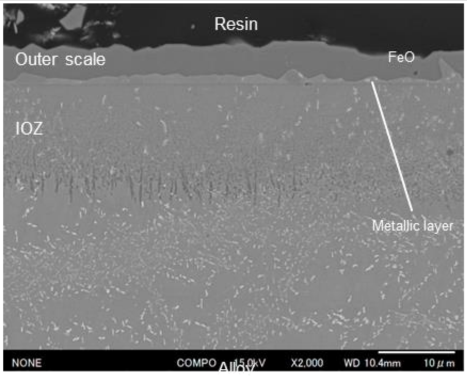

Figure 2.29 BE images of the cross-sectional of FC 6W and WQ 6W after the oxidation test up to 345.6 ks.

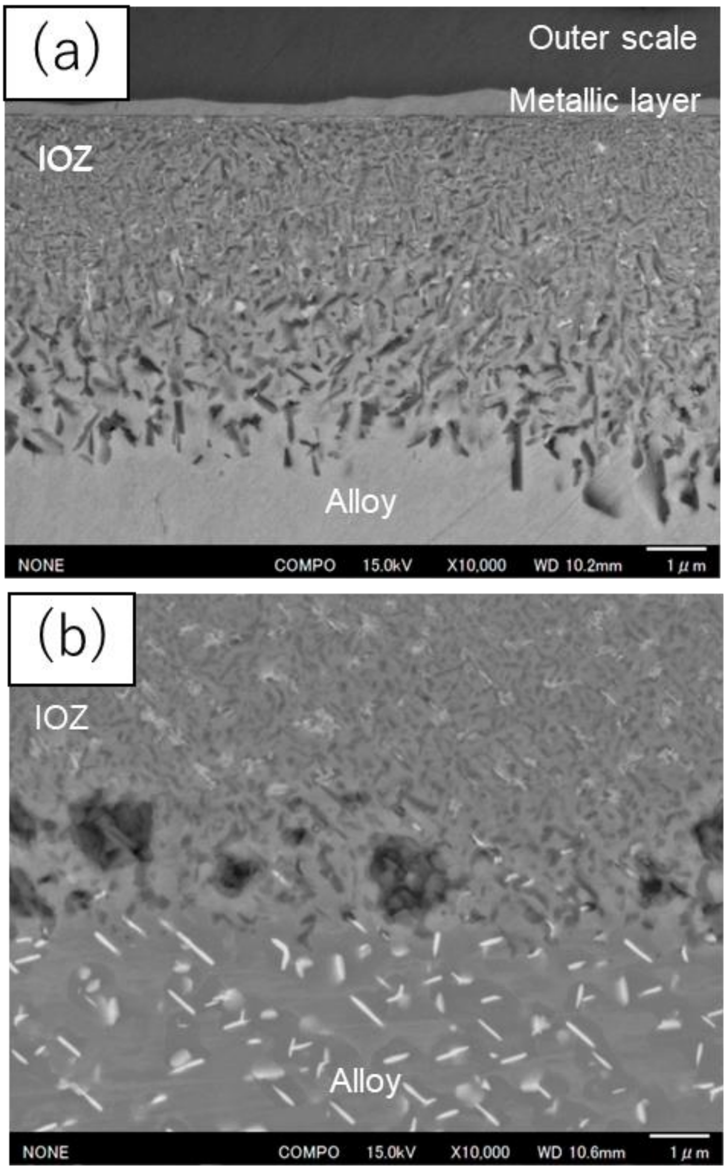

Figure 2.30 High magnification BE images of the cross-sectional of (a) FC 6W and (b) WQ 6W after the oxidation test for 345.6 ks.

Figure 2.31 shows the elemental mapping on the cross-sectional FC 6W sample after oxidation test for 172.8 ks. The elemental mapping showed almost the same behavior as the thinner part observed on FC 3W (Fig. 2.27). However, a more homogeneous Cr enrichment was found on the FC 6W alloy. The W enrichment was also found mostly on IOZ and precipitates. The elemental mapping confirmed the metal (mostly Fe) layer, which was not oxidized. Figure 2.32 shows the elemental mapping of the cross-sectional area observed on WQ 6W after the oxidation test for 172.8 ks. It could be seen that the darker parts, which were more distinct in WQ 6W, were rich in Cr. The other behavior was about the same with the FC 6W.

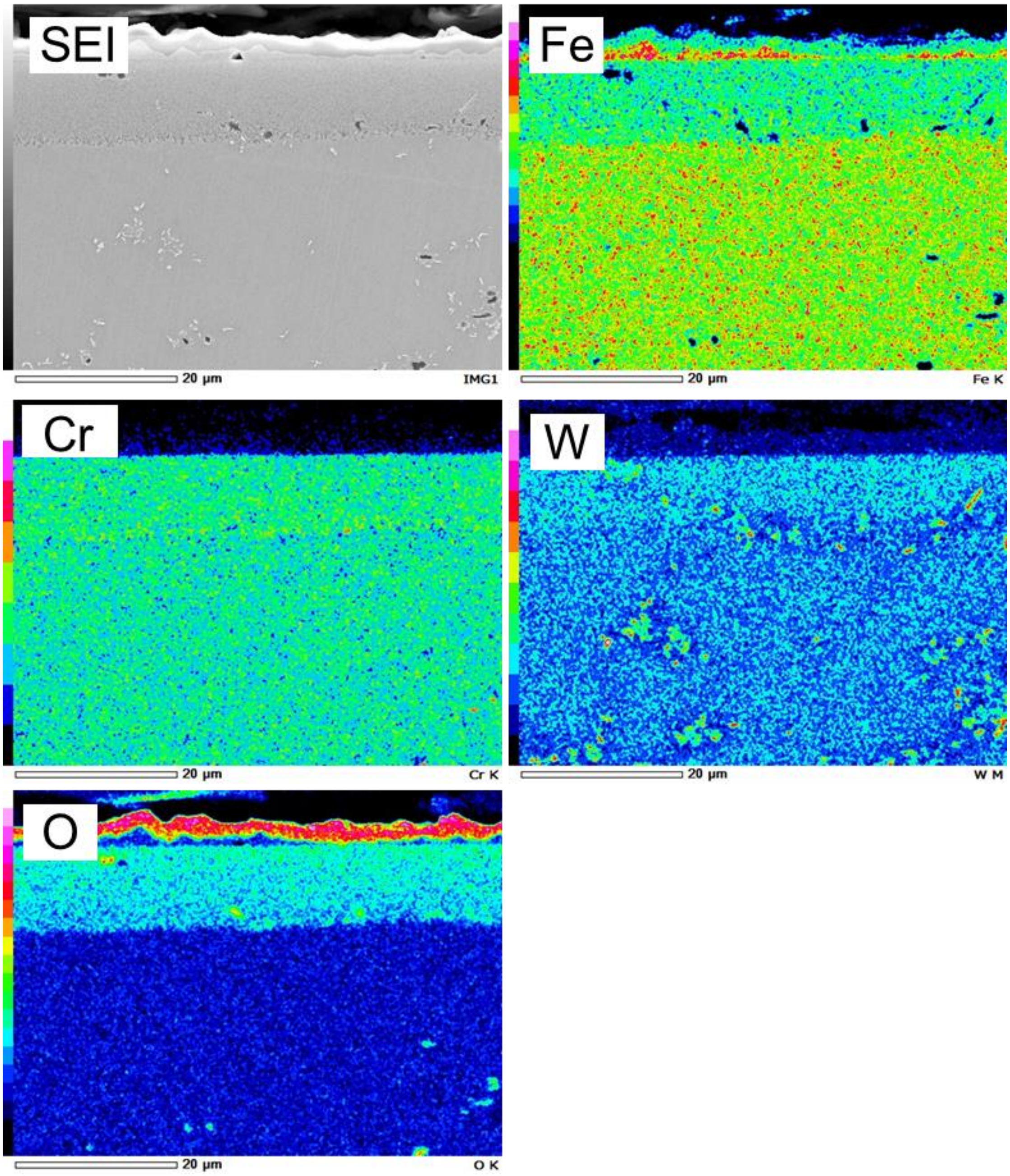

Figure 2.31 Elemental mapping of the cross-sectional of FC 6W after the oxidation test for 172.8 ks.

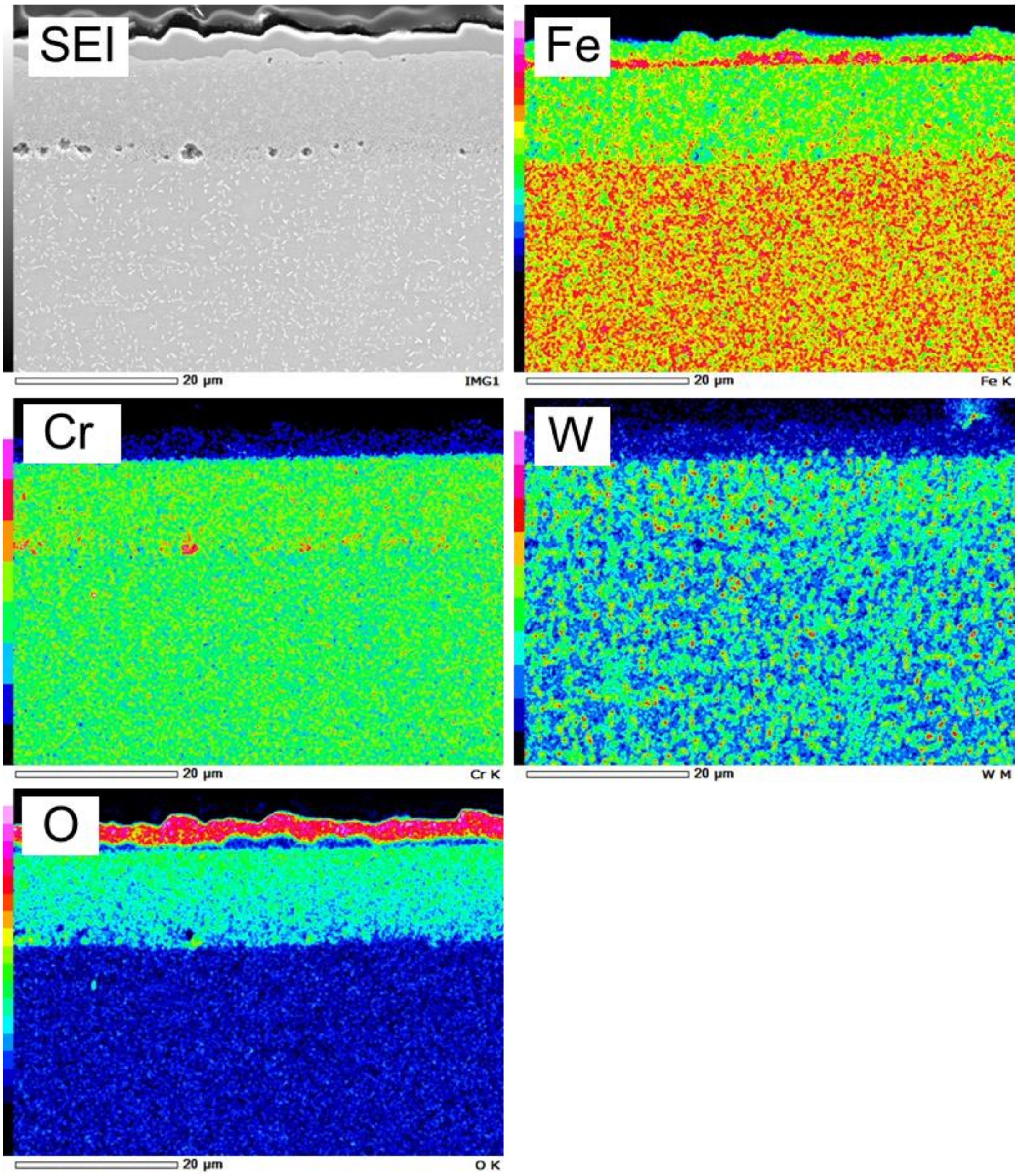

Figure 2.32 Elemental mapping of the cross-sectional of WQ 6W after the oxidation test for 172.8 ks.

2.3.6 Thickness of the oxide scale

Figure 2.33 shows the thickness trend of the inner part (inner scale + IOZ) and the total scale obtained from 10 points of each sample. The thickness of the FC 1.5W alloy was not included due to instability observed by the mass change profile. It could be seen that W-added alloys developed extremely thin oxide compared to the binary alloy. From the graph, no distinct differences were observed in both FC and WQ 0W. both alloys showed nearly equal thickness between the outer and inner parts of the scale. In contrast, all ternary alloys formed thin oxide scales where the inner scale occupied more than half of the scale. Due to the instability mass change and formed oxide structure, the thickness profile of the oxide on FC 1.5W was not presented in this work. The scale thickness formed on 3W is presented separately, the open mark represents the thick part, and the close dot represents the thinner part. It could be seen that the scale thickness jumped on the WQ 3W sample oxidized for 345.6 ks due to the formation of the duplex scale. Compared to the 3W, 6W developed a thicker metal layer, but the thickness of the IOZ was almost the same as the observed thinner area of 3W. Furthermore, it was found that IOZ od FC 6W grew by the oxidation time, but in the WQ 6W, the growth of IOZ was relatively small after oxidation for 86.4 ks.

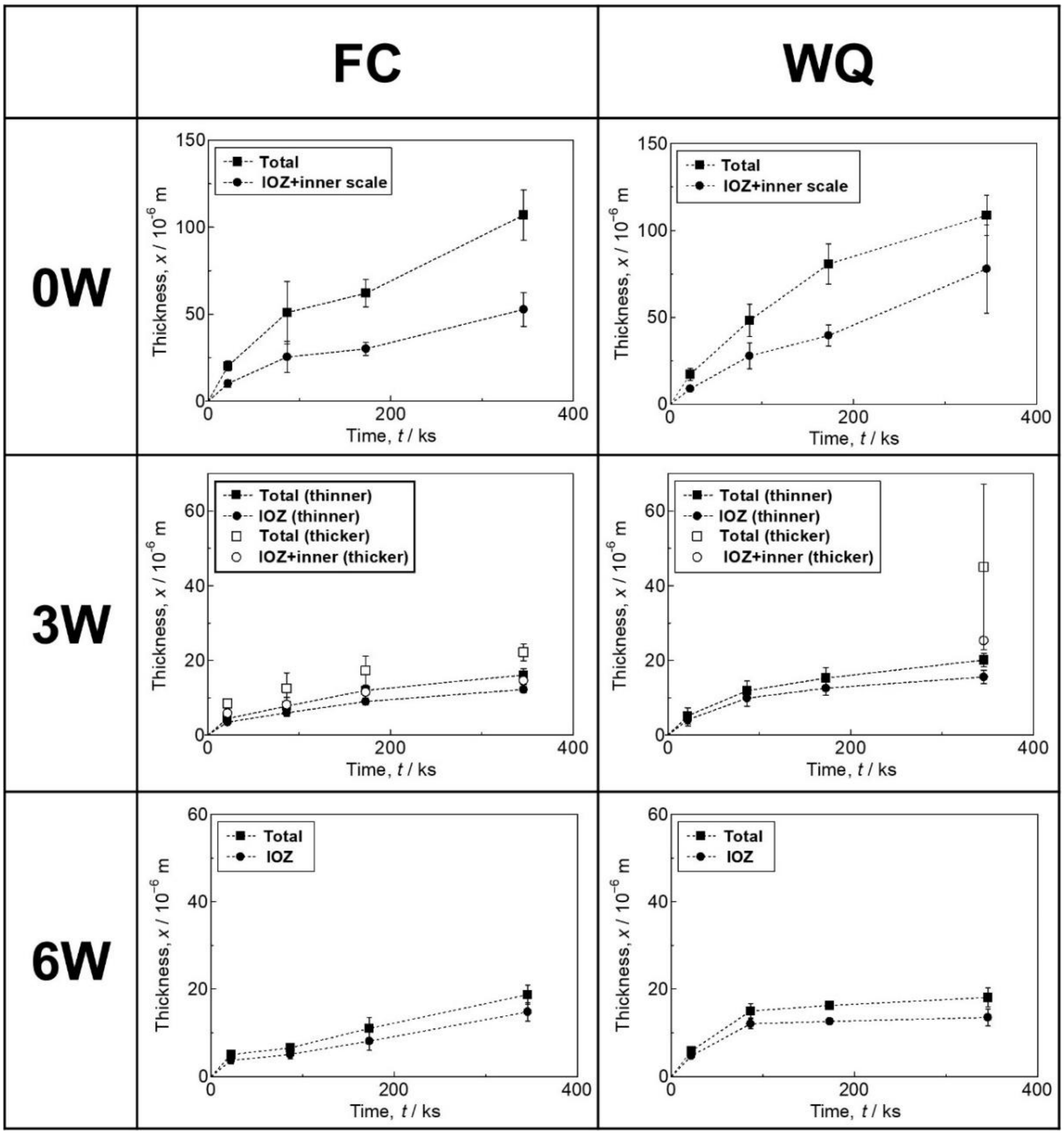

Figure 2.33 Thickness of each scale layer on all samples after oxidation test up to 345.6 ks.

2.3.7 Brief summary of the results

Binary FC 0 W and WQ 0W formed a duplex scale. The FC 1.5W formed a mixed structure of the duplex scale and a thin scale without an inner scale. The ratio of the thinner to the thicker area was about 7:3. Adding 3W improves the oxidation rate significantly, represented by low mass change. Similar to FC 1.5W, FC 3W has a mixed scale structure, but the thinner to thicker scale area was 1:1. The WQ 3W formed a uniform thin structure, but a thick scale started to be found after 345.6 ks. FC 6W and WQ 6W give a stable structure of a thinner structure, but the mass change was not significantly different from FC 3W and WQ 3W. The elemental mapping reveals that the thinner part has well distributed Cr in the IOZ, and the thicker part forms a Cr-rich layer at the bottom part of the inner scale. Both structures showed fine new Laves phase particles precipitated in the IOZ.

2.4 Discussion

2.4.1 Development of the oxide scale on the Fe-9Cr and W-added Fe-9Cr alloys

The scale formation mechanism of typical 9Cr steel or Fe-Cr alloys is widely reported in many studies [10-12]. Based on the obtained data, the scale formation mechanism for Fe-9Cr alloy and the thin part of the oxide formed on W-added Fe-9Cr alloys is proposed in this work, as shown in figure 2.34. In the case of Fe-9Cr alloy, the Cr, which has higher oxygen affinity, will be oxidized earlier to form Cr_2O_3 particles in the matrix Fe to form IOZ. Fe diffused outward, developed Fe nodule, then the nodule oxidized to form an outer scale. Because the oxygen partial pressure during the test was maintained at the stable region of Fe_3O_4, the outer part was supposed to consist of FeO and Fe_3O_4 layers.

By the penetration of oxygen, old Cr_2O_3 particles react with the matrix of Fe to form $FeCr_2O_4$ in the IOZ, and new Cr_2O_3 particles nucleated at the IOZ front. Because of the growth of IOZ, the chemical potential of oxygen in the IOZ increased and oxidized the matrix of IOZ to form an inner scale (FeO). The recession of the IOZ/inner scale interface happened because Fe ions diffuse outward through the inner scale to build the outer scale. Therefore, the oxygen partial pressure at the IOZ/inner scale interface was in the Fe/FeO/$FeCr_2O_4$ equilibrium. However, because the solubility limit of Cr in FeO at 923 K is negligibly small, the oxygen partial pressure at this interface is close to the Fe/FeO equilibrium. The IOZ/matrix interface was at the $\underline{Cr}/Cr_2O_3$ equilibrium.

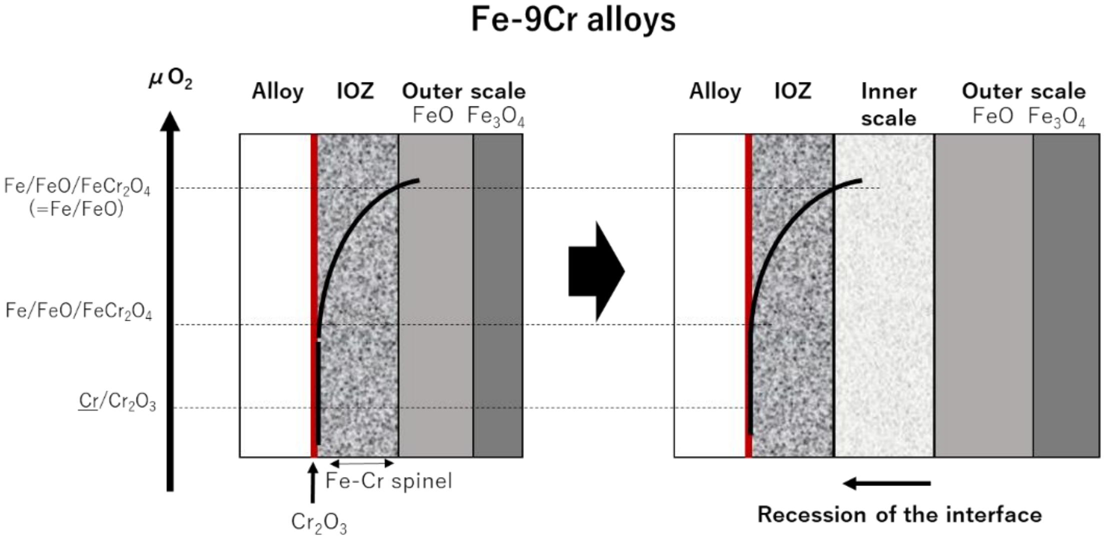

Figure 2.34 Schematic representation of the proposed mechanism for scale formation on the Fe-9Cr alloy.

To explain the scale formation mechanism in W added 9Cr alloy, it is important to consider the phenomenon of the formation of new laves phase in the oxidized area. It could be seen that there are two types of Fe_2W laves phase with different sizes in figures 2.25 and 2.30. The coarse Fe_2W was found along the grain boundaries, and the fine laves phase precipitated in the IOZ within the oxide particle. The fine Fe_2W was not observed at the IOZ front. Besides FC and WQ 6W, this phenomenon was observed in both the thick and thin oxide structure of FC 3W alloy and a very low fraction in FC 1.5W. In addition, to examine the phases that existed in the IOZ, an XRD analysis was performed on the surface polished FC 6W sample oxidized for 172.8 ks, as shown in figure 2.35. The XRD confirmed the formation of $FeCr_2O_4$ and $FeWO_4$ in the IOZ of the polished sample.

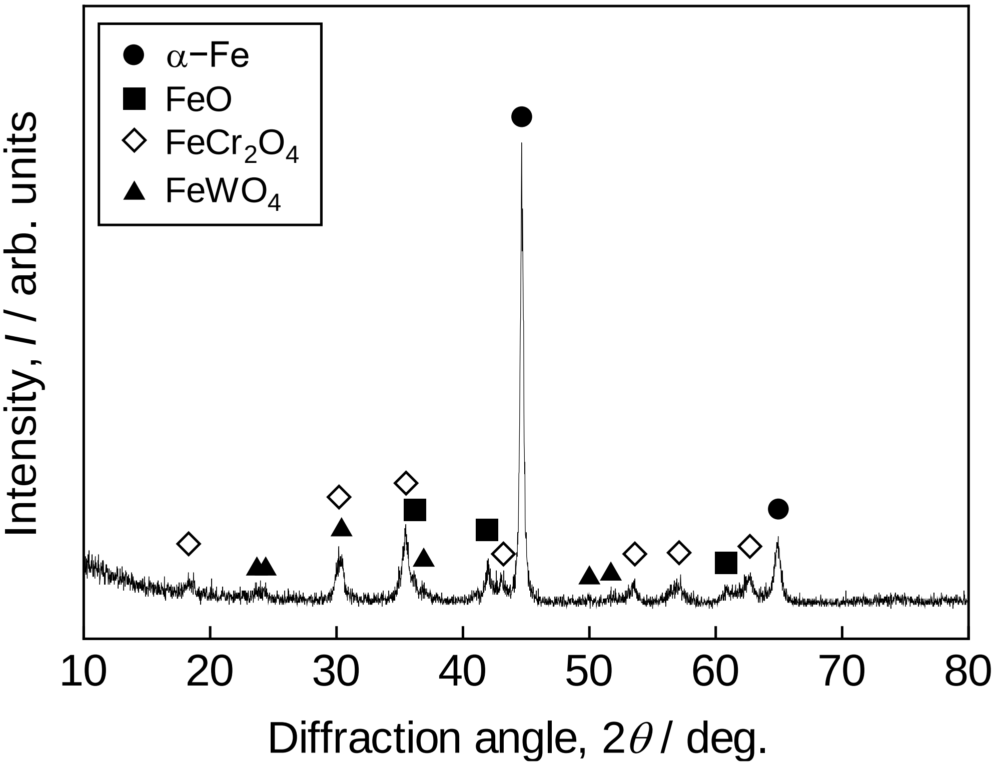

Figure 2.35 XRD pattern of surface polished FC 6W sample oxidized for 345.6 ks

One of the possibilities to explain this phenomenon is oxidation-induced precipitation or W accumulation near the oxide particles. According to a study, the formation of the Laves phase at the steel/oxide interface in ferritic stainless steel may occur due to the rejection and accumulation of the Laves phase former element induced by selective oxidation of Cr [13]. Therefore, in this study, fine Laves phase precipitates in the IOZ are considered to form as a result of W accumulation in the IOZ matrix during the formation and development of Cr-containing internal oxidation in the alloys.

Figure 2.36 shows the Fe-W-O phase diagram from reference [14]. It could be understood that W oxides are not directly equilibrated with the alloys for the composition applied in this experiment. In addition, under the Fe/FeO equilibrium, W dilute alloys are equilibrated with $FeWO_4$. Considering the thermodynamics data from references [14-16], the oxygen potential - composition diagram of the Fe-W-O system at 923 K is estimated and presented in Fig. 2.37. Then, the scale formation mechanism of W added Fe-9Cr alloys is proposed. In particular, the mechanism is separated into thin and thick structures, as shown in figure 2.38.

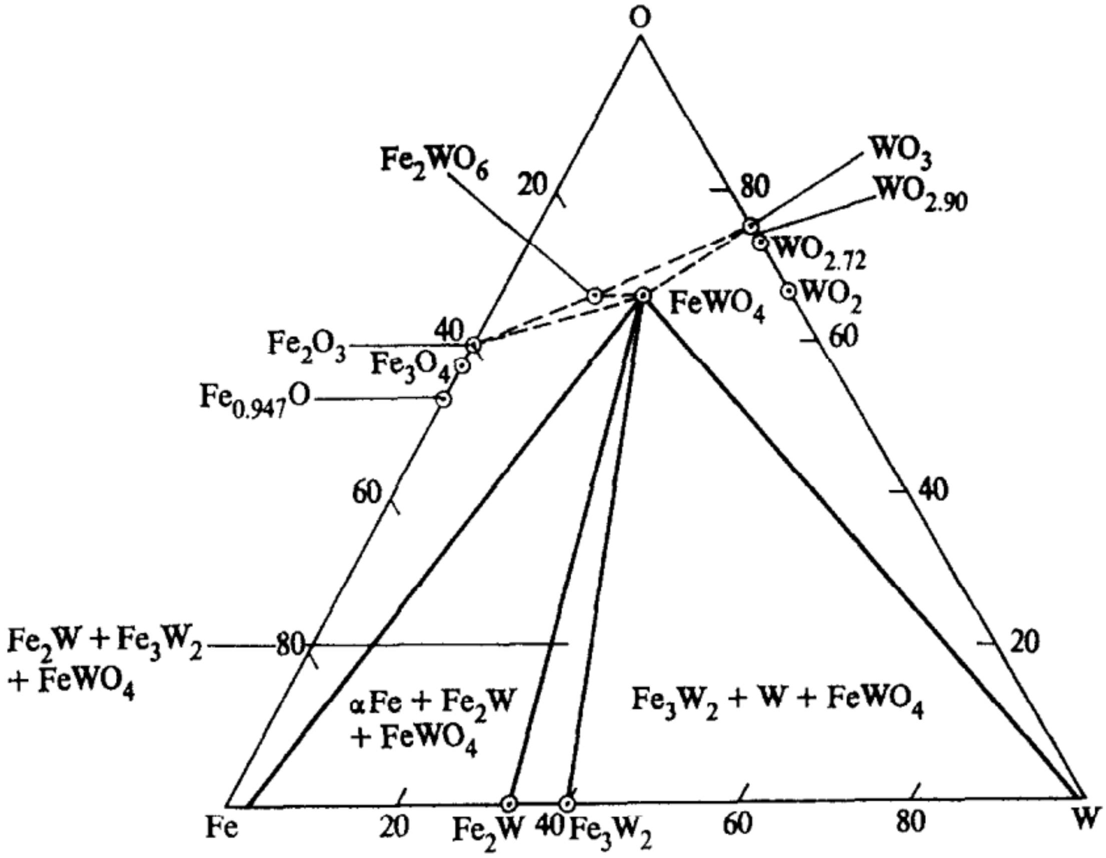

Figure 2.36 Fe-W-O phase diagram at 1200 K from reference [14].

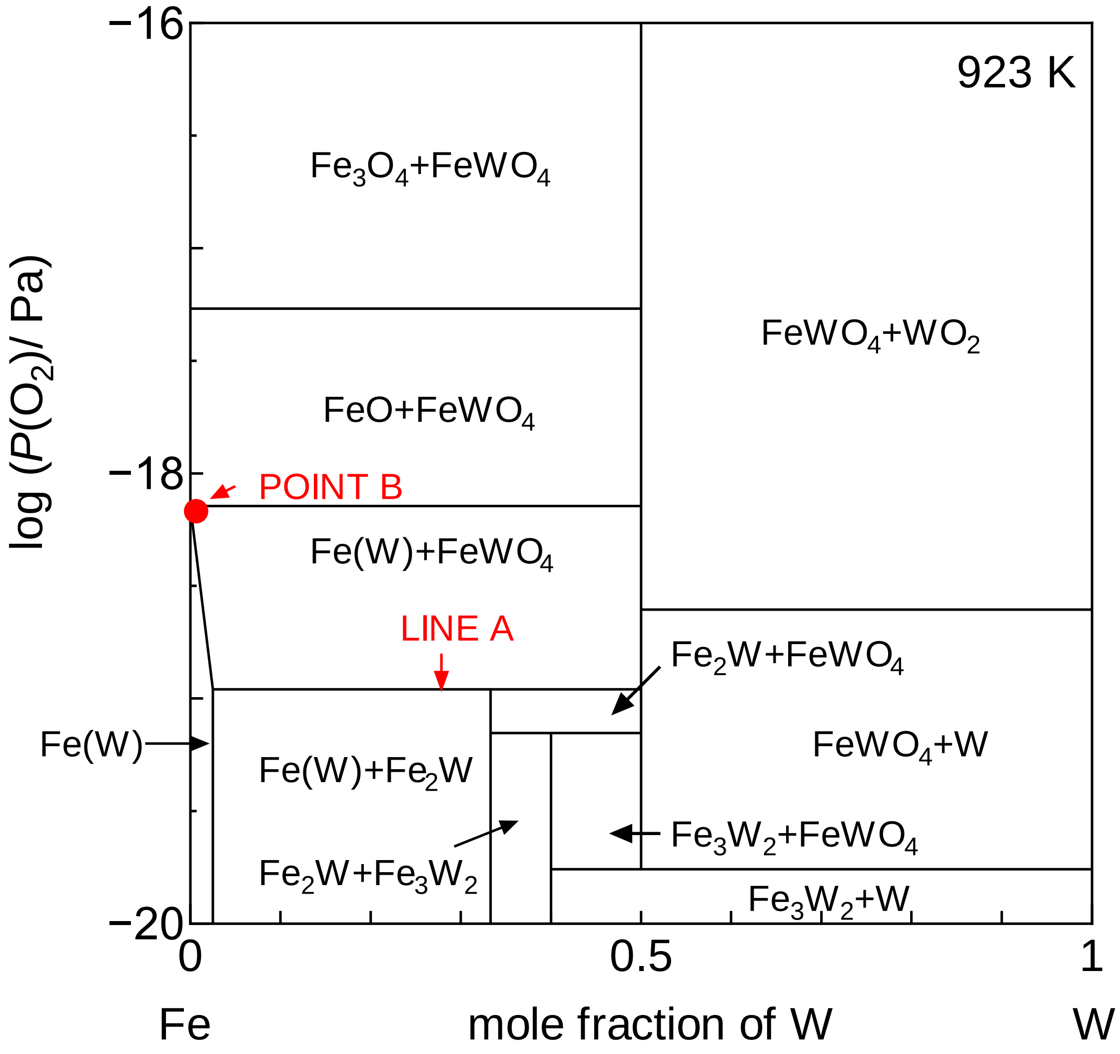

Figure 2.37 Oxygen potential - composition diagram of the Fe-W-O system at 923 K estimated from references [14-16].

(a) Thin area of Fe-9Cr-3 W alloys and Fe-9Cr-6W alloys

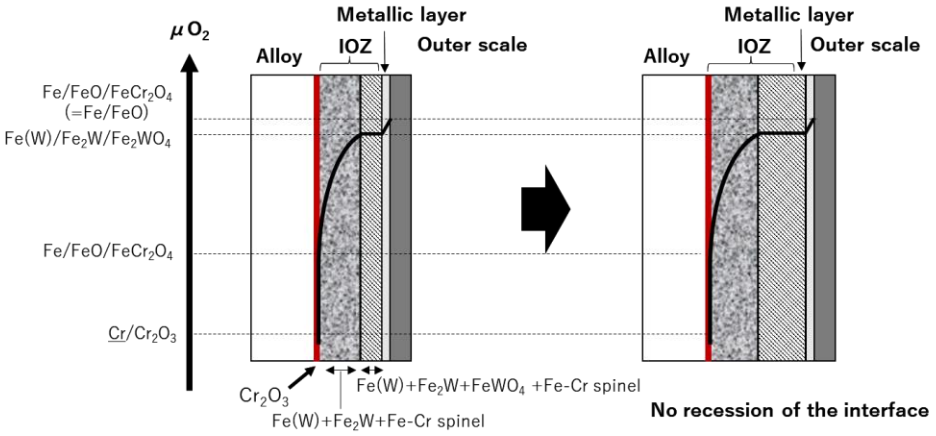

(b) Thick area of Fe-9Cr-1.5W and Fe-9Cr-3W alloys

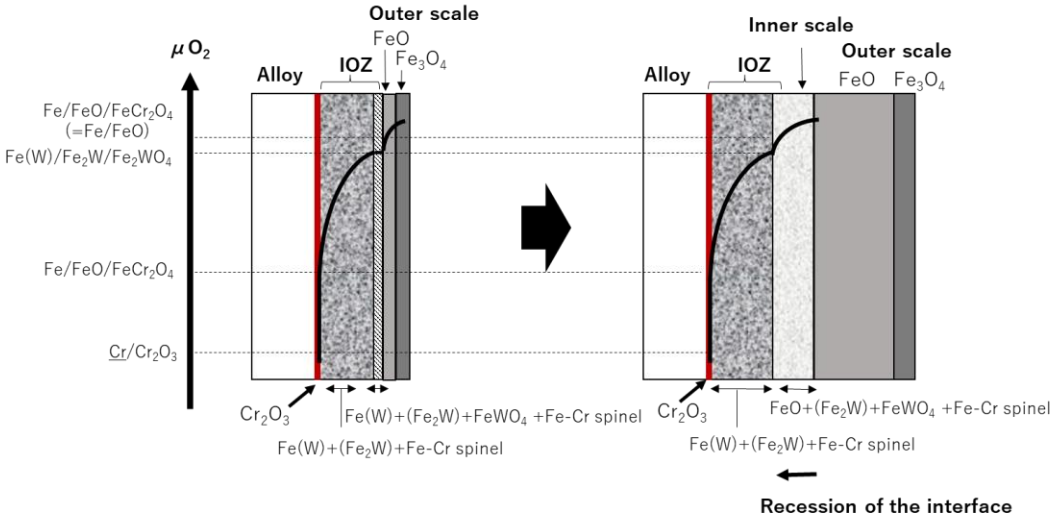

Figure 2.38 Proposed mechanism for scale formation on the W added Fe-9Cr alloys. (a) Thin oxide scale and (b) thick oxide scale.

Since two types of oxide structures on low W alloys showed almost similar thicknesses and morphologies to the IOZ (Figs. 2.19 and 2.23), which indicated the growth mechanism on both structures was similar. In general, scale formation on thick and thin structures formed on W-added 9Cr alloys is started by the internal oxidation of Cr and W to develop IOZ. At the same time, the Fe nodule formed on the sample's surface.

In the case of thinner oxide structure (Fig. 2.38 (a)), the Cr_2O_3 particles preferentially precipitate near the front of the IOZ because Cr has a higher oxygen affinity than other elements. By oxygen penetration, the Cr_2O_3 reacts with the matrix to form $FeCr_2O_4$. The formation of $FeCr_2O_4$ consumes Fe and Cr, which results in the accumulation of W in the matrix of IOZ. Then, the W content in the matrix reached the two phases region in the Fe-W-O system. The accumulated W reacted with Fe and dissolved O to form Fe_2W and/or $FeWO_4$ in the IOZ. Considering the oxygen affinity data shown in figure 2.37, the Cr_2O_3 particles are supposed to be located at the IOZ front, the $FeCr_2O_4$ at the bottom of IOZ, and the $FeWO_4$ at the upper part of IOZ. The accumulation of W in the matrix of IOZ led the matrix Fe to shift and stabile at line A.

After developing $FeWO_4$ in the IOZ, there will be Fe_2W, $FeWO_4$, and the matrix of Fe that exists in the IOZ. At this point, the IOZ is in the Fe(W)/Fe_2W/$FeWO_4$ equilibrium, which was calculated to be 1.1×10^{-19} Pa at 923 K (Line A in Fig. 2.37). This value is slightly lower than the Fe/FeO equilibrium (Point B in Fig. 2.37, $P(O_2) = 7.2 \times 10^{-19}$ Pa), which prevents oxidation of the matrix of IOZ from forming FeO inner scale. Therefore, it explained the absence of inner scale in the thin structure (Fig. 2.38 (a)). Further growth of the IOZ may be governed only by the formation of Cr_2O_3 at the front. At the same time, the diffusion of oxygen and iron atoms through the matrix of the IOZ is suppressed by the small potential gradient of oxygen.

Another phenomenon found in the thin area (Fig. 2.38(a)) is the formation of a metallic layer and a very thin oxide scale. In the case of FC and WQ 6W, peaks of Fe_3O_4 were negligible low compared to FeO (Fig. 2.10). As shown in figures 2.29 and 2.33, white particles suggested as laves phase formed at the metallic layer. Therefore, the accumulation of W in the metallic layer can be formed, but since it was not clearly observed, this area was suggested to be very thin. Taking the same phenomenon of formation Fe(W)/Fe_2W/$FeWO_4$ occurred and located near the pure FeO, this layer can suppress the penetration of oxygen into the substrate as well as the supply of Fe outward. Further, the local equilibrium sets the potential oxygen low at the metallic layer/FeO interface, which may induce the decomposition of iron oxides. The FeO may decompose into Fe^{2+} (in FeO) and O (in IOZ), in which the Fe^{2+} not only reacts with oxygen to form Fe_3O_4 but also react with Fe_3O_4 to form FeO. Then, the supply of Fe^{2+} and O^{2-} from the

FeO controls the competition of the reactions through the oxide scale. The decomposition of iron oxides leads to a very low growth rate on the outer scale (mainly FeO) and the absence of Fe_3O_4 at the outer scale. However, further investigation is needed to check the actual oxygen potential in the scale surface.

In the case of the thicker oxide structure (Fig. 2.38(b)), the equilibrium of $Fe(W)/Fe_2W/FeWO_4$ is suggested not to be achieved due to the low volume fraction of the constituent, moreover Fe_2W. In other words, the accumulation of W cannot stabilize the matrix of IOZ in line A (Fig. 2.37). Therefore, the matrix of IOZ is oxidized to form the inner scale of FeO. In this structure, the enrichment of Cr and W at the front of the inner scale was found. It is suggested the oxidized matrix of IOZ can form a more protective layer to help hinder the outward diffusivity of the metal.

Although all W added 9Cr alloy formed a thin structure without forming an inner scale, low W concentration Fe-9Cr alloy developed two types of scale structures. In addition, the lath structure started to transform into ferrite WQ 3W samples oxidized for 345.6 ks. In the proposed mechanism, the established $Fe(W)/Fe_2W/FeWO_4$ equilibrium in the IOZ is the key phenomenon that prevents the formation of inner scale in the W-added alloys. Therefore, the formation of $Fe(W)/Fe_2W/FeWO_4$ equilibrium is likely to be independent of the volume fraction of Fe_2W and the nominal W content in the alloys.

2.4.2 Effects of W content and initial microstructure on the scale development

The oxidation rate of FC 1.5W is better than the binary alloy, but the formed scale structure was unstable. The oxidation rates became drastically improved when W content increased to 3%, but still, the instability of the formed oxide structure was observed. Adding more volume fractions of the Fe_2W phase did not significantly affect the oxidation rates, but the alloys formed a uniform oxide structure. The previous section suggested that this phenomenon occurred because the W content in the low W alloys was insufficient to establish more fraction of Fe_2W or $FeWO_4$ in the IOZ or stabilize the matrix of IOZ, the local $Fe(W)/Fe_2W/FeWO_4$ equilibrium for a longer time. Therefore, the formation of the inner scale occurs in the lower W alloys as the oxygen partial pressure at the IOZ reaches for the FeO formation.

By conducting rapid cooling, the matrix became more complex. The 0W formed massive-transformed ferrite instead of a ferrite matrix. In the case of 3W alloy, the microstructure changed into a dual-phase of ferrite-martensite by rapid cooling. It was found that there was no significant difference between the oxidation rate on all FC and WQ samples. For the 0W alloys, rapid cooling contributes to a slightly more even and noticeable Cr enrichment in the inner part of the scale. High cooling rates result in a higher density of dislocations in the alloy, promoting a higher density of fine and homogeneous precipitates [17,18]. In the ternary alloys, the rapid cooling increased the volume fraction of laves phase. In the case of WQ 3W, the lath microstructure provides preferable sites for forming the laves phase. As a result, more volume fraction of the Laves phase in WQ 3W than in FC 3W.

As the key phenomenon for forming a thin structure, Fe(W)/Fe_2W/$FeWO_4$ equilibrium seems to be not established in some parts or grains in the low W alloys. Further oxidation on the matrix of IOZ grows an inner scale of FeO. In the thicker part, the enrichment of Cr and W at the front of the inner scale was found. This enrichment was more noticeable in the 3W alloys than in the FC 1.5W alloy. The inner part of the duplex scale formed on FC 1.5 W was also thicker with a higher proportion of inner scale than the 3W alloys. It suggested that W as a solid solution element contributes to Cr enrichment in the inner scale and plays the main role in improving the oxidation resistance. Besides, the precipitation helped increase the fraction of Fe_2W in the IOZ to sustain the Fe(W)/Fe_2W/$FeWO_4$ equilibrium. The W in the precipitate contributed to developing and maintaining the Fe(W)/Fe_2W/$FeWO_4$ equilibrium in the IOZ. Furthermore, the Cr enrichment distribution was better in the IOZ of the WQ 6W, which precipitated finer and denser Laves phase fractions. It is suggested that Cr-rich oxides formation was initiated by the Cr included in the Laves phase.

In addition, a higher W concentration followed by rapid cooling increases the magnitude of stress in the matrix metal and the IOZ. It is causing more outward metal diffusion that produces nodules or metallic layers during the IOZ formation. Although the thickest metallic layer formed on the WQ 6W alloy, the outer scale grew slower and thinner in the 6W alloys due to the small potential gradient of oxygen in the IOZ suppressing the outward diffusion of iron atoms through the matrix.

2.5 Conclusion

The effect of tungsten on the steam oxidation behavior of Fe-9Cr at 923 K was investigated. Adding W into Fe-9Cr alloy significantly improves the oxidation resistance of the alloy. Formation of the inner scale was absent in the high concentration alloys. In the low concentration alloy, this structure was mixed with a duplex scale in some parts of the alloy. A possible mechanism for scale formation in W added 9Cr alloys was proposed. Three phases of $Fe(W)/Fe_2W/FeWO_4$ were formed during the development of IOZ. In the $Fe(W)/Fe_2W/FeWO_4$ equilibrium, the oxygen partial pressure of IOZ will be slightly lower than the Fe/FeO equilibrium, which suppresses the formation of the inner scale.

The role of W is divided into two. As a solute element, W promoted Cr enrichment at both the IOZ/inner scale and the IOZ/alloy interfaces, which suppress the outward diffusion of metal ions. Solute W may induce the accumulation of W in the IOZ during development of IOZ, which can lead to the formation of $Fe(W)/Fe_2W/FeWO_4$ equilibrium in the matrix of IOZ. A finer and higher fraction of the Fe_2W phase produced by more W concentration and rapid cooling helps sustain $Fe(W)/Fe_2W/FeWO_4$ equilibrium in the IOZ and contributes to better Cr enrichment in the inner part of the oxide scale.

2.6 References

[1] F. Masuyama, *ISIJ Int.*, **41(**6**)**, 2001, (612–625).

[2] F. Abe, *Engineering*, **1(**2**)**, 2015, (211–224).

[3] F. Abe, *Science and Technology of advanced materials*, **9(**1**)**, 2008, (013002).

[4] Knežević, V., Balun, J., Sauthoff, G., Inden, G., & Schneider, A. *Materials Science and Engineering: A*, 477**(1-2)**, 2008, (334-343).

[5] V. T. Paul, V. D. Vijayanand, C. Sudha, and S. Saroja, *Materials Science and Engineering: A*, **48(**1**)**, 2017, (425–438).

[6] S. Tang, S. Zhu, X. Tang, H. Pan, and Z. D. Xiang, *Corros. Sci.*, **82**, 2014, (255–264).

[7] F. Abe, H. Kutsumi, H. Haruyama, and H. Okubo, *Corros. Sci.*, **114**, 2017, (1–9).

[8] V. Lepingle, G. Louis, D. Allué, B. Lefebvre, and B. Vandenberghe, *Corros. Sci.*, **50(**4**)**, 2008, (1011–1019).

[9] Liu, S. *J. Jpn. Inst. Met.* **52**.(10), 1988, (927-934).

[10] E. Essuman, G. H. Meier, J. Żurek, M. Hänsel, and W. J. Quadakkers, *Oxid. Met.*, **69(**3–4**)**, 2008, (143–162).

[11] Ani, Mohd Hanafi Bin and Kodama, Toshiya and Ueda, Mitsutoshi and Kawamura, Kenichi and Maruyama, Toshio, *Material Transactions*, **50(**11**)**, 2009, (2656–2663).

[12] A. Agüero, V. González, M. Gutiérrez, and R. Muelas, *Surf. Coat. Technol.*, **237**, 2013, (30–38).

[13] L. Wei, L. Chen, H. Liu, L. Han, N. Gong, and R. D. K. Misra, *Oxid. Met.*, **93(**1–2**)**, 2020, (195–213).

[14] T. N. Rezukhina and T. A. Kashina, *J. Chem. Thermodyn.*, **8(**6**)**, 1976, (519–523).

[15] N. G. Schmahl and H. Dillenburg, *Zeitschrift für Phys. Chemie*, **77(**1–6**)**, 1972, (113–126).

[16] D. J. Young, *Elsevier*, High temperature oxidation and corrosion of metals, **1**. 2008.

[17] A. R. Massih and L. O. Jernkvist, *Comput. Mater. Sci.*, **39(**2**)**, 2007, (349–358).

[18] N. H. Pryds and X. Huang, *Metall. Mater. Trans. A Phys. Metall. Mater. Sci.*, **31(**12**)**, 2000, (3155–3166).

Part of this chapter has been published in:

Lidyana Utami and Mitsutoshi Ueda, "The Effect of Tungsten Addition to Fe-9Cr Alloy on Steam Oxidation Behavior at 923 K", Oxidation of Metals, 97, 341-358(2022).

Chapter 3 The Effect of Niobium Addition on the Steam Oxidation Behavior of Fe-9Cr Alloy at 923 K

3.1 Introduction

In the previous chapter, the effect of tungsten (W) on the steam oxidation behavior of Fe-9Cr alloy at 923 K was divided into the effect of W as a solute element and precipitate. Because the solubility limit of Nb in the matrix Fe is very narrow (Fig. 1.7), the effect of Nb as a solute element on the oxidation behavior of metallic alloys will be difficult to be elucidated. Therefore, in this chapter, the addition of Nb is focused on clarifying the effect of intermetallic compounds, in particular Fe_2Nb, on the oxidation behavior of ferritic 9Cr alloy.

Unlike W, adding Nb to 9-12%Cr ferritic/martensitic steel is not addressed to give precipitation hardening by forming Fe_2Nb along the grain boundaries. The addition of 0.05 mass% of Nb into 9-10% Cr steel is well known to improve the mechanical property by forming MX type of carbonitrides and prevent unwanted precipitation of Cr carbides by forming NbC [1,2]. NbC has a very low coarsening rate at 600°C and 650°C. It is reported that a combination of NbC, V(C,N), and $M_{23}C_6$ provided large dislocation pinning that helped to reduce boundary migration in typical 9Cr steel [3]. In terms of oxidation resistance, Nb is reported to give a better oxide scale adhesion and spallation resistance to steels and nickel-based alloys. It also reported reducing expansion crack during cyclic oxidation and reducing voids and gaps in the scale and scale/metal interface [4,5]. Nb is beneficial in improving Cr activity in Ni-Cr-Fe alloy [6]. Adding Nb into high Cr steel without other minor alloying elements such as Si forms Nb-rich oxide at the metal/surface interface [7]. Besides, it is believed that Nb^{4+} and Nb^{5+} ions doped Cr_2O_3 increase the growth rate of Cr_2O_3.

Although the formation of Fe_2Nb is not proposed in typical ferritic/martensitic steels, the effectiveness of the Fe_2Nb Laves phase is reported in the ferritic stainless steel or heat resistance steels with Cr concentrations above 18% [8,9]. During aging, the Laves phase precipitated along the grain boundaries and inside the grain interior. The Laves phase former elements diffuse to vacancies in the lattice and occupy a favorable site, leading to the formation of elongated Fe_2Nb along grain boundaries [10]. These precipitates along the grain boundaries were reported can retard the diffusivity of cation in the matrix metal. In other work on ferritic stainless steel that precipitates Laves phases, mainly Fe_2Nb, it is reported that the addition of Ce followed by W reduces the number of dissolved Laves phases along grain boundaries or grain interior. It helped to suppress the diffusion and hinder the inward growth of oxide. A higher amount of W leads to precipitation of coarse Laves phase at the oxide/metal interface, thus significantly reducing the oxide scale adhesion [1].

Further, the slower diffusion contributes to the formation of a thinner Cr_2O_3 scale instead of forming layers of Cr-Mn-Fe spinel oxide and Cr_2O_3 in ferritic stainless steel. It was reported that the diffusivity of Fe in the $(Fe,Cr,Mn)_3O_4$ is estimated to be 10^{-13} cm^2s^{-1} at $P(O_2) = 10^{-7}$ bar at 1073 K, while the diffusivity of Fe in the Cr_2O_3 is estimated to be 10^{-20} $cm^{-2}s^{-1}$ [9]. Although Fe_2Nb Laves phase precipitation is found to give better oxidation resistance in the high Cr ferritic steel, the effect of precipitation of Fe_2Nb on the oxidation behavior of typical 9-12Cr ferritic/martensitic steel is still unclear.

3.2 Experimental

3.2.1 Sample preparation

The binary sample used in this chapter is the same as the FC 0W alloy in chapter 2. Figure 3.1 [11] shows the ternary phase diagram of the Fe-Cr-Nb system at 973 K from reference. The solubility limit of Nb in Fe-rich areas is very narrow at 973 K. Pandat software [12] predicts the solubility limit of Nb at 923 K in Fe-9Cr alloy is around 0.1 mass%. From this, the investigation of the solid solution effect becomes difficult. In this chapter, the composition of Fe-9Cr-2Nb (mass%) was decided by considering the almost same volume fraction of Laves phase precipitated in Fe-9Cr-6W alloys in chapter 2.

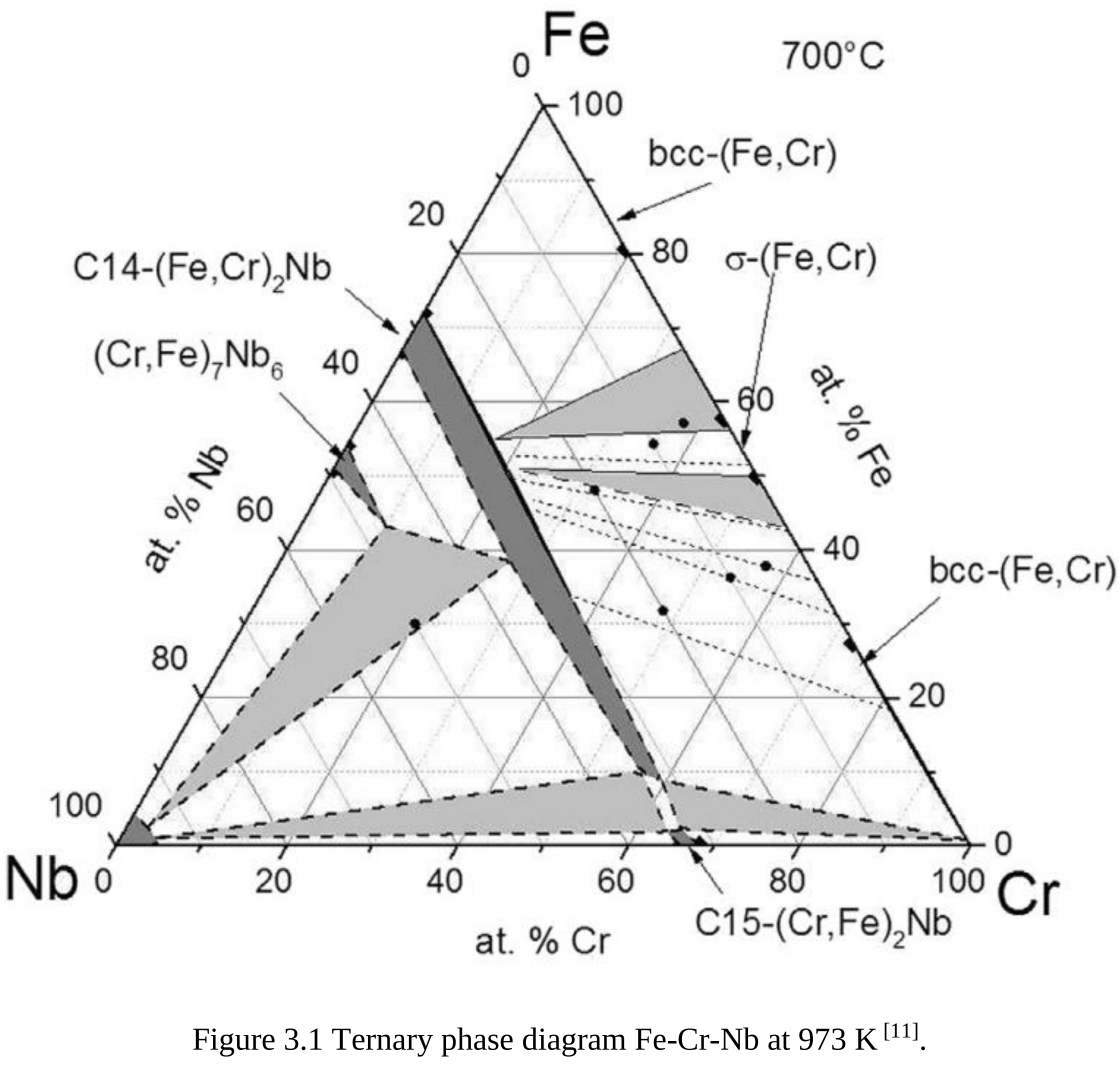

Figure 3.1 Ternary phase diagram Fe-Cr-Nb at 973 K [11].

The ingot of Fe-9Cr (mass%) and Fe-9Cr-2Nb (mass%) were prepared from Fe (purity 99.99%), Cr (99.999+%), and Nb (99.9%) by arc melting method. The Fe-9Cr alloy which was used in this chapter was the same sample as WQ 0W samples from chapter 2. The semiquantitative chemical composition obtained by X-Ray Fluorescence spectrometry (XRF) is listed in table 3.1. The heat treatments were conducted inside a vacuum ampule. The heat treatment temperature and time of each ingot are presented in table 3.2. The ingots were solution-treated in a vacuum ampule. The ingots were cut into a coupon sample thickness of around 1.5 mm. The coupon then experienced a cold roll with a rolling rate with a thickness reduction ± 30%. A hole was drilled into the sample to hang the sample inside the testing apparatus. Recrystallization treatment was conducted inside the vacuum ampule. An aging treatment was conducted for the ternary alloy to ensure the precipitation of Laves phase in the ferrite matrix. Water quenching was performed after all heat treatments.

Table 3.1 Chemical composition of the alloys (mass%).

Alloy	Fe	Cr	Nb
Fe-9Cr	Bal.	9.03	-
Fe-9Cr-2Nb	Bal.	9.01	1.27

Table 3.2 Heat treatment conditions of the alloys.

Alloy	Heat Treatment					
	Solution Treatment		Recrystallization		Aging Treatment	
	T / K	t / ks	T / K	t / ks	T / K	t / ks
Fe-9Cr	1273	86.4	1273	0.6	-	-
Fe-9Cr-2Nb	1573	43.2	1573	0.6	923	864

After the heat treatments, all the samples were grounded with abrasive (#600 ~ #5000) and polished with a series of diamond pastes (9 μm ~ 0.25 μm) until the mirror was finished. The thickness and circumference of the sample were measured, and the surface area of the sample was estimated using 'Image J' software. Before the oxidation test, the samples were washed in ethanol using an ultrasonic cleaner for 0.6 ks, and the mass of the sample was measured by an electronic scale.

3.2.2 Experimental procedure and analytical methods

The experimental procedure and analytical method in this chapter are similar to chapter 2. The steam oxidation test was conducted in a vertical furnace up to 345.6 ks. The oxidation test was conducted at 923 K in the Ar-15%H_2O gas mixture. The flow rate of the gas mixture was controlled to be $1.67\text{x}10^{-6}$ m^3s^{-1}. The oxygen partial pressure inside the furnace was maintained to be $1.3\text{x}10^{-11}$ Pa, which is in the stable region of magnetite at 923 K. During the test, the temperature oxygen partial pressure in the vicinity of the sample was continuously monitored by using a ZrO_2 oxygen sensor. The mass change of samples after the oxidation test was measured to evaluate the oxidation rates. The scale was identified by X-Ray Diffraction (XRD). The surface and cross-sectional morphologies of the sample before and after oxidation tests were observed by a Field Emission Scanning Electron Microscope (FE-SEM) equipped with an Energy Dispersive Spectroscopy (EDS). Similar to chapter 2, the thickness of the oxide scale was also measured from 10 points from cross-sectional BE images, as shown in figure 2.3.

3.3 Results

3.3.1 Microstructure and phases of sample before oxidation test

Before the oxidation test, the samples were characterized by XRD and FE-SEM. In Figure 3.2, only the peaks of ferrite appeared on both Fe-9Cr alloy and Fe-9Cr-2Nb alloy. However, no Laves phase peak was observed in the ternary alloy. Figure 3.3 shows the BE image of the microstructure of the etched samples. The chemical etching was performed on Fe-9Cr alloy using a solution mixture of HNO_3, HCl, and ethanol for a certain time. It was found that the grain was not observed on Fe-9Cr alloy. It suggested that by the absence of carbon in the alloy, the alloy will form massive-transformed ferrite instead of a martensitic phase.

In the case of ternary alloy, the coarse gain was observed on the ternary alloy, which may be because all Nb was not dissolved into matrix Fe. As shown in Fig. 1.9, the solution treatment temperature is in the BCC phase region. The presence of intermetallic compounds appeared as a white particle in the BE images. The intermetallic compounds were found in coarse particles and fine particles along grain boundaries and grain interior of the ferrite matrix of solution-treated samples. Therefore, it can conclude that the time for solution treatment is not enough. Besides, the grain size of the Fe-9Cr-2Nb alloy sample was estimated using the mean linear intercept method to be around 30 μm.

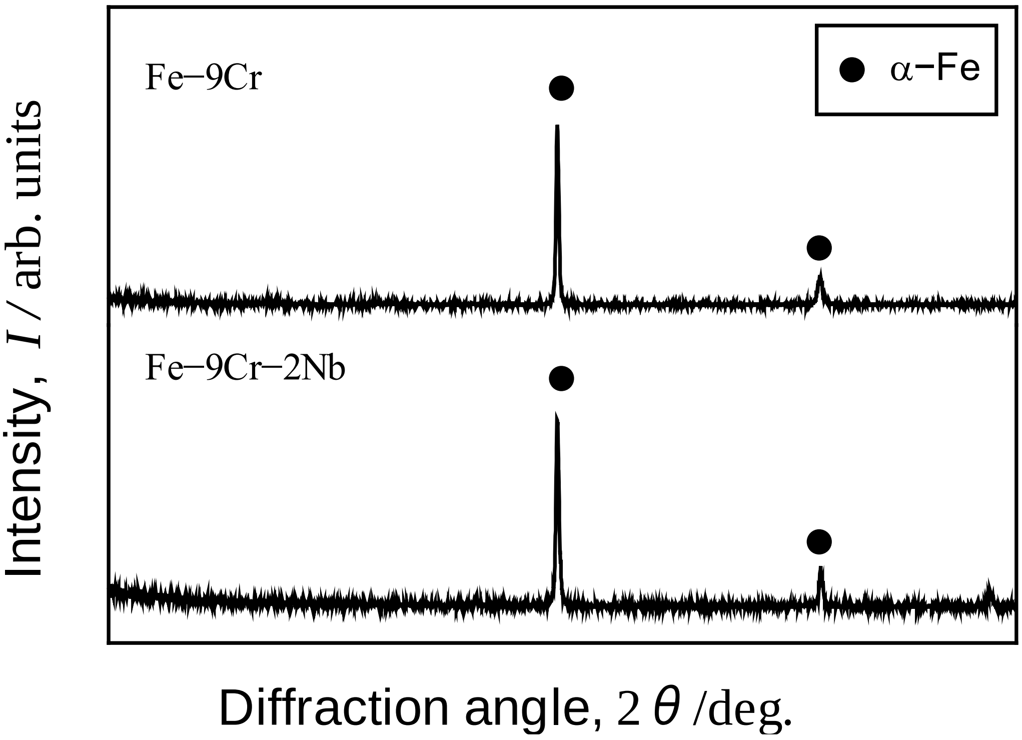

Figure 3.2 XRD patterns of Fe-9Cr and Fe-9Cr-2Nb alloys before test.

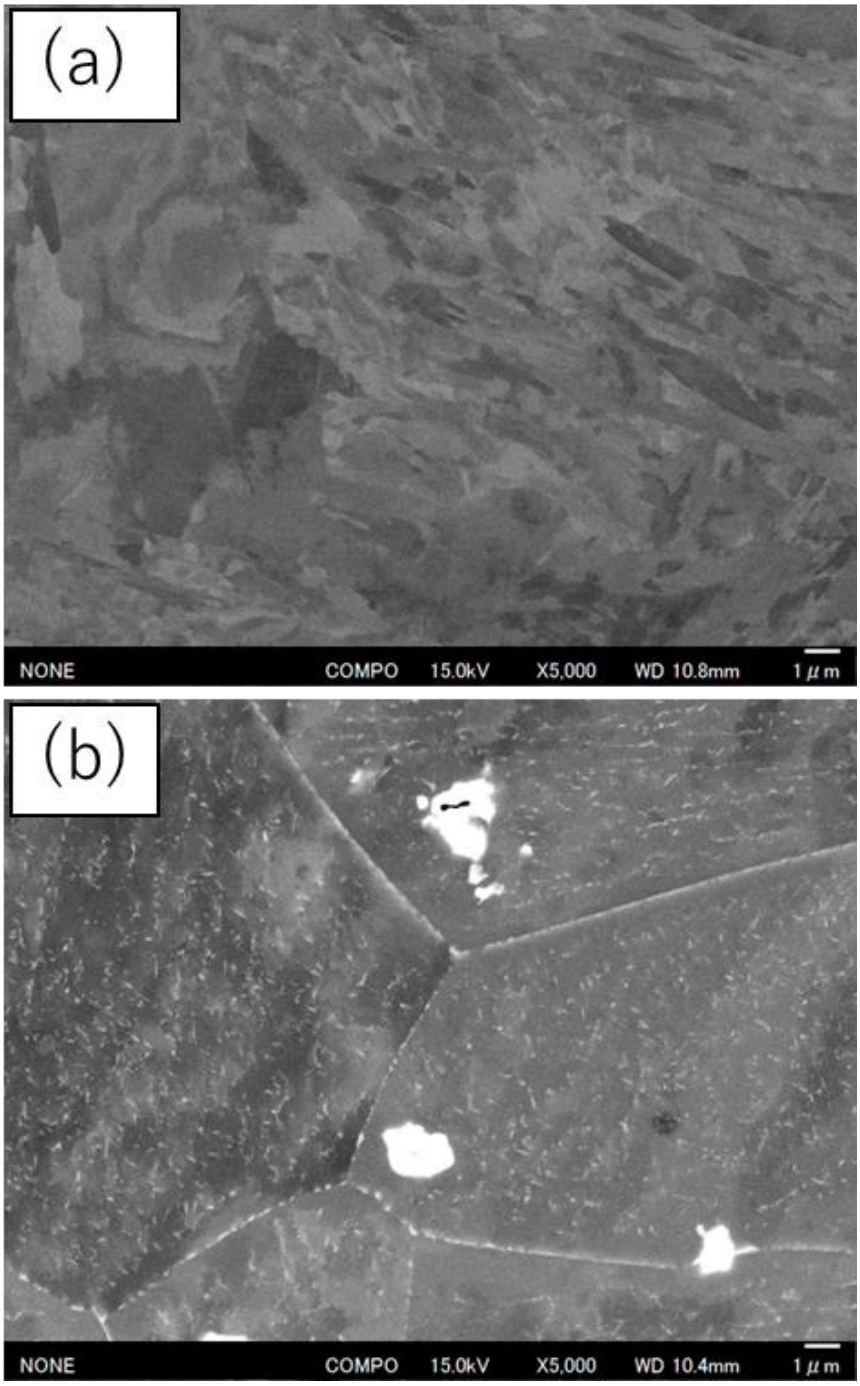

Figure 3.3 BE images of sample microstructure before oxidation test:
(a) Fe-9Cr and (b) Fe-9Cr-2Nb alloys.

3.3.2 Mass change of the samples

Figure 3.4 shows the mass change of the sample after the oxidation test at 923 K for up to 345.6 ks for all alloys. All samples showed no spallation after the test. It could be seen that Fe-9Cr-2Nb alloy showed a smaller mass gain compared to binary Fe-9Cr alloy. The growth rate of both alloys follows the parabolic rate manner. Therefore, the addition of Nb into the Fe-9Cr alloy improves the oxidation resistance of the alloy.

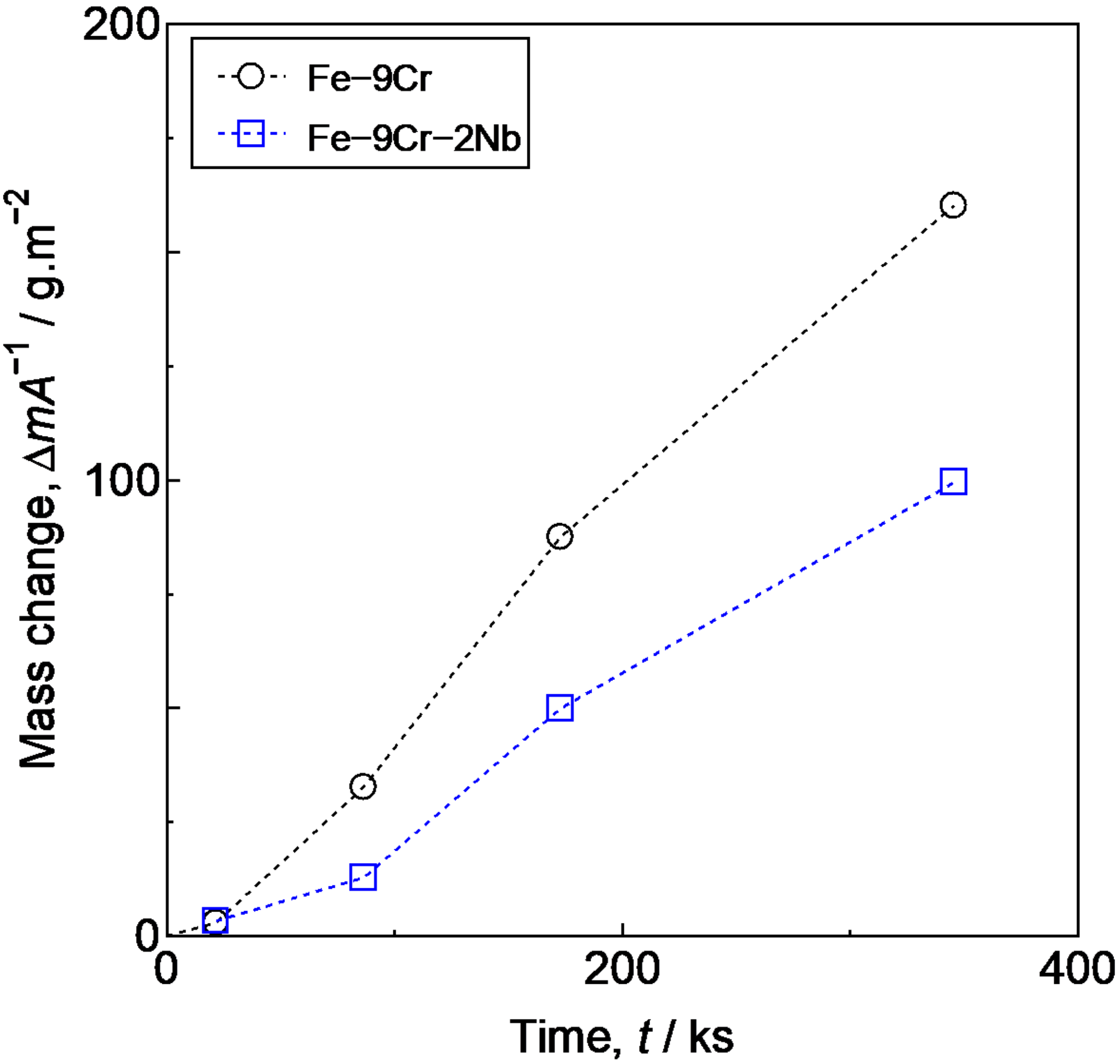

Figure 3.4 Mass change of after oxidation test up to 345.6 ks.

3.3.3 Identification of the oxide scale

Figures 3.5 shows the XRD pattern from all samples after the oxidation test up to 345.6 ks. Both alloys showed almost similar behavior. It was observed that FeO was observed in the early stages, and in the longer oxidation period, the Fe_3O_4 was found to dominate the surface of the alloys. However, the peak of Fe_3O_4 was observed earlier in the Fe-9Cr-2Nb alloy.

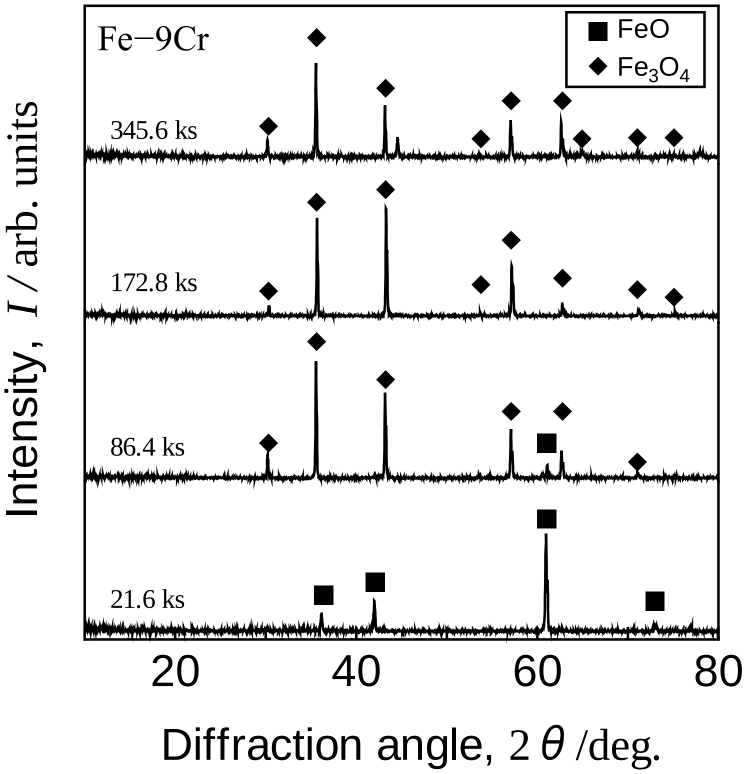

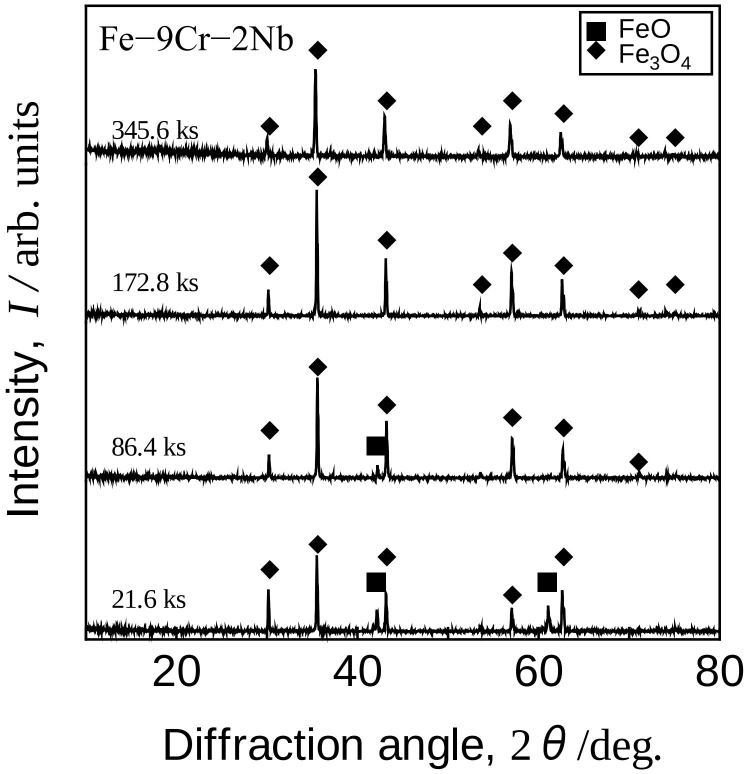

Figure 3.5 XRD patterns of Fe-9Cr and Fe-9Cr-2Nb alloy after oxidation test up to 345.6 ks.

3.3.4 Surface morphology after oxidation

Figure 3.6 shows the SE images of the surface morphology of each sample after the oxidation test up to 345.6 ks. XRD analysis confirmed that iron oxides covered all the sample's surfaces. The scale morphology was uniform on the whole sample. Different morphology was observed in the initial stage, which is also shown in the XRD pattern. Both alloys showed similar oxide morphology after a more extended oxidation test, but the Fe-9Cr-2Nb alloy showed a homogeneous fine oxide grain. No spallation was observed on both alloys; however, cracks were found to propagate on several parts on the samples oxidized for 345.6 ks.

Time	**Fe-9Cr**	**Fe-9Cr-2Nb**
21.6 ks	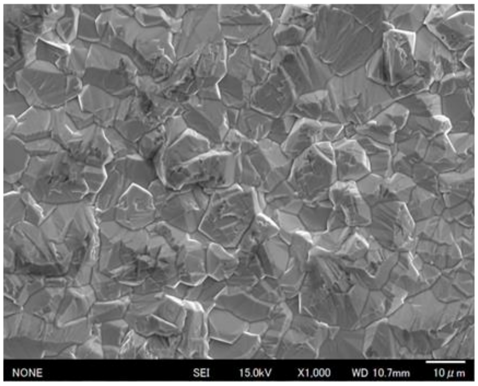	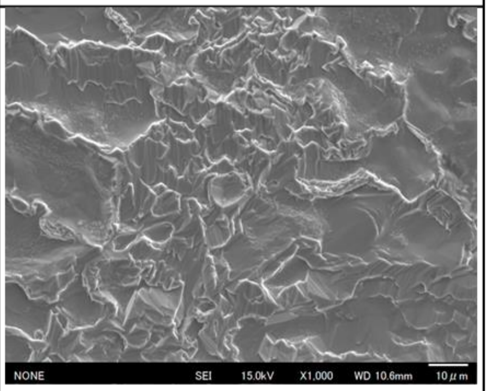
86.4 ks	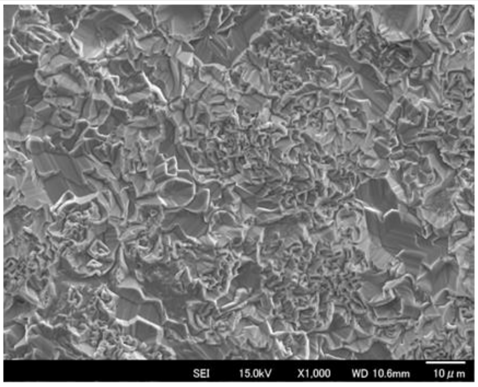	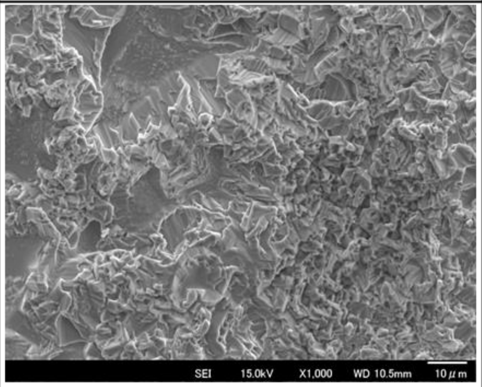
172.8 ks	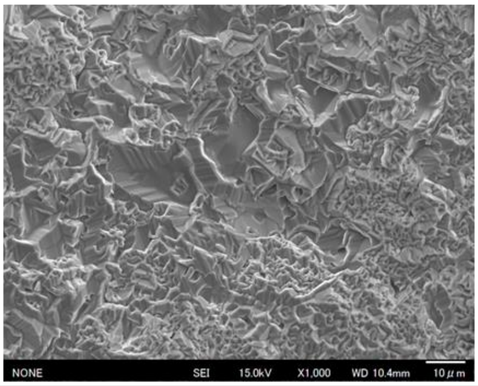	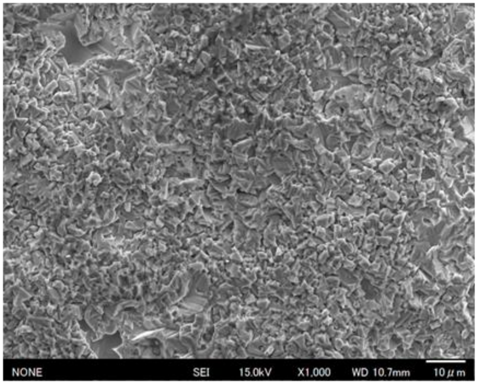
345.6 ks	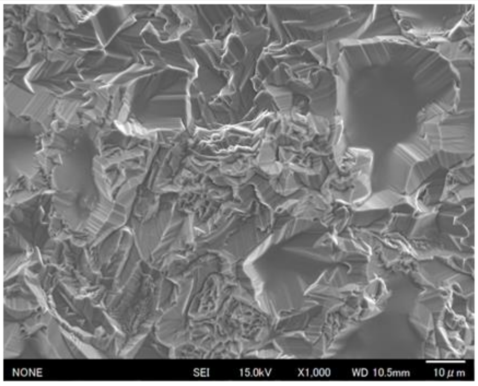	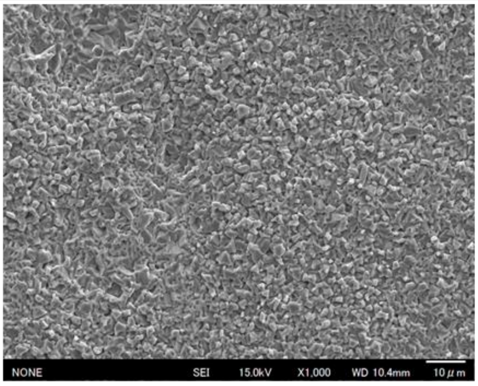

Figure 3.6 SE images of the surface morphology of all samples after the oxidation test up to 345.6 ks.

3.3.5 Cross-sectional images of the oxidized samples

Figure 3.7 shows the BE image of the cross-sectional area of all alloys oxidized up to 345.6 ks. The different phases could be distinguished from the distinct contrast in BE images. It could be seen that Fe-9Cr and Fe-9Cr-2Nb alloys show similar oxide structures of thick duplex scale with two different layers of outer scale and two different layers of the inner part. The scale formed on Fe-9Cr alloy was thicker after a longer oxidation time. The inner part of the Fe-9Cr and Fe-9Cr-2Nb alloy could be divided into the inner scale and internal oxidation zone (IOZ). Both IOZ and inner scale were found flatter in the Fe-9Cr-2Nb alloy. The ratio of inner scale to IOZ formed in the Fe-9Cr-2Nb alloy was bigger than Fe-9Cr alloy. Darker parts/bands in the inner part were found to form more in the matrix of IOZ of Fe-9Cr alloy, indicating oxidation reaction on Fe-9Cr was more severe.

Figure 3.8 shows the high magnification images of the inner part of the oxide scale formed on each alloy oxidized for 345.6 ks. IOZ of Fe-9Cr-2Nb alloy presented a high density of finer inner oxide grain. Enrichment of Cr was found in the inner scale of Fe-9Cr-2Nb alloy. Additionally, the presence of niobium was only detected rich in the grain boundaries and low in the matrix. Point analysis was taken into the same area. The Cr concentration in the inner scale and IOZ was higher than in the matrix. Nb was not detected in the matrix by point analysis. In addition, coarse intermetallic contained around 6.5 at.% of Cr and more than 61 at.% of Fe.

Figures 3.9 and 3.10 show the element mapping of Fe-9Cr and Fe-9Cr-2Nb samples after the oxidation test for 84.6 ks. Similar to the contrast in BE images, two phases on both outer and inner parts could be distinguished by the different colors (mostly the oxygen). Considering the XRD results, the outer scale consisted of FeO in the region close to the substrate and magnetite on the outer side. Further, the Fe-9Cr-2Nb alloy presented a higher ratio of Fe_3O_4 on the outer scale than the Fe-9Cr alloy.

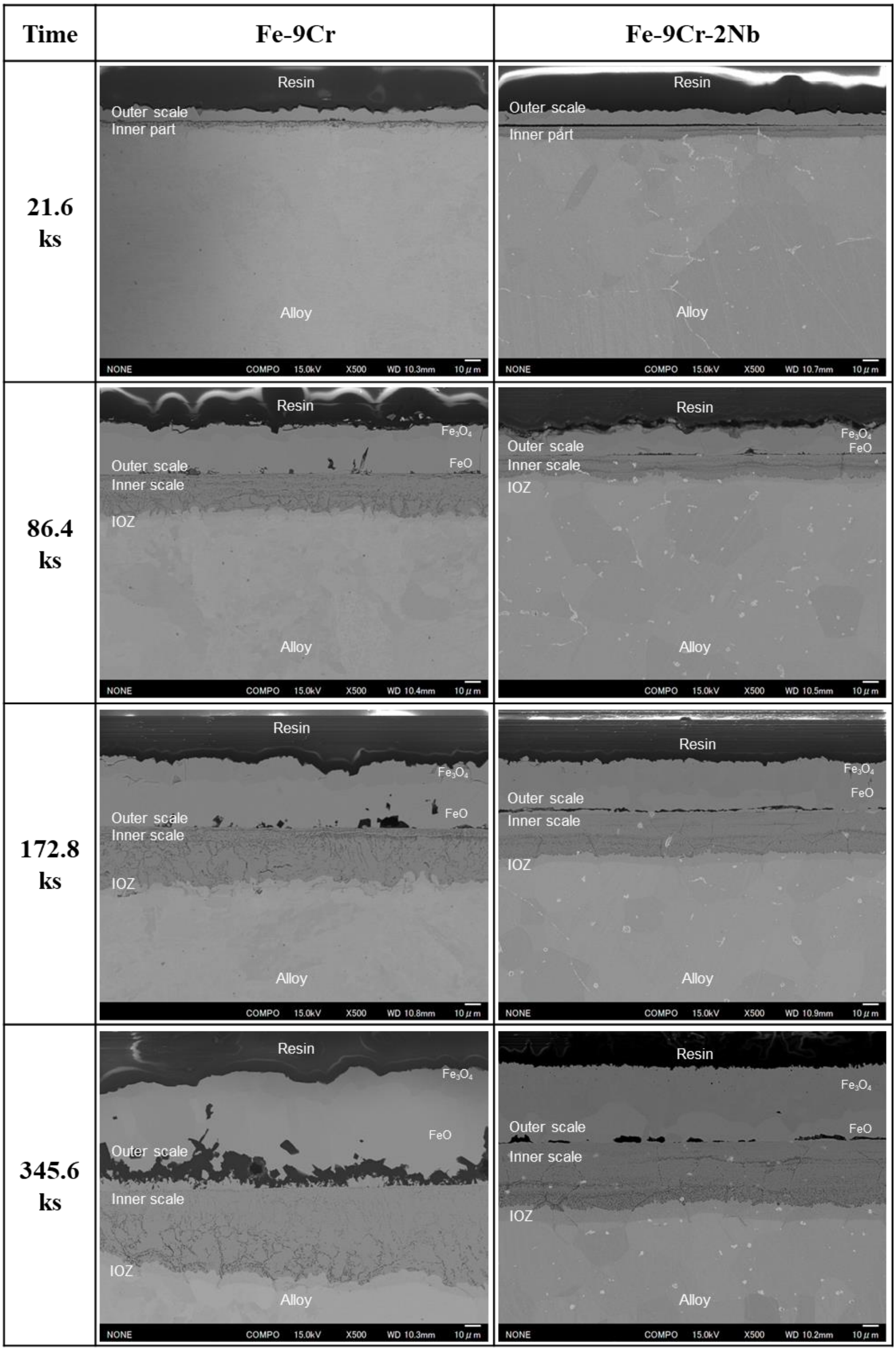

Figure 3.7 Cross-sectional images of all samples after oxidation test up to 345.6 ks.

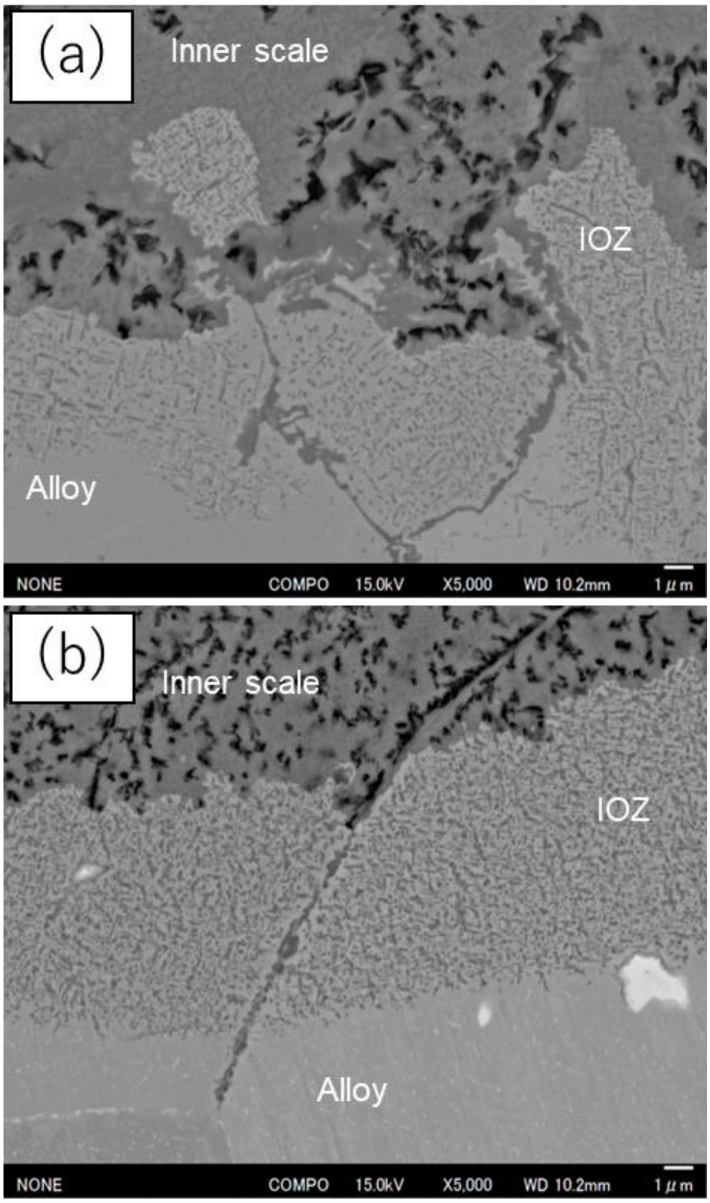

Figure 3.8 High magnification of cross-sectional images of all samples after oxidation test up to 345.6 ks.

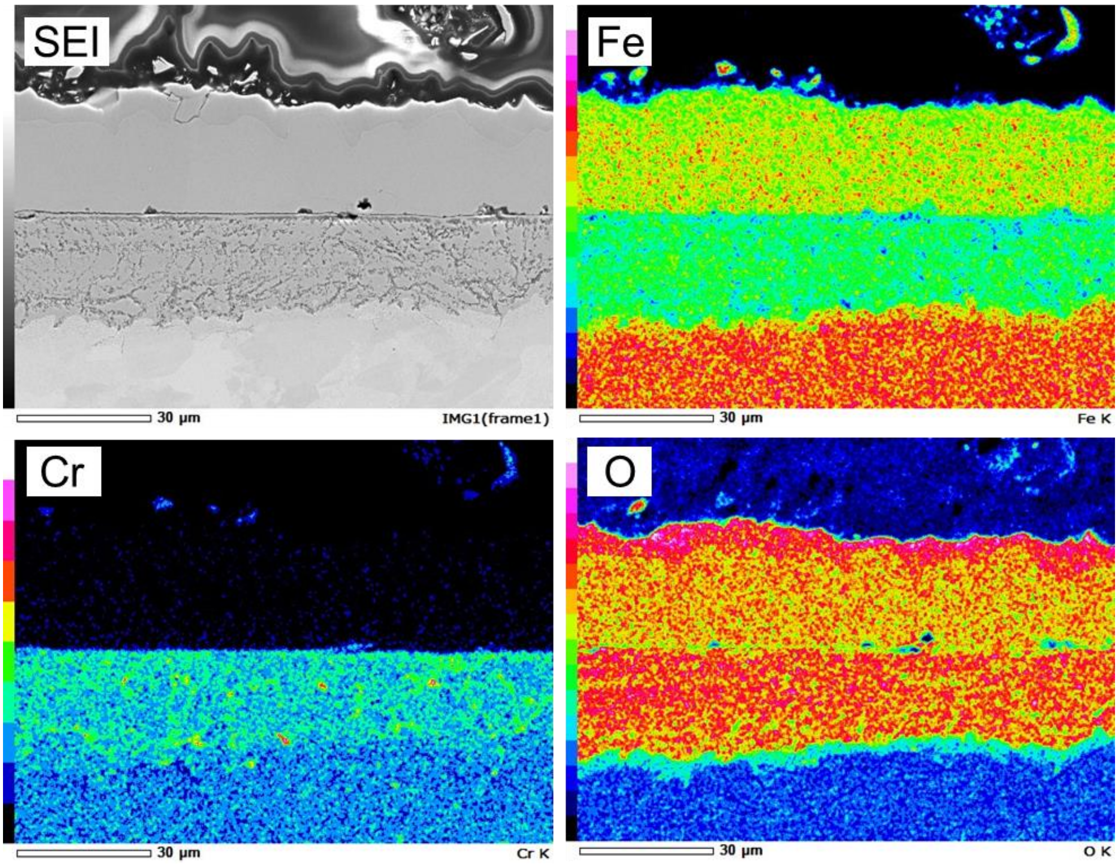

Figure 3.9 Element mapping of the Fe-9Cr alloy oxidized for 86.4 ks.

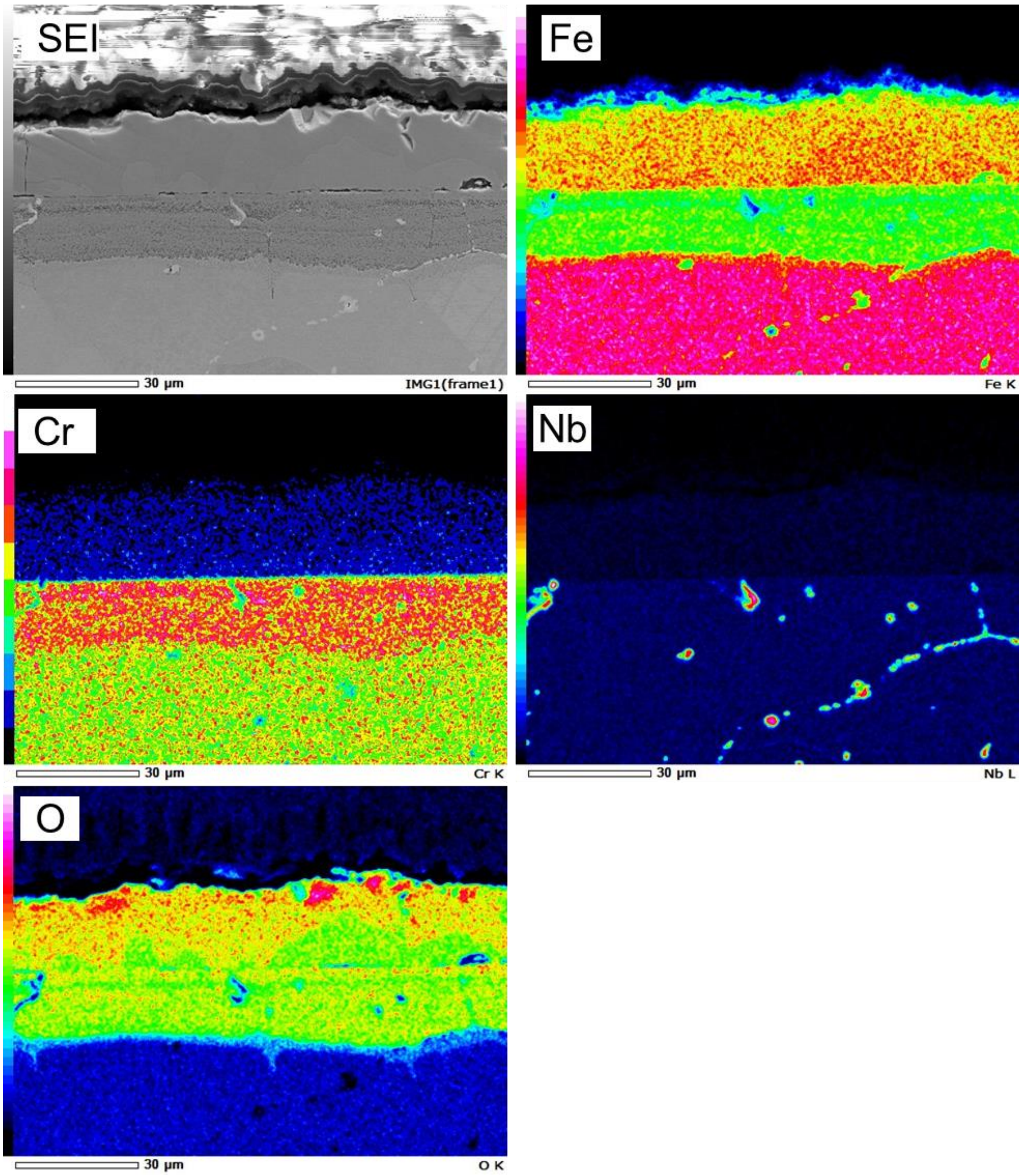

Figure 3.10 Element mapping of the Fe-9Cr-2Nb alloy oxidized for 86.4 ks.

3.3.6 Thickness of the oxide scale

The scale thickness trend was measured from BE images from 10 points. In this research, the inner part of the scale is divided into the inner scale and internal oxidation zone (IOZ). The inner scale is defined as IOZ with the oxidized matrix, while the IOZ is defined as the zone consisting of oxide particles within the metal bulk. Figure 3.11 shows the trend of the inner part and total scale thickness versus oxidation time. Similar to the trend of mass change data, the growth of scale decreased by the oxidation time. Fe-9Cr-2Nb alloy showed a thinner oxide scale, both inner part and total oxide, which suggested that the addition of Nb was useful to suppress the growth of the inner scale.

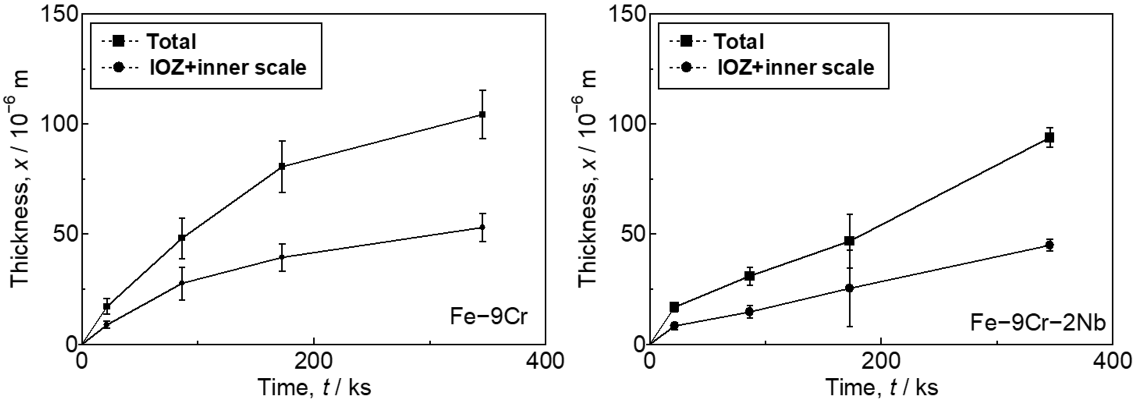

Figure 3.11 Thickness of the oxide scale after the oxidation at 923 K.

Figure 3.12 compares the thickness from each layer formed on the duplex scale of Fe-9Cr and Fe-9Cr-2Nb alloys. It was found that the thickness of magnetite grew earlier in the Fe-9Cr-2Nb alloy, which was also confirmed by XRD analysis. Compared to the Fe-9Cr alloy, the Fe-9Cr-2Nb alloy exhibits a thicker magnetite layer, and a thinner wüstite layer was found thinner than the Fe-9Cr alloy. Further, the growth of the wüstite and magnetite in the Fe-9Cr-2Nb alloy decreased in a longer oxidation time. In addition, the growth of the inner scale decreased after 21.6 ks, and the thickness of IOZ was almost the same for both alloys.

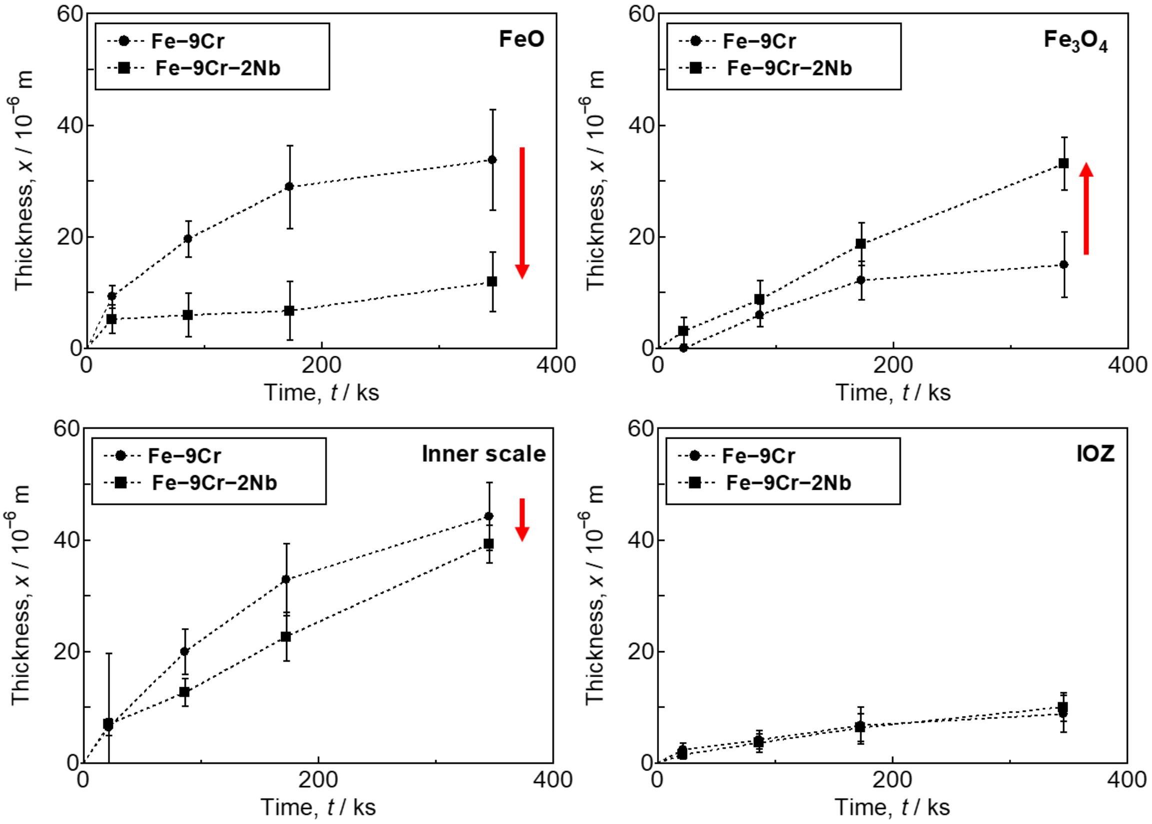

Figure 3.12 Thickness of each scale layer of Fe-9Cr and Fe-9Cr-2Nb alloy as a function of oxidation time.

3.4 Discussion

3.4.1 Development of the oxide scale on the Fe-9Cr and Nb-added Fe-9Cr alloys

Oxidation behavior of Fe-9Cr alloys in the same condition is reported in chapter 2. No significant difference in the oxide structure was found in both Fe-9Cr and Fe-9Cr-2Nb alloys, indicating the scale mechanism formation was similar. However, as shown in figures 3.7 and 3.8, the Fe-9Cr-2Nb alloy performed thinner and more compact inner part (inner scale and IOZ). Based on the phase diagram (Fig. 3.1), this study assumes that Nb in the matrix was neglected, and all Nb only formed intermetallic compounds. Therefore, the accumulation of Nb in the matrix of IOZ is unpreferable. In addition, intermetallic compounds containing Cr were observed in the matrix as fine Fe_2Nb and coarse intermetallic particles. Therefore, the scale formation mechanism in Fe-9Cr-2Nb alloy is proposed considering the Fe-Cr binary system with Cr dissolved in the intermetallic phases. Figure 3.13 shows the proposed mechanism for scale development on Nb added Fe-9Cr alloy. In addition, the proposed mechanism for scale formation on the Fe-9Cr alloy from chapter 2 is presented in Fig. 3.13(a) to help differentiate the proposed mechanism for duplex scale formation on the Fe-9Cr-2Nb alloy.

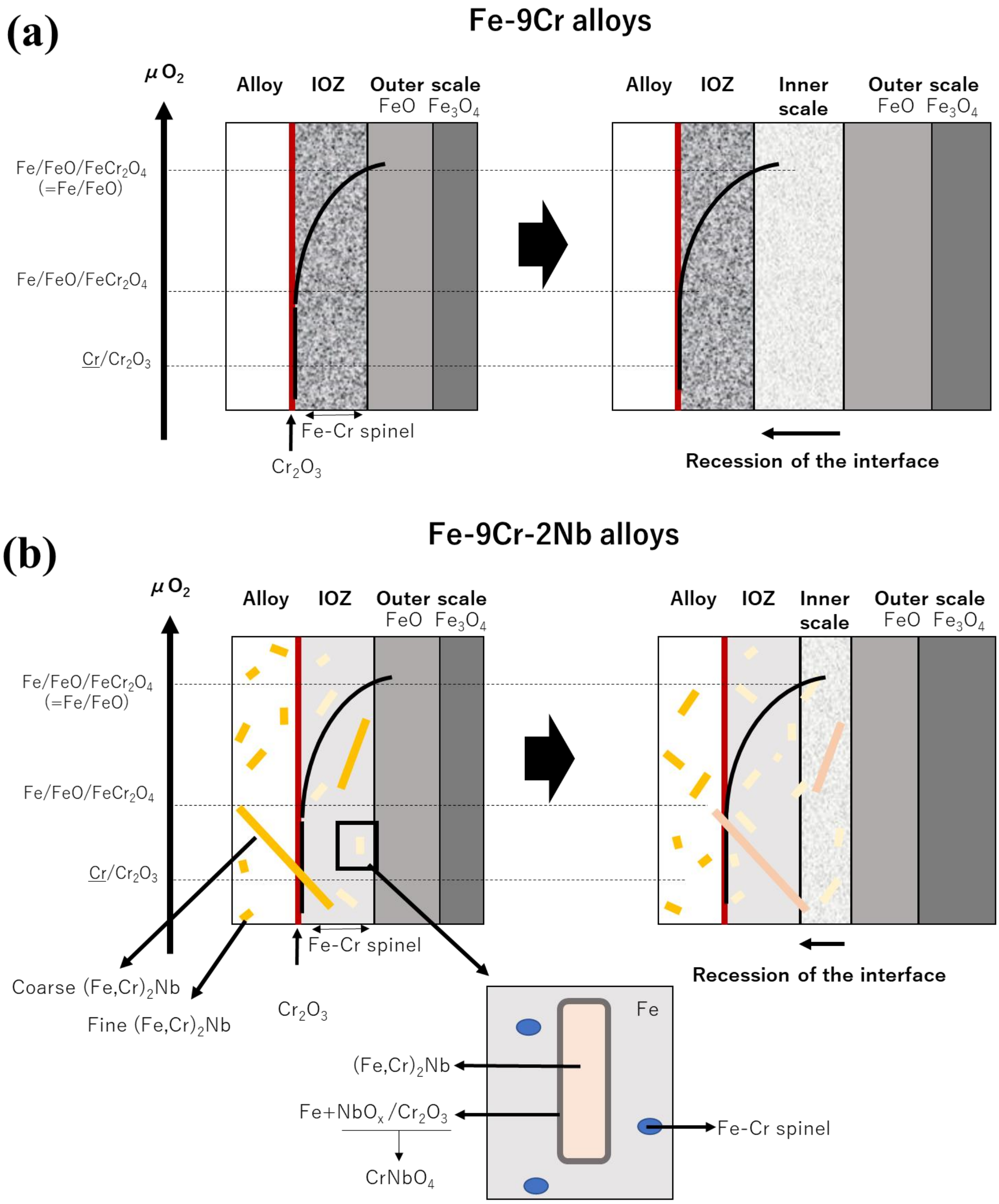

Figure 3.13 Proposed mechanisms for scale formation on the (a) Fe-9Cr alloy and (b) Fe-9Cr-2Nb alloys.

The dissociation oxygen partial pressure of FeO, $FeCr_2O_4$ [13], Cr_2O_3 [14], and Nb-containing oxide [15] is presented in table 3.3. From the data, the formation of Cr_2O_3 is more stable than NbO_2 and $NbO_{2.44}$ (Nb_2O_5). However, considering the activity of Cr in the alloy, the value of dissociation oxygen partial pressure of $\underline{Cr}/Cr_2O_3$ becomes higher than the presented value. Besides, Nb is negligibly small in the matrix. Therefore, in the early stages of oxidation, it is easier for Cr in the matrix to oxidize internally into Cr_2O_3 and develops IOZ. At the same time, Fe diffused outward to develop an outer scale. By the inward diffusion of oxygen, the old Cr_2O_3 will react with the matrix of Fe to form $FeCr_2O_4$, and deeper penetration of O nucleate new Cr_2O_3.

Table 3.3 Estimated dissociation oxygen partial pressure at 923 K from references [13-15].

Oxides	Reaction	PO_2 (Pa)
FeO	$Fe + \frac{1}{2} O_2 \rightarrow FeO$	7.15×10^{-19}
$NbO_{2.44}$	$NbO_2 + 0.211\ O_2 \rightarrow NbO_{2.44}$	1.29×10^{-22}
$FeCr_2O_4$	$2Fe + 2Cr_2O_3 + O_2 \rightarrow 2FeCr_2O_4$	5.49×10^{-24}
NbO_2	$NbO + \frac{1}{2} O_2 \rightarrow NbO_2$	6.46×10^{-29}
Cr_2O_3	$2Cr + \frac{3}{2} O_2 \rightarrow Cr_2O_3$	4.17×10^{-29}
NbO	$Nb + \frac{1}{2} O_2 \rightarrow NbO$	1.29×10^{-33}

Figure 3.14 shows the oxygen potential – mole fraction diagram of the Fe-Nb-O system [16]. The oxidation products in this system are internal oxidation of niobium oxide, double oxide $FeNb_2O_6$ (d.o), α(Fe), and intermetallic compounds: β (25 at.% Nb) and γ (50 at.% Nb) [16]. During the oxidation reaction in the Fe-Nb system, the α (Fe) phase transformed

the fine Laves phase, which was precipitated in the matrix of IOZ, into a fine mixture of niobium oxide and iron. It explained the reason for the disappearance of the fine Laves phase in the inner scale and the IOZ. In the system of Fe-Cr-Nb, it is necessary to consider Cr in the Laves phase.

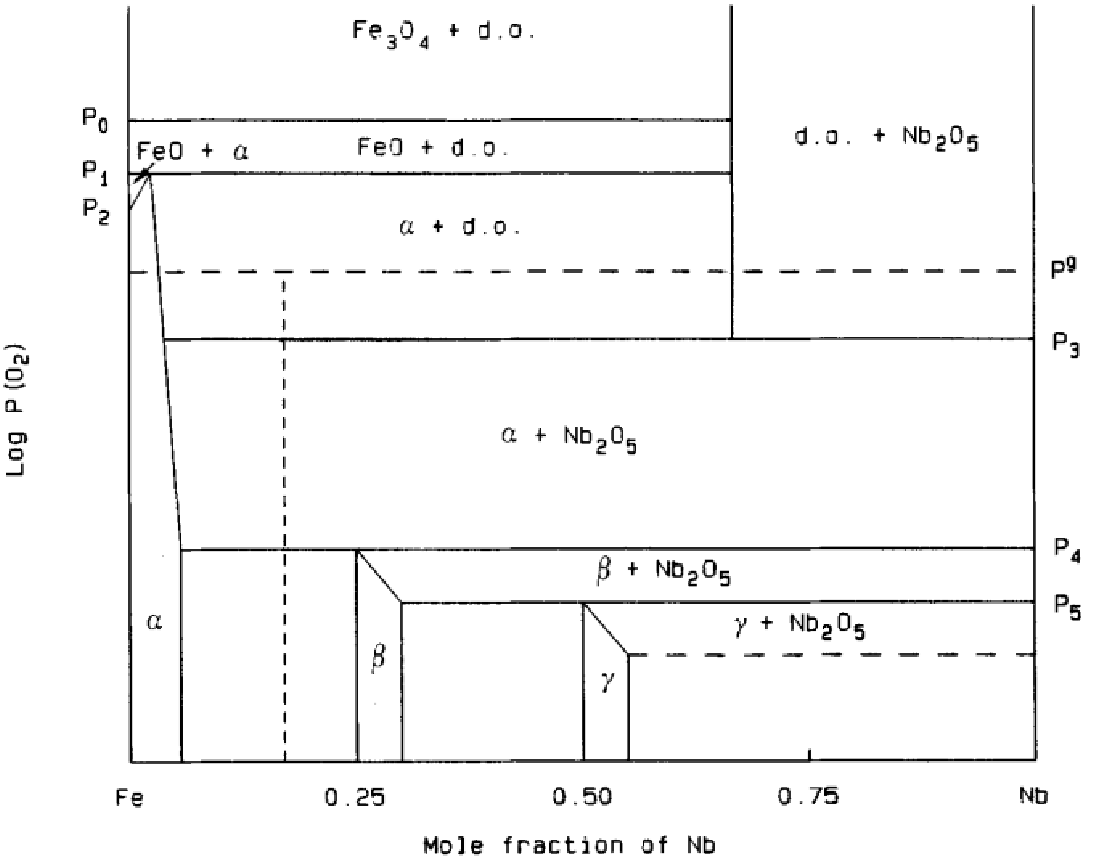

Figure 3.14 Map of oxygen potential - mole fraction diagram of the Fe-Nb-O system at 873-1073 K [16].

The IOZ grows deeper, and the matrix of IOZ will be equilibrated with Cr_2O_3 particles and the oxidation products of Laves phase. It is reported that the Ni-Fe-Cr alloy, Nb can be oxidized together with Cr_2O_3 particles to form $CrNbO_4$ particles in the IOZ [17]. Considering this reaction, the IOZ will consist of Fe matrix, Cr_2O_3, NbO_x, or $CrNbO_4$ (estimated product from oxidation reaction of laves phase containing Cr), and the coarse intermetallic particles which were not fully oxidized. Further oxidation reaction will oxidize the matrix of IOZ to form an inner scale that consists of FeO, $CrNbO_4$, and the coarse intermetallic particle.

Figure 3.15 showed the elemental mapping from the inner scale of Fe-9Cr-2Nb. The surface of the oxidized coarse intermetallic compound is rich in Cr, followed by Nb in the inner part of the particle. The main constituent of Laves phase is Fe, Cr, and Nb. Therefore, the Laves phase may act as a Cr reservoir. The fine and distributed Laves phase may contribute to finer and compact inner scales and IOZ. The enrichment of Cr in the inner scale indicated that the precipitation density of spinel increased by the presence of Laves phase. In addition, the density of $CrNbO_4$ is reported to be two times larger than $CrNbO_4$ [17]. This volume fraction of $CrNbO_4$ is increased by adding more Nb into the alloy. Further, the $CrNbO_4$ and Cr-rich oxide particles in the inner scale and IOZ may suppress the outward diffusion of the Fe atoms.

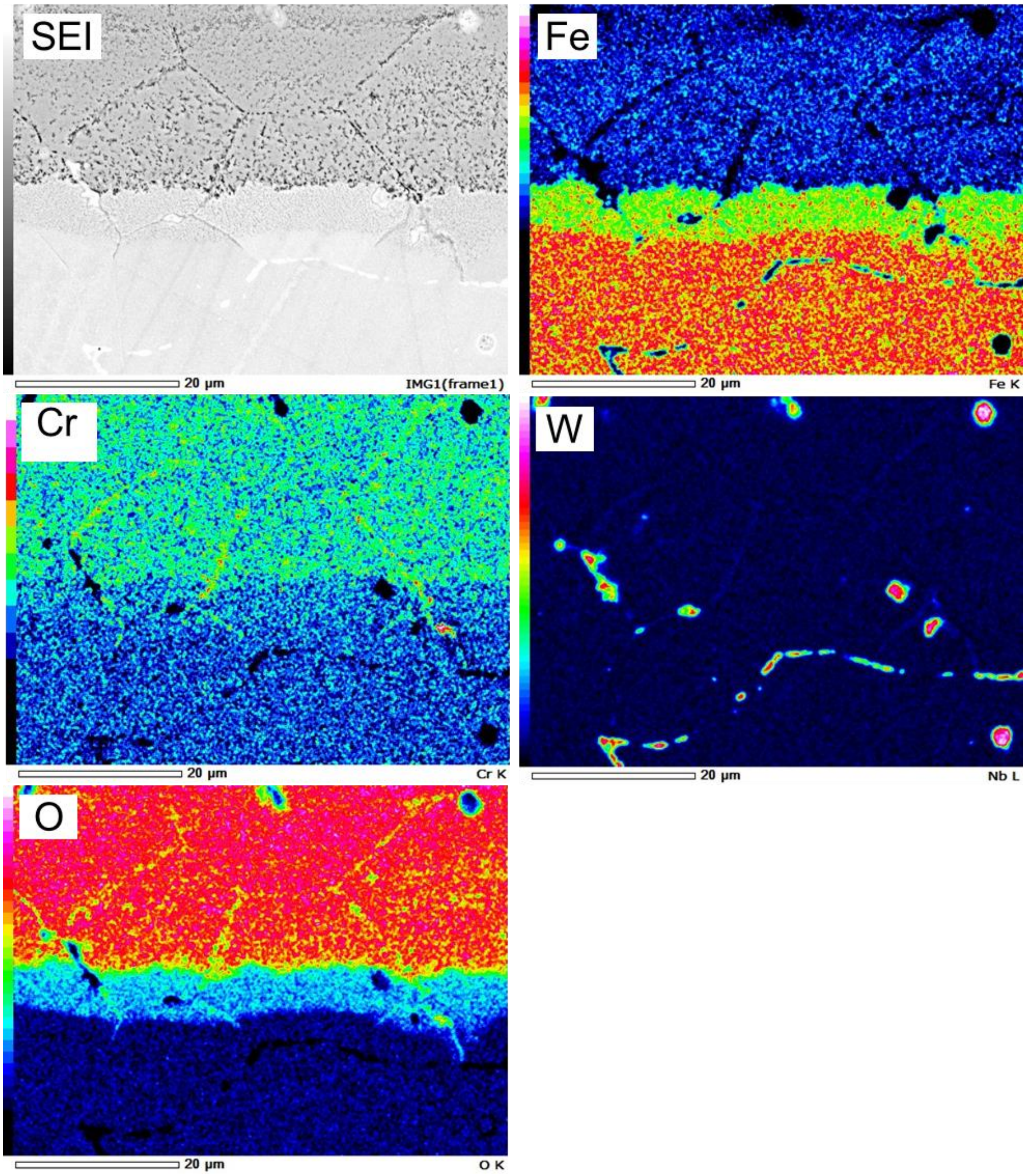

Figure3.15 Element mapping of the Fe-9Cr-2Nb alloy oxidized for172.8 ks.

Although the Fe-9Cr-2Nb alloy performs better Cr distribution in the inner scale and IOZ, the protective layer has not been established on this alloy. Therefore, the oxygen still penetrates into the metal, and partial pressure beneath the inner scale becomes sufficiently high to oxidize the alloy internally. As compensation for the inward diffusion of oxygen, the outward diffusion of metal atoms in equal amounts is needed. However, since the inner scale is good enough to retard the iron diffusivity, the less supply of Fe develops a thinner outer scale. The oxygen partial pressure at the outer/inner scale interface increases to transform wüstite in the outer scale into magnetite, which is more stable in higher oxygen partial pressure. According to this explanation, the earlier formation of magnetite, as well as the smaller ratio of wüstite to magnetite on the Fe-9Cr-2Nb alloy, could be explained.

3.4.2 Effect of initial microstructure on the scale development

The removal of Nb in the matrix is reported in the alloy that precipitated Laves intermetallic phase during aging [7]. Consequently, instead of forming NbO_x, the Cr_2O_3 formation in the matrix is preferable. According to the Fe-9Cr-Nb phase diagram (Fig. 1.7), all Nb in the system of Fe-9Cr-2Nb alloy is supposed to be dissolved in the matrix of BCC during the solution treatment. Then precipitate Fe_2Nb Laves phase during the aging. However, the coarse intermetallic compound was observed in the matrix together with the fine Fe_2Nb Laves phase. From the elemental mapping, this particle contains Fe, Cr, and Nb, so the volume fraction of Laves phase found in the alloy becomes less than the estimated from the phase diagram of the Fe-9Cr-2Nb system. This phenomenon might be because the solution treatment time was not long enough to allow all metals to dissolve into the BCC matrix.

Figure 3.16 shows a high magnification of the Fe-9Cr-2Nb sample oxidized for 345.6 ks. It could be seen that the grain boundary acts as an effective diffusion path for the inward diffusion of oxygen. This oxygen may penetrate into the intermetallic compound along grain boundaries and react with the Cr in the intermetallic compound. Therefore, the surface of coarse intermetallic compounds started to oxidize. However, this phenomenon did not induce internal oxidation formation beneath the oxidized intermetallic compound, as Huang *et al*. [18] reported. In this case, the coarse intermetallic compound also acts as a Cr reservoir that consumes some oxygen along the grain boundaries. While the fine and well-distributed Laves phase gave better Cr enrichment in the inner scale and IOZ in the same manner as coarse intermetallic compounds. In addition, a narrow depletion zone was found beneath the IOZ. In this area, the volume fraction of the fine Laves phase was found to be less than in the matrix. The possibility is the development of IOZ consumes

Cr in the matrix and intermetallic phase, which changes the solubility limit of Nb in the matrix. It results in the Nb becoming depleted below the IOZ.

In the Fe-Cr-Nb system, the Fe_2Nb Laves phase can act as a Cr reservoir and contribute to the formation of higher density of IOZ and inner scale by forming $CrNbO_4$. This effect is very different from the Laves phase in the Fe-Cr-W system that can develop the phases that have slightly lower oxygen partial pressure of IOZ than the Fe/FeO, which suppresses the formation of the inner scale.

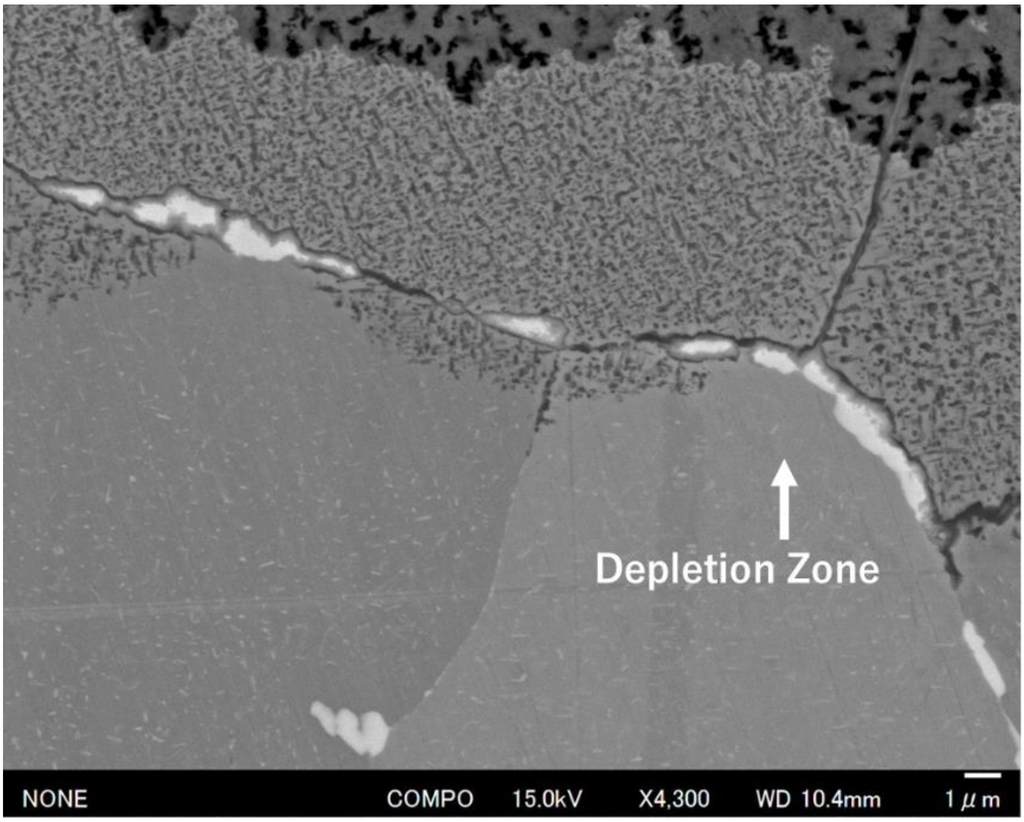

Figure 3.16 BE images of the oxide scale from the cross-sectional of the Fe-9Cr-2Nb sample after the oxidation test for 345.6 ks.

3.4.3 Comparison of Fe-Cr-Nb and Fe-Cr-W systems

The oxidation behavior observed on Fe-Cr-Nb alloy is different from the Fe-Cr-W system. First, the accumulation of W in IOZ during the development of IOZ is possible in the system of Fe-Cr-W, but in the system of Fe-Cr-Nb, all Nb is suggested to form precipitates. Although there was an accumulation of Nb, the formation of FeO is preferable, and the FeO has no connection to the intermetallic Fe_2Nb based on Fig. 3.14. The phase diagram of the systems is presented to help understand the correlation between the phases of the Fe-Nb-O and Fe-W-O systems. Figure 3.17 [19] shows the phase diagram of the Fe-Nb-O system at 1473 K. In comparison, the phase diagram of the Fe-W-O system at 1200-1300 K is presented in figure 2.35. According to the explanation of the scale formation mechanism on Fe-Cr-W in chapter 2, the formation of Fe(W)/Fe_2W/$FeWO_4$ effectively keeps the oxygen partial pressure in the IOZ in the low PO_2 to suppress the formation of FeO. This equilibrium can be obtained because there is an area where the Fe, Fe_2W, and $FeWO_4$ exist in a triangle. In addition, the accumulation of W can help the formation of Fe_2W and $FeWO_4$ in the matrix Fe. In this system, Fe_2W was not oxidized but continuously formed. On the other hand, in figure 3.17, the matrix Fe is directly connected to the FeO and Fe-Nb complex oxide. In particular, the presence of Fe_2Nb was not reported. The missing connection between the matrix, substrate, and oxide was also observed in Fig. 3.14. The Laves phase will be oxidized to form Fe and Nb_2O_5. Furter oxidation of these phases forms Fe and $FeNb_2O_6$ (d.o), then Fe will be oxidized to form FeO. Therefore, the strategy to employ the phase relationship between matrix, oxide, and intermetallic compounds found in the Fe-Cr-W system is not applicable in the Fe-Cr-Nb system.

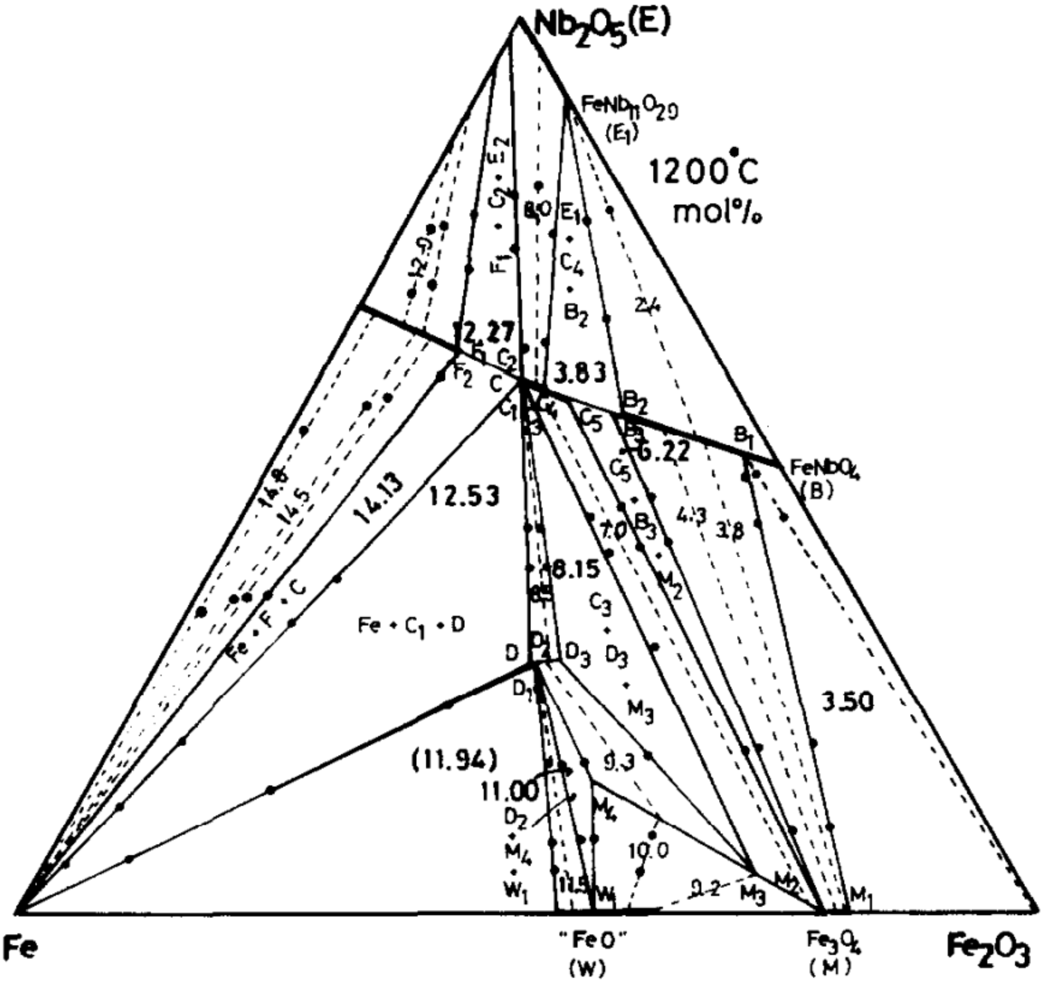

Figure 3.17 Phase diagram of Fe-Nb-O system at 1473 K [19].

3.5 Conclusion

The effect of Nb on the steam oxidation behavior of Fe-9Cr alloy at 923 K was investigated. Adding Nb into Fe-9Cr alloy improves the oxidation resistance of the alloy. The results show that the Fe-9Cr-2Nb alloy has a slower oxidation rate than the Fe-9Cr alloys. A duplex scale with a thinner and more compact inner scale was observed. The fine Laves phase acted as a Cr reservoir and contributed to the formation higher density of IOZ and inner scale by oxidizing Laves phase to provide a better Cr enrichment in the inner scale, which retarded the outward diffusion of Fe ion through the inner scale. As the grain boundaries act as an effective diffusion path, the precipitation of Laves phase along the grain boundaries consumes the inward oxygen. The oxidation behavior of Fe-Cr-Nb system is very different from the Laves phase in the Fe-Cr-W system, which can develop the phases with a lower oxygen partial pressure of IOZ s than the Fe/ FeO equilibrium. This phenomenon suppresses the formation of the inner scale. In this system, there was no useful phase relationship between the substrate, IMCs, and oxide scale that was similar to the phases relation in the Fe-Cr-W system.

3.6 References

[1] W. Yan, W. Wang, Y. Y. Shan, and K. Yang, *Frontiers of Materials Science*, **7**(1), 2013, (1–27).

[2] Jara, D. R. Doctoral dissertation, Univ.-Bibliothek. 2011.

[3] Prat, O., García, J., Rojas, D., Sanhueza, J. P., & Camurri, C. *Materials Chemistry and Physics*, **143**(2), 2011, (754-764)

[4] A. Safikhani, M. Esmailian, T. Tinatiseresht, and G. B. Darband, Int. J. *Hydrogen Energy*, **41**(14), 2016, (6045–6052).

[5] P. A. Ramos, R. S. Coelho, H. C. Pinto, F. Soldera, F. Mücklich, and P. P. *Brito, Mater. Chem. Phys.*, **263**, 2021.

[6] Y. Xu, J. Lu, X. Yang, J. Yan, and W. Li, *Corros. Sci.*, **127**, 2017, (10–20).

[7] H. Ali-Löytty, P. Jussila, and M. Valden, Int. J. *Hydrogen Energy*, **38**(2), 2013, (1039–1051).

[8] S. Ide, Y. Funakawa, Y. Kato, and O. Furukimi, *Materials science forum*, 2007, **539**, (4887–4890).

[9] T. Horita et al., *J. Power Sources*, **176**(1), 2008, (54–61).

[10] Emmrich, R., & Krupp, U. *Metals*, **11**(**11**), 2021, (1693).

[11] A. Jacob, C. Schmetterer, D. Grüner, E. Wessel, B. Hallstedt, and L. Singheiser, *J. Alloys Compd.*, **648**, 2015, (168–177).

[12] Pandat 2020 software with PanFe.

[13] D. J. Young, *High temperature oxidation and corrosion of metals*, **1**. *Elsevier*, 2008.

[14] K. T. Jacob, J. *Mater. Sci.*, **15**(9), 1980, (2167–2174).

[15] K. T. Jacob, C. Shekhar, M. Vinay, and Y. Waseda, *J. Chem. & Eng. Data,* **55**(11), 2010, (4854–4863).

[16] Y. Niu, M. C. Rebelo, F. Gesmundo, and F. C. Rizzo, *J. Chinese Soc. Corros. Prot.*, **16**(2), 1996, (114).

[17] Kuo, Yen-Ling and Hayashi, Shigenari and Kakehi, Koji, *Oxidation of Metals*, **95**(1), 2021, (189–202).

[18] Huang, Dong and Lu, Jiashen and Zhuang, Yanxin and Tian, Chunxu and Li, Yibo, *Corrosion Science*, **158**, 2019, (108088).

[19] Kitayama, Kenzo, *Journal of Solid State Chemistry*, **69**(1), 1987, (101-108).

Part of this chapter has been published in:

Lidyana Utami and Mitsutoshi Ueda, "THE EFFECT OF NIOBIUM ADDITION ON STEAM OXIDATION BEHAVIOR OF FERRITIC HEAT RESISTANT STEELS AT 923 K", Joint EPRI-123HiMAT International Conference on Advances in High-Temperature Materials, J. Shingledecker and M. Takeyama, editors, 327-335(2019).

Chapter 4 The Effect of Tungsten and Niobium on the Cr Diffusivity in the Fe-9Cr Alloys with the Alloying Element

4.1 Introduction

In the previous chapter, the effect of W and Nb addition on the oxidation behavior of Fe-9Cr alloys has been clarified. Cr enrichment was found at the inner scale on both Nb added 9Cr alloys or low W added alloys. However, Cr_2O_3 layer was not formed on all alloys. This chapter investigates the other effect of alloying elements, particularly W and Nb, on Cr diffusivity in the alloy. It was found that the oxidation properties were different in the Fe-9Cr alloy with and without precipitates. Therefore, it is important to understand the microstructural effect which is caused by the addition of the alloying elements on the Cr diffusivity. In this chapter, the temperature was raised to 1073 K to accelerate the diffusivity rate of Cr without changing the phase of the ferrite matrix. In addition, the experiment was conducted in a dry atmosphere. Hanafi *et al.* [1] reported that the interdiffusion of Cr in the dry and humid atmosphere was close and scattered from 6×10^{-16} to 10×10^{-16} m^2s^{-1}, which indicated the effect of hydrogen on Cr diffusivity is negligible. Although there are studies reporting the Cr diffusivity in Fe-based alloy, there is limited study on ternary Fe-Cr-W and Fe-Cr-Nb alloys at a lower temperature.

4.2 Experimental

4.2.1 Sample preparation

By considering the phase relation, diffusion path couples of Fe-Cr-W and Fe-Cr-Nb systems investigated in this chapter are plotted in figure 4.1. The couple with Fe/Fe-Cr system will be used as a data reference for the interdiffusion coefficient of Cr in the Fe matrix ($\widetilde{D}_{\mathrm{CrCr}}^{\mathrm{Fe}}$). To estimate the $\widetilde{D}_{\mathrm{CrCr}}^{\mathrm{Fe}}$ with the presence of alloying element, the same strategy to separate the effect of solid solution and precipitation was employed in this chapter. The $\widetilde{D}_{\mathrm{CrCr}}^{\mathrm{Fe}}$ in supersaturated Fe will be estimated from the couple of Fe-3W/Fe-9Cr-3W. The couple Fe-6W/Fe-9Cr-6W will represent the effect of W as solute element and precipitate. In addition, only the effect of precipitation was investigated only in the Fe-Cr-Nb system due to the low solubility limit of Nb in the matrix Fe, which will be represented by couple Fe-2Nb/Fe-9Cr.

The plate of Fe used on Fe- Fe-9Cr couple was prepared from a Fe plate (purity 99.99%). The plate was cut into 10 x 10 x 1 mm^3 sizes without following further heat treatment. The ingot of Fe-9Cr, Fe-2Nb, Fe-3W, Fe-6W, Fe-9Cr-2Nb, Fe-9Cr-3W, and Fe-9Cr-6W alloys are made from Fe (purity 99.99%), Cr (99.999+%), Nb (99.9%) and W (99.95%) using arc melting methods. The ingots were homogenized at a certain condition. Table 4.1 shows the semiquantitative chemical composition obtained by X-Ray Fluorescence spectrometry (XRF).

The ingots were then cut into a 1.5 mm thickness coupon followed by cold rolling with a 30% rolling rate. The coupon samples were recrystallized, then aged to allow the precipitation of Laves phase. All heat treatments (homogenization, recrystallization, and aging) were conducted in a vacuum ampule at the temperature and time listed in table 4.2. Before being assembled into a couple, the sample was grounded with abrasive papers (#600 ~ #5000) and polished with a series of diamond pastes (9 µm ~ 0.25 µm) until the mirror was finished., then was cleaned with ethanol using an ultrasonic cleaner for 0.6 ks. The assembled diffusion couples are listed in table 4.3.

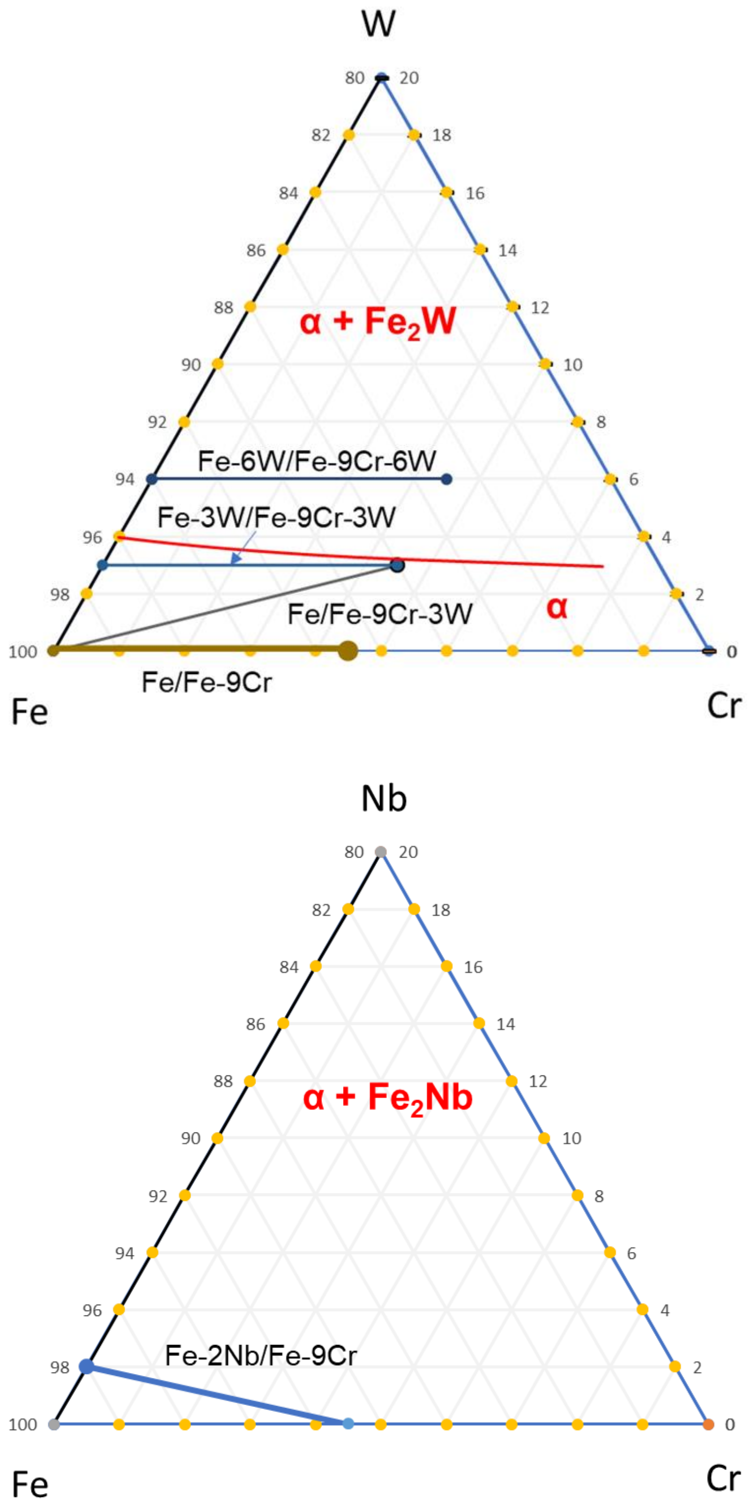

Figure 4.1 Schematic diffusion paths in diffusion couple Fe-Cr-W and Fe-Cr-Nb systems.

Table 4.1 Chemical composition of the alloys (mass%).

	Fe	Cr	Nb	W
Fe-9Cr	Bal.	9.05	-	-
Fe-2Nb	Bal.	-	1.37	-
Fe-9Cr-2Nb	Bal.	9.01	1.27	-
Fe-3W	Bal.	-	-	3.07
Fe-9Cr-3W	Bal.	9.1	-	2.98
Fe-6W	Bal.	-	-	6.11
Fe-9Cr-6W	Bal.	9.16	-	6.14

Table 4.2 Heat treatment conditions of the alloys.

Heat Treatment	Solution Treatment		Recrystallization		Aging Treatment	
	T / K	*t* / ks	*T* / K	*t* / ks	*T* / K	*t* / ks
Fe-9Cr	1273	86.4	1273	0.6	-	-
Fe-2Nb	1573	43.2	1573	0.6	923	864
Fe-9Cr-2Nb						
Fe-3W	1623		1623			
Fe-9Cr-3W						
Fe-6W	1623		1623			
Fe-9Cr-6W						

Table 4.3 Diffusion couple and experiment conditions.

Couple	Alloys	Temperature	Time
A	Fe / Fe-9Cr	1073 K	691.2 ks
B			1382.4 ks
C	Fe-3W / Fe-9Cr-3W		691.2 ks
D			1382.4 ks
E	Fe-6W /Fe-9Cr-6W		691.2 ks
F			1382.4 ks
G	Fe / Fe-9Cr-3W		691.2 ks
H			1382.4 ks
I	Fe-9Cr / Fe-2Nb		691.2 ks
J			1382.4 ks

4.2.2 Experimental

Figure 4.2 shows the schematic illustration of the experimental setup for the interdiffusion experiment. Two alloys were attached, supported by an alumina plate, Kanthal A-1 plate, and spring washers fastened. The diffusion couple was put inside the ceramic tube, hanging close to the R-type thermocouple. A zirconium sponge was inserted at the bottom of the tube to reduce the oxygen partial pressure inside the ceramic tube. Then the tube was evacuated with a vacuum pump for 0.9 ks, and the valve was closed. Another R-type thermocouple was attached to the outside of the ceramic tube, located below the sample, to ensure the sample would be in the soaking area. The tube was then inserted into the furnace, and then the temperature rose to 1073 K with heating rates of about 5 K/min. The diffusion annealing was conducted for 691.2 ks and 1382.4 ks and cooled down inside the furnace. After the test, the sample was mounted and cut in half. The cross-section area is then observed by a Field Emission Scanning Electron Microscope (FE-SEM) equipped with an Energy Dispersive Spectroscopy (EDS). The concentration of Fe, Cr, W, and Nb was quantitatively determined by point analysis from 41 points within a 200 μm line.

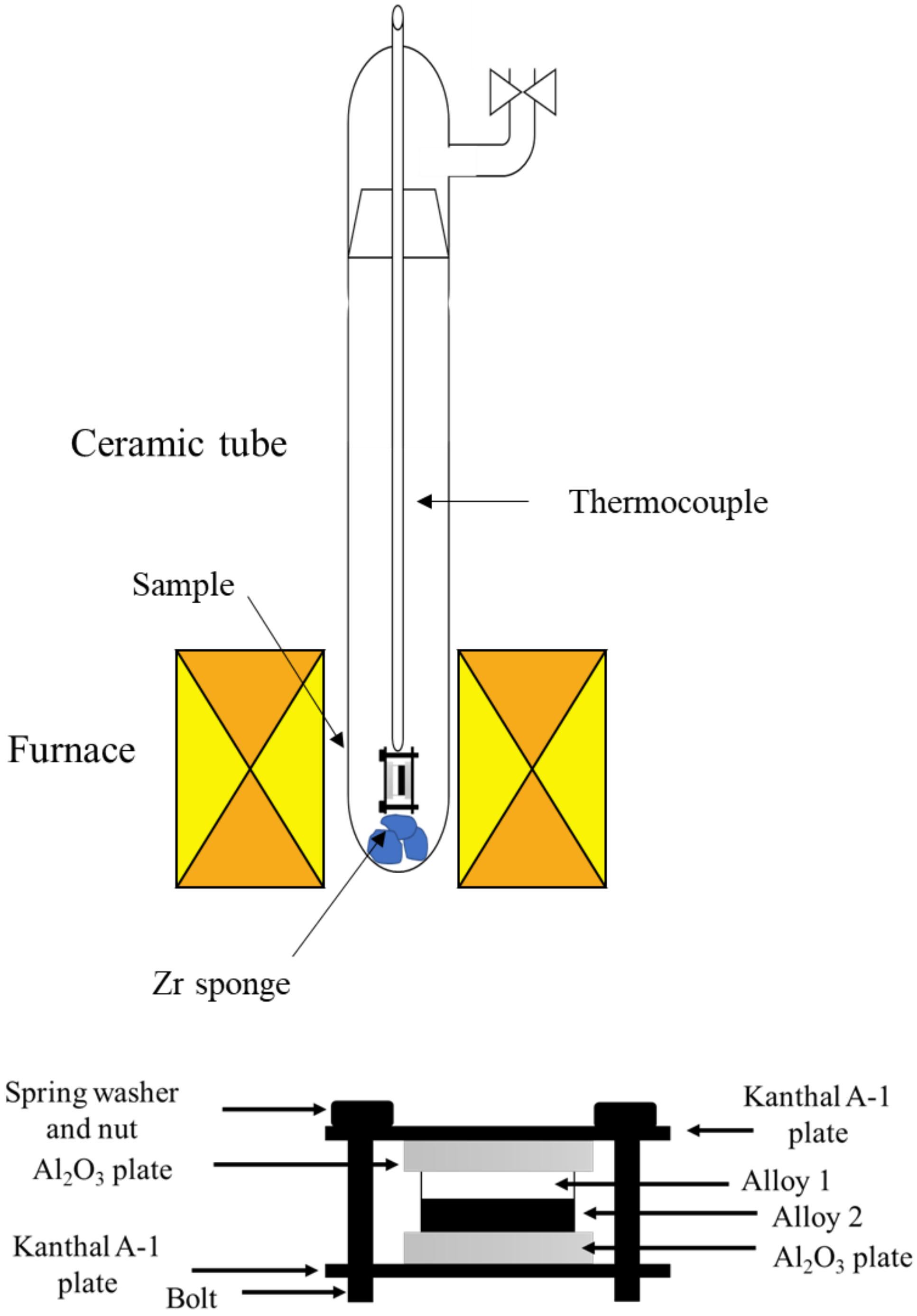

Figure 4.2 Experimental apparatus.

4.3 Results

4.3.1 Microstructure of the alloys before interdiffusion experiments

Figure 4.3 shows the XRD pattern of the alloys before the interdiffusion annealing experiments. The matrix of all alloys was confirmed as α-Fe (ferrite). Figure 4.4 presents the BE images of the microstructural from samples observed by FE-SEM. Etching was conducted using a mixture of HNO_3, HCl, and ethanol for a certain time to observe the grain of the Fe-9Cr alloy. The intermetallic phase precipitation was observed to be precipitated in the matrix of ternary alloys as white particles.

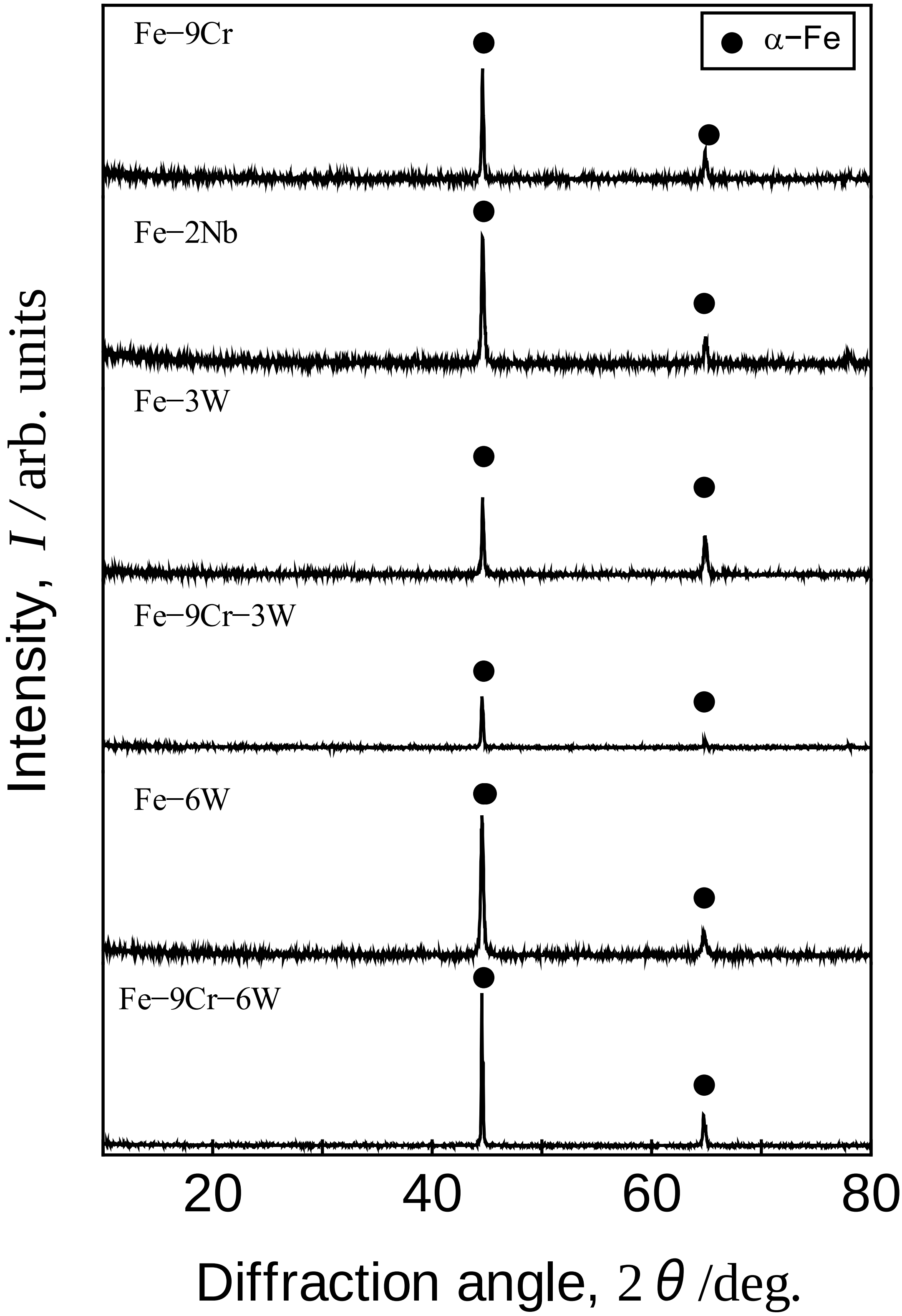

Figure 4.3 XRD pattern from all alloys before annealing.

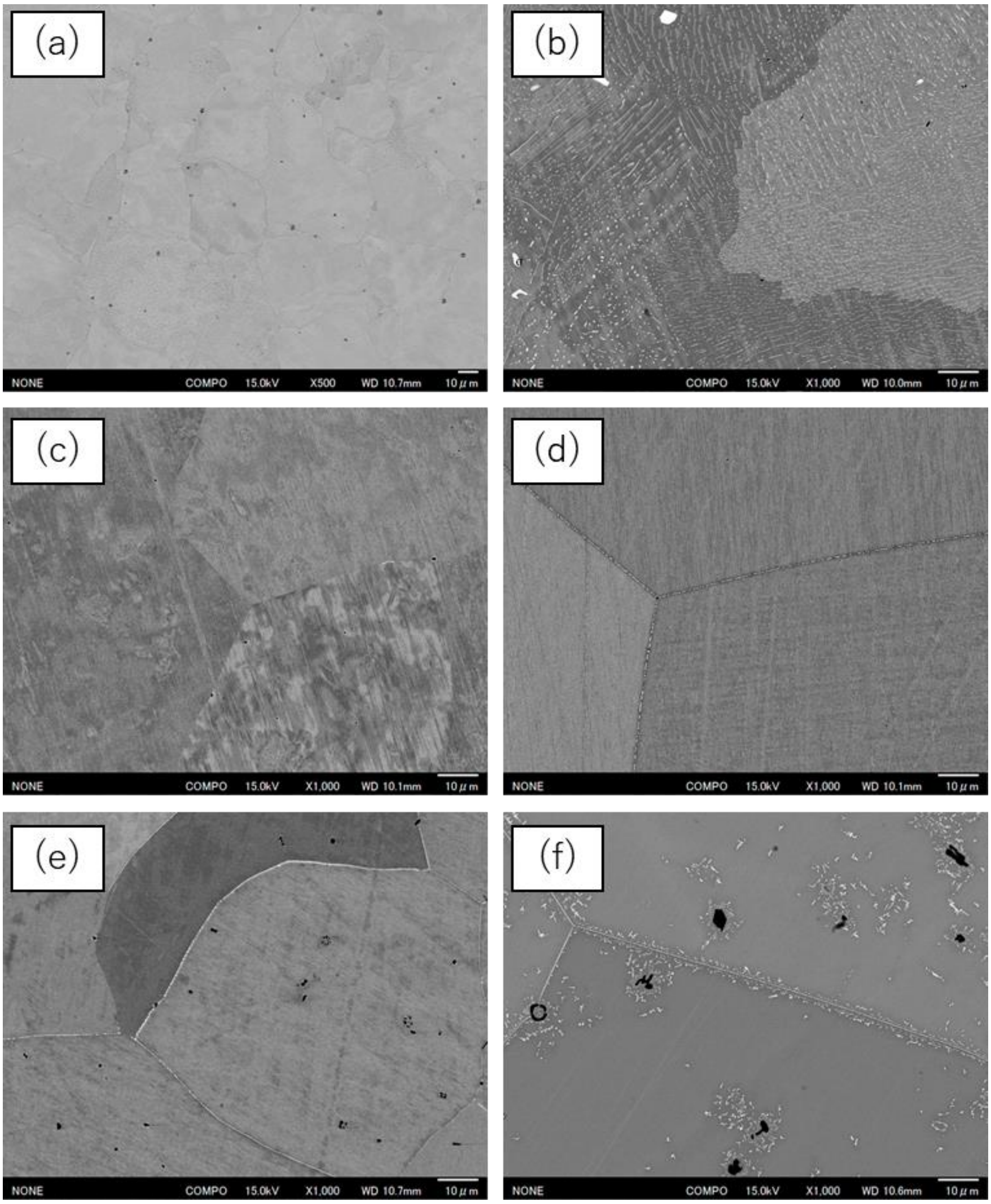

Figure 4.4 BE images of the surface morphology of all sample before the test.
(a) Fe-9Cr, (b) Fe-2Nb, (c) Fe-3W (d) Fe-9Cr-3W, (e) Fe-6W, (f) Fe-9Cr-6W alloys.

4.3.2 Cross-section of diffusion couple and diffusion profile

The concentration profile was taken in the bonded region of couples. Figure 4.5 shows the cross-section area where the profile was taken on diffusion couples A and B. Both Fe and Fe-9Cr alloy showed non-porous with no visible interface but only the trace of the initial, which appear as pores. On both diffusion couples A and B, no Kirkendall porosity was observed. The graph shows the plot of Cr concentration against the distance on both diffusion couples A and B are presented in figure 4.6. Both curves show similar shapes with the Cr diffusion observed within 100 µm from the bonded area.

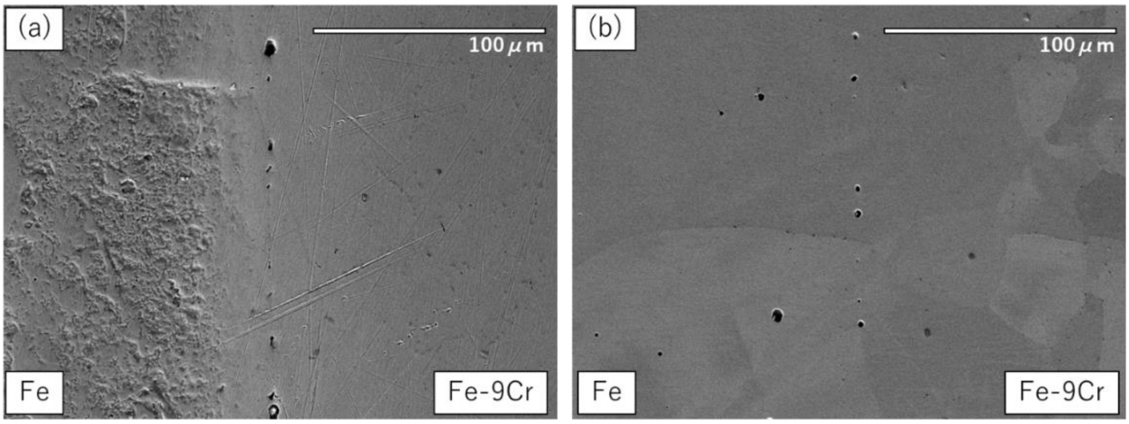

Figure 4.5 SE images of the cross-sectional morphology of (a) diffusion couple A and (b) diffusion couple B after annealing at 1073 K.

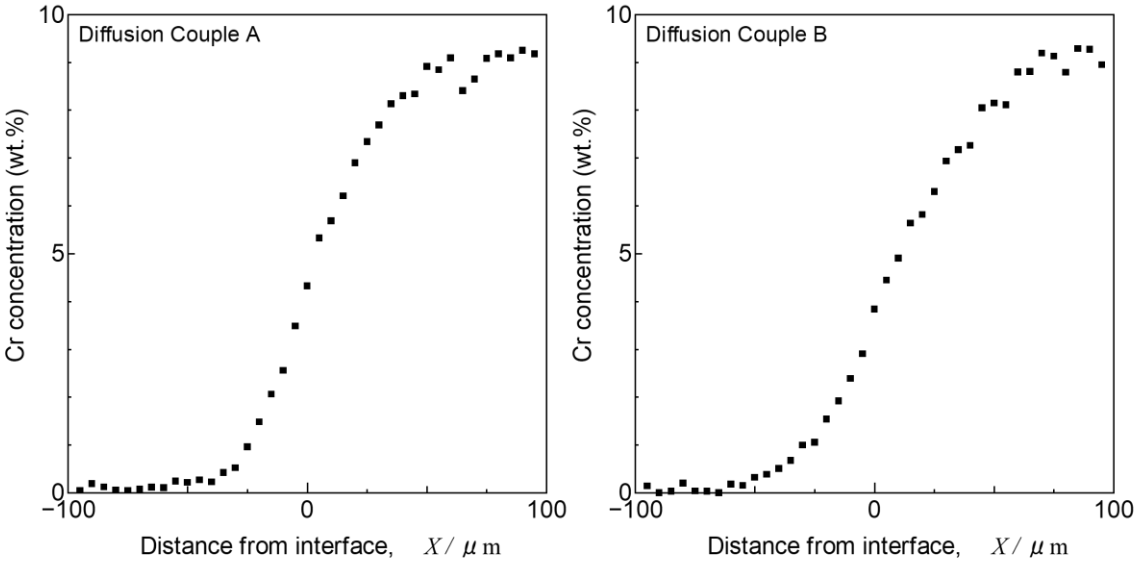

Figure 4.6 Cr concentration profile against distance for diffusion couple A and B after annealing at 1073 K.

Figure 4.7 shows the SE images of the cross-section area where the profile was taken on the Fe-3W/Fe-9Cr-3W couples. Precipitates were found only in some parts along the grain boundaries on both alloys, which suggested most of W is solute in the matrix of Fe on both alloys. It was observed that only samples annealed for a longer time were bonded, while the sample annealed for a shorter time showed a gap of about 1 μm, and only a small portion of the couple attached but showed a crack in the area of Fe-3W alloy. The line analysis was taken at the interface.

Figure 4.8 shows the concentration profile of Cr against the distance from the interface for diffusion couples C and D. The shape of the Cr profile was steep in the crack area of the sample anneal for 691.2 ks (couple C). The sample anneal for a longer time (couple D) shows a profile similar to the diffusion couple A and B. Figure 4.9 shows the concentration profile of W for diffusion couples C and D. In the case of diffusion couple C, the W profile showed depletion in the crack area. While in the diffusion couple D, the W concentration was stable at about 2.5-3 wt.% on both alloy’s sides.

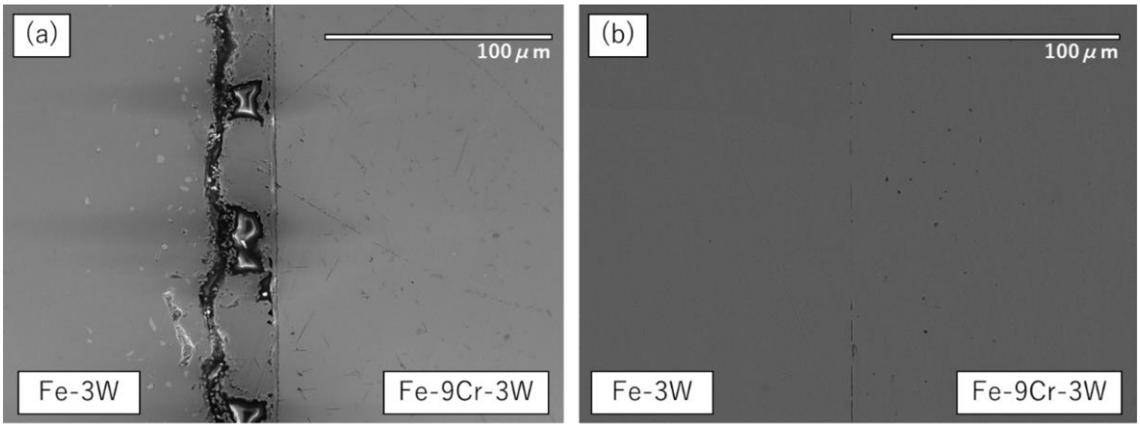

Figure 4.7 SE images of the cross-sectional morphology of (a) diffusion couple C and (b) diffusion couple D after annealing at 1073 K.

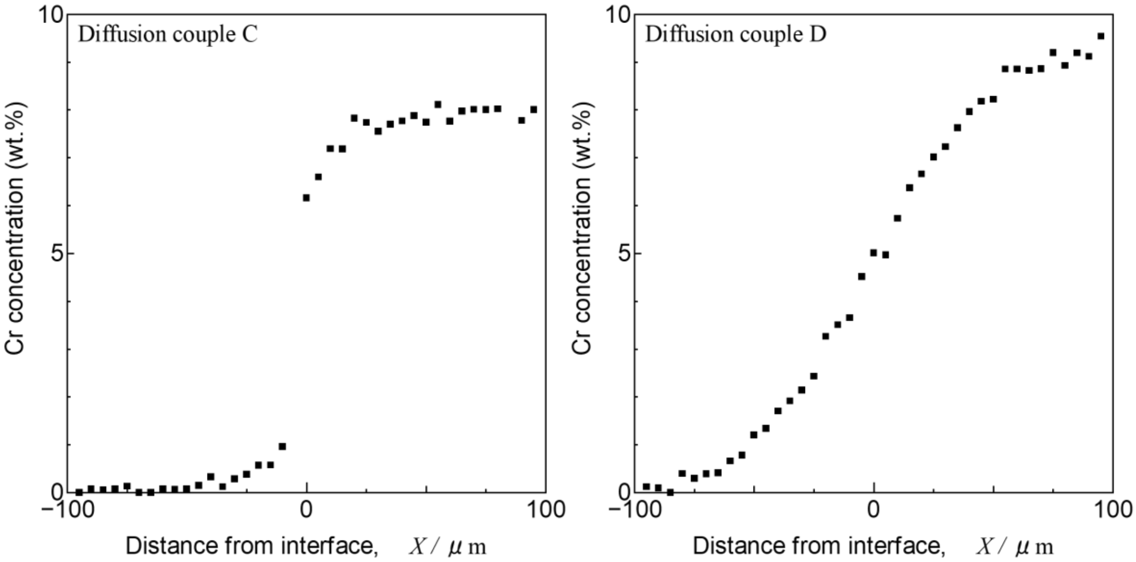

Figure 4.8 Cr concentration profile against distance for diffusion couples C and D after annealing at 1073 K.

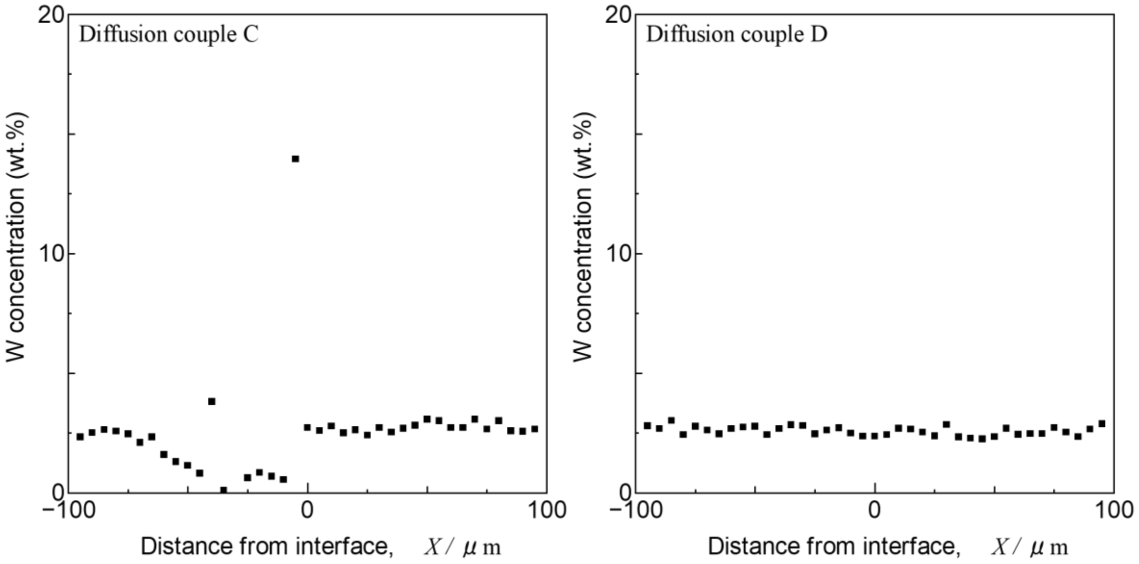

Figure 4.9 W concentration profile against distance for diffusion couples C and D after annealing at 1073 K.

Figure 4.10 shows the SE images of the cross-section area where the profile was taken on the Fe-6W/Fe-9Cr-6W diffusion couples. Precipitates were found along the grain boundaries of both alloys and in the grain interior of Fe-9Cr-6W alloy. The diffusion couples annealed for a shorter time (diffusion couple E) were not bonded with a gap of about 1 μm. Voids were observed near the interface of the alloys in the Fe-6W alloy's side on both diffusion couples E and F, which was suggested as a Kirkendall effect. This effect was observed clearly in the diffusion couple F. In addition, new precipitation of intermetallic particles was found along the interface of the alloys after annealing for 1382.4 ks.

Figure 4.11 presents the concentration profile of Cr against distance for diffusion couples E and F. Figure 4.12 shows the concentration profile of W against the distance from the interface for diffusion couples. The unbonded diffusion couples (diffusion couple E) showed a steep profile, similar to the diffusion couple C. Slight change in Cr concentration at the bonded interface showed initial concentration profiling, indicating the alloys at the interface touched at a high temperature. The S curve was observed in the Cr profile of diffusion couple F. In general, the W concentration was higher than 3.5

mass% on the side of Fe-6W, then decreased to be stable at 3 mass% with some points showing higher W concentration at the point analysis met the precipitates. Moreover, new precipitates were found at the bound interface. At this point, the W concentration increased to above 16 mass%.

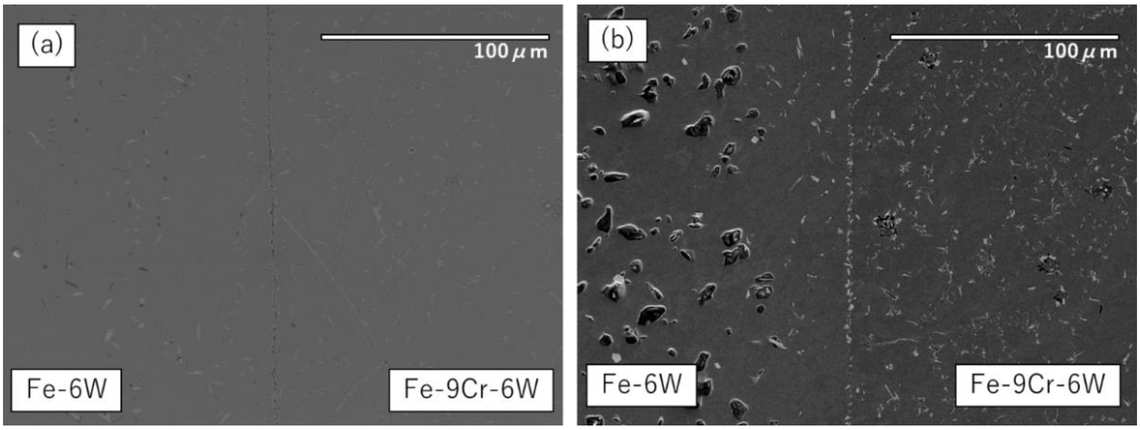

Figure 4.10 SE images of the cross-sectional morphology of diffusion couple (a) E and (b) diffusion couple F after annealing at 1073 K.

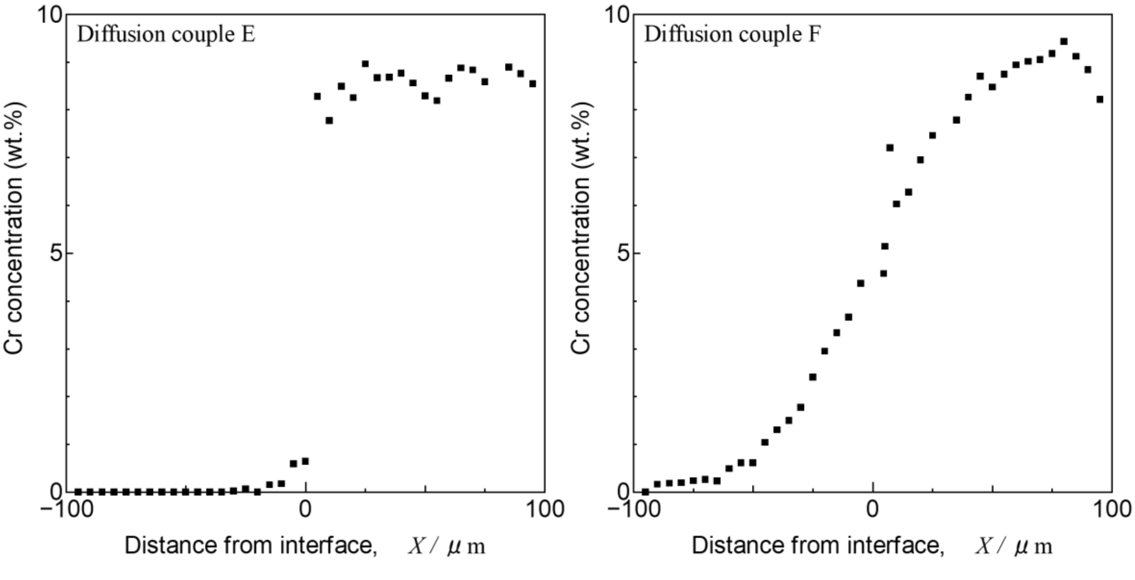

Figure 4.11 Cr concentration profile against distance for diffusion couples E and F after annealing at 1073 K.

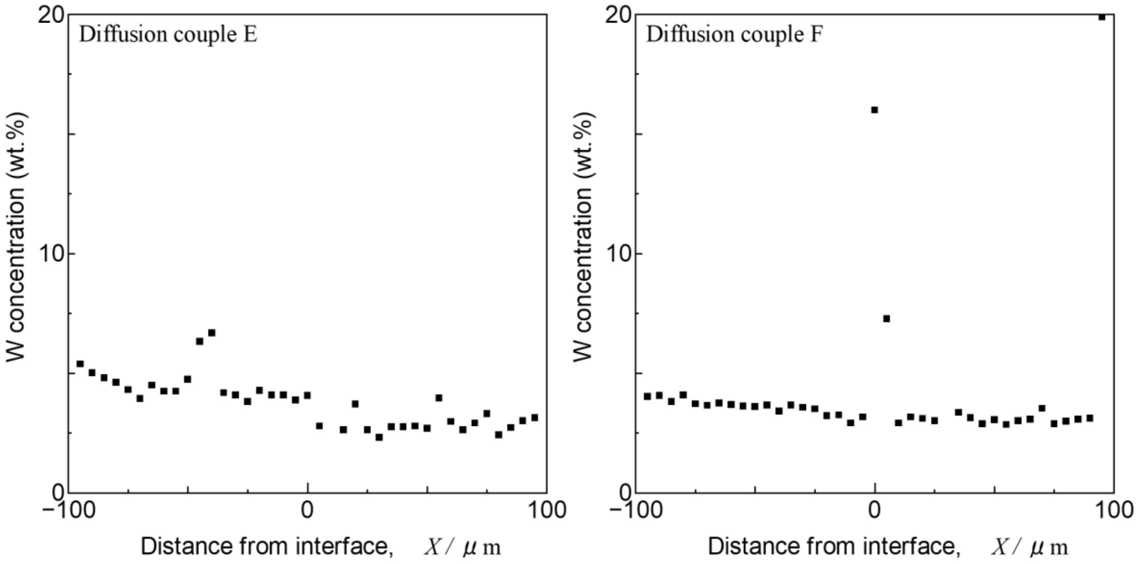

Figure 4.12 W concentration profile against distance for diffusion couples E and F after annealing at 1073 K.

Figure 4.13 shows the SE images of the cross-section area where the profile was taken on the Fe/Fe-9Cr-3W diffusion couples. Precipitates were found only in some parts along the grain boundaries of the Fe-9Cr-3W alloy, which suggested W is solute in the matrix of Fe on the ternary alloy. The diffusion couple H showed a gap between the metals. Point analysis found that the gap is filled by a metal that mainly consists of Fe. Figure 4.14 shows the concentration profile of Cr against distance, while Figure 4.15 shows the concentration profile of W. Both curves for Cr and W profiles showed S shapes with almost the same penetration range.

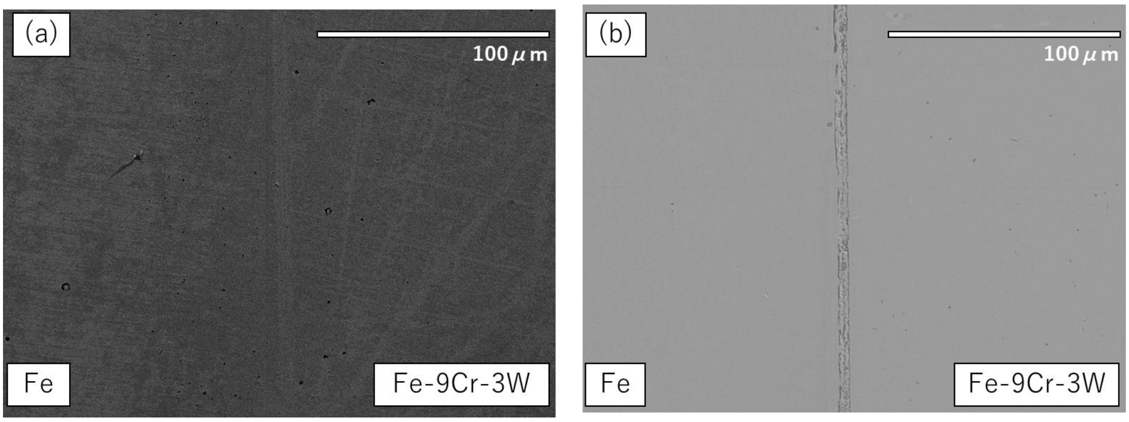

Figure 4.13 SE images of the cross-sectional morphology of diffusion couple (a) G and (b) diffusion couple H after annealing at 1073 K.

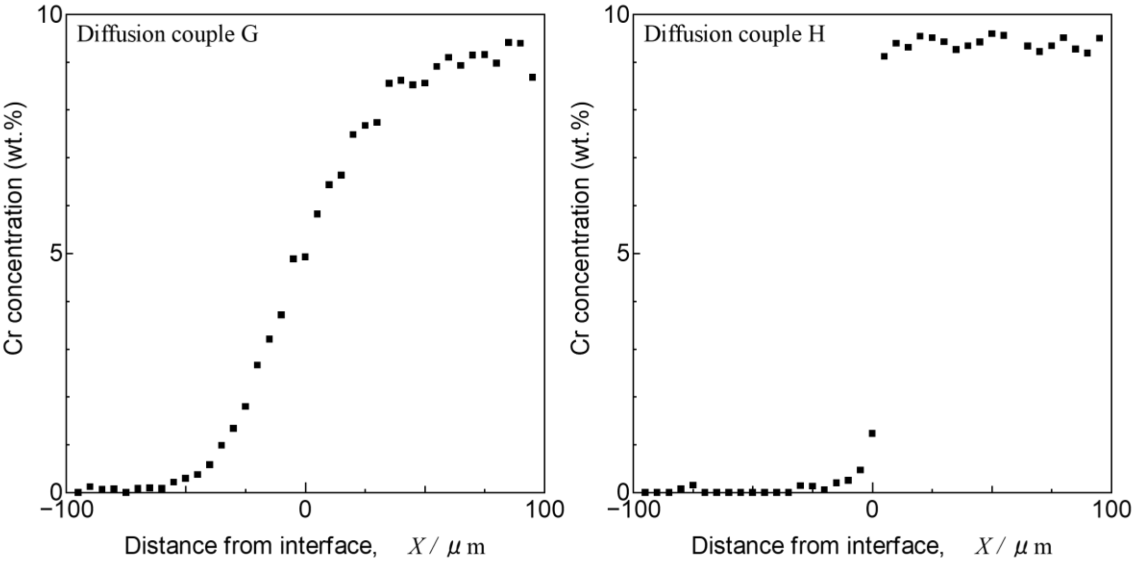

Figure 4.14 Cr concentration profile against distance for diffusion couples G and H after annealing at 1073 K.

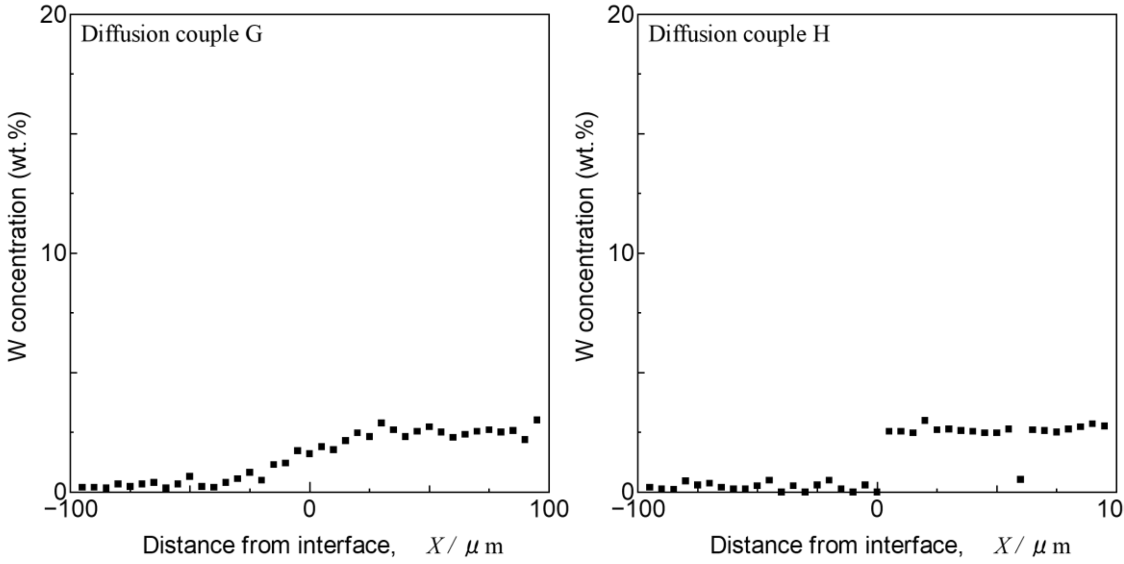

Figure 4.15 W concentration profile against distance for diffusion couples G and H after annealing at 1073 K.

Figure 4.16 shows the SE images of the cross-section area where the profile was taken on the Fe-9Cr/Fe-2Nb alloys. Similar to diffusion couple C and E, the shorter annealing time sample showed a gap between the alloys. For the couple I, both alloys were bonded in some parts. White particles appear in the Fe-9Cr alloy, suggesting the diffused Nb precipitates intermetallic compounds in the Fe-9Cr alloy. Figure 4.17 presents the comparison of the concentration profile of Cr against the distance from the interface for diffusion couples I and J after annealing at 1073 K. The diffusion couple I showed steep data for Cr concentration. Suggesting that Nb diffused into Fe-9Cr alloy and reacted with the matrix alloy to form precipitates during annealing.

Figure 4.18 shows the concentration profile of Nb against distance for diffusion couples I and J. The Nb concentration was scattered due to precipitation on both alloys. The Nb was found to be 0 in some parts of the Fe-2Nb alloy, which suggested most of the Nb was in the precipitates. On the other hand, the Nb was found high enough in the Fe-9Cr alloy.

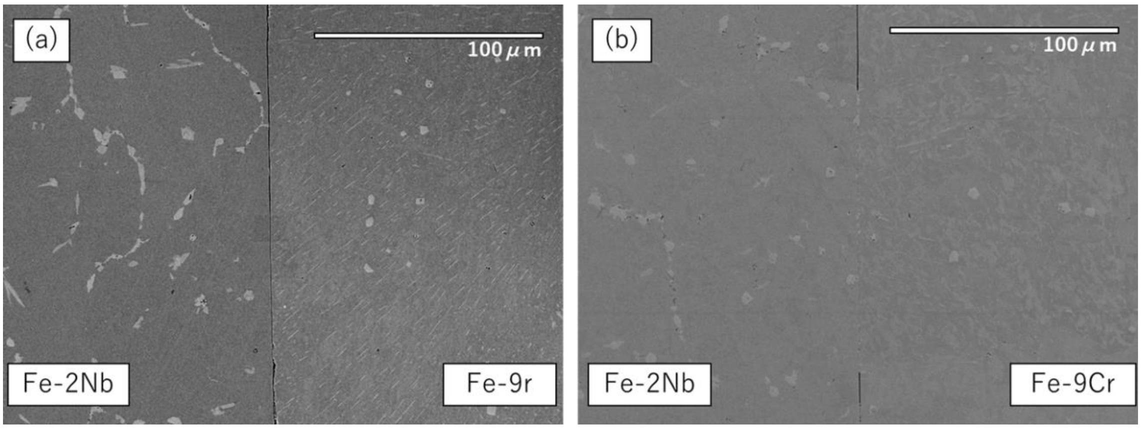

Figure 4.16 SE images of the cross-sectional morphology of diffusion couple I and J after annealing at 1073 K.

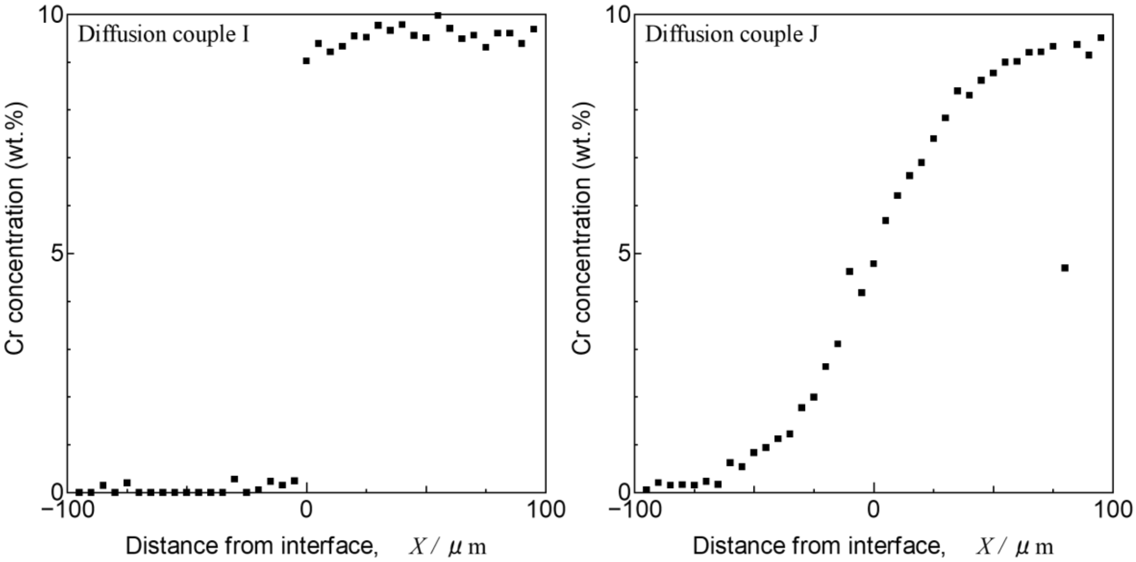

Figure 4.17 Cr concentration profile against distance for diffusion couples I and J after annealing at 1073 K.

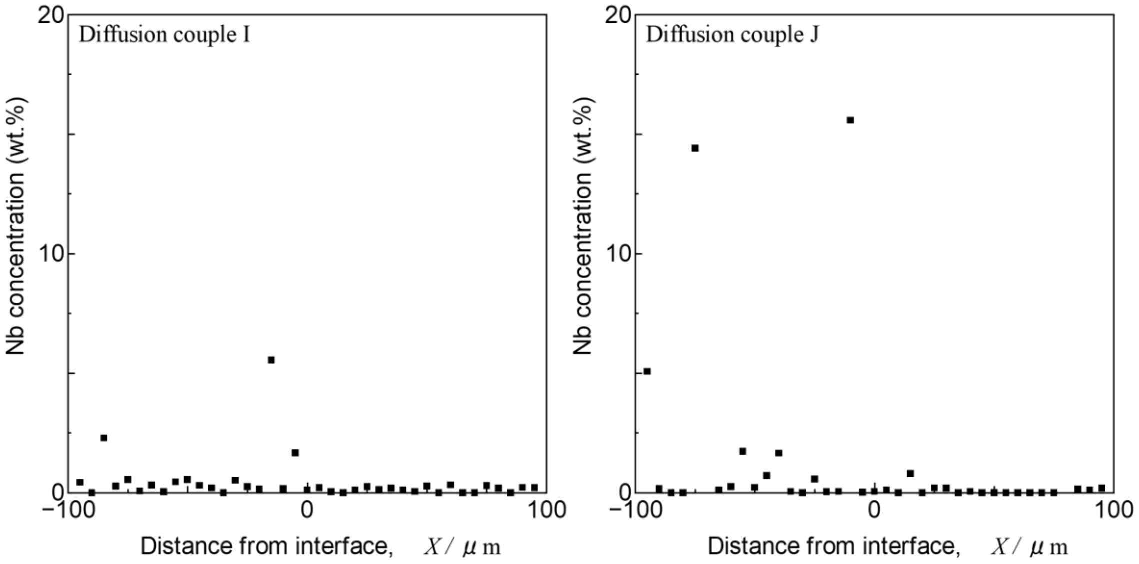

Figure 4.18 Cr concentration profile against distance for diffusion couples I and J after annealing at 1073 K.

4.4 Analysis technique

4.4.1 Analysis technique to determine the interdiffusion coefficient on binary alloys

A semi-infinite one-dimensional diffusion of solid is considered to calculate the diffusivity in the diffusion couple. For binary alloy, it is considered as one end of alloy with uniform *i* concentration of C_o is contacted with one end of semi-infinite another alloy with *i* concentration at ∞ is 0 [2-3]. In case of that, the data analysis for the diffusion of *i* solute atoms in matrix j can be described following Fick's second law:

$$\frac{\partial C_i}{\partial t} = \frac{\partial}{\partial x}\left\{D\left(\frac{\partial C_i}{\partial x}\right)\right\} \tag{4.1}$$

or for constant *D*,

$$\frac{\partial C_i}{\partial t} = D\left(\frac{\partial^2 C_i}{\partial x^2}\right) \tag{4.2}$$

Where *c* is concentration, *t* is time, *x* is the coordinate, and *D* is the interdiffusion coefficient as a function of *i* element concentration. Equations (4.1) or (4.2) can be solved by considering the same method for solving the one-dimensional heat flow in the situation on one end of a semi-infinite rod.

The rod temperature was uniformly in T_i and instantaneously increased to a higher temperature of T_o. The heat flow in the rod by conduction is given as:

$$\frac{\partial T}{\partial t} = \alpha\left(\frac{\partial^2 T}{\partial x^2}\right) \tag{i}$$

Where *T* is temperature and α is thermal diffusivity. A new variable η is introduced to help solve the Eq.(i):

$$\eta = \frac{x}{2\sqrt{\alpha t}} \tag{ii}$$

$$\frac{\partial \eta}{\partial t} = -\frac{x}{4\sqrt{\alpha t^3}} \tag{iii}$$

$$\frac{\partial \eta}{\partial x} = \frac{1}{2\sqrt{\alpha t}} \tag{iv}$$

Substitute the Eq. (iii) and (iv) into Eq. (1):

$$\frac{dT}{dt} = -\frac{x}{4\sqrt{\alpha t^3}}\frac{dT}{d\eta} \qquad \text{(v)}$$

$$\frac{d^2T}{x^2} = \frac{x}{4\alpha t}\frac{d^2T}{d\eta^2} \qquad \text{(vi)}$$

$$\frac{dT}{d\eta} = -\frac{\sqrt{\alpha t}}{x}\frac{\partial^2 T}{\partial \eta^2} \qquad \text{(vii)}$$

Introduce new variable:

$$y = \frac{dT}{d\eta} \qquad \text{(viii)}$$

Then, rewrite Eq. (ii) to be:

$$y = -\frac{1}{2\eta}\frac{dy}{d\eta} \qquad \text{(ix)}$$

$$-2\eta\, d\eta = -\frac{1}{y}dy \qquad \text{(x)}$$

Integration the equation:

$$-\eta^2 = \ln y + \text{constant} \qquad \text{(xi)}$$

Set the constant to -ln *A*, the *y* can be written as:

$$y = \frac{dT}{d\eta} = A\exp(-\eta^2) \qquad \text{(xii)}$$

Second integration the equation in the range limit of T_i as η is ∞ ($t = 0$, any x) and T_o at η is 0 ($x = 0$, $t > 0$), the equation be:

$$\int dT = A\int e^{-\eta^2}\, d\eta \qquad \text{(xiii)}$$

$$T_i - T_o = A\int_0^\infty e^{-\eta^2}\, d\eta \qquad \text{(xiv)}$$

Because $\int_0^\infty e^{-\eta^2}\ \mathrm{d}\eta = \frac{\sqrt{\pi}}{2}$, the *A* is:

$$A = \frac{\sqrt{\pi}}{2}\ (T_i - T_\mathrm{o}) \tag{xv}$$

Set another limit for Eq. (xiii) limit of *T* at η and $T = T_\mathrm{i}$ are ∞ the equation becomes:

$$\begin{aligned} T - T_i &= \frac{2}{\sqrt{\pi}}(T_i - T_\mathrm{o}) \int_\infty^\eta e^{-\eta^2}\ \mathrm{d}\eta \\ &= -\ \frac{2}{\sqrt{\pi}}(T_i - T_\mathrm{o}) \int_\eta^\infty e^{-\eta^2}\ \mathrm{d}\eta \end{aligned} \tag{xvi}$$

Considering the error function complement, the Eq.(xvi) can be written as:

$$\frac{T-T_i}{T_i-T_\mathrm{o}} = \mathrm{erfc}\ (\eta) = \mathrm{erfc}\ \left(\frac{x}{2\sqrt{\alpha t}}\right) \tag{xvii}$$

In the case of mass transport by diffusion in solid state, the variable in Eq.(iii) should be modified into:

$$\eta = \frac{x}{2\sqrt{Dt}} \tag{4.3}$$

Using the same manner to convert this variable to the ordinary differential equation

$$\frac{dC}{d\eta} = -\frac{1}{2\eta}\,\frac{\partial^2 C}{\partial \eta^2} \tag{4.4}$$

To calculate the variable *D* from the Eq. (1) or (2), the boundary conditions is set to as shown in Fig. 4.19.

$$C_i = \begin{cases} C_i^s & \text{at } x = 0 \text{ and } t > 0 \\ C_i^o & \text{at } t = 0 \text{ and } x > 0 \end{cases}$$

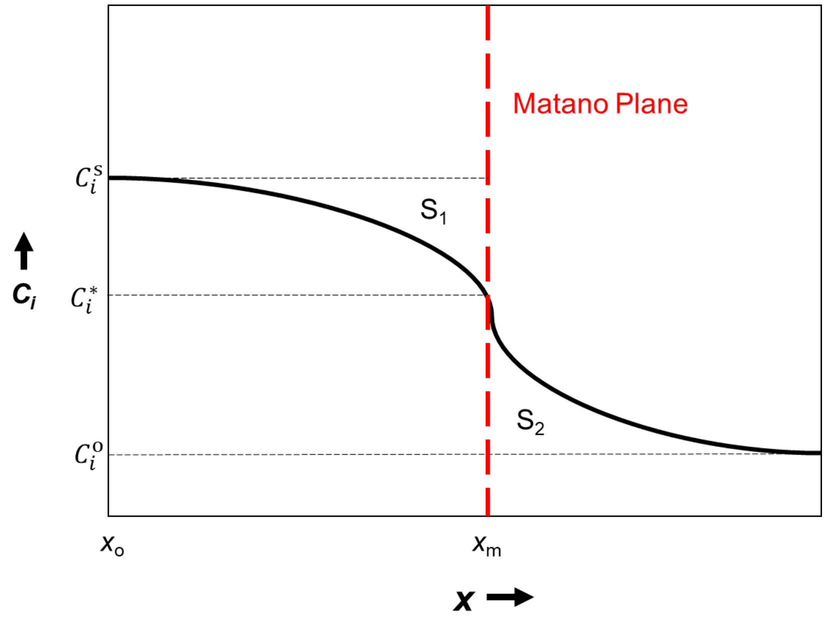

Figure 4.19 Schematic diffusion of *i* in the *x* direction.

Where, C_i^s and C_i^o are the concentration of *i* element in terminal. For binary Fe/Fe-Cr couples, it is considered as one end of alloy with uniform Cr content C_{Cr}^o is contacted with one end of semi-infinite of pure iron [2,3]. The equation (4.1) and (4.2), can be solved by considering the same method for solving the one-dimensional heat flow by consideration:

$$\frac{c_i - C_i^{\mathrm{s}}}{C_i^{\mathrm{o}} - C_i^{\mathrm{s}}} = 1 - \frac{c_i - C_i^{\mathrm{o}}}{C_i^{\mathrm{s}} - C_i^{\mathrm{o}}} = \mathrm{erf}\,(\eta) \qquad (4.5)$$

By substituting the η value into the equation:

$$\frac{c_i - C_i^{s}}{C_i^{o} - C_i^{s}} = \mathrm{erf}\left(\frac{x}{2\sqrt{Dt}}\right) \qquad (4.6)$$

In a diffusion couple of semi-infinite, the interdiffusion coefficient is constant D, therefore, the solute concentration of i at position x after annealing time t is:

$$c_i\;(x, t) = \frac{C_i^{s} + C_i^{\mathrm{o}}}{2} + \frac{C_i^{s} - C_i^{\mathrm{o}}}{2}\;\mathrm{erf}\left(\frac{x - x_{\mathrm{o}}}{2\sqrt{Dt}}\right) \qquad (4.7)$$

Where the x_{o} is the coordinate of terminal. To ease the calculation, define $q\ (x, t)$ as [4]:

$$\frac{x - x_{\mathrm{o}}}{2\sqrt{Dt}} = \mathrm{erfc}\left\{\frac{2c_i(x, t) - C_i^{s} - C_i^{o}}{C_i^{s} - C_i^{\mathrm{o}}}\right\} \equiv q\ (x,t) \qquad (4.8)$$

The D can be estimated by determining the slope of q value plotted to x - x_{o}, which is defined as a function of concentration. This type of plot is called probability plot.

The most common method used in metallurgical diffusion study to estimate the D is Boltzmann-Matano. This method considered diffusion coefficient might vary along with the position, which is applied to the curve concentration profile. To adopt this method to the Fick’s law, it is assumed that the diffusivity will be independent to x in a range of q [4]. In this work the range of $-1 < q < 1$ is set by the consideration that this range will covers around 70% of concentration windows and crosses the bonded interface and the Matano plane which will be explained later. This range is reported to cover 80% of the concentration windows [4]. In that case, the Fick’s second law (equation (4.1)) can be transformed into an ordinary differential equation for the system of Cr solute in the Fe, written as:

$$-\frac{\lambda}{2}\frac{dC}{d\lambda} = \frac{d}{d\lambda}\left\{\widetilde{D}_{\mathrm{Cr}}^{\mathrm{Fe}}\left(\frac{dc}{d\lambda}\right)\right\} \qquad (4.9)$$

Where λ is Boltzmann parameter, defined as:

$$\lambda = \frac{x - x_{\mathrm{m}}}{\sqrt{t}} \qquad (4.10)$$

And x_{m} is the position of Matano plane, which at this position $S_1 = S_2$, and follow:

$$\int_{C_{\mathrm{Cr}}^{\mathrm{o}}}^{C_{\mathrm{Cr}}^{\mathrm{S}}}(x - x_{\mathrm{m}})dC_{\mathrm{Cr}} = 0 \qquad (4.11)$$

Therefore, the equation (4.9) can be solved to be

$$\int_{C_{\mathrm{Cr}}^{\mathrm{o}}}^{C_{\mathrm{Cr}}^{*}}(x - x_{\mathrm{m}})dC_{\mathrm{Cr}} = -2t\widetilde{D}_{\mathrm{Cr}}^{\mathrm{Fe}}\left[\frac{dC_{\mathrm{Cr}}}{dx}\right]_{C_{\mathrm{Cr}}^{*}} \qquad (4.12)$$

$$\widetilde{D}_{\mathrm{Cr}}^{\mathrm{Fe}*} = \frac{1}{2t}\left(\frac{dx}{dC_{Cr}}\right)_{C_{\mathrm{Cr}}^{*}}\int_{C_{\mathrm{Cr}}^{\mathrm{o}}}^{C_{\mathrm{Cr}}^{*}}(x - x_{\mathrm{m}})dC_{\mathrm{Cr}} \qquad (4.13)$$

As shown in Fig. 4.1, the $c_{\mathrm{Cr}}^{\mathrm{o}}$ and c_{Cr}^{*} are the concentration of Cr in the end of the infinite diffusion couple and the concentration at the Boltzmann plane. As Boltzmann Matano methods include the time parameter, therefore, the plotted concentration profile against the Boltzmann parameter should be identical for different annealing times, in this case, binary couple of A and B.

In addition, by the set range of -1 < q < 1 the $\widetilde{D}_{\mathrm{Cr}}^{\mathrm{Fe}}$ from the slope of probability plot of q (Eq. 4.8) is suggested to be same as Eq. 4.13. In that case the method to employ the probability plot is used to simply the calculation.

4.4.2 Analysis technique to determine the interdiffusion coefficient on ternary alloy

In the case of the couple with ternary alloys, the diffusion of each component will be affected by the interaction of the component themselves and other components. Therefore, For the Fe-Cr-A (A = W, Nb) system, the Eq. 4.1 can be modified to be:

$$\frac{\partial C_{\mathrm{Cr}}}{\partial t} = \frac{\partial}{\partial x}\left\{\widetilde{D}_{\mathrm{CrCr}}^{\mathrm{Fe}}\left(\frac{\partial C_{\mathrm{Cr}}}{\partial x}\right)\right\} + \frac{\partial}{\partial x}\left\{\widetilde{D}_{\mathrm{CrA}}^{\mathrm{Fe}}\left(\frac{\partial C_{\mathrm{A}}}{\partial x}\right)\right\} \qquad (4.14)$$

$$\frac{\partial C_{\mathrm{A}}}{\partial t} = \frac{\partial}{\partial x}\left\{\tilde{D}_{\mathrm{AA}}^{\mathrm{Fe}}\left(\frac{\partial C_{\mathrm{A}}}{\partial x}\right)\right\} + \frac{\partial}{\partial x}\left\{\tilde{D}_{\mathrm{ACr}}^{\mathrm{Fe}}\left(\frac{\partial C_{\mathrm{Cr}}}{\partial x}\right)\right\} \tag{4.15}$$

Where $\tilde{D}_{\mathrm{CrCr}}^{\mathrm{Fe}}$,$\tilde{D}_{\mathrm{AA}}^{\mathrm{Fe}}$, are the major interdiffusion coefficient for the element, which indicate the influence of their own concentration gradient on their own fluxes. While $\tilde{D}_{\mathrm{ACr}}^{\mathrm{Fe}}$, $\tilde{D}_{\mathrm{CrA}}^{\mathrm{Fe}}$ are the minor interdiffusion coefficients for the elements, which the concentration gradient influenced other element's flux; for example, $\tilde{D}_{\mathrm{CrA}}^{\mathrm{Fe}}$ is the influence of the concentration gradient of Cr on the flux of A.

Some constraints are supposed to be considered in validating the interdiffusion coefficient of the ternary system as written in the equation (4.14) and equation (4.15). Kirkaldy suggested that the stability of solid solution [4,5]:

$$\tilde{D}_{\mathrm{CrCr}}^{\mathrm{Fe}} + \tilde{D}_{\mathrm{AA}}^{\mathrm{Fe}} > 0 \tag{4.16}$$

$$(\tilde{D}_{\mathrm{CrCr}}^{\mathrm{Fe}} . \tilde{D}_{\mathrm{AA}}^{\mathrm{Fe}} - \tilde{D}_{\mathrm{CrA}}^{\mathrm{Fe}} . \tilde{D}_{\mathrm{ACr}}^{\mathrm{Fe}}) > 0 \tag{4.17}$$

$$(\tilde{D}_{\mathrm{CrCr}}^{\mathrm{Fe}} + \tilde{D}_{\mathrm{AA}}^{\mathrm{Fe}})^2 > 4\left(\tilde{D}_{\mathrm{CrCr}}^{\mathrm{Fe}} . \tilde{D}_{\mathrm{AA}}^{\mathrm{Fe}} - \tilde{D}_{\mathrm{CrA}}^{\mathrm{Fe}} . \tilde{D}_{\mathrm{ACr}}^{\mathrm{Fe}}\right) \tag{4.18}$$

In addition, there are interdependence of diffusion coefficients:

$$\tilde{D}_{\mathrm{CrCr}}^{\mathrm{Fe}} > 0 \tag{4.19}$$

$$\tilde{D}_{\mathrm{AA}}^{\mathrm{Fe}} > 0 \tag{4.20}$$

$$\tilde{D}_{\mathrm{CrA}}^{\mathrm{Fe}} . \tilde{D}_{\mathrm{ACr}}^{\mathrm{Fe}} > 0 \tag{4.21}$$

$$(\tilde{D}_{\mathrm{CrCr}}^{\mathrm{Fe}} . \tilde{D}_{\mathrm{AA}}^{\mathrm{Fe}} - \tilde{D}_{\mathrm{CrA}}^{\mathrm{Fe}} . \tilde{D}_{\mathrm{ACr}}^{\mathrm{Fe}}) > 0 \tag{4.22}$$

In this work, the effect of alloying elements, particularly W and Nb, as solute elements and precipitate on the Cr diffusivity in the Fe matrix will be separated. The ternary phase diagram of Fe-Cr-W and Fe-Cr-Nb systems are presented in figures 2.1 and 3.1, respectively. The interdiffusion annealing was conducted at 1073 K to accelerate the diffusivity in the matrix α-Fe of the Fe-Cr-W system. By considering the phase relation, diffusion path couples of Fe-Cr-W and Fe-Cr-Nb systems investigated in this chapter are plotted in figure 4.1. In the present work, all diffusion paths did not form any cross-section. It makes the four interdiffusion coefficients in the equations (4.14) - (4.15) cannot be obtained. Therefore, this work only will determine the $\tilde{D}_{\mathrm{CrCr}}^{\mathrm{Fe}}$ by using some assumptions:

(1) The diffusion couples Fe-3W/Fe-9Cr-3W and Fe-6W/Fe-9Cr-6W will have a small gradient concentration of W. Therefore, the interdiffusion of W in the matrix is neglected by using the Fick's first law.

(2) Although there is a concentration gradient of W in the diffusion couple Fe/Fe-9Cr-3W, other interdiffusion coefficients cannot be determined. In case of that, the exact value of $\tilde{D}_{\mathrm{CrCr}}^{\mathrm{Fe}}$ cannot be determined.

(3) Since the Nb has a narrow solubility limit in matrix Fe, all Nb is assumed to form precipitates. Therefore, the Cr diffusivity in the Fe-Cr-Nb system can be determined by neglecting the effect of Nb in the matrix.

Applying the suggestions into Eq. 4.15, the equation become:

$$\frac{\partial C_{\mathrm{Cr}}}{\partial t} \approx \frac{\partial}{\partial x}\left\{\tilde{D}_{\mathrm{CrCr}}^{\mathrm{Fe}}\left(\frac{\partial C_{\mathrm{Cr}}}{\partial x}\right)\right\} \tag{4.23}$$

In addition, the Boltzmann Matano method can be applied the diffusion couples in ternary system in the same manner as binary system. However, this method is not applicable to the system of Fe/Fe-9Cr-3W as mentioned in assumption (2).

4.5 Discussion

4.5.1 Estimation of interdiffusion coefficient of Fe-Cr binary system

Figure 4.20 shows the concentration profiles on both diffusion couple A and B with the plotted Matano plane. The Matano plane was estimated to be located at 4.3 μm and 9.1 μm from the bonded interface in the Fe-9Cr alloy for diffusion couples A and B, respectively. Mentioned that the lines were 200.1 and 200.1 μm in length across the alloys. At this Matano plane, the concentration of Cr was 4.6 mass% and 4.7 mass%, respectively, for diffusion couples A and B. Plots from the Boltzmann parameter (Eq. (4.9)) against the Cr concentration obtained from two diffusion couples with different annealing times were compared to confirm the Boltzmann-Matano method can be applied to the system. Figure 4.21 shows diffusion couples in the Fe/Fe-9Cr system showed a profile of Cr concentration against the Boltzmann parameter, which suggests that the Boltzmann-Matano method is applied in this system.

Figure 4.22 shows the probability plot against distance for diffusion couples A and B. The *q* value is scattered from the plot, especially at the edge of the windows. Since the interdiffusion coefficient can be estimated from the slope of the probability plot, the interdiffusion coefficient is calculated as $1/(2(\tilde{D}_{\mathrm{Cr}}^{\mathrm{Fe}}t)^{0.5})$. The result is presented in table. 4.4.

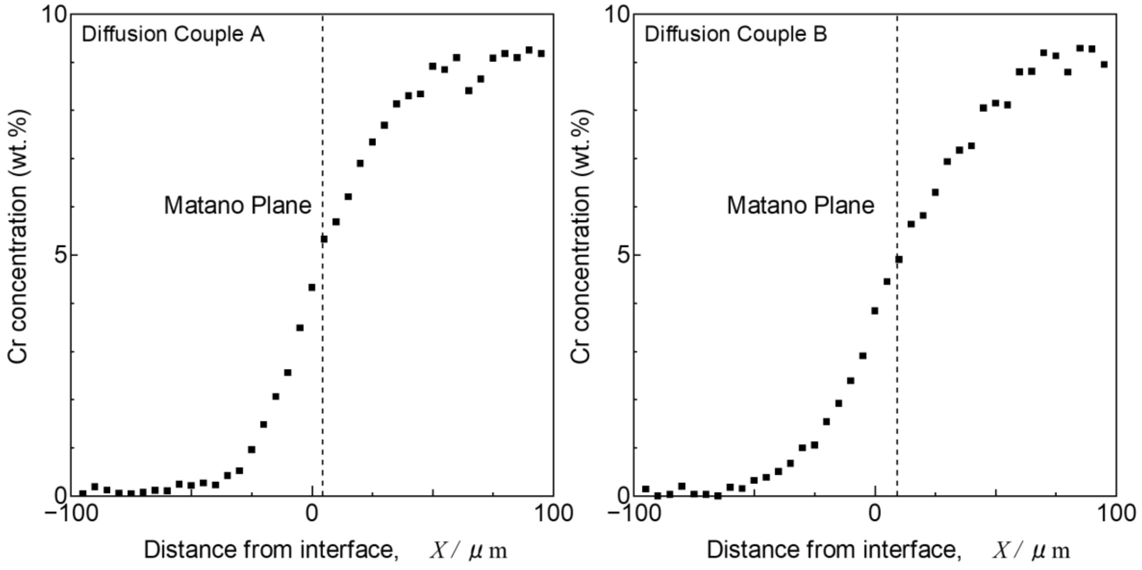

Figure 4.20 Concentration profile against distance and estimated Matano plane for diffusion couples A and B after annealing at 1073 K.

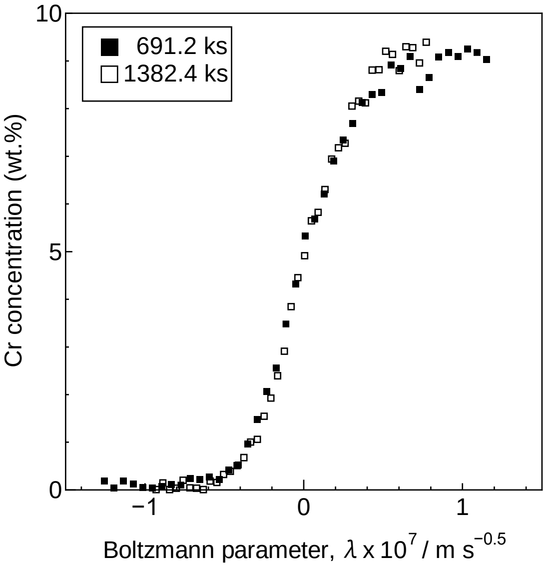

Figure 4.21 Concentration profile against Boltzmann parameter for diffusion couples A and B after annealing at 1073 K.

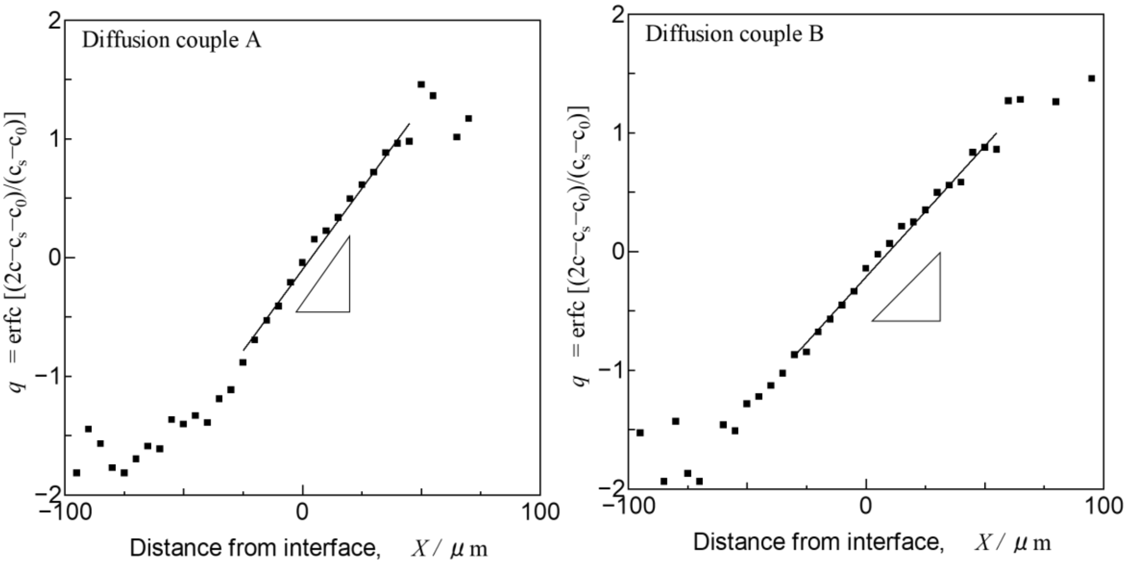

Figure 4.22 Probability against distance for diffusion couples A (left) and B (right) after annealing at 1073 K.

Table 4.4 Average interdiffusion coefficient for all diffusion couples for Fe-Cr system.

Diffusion couple	$\widetilde{D}_{Cr}^{Fe}$ / m^2 s^{-1}
A	4.8 x 10^{-16}
B	3.8 x 10^{-16}

4.5.2 Estimation of interdiffusion coefficient of Fe-Cr-W ternary system

The data from diffusion couples C, E, and H cannot be used because the alloys were not bonded during the interdiffusion annealing. In addition, mentioning that there are three assumptions to estimate $\widetilde{D}^{\mathrm{Fe}}_{\mathrm{CrCr}}$ stated in the analytical method part, the interdiffusion coefficients of Cr in the diffusion couples D, F, and G will only consider the Cr concentration profile. The first assumption is the flux of W in the diffusion couple D, and F is predicted to be zero in this system from Fick's first law. This assumption is confirmed by low concentration profiles of W, as shown in figures 4.10 and 4.14. Therefore, the Matano method is applied in those couples by only considering the Cr diffusivity, and the Matano parameter and Matano plane only use the data from Cr profiles. In addition, because Matano methods included the parameter time, by neglecting the data from diffusion couple C, the Matano plane was estimated by using the same manner as binary alloy only for diffusion couple D. The Matano plane was estimated to be located at 2.8 µm from the interface to the Fe-3W alloy direction. At this point, the Cr concentration is calculated to be 4.6 mass.%. The Matano plane for Cr was estimated to be the couple F by using the same method. For diffusion couple F, the Matano plane for Cr was located at 0.9 µm from the interface in the Fe-6W alloy. At this point, the Cr concentration was calculated as 4.7 mass%. In the case of diffusion couple H, further interdiffusion calculation was not conducted in this present work due to a lack of data. The concentration profile plotted to the Matano plane for diffusion couples D and F are presented in Fig. 4.23.

The plot of Cr concentration against the Boltzmann parameter for diffusion couples D and F are presented in figure 4.24. It could be seen that all diffusion couples showed a similar profile and penetration length to each other's, which indicates the Boltzmann-Matano method from Cr element, the interdiffusion coefficients from the diffusion couples have the same order. It can be seen that the diffusion couple consisting of saturated alloy (Fe-3W/Fe-9Cr-3W) has a slightly higher Cr concentration (left side) than the diffusion couple consisting of the alloy with a high-volume fraction of Laves phase (Fe-6W/Fe-9Cr-6W). It indicates that Cr penetrated faster in the saturated alloy (Fe-3W/Fe-9Cr-3W).

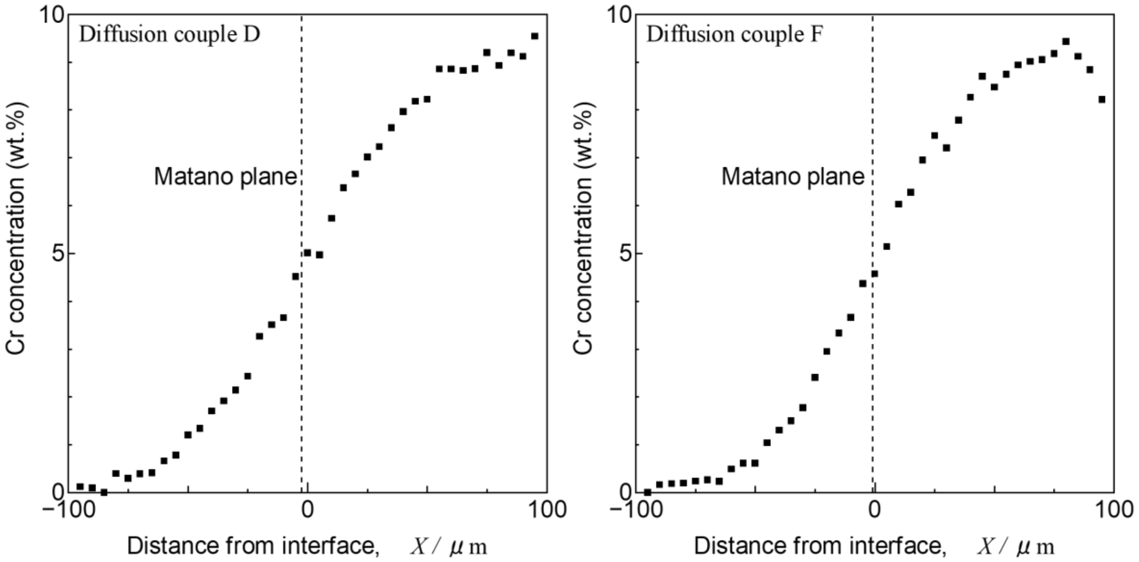

Figure 4.23 Concentration profile against distance and estimated Matano plane for diffusion couples D and F after annealing at 1073 K.

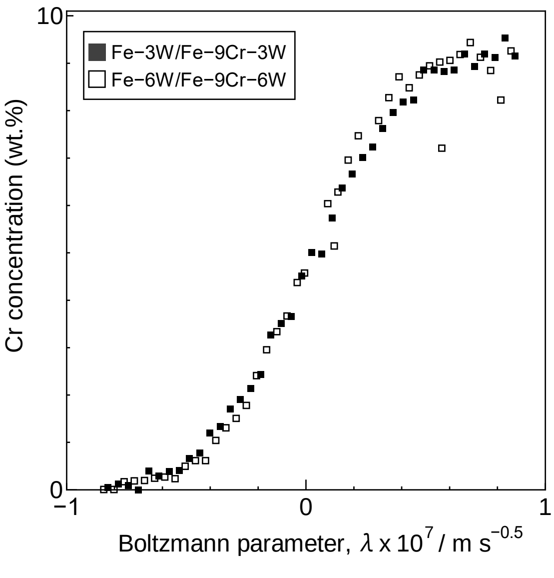

Figure 4.24 Concentration profile against Boltzmann parameter for diffusion couples D and F after annealing at 1073 K.

Figure 4.25 shows the probability plot against distance for diffusion couples on the Fe-Cr-W system. Similar to the binary system, the interdiffusion coefficient was estimated from the slope of the probability plot by a straight line which was limited only to the range of -1 < q < 1. The interdiffusion coefficient is calculated as $1/(2(\widetilde{D}^{\mathrm{Fe}}_{\mathrm{CrCr}}\ t)^{0.5})$. The average value of the interdiffusion coefficient in the Fe-Cr-W system is listed in table 4.5

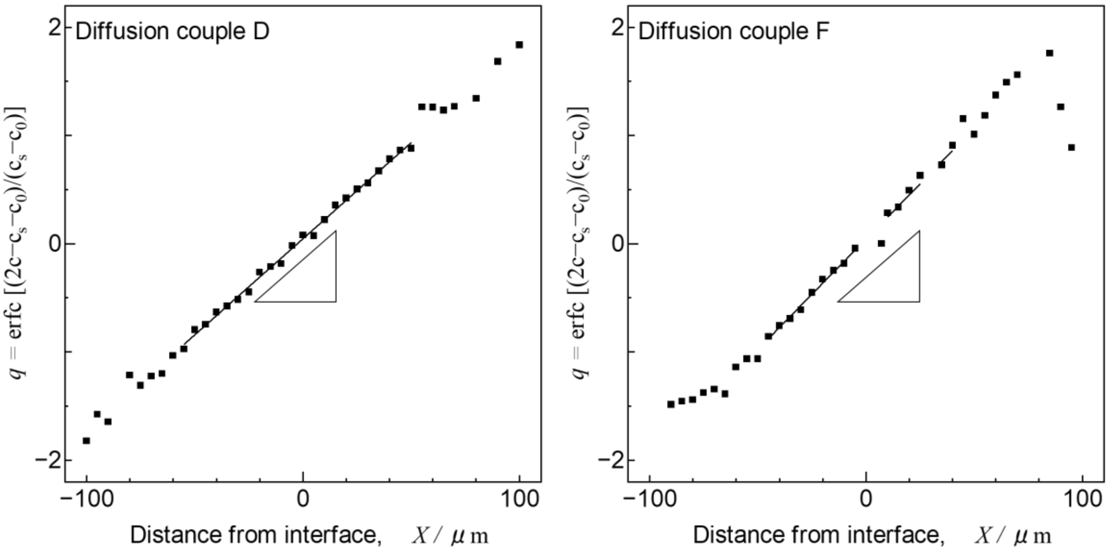

Figure 4.25 Probability against distance for diffusion couples D and after annealing at 1073 K.

Table 4.5 Average interdiffusion coefficient for all diffusion couples for Fe-Cr-W system.

Diffusion couple	$\widetilde{D}^{Fe}_{CrCr}$ / m^2 s^{-1}
D	5.7 x 10^{-16}
F	4.3 x 10^{-16}

4.5.3 Estimation of interdiffusion coefficient of Fe-Cr-Nb ternary system

In the system of Fe-Cr-Nb, the analysis was taken only on the diffusion couple J. The $\widetilde{D}_{\mathrm{CrCr}}^{\mathrm{Fe}}$ was estimated by considering assumption (3), which was listed in the analytical method in section 4.2.2. The low solubility limit of Nb in the matrix Fe made the Nb preferred to form an intermetallic compound, making the Nb concentration in the matrix very low. It results in the low concentration gradient of Nb in the matrix alloys, and some scattered values came from precipitates on both Fe-2Nb and Fe-9Cr alloy’s sides. Fig.4.19 confirmed the low concentration of Nb in the matrix, and Nb exists as a precipitate in both Fe-2Nb and Fe-9Cr alloys (Fig. 4.17). The Matano parameter, Matano plane, and interdiffusion coefficient were estimated only by using the Cr profile data. In addition, because the Boltzmann parameter included the parameter time, the data from diffusion couple I is not counted. Figure 4.26 shows the Cr concentration of diffusion couple J plotted against the Matano plane. The Matano plane was estimated to be 2.7 μm from the bonded interface in the Fe-2Nb alloy part. At this point, the Cr concentration was calculated to be 5 mass%. Figure 4.27 shows the comparison of Cr concentration against the Boltzmann parameter for diffusion couple B and J after interdiffusion annealing. The profile was similar in both couples indicating the Cr penetrated in almost the same manner in both couples.

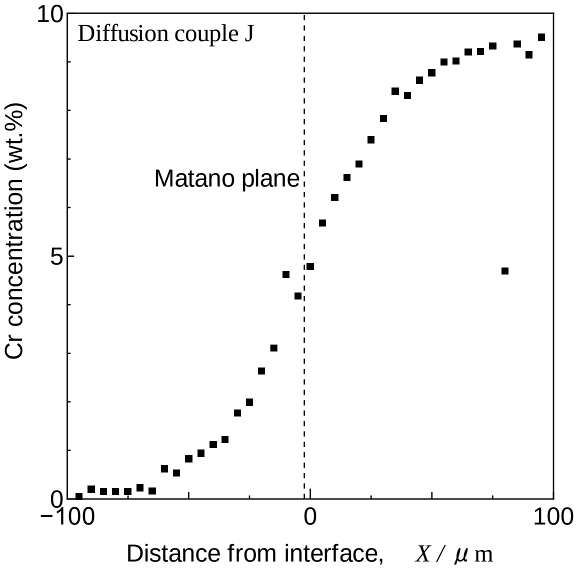

Figure 4.26 Concentration profile against distance and estimated Matano plane for diffusion couples J after annealing at 1073 K.

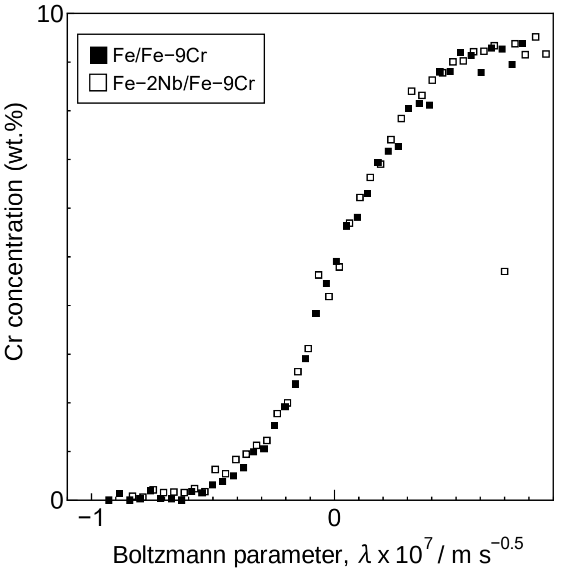

Figure 4.27 Concentration profile against Boltzmann parameter for diffusion couples B and J after annealing at 1073 K.

Figure 4.28 shows the probability plot against distance from the bonded interface of diffusion couple J. Using the same methods as other systems, $\widetilde{D}_{\mathrm{CrCr}}^{\mathrm{Fe}}$ was estimated from the gradient of the probability plot by a straight line fit which was limited to the range of -1 < q < 1. The $\widetilde{D}_{\mathrm{CrCr}}^{\mathrm{Fe}}$ is listed in Table 4.6. In this system, the other interdiffusion coefficient cannot be estimated in this present work.

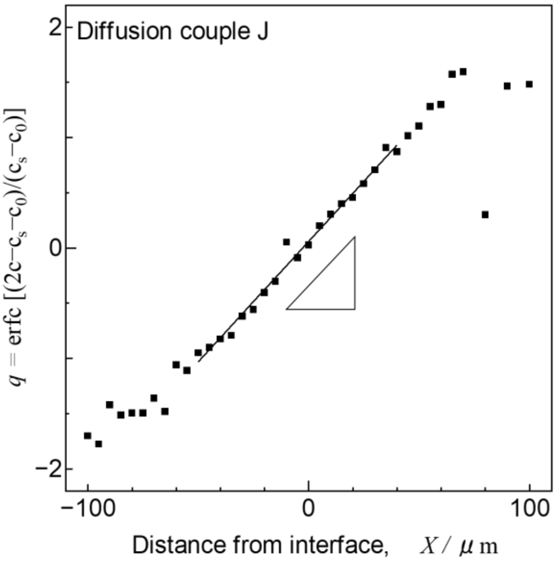

Figure 4.28 Probability against distance for diffusion couples J after annealing at 1073 K.

Table 4.6 Average interdiffusion coefficient for all diffusion couples for Fe-Cr-Nb system.

Diffusion couple	$\widetilde{D}_{CrCr}^{Fe}$ / m^2 s^{-1}
J	3.8×10^{-16}

4.5.4 Comparison of Cr diffusivity in the binary and ternary system

The comparison of the $\tilde{D}_{\mathrm{CrCr}}^{\mathrm{Fe}}$ for binary and ternary alloy can be explained from the obtained data. Using the Boltzmann-Matano method, the calculated interdiffusion coefficients from all systems are again summarized in table 4.7. Figure 4.29 shows the interdiffusion coefficient of the Cr in the Fe matrix from the reference [4]. The interdiffusion value obtained from the diffusion couple A and B showed the same order as the references [1-3,5]. The same order of $\tilde{D}_{\mathrm{CrCr}}^{\mathrm{Fe}}$ was also found in ternary systems. The $\tilde{D}_{\mathrm{CrCr}}^{\mathrm{Fe}}$ was slightly higher in the Fe-Cr-W system than the Fe-Cr system, and lower in the Fe-Cr-Nb system.

Table 4.7 Interdiffusion coefficient in the Fe-Cr, Fe-Cr-W, and Fe-Cr-Nb system at 1073 K.

Diffusion Couple		$\tilde{D}_{\mathrm{CrCr}}^{\mathrm{Fe}}$ / $m^2 s^{-1}$	$\frac{\tilde{D}_{\mathrm{CrCr}}^{\mathrm{Fe}}\ (\mathrm{ternary})}{\tilde{D}_{\mathrm{CrCr}}^{\mathrm{Fe}}\ (\mathrm{binary})}$
A	Fe/Fe-9Cr	4.8×10^{-16}	
B		3.8×10^{-16}	1
D	Fe-3W / Fe-9Cr-3W	5.7×10^{-16}	1.52
F	Fe-6W /Fe-9Cr-6W	4.3×10^{-16}	1.15
J	Fe-9Cr / Fe-2Nb	3.8×10^{-16}	1

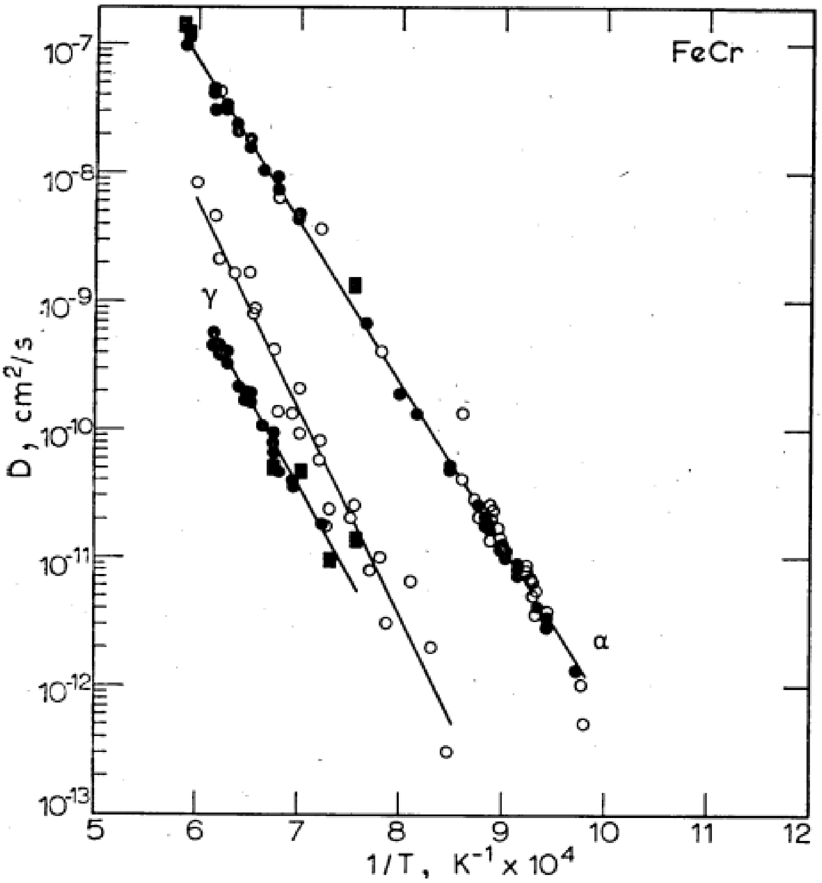

Figure 4.29 Interdiffusion coefficient for Fe-Cr alloy in different temperature from reference [4].

As the penetration of W was observed with the same as Cr penetration (Fig 4.16), the diffusivities of the Cr and W are supposed to be in the same order. This assumption was confirmed by the previous study [6]. Figure 4.30 shows the interdiffusion coefficient for Fe-W alloy at different temperatures from the reference [5,6]. The $\tilde{D}_{\mathrm{W}}^{\mathrm{Fe}}$ was estimated to be 2.48 x 10^{-16} m^2s^{-1} at 1073 K [6]. This value is in the same order as $\tilde{D}_{\mathrm{CrCr}}^{\mathrm{Fe}}$ obtained in this work. In addition, the value of $\tilde{D}_{\mathrm{CrCr}}^{\mathrm{Fe}}$ in all diffusion couples in this study showed a higher value than the $\tilde{D}_{\mathrm{WW}}^{\mathrm{Fe}}$ from the reference [5,6], which was also observed by comparing figures 4.29 and 4.30.

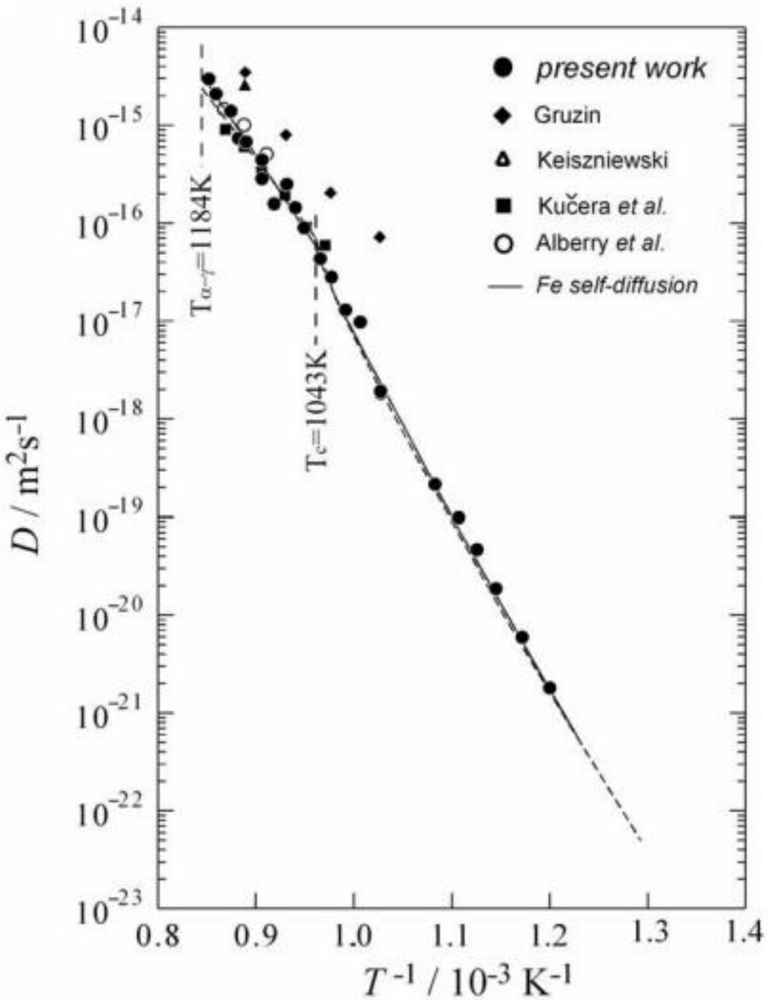

Figure 4.30 Interdiffusion coefficient for Fe-W alloy in different temperature from reference [6].

4.5.5 The effect of alloying elements and microstructure on the Cr diffusivity in the ferrite matrix

The data confirmed that the presence of W as solute and precipitates increases the value of $\widetilde{D}^{\mathrm{Fe}}_{\mathrm{CrCr}}$ in supersaturated Fe(W) for a factor of 1.52. In the case of Fe-2Nb/Fe-9Cr diffusion couples, only the precipitation effect can be elucidated. The effect of precipitation retarded the $\widetilde{D}^{\mathrm{Fe}}_{\mathrm{CrCr}}$ by a factor of 1. Table 4.8 shows the Arrhenius parameters for self-diffusion of Fe and interdiffusion of solute atom in α-iron. The relationship between activation energy and atomic radii in paramagnetic α-iron [6]:

$$Q^{\mathrm{P}} = 252 + 291 \left(\frac{r_{\mathrm{Solute}} - r_{\mathrm{Fe}}}{r_{\mathrm{Fe}}}\right) \text{ kJ/mol} \tag{4.24}$$

Where Q^{P} is the enthalpy for activation energy, r_{Solute} is the radius of the solute atom, and r_{Fe} is the radii of the iron atom. Considering the size of the Fe atom is close to the Cr atom, but Nb and W have larger atom radii, the activation energy for the diffusion of W in is α-iron smaller than Cr. This relation is applied in both paramagnetic and ferromagnetic phases [6,7]. It explained that the $\widetilde{D}^{\mathrm{Fe}}_{\mathrm{CrCr}} > \widetilde{D}^{\mathrm{Fe}}_{\mathrm{WW}}$ in the present work.

Table 4.8 The pre-exponential factor, activation energy, and constant α data in α-Fe from reference at 1173 K [6].

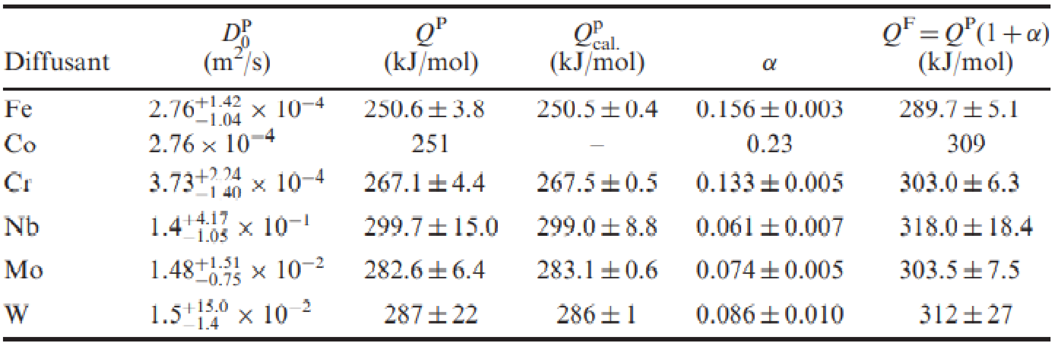

Diffusant	D_0^{P} (m^2/s)	Q^{P} (kJ/mol)	$Q^{\mathrm{P}}_{\mathrm{cal.}}$ (kJ/mol)	α	$Q^{\mathrm{F}} = Q^{\mathrm{P}}(1+\alpha)$ (kJ/mol)
Fe	$2.76^{+1.42}_{-1.04} \times 10^{-4}$	250.6 ± 3.8	250.5 ± 0.4	0.156 ± 0.003	289.7 ± 5.1
Co	2.76×10^{-4}	251	–	0.23	309
Cr	$3.73^{+2.24}_{-1.40} \times 10^{-4}$	267.1 ± 4.4	267.5 ± 0.5	0.133 ± 0.005	303.0 ± 6.3
Nb	$1.4^{+4.17}_{-1.05} \times 10^{-1}$	299.7 ± 15.0	299.0 ± 8.8	0.061 ± 0.007	318.0 ± 18.4
Mo	$1.48^{+1.51}_{-0.75} \times 10^{-2}$	282.6 ± 6.4	283.1 ± 0.6	0.074 ± 0.005	303.5 ± 7.5
W	$1.5^{+15.0}_{-1.4} \times 10^{-2}$	287 ± 22	286 ± 1	0.086 ± 0.010	312 ± 27

The diffusivity in the ferrite matrix is mostly conducted by the movement of vacancy, the presence of solute elements, and the vacancies in the surroundings of the solute atom [8]. Then the presence of solute atom affects the exchange rates of atoms (solute and solvent) in the matrix. The addition large solute atom induces higher vacancy concentrations around the solute atoms [6]. It was reported that, adding 1-2 mass% of W will create equal vacancies to the addition of 9 mass% of Cr at temperature below 600 K [9]. W was reported do not have strong binding to self-interstitial Fe and Cr while it has stronger binding energy with a vacancy [9]. The vacancy is easier to migrate from a W atom to another W atom than in pure Fe [9]. In addition, the diffusivity of Cr is reported can diffuse ~2-150 times faster than Fe by a vacancy mechanism and between 10-30 % by interstitial atom [10]. Therefore, by adding more large-size alloying elements, especially W, more vacancies can be created in the Fe matrix, which results in the higher diffusion of Cr and Fe in the Fe matrix.

The diffusion behavior in a multiphase ternary system becomes complicated if there are phase differences. In that case, it employs discontinuously virtual paths [3]. In Fe/Fe-9Cr-3W diffusion couples, the ternary was supersaturated with a very low volume fraction of Laves phase along the grain boundary. Although the $\widetilde{D}_{\mathrm{CrCr}}^{\mathrm{Fe}}$ increase by the presence of W, further analysis is needed to confirm the ratio of $\widetilde{D}_{\mathrm{CrW}}^{\mathrm{Fe}}$ to the Cr diffusion in the ternary system.

The ratio of $\widetilde{D}_{\mathrm{CrCr}}^{\mathrm{Fe}}$ in ternary alloy was about the same with the presence of high-volume fraction of Laves phase on diffusion couple F. This phenomenon was not the same as the diffusion couple F. It suggested the presence of Laves phase is not affected the interdiffusion of Cr, but the new precipitated Laves phase along the bonded interface reduces the effective diffusion area or interface for the diffusion. Besides, it was reported that precipitating disperse phases will reduce the vacancy concentration in the matrix [11]. It explained that precipitating a high-volume fraction of Laves phase may reduce the vacancy concentration created by additional W, which facilitates the Cr diffusion in the matrix Fe.

The Kirkendall voids were observed near the bonded interface of diffusion couple F on the Fe-6W alloy side. W concentration profile showed the decline in both Fe-6W and Fe-9Cr-6W alloy’s parts from above 3.5 mass% in the matrix alloy to around 3 mass% near the bonded interface before it reached the peak by forming an intermetallic phase along the bonded interface. Those phenomena were not observed on the diffusion couple C, which has a lower concentration of W. The formation of precipitation can be explained by diffusion induce precipitation.

The formation of Fe-W intermetallic formation was controlled by the solid-state diffusion reaction between Fe and W. Mentioning all ternary alloys used in this work are pre-aged at 923 K, which the solubility limit of W in the matrix Fe is higher than at 1073 K. Therefore, more precipitation reaction may occur during annealing. Moreover, diffusion of W from the binary to ternary alloy through the bounded interface took place at the same time as the Fe. Therefore, the diffusion phenomenon may induce precipitation of more intermetallic compounds in the bonded area. The Cr profile was good in the sample annealed up to 1382.4 ks due to the line mapping being taken in the area with a lower volume fraction of Laves phase. However, after a long time, the diffusivity through the interface is supposed to be governed by the diffusion of Fe.

One of the studies reported the slower diffusion of Nb (large element of Laves phase former element) in the Co_2Nb Laves phase [8]. Relatively low self-diffusion of large Nb is restricted to the Nb sublattice, while fast self-diffusion of Co occurs via thermal vacancies. It suggested that in the Fe-Cr-W system, large W will have relatively slow diffusivity both in the Fe matrix and Fe_2W Laves phase. In addition, it is reported that the dislocation near the precipitate interface acts as a fast pipe for diffusion will accommodate the precipitate coarsening [10]. It explained that the slow diffused W slightly depleted near the bonded interface, where the intermetallic precipitated.

Kirkendall voids form because of different diffusivity rates between two atoms [12]. In many studies, the Kirkendall voids that appeared on the alloy side contain a higher concentration of higher diffusion coefficient atoms. However, in the diffusion couple F, the voids were observed in the Fe-6W alloy area, which was supposed to be on the Fe-9Cr-6W side because the interdiffusion of Cr in Fe is higher than W in Fe [5,6]. It can be explained as the W was not penetrated deeper into the Fe-9Cr-6W side, but it reacted with the Fe in the bonded interface. The vacancy of W diffused in the opposite direction from the interface into the Fe-6W alloy side. The vacancy density in the Fe-6W alloy increased and induced the formation of pores, which in the future can be an attempt to restore equilibrium [12].

4.6 Conclusions

The effect of alloying elements on the diffusivity of Cr in the Fe-9Cr alloys was investigated. The calculation showed the ratio of $\widetilde{D}_{\mathrm{CrCr}}^{\mathrm{Fe}}$ (ternary)/$\widetilde{D}_{\mathrm{CrCr}}^{\mathrm{Fe}}$(binary) increases to 1.52 times in the saturated matrix Fe(W). The ratio of $\widetilde{D}_{\mathrm{CrCr}}^{\mathrm{Fe}}$ in ternary alloy decreased with the presence of more volume fraction of Laves phase on diffusion couple of Fe-6W/Fe-9Cr-6W. In this system, a new Laves phase precipitated along the bonded interface, which suggested reducing the effective diffusion area in the couple. In the Fe-2Nb/Fe-9Cr diffusion couple, $\widetilde{D}_{\mathrm{CrCr}}^{\mathrm{Fe}}$ (ternary)/$\widetilde{D}_{\mathrm{CrCr}}^{\mathrm{Fe}}$(binary) is 1, which suggests that the presence of Laves phase in this system has no effect on the Cr diffusivity.

4.7 References

[1] Ani, Mohd Hanafi Bin and Kodama, Toshiya and Ueda, Mitsutoshi and Kawamura, Kenichi and Maruyama, Toshio, *Material Transactions*,, **50(**11**)**, 2009, (2656–2663).

[2] GASKELL, David, *Momentum Press*, An introduction to transport phenomena in materials engineering. 2012.

[3] J. S. Kirkaldy and L. C. Brown, *Canadian Metallurgical Quarterly*, **2(**1**)**, 1963, (89–115).

[4] Sekido, N., Hoshino, A., Fukuzaki, M., Maruko, T., & Yamabe-Mitarai, Y., *Journal of phase equilibria and diffusion*, **32**(3), 2011, 219-225.

[5] P. J. Alberry and C. W. Haworth, *Metal Science*, **8(**1**)**, 1974, (407–412).

[6] S. Takemoto, H. Nitta, Y. Iijima, and Y. Yamazaki, *Philosophical Magazine*, 87**(11)**, 2007, (1619–1629)..

[7] S. Huang, D. L. Worthington, M. Asta, V. Ozolins, G. Ghosh, and P. K. Liaw, *Acta Materiala*, **58(**6**)**, 2010, (1982–1993).

[8] Mehrer, Helmut, *Springer Science & Business Media* Diffusion in solids: fundamentals, methods, materials, diffusion-controlled processes, **155**., 2007.

[9] G Bonny, N Castin, J Bullens A Bakaev, T C P Klaver and D Terentyev, J*ournal of Physics: Condensed Matter*, **25**(31), 2013, (315401).

[10] K. L. Wong, H. J. Lee, J. H. Shim, B. Sadigh, and B. D. Wirth, *Journal of nuclear materials*, **386**, 2009, (227–230).

[11] Tomoshi Takahashi, Yoritoshi Minamino; Toshimi Yamane, *Materials Transactions*, **43**(2), 2002, (232-238).

[12] F. Seitzt, *Acta Metallurgical*, **1(**3**)**, 1953, 355-369.

Chapter 5 Engineering Design of Future 9Cr Ferritic/Martensitic Steel with a Better Steam Oxidation Resistance for Application of A-USC Power Plant

5.1 Introduction

The operating temperature limit of ferritic steels is a bottleneck for improving the efficiency of the power plant. In past years, various efforts to design typical 9-12%Cr ferritic/martensitic steel have been conducted for better creep properties and toughness at the operating temperature of A-USC power plants [1]. The chemical composition of typical 9-12Cr ferritic/martensitic steel is listed in table 5.1 [2]. In the past year, traditional 9Cr ferritic/martensitic steels such as P91, P92, and modified 9Cr-1Mo martensitic steel have the issue of microstructure instability after creep test for a longer time. Therefore, a newly developed grade steel (ASME Code 2839, ASTM T93/P93) is suggested to have better stability and creep at 923 K [3]. This type of steel contains 3W and 3Co, which is similar to G115 martensitic heat resistance steel developed in China [4]. The presence of W in these steels is meant to give a better creep strength from solid solution strengthening [3]. The presence of Co is meant to suppress delta ferrite formation and reduce the coarsening rate of $M_{23}C_6$ [3,5]. Besides those two constituents, this steel contains boron which can stabilize $M_{23}C_6$ carbides and suppress the coarsening, resulting in better microstructure stability of grain boundaries and a longer duration of transient creep [6,7].

Table 5.1 Chemical composition of typical 9-12%Cr steel for power plant (mass%) [2].

Steel	C	Cr	Mo	W	Co	Ni	V	Nb	N	B
12CrMoV	0.2	12	1	-	-	0.5	0.3	-	-	-
P91	0.1	9	1	-	-	0.1	0.2	0.05	0.06	-
E911	0.1	9	1	1	-	0.3	0.2	0.05	0.07	-
E92	0.1	9	0.5	1.8	-	0.05	0.2	0.06	0.06	0.001
9Cr3W3CoB	0.1	9	-	3	3	-	0.2	0.05	-	0.014

It is known that degradation, in particular, steam oxidation resistance is one of the crucial issues for power plants besides the mechanical properties. Since there are many ways to improve mechanical properties, the knowledge of employing the same strategy for high-temperature oxidation is essential. This chapter proposed the guidelines for designing typical 9Cr ferritic/martensitic steels from the perspective of oxidation behavior obtained in this study. In particular, the knowledge of the effect of solid solution and precipitation on scale formation and Cr diffusion through the ferrite matrix at elevated temperatures.

In chapters 2 and 3, the effect of adding alloying elements, W and Nb, on the oxidation behavior of Fe-9Cr alloys has been clarified by dividing the effect into solid solution and precipitation. Interdiffusion analysis in the Fe-Cr-W and Fe-Cr-Nb systems has also been clarified in chapter 4. In particular, the interdiffusion coefficient of Cr was compared in the precipitated alloy and alloy without precipitates. Although the diffusion annealing temperature was increased to 1073 K to accelerate the interdiffusion of metal atoms, no phase transformation occurred.

5.2 Characteristic of oxide film formed on Fe-Cr alloys

The oxidation behavior of Fe-Cr steels at high temperatures is briefly explained in chapter 1. To improve steam oxidation behavior of the steel, it is necessary to form a protective chromia scale in the initial stage of oxidation. Wagner [8] proposed two criteria that should be achieved to develop a continuous external chromia scale [8,10]. First, the Cr concentration in Fe alloy must exceed the necessary concentration for outward diffusion to develop an external chromia layer. Low Cr concentration will lead to the formation of internal oxidation of chromia in the matrix Fe or desired chromia will co-exist with the iron-rich oxide. Second, once the external chromia scale is formed, the outward diffusion of Cr must be fast enough to supply Cr at least to being consumed by scale growth reaction. Insufficient Cr supply may fail to form a continuous scale even after the external chromia scale has been established.

Wagner [8] proposed an expression of the minimum concentration of B to form a continuous protective oxide scale of atom B in a general binary A-B alloy. In the case of Fe-Cr alloy, the minimum Cr required to develop a continuous external chromia layer is expressed as [8,10]:

$$N_{\mathrm{Cr}}^{*} > \left[\frac{\pi g^{*} N_{\mathrm{O}}^{(\mathrm{s})} D_{\mathrm{O}} V_{\mathrm{alloy}}}{2\upsilon \widetilde{D}_{\mathrm{Cr}}^{\mathrm{Fe}} V_{\mathrm{CrO}_{1.5}}}\right]^{\frac{1}{2}} \tag{5.1}$$

To maintain the external chromia layer is expressed as [9,11]:

$$N_{\mathrm{Cr}}^{**} = \frac{V_{\mathrm{alloy}}}{32\upsilon}\left(\frac{\pi k_p}{\widetilde{D}_{\mathrm{Cr}}^{\mathrm{Fe}}}\right)^{\frac{1}{2}} \tag{5.2}$$

Where g^{*} is the volume fraction of internal oxide precipitate when external oxide is taken place, υ is atomic ratio of O to Cr in Cr_2O_3 (1.5), k_p is the parabolic rate constant, $N_{\mathrm{O}}^{(\mathrm{s})}$ is the mole fraction of oxygen at the metal surface, D_{O} and $\widetilde{D}_{\mathrm{Cr}}^{\mathrm{Fe}}$ are the diffusion coefficient of oxygen and Cr, respectively, in the alloy, V_{alloy} and $V_{\mathrm{CrO}_{1.5}}$ are molar volume of the alloy and $CrO_{1.5}$ [10].

In an environment consisting of H_2O, the inward flux of oxygen may be larger than in the dry atmosphere. However, the interdiffusion coefficient of Cr in dry and humid conditions is similar. Therefore, the minimum Cr concentration on the developing external scale of chromia in the wet atmosphere increase, as shown in Fig. 5.1 [10].

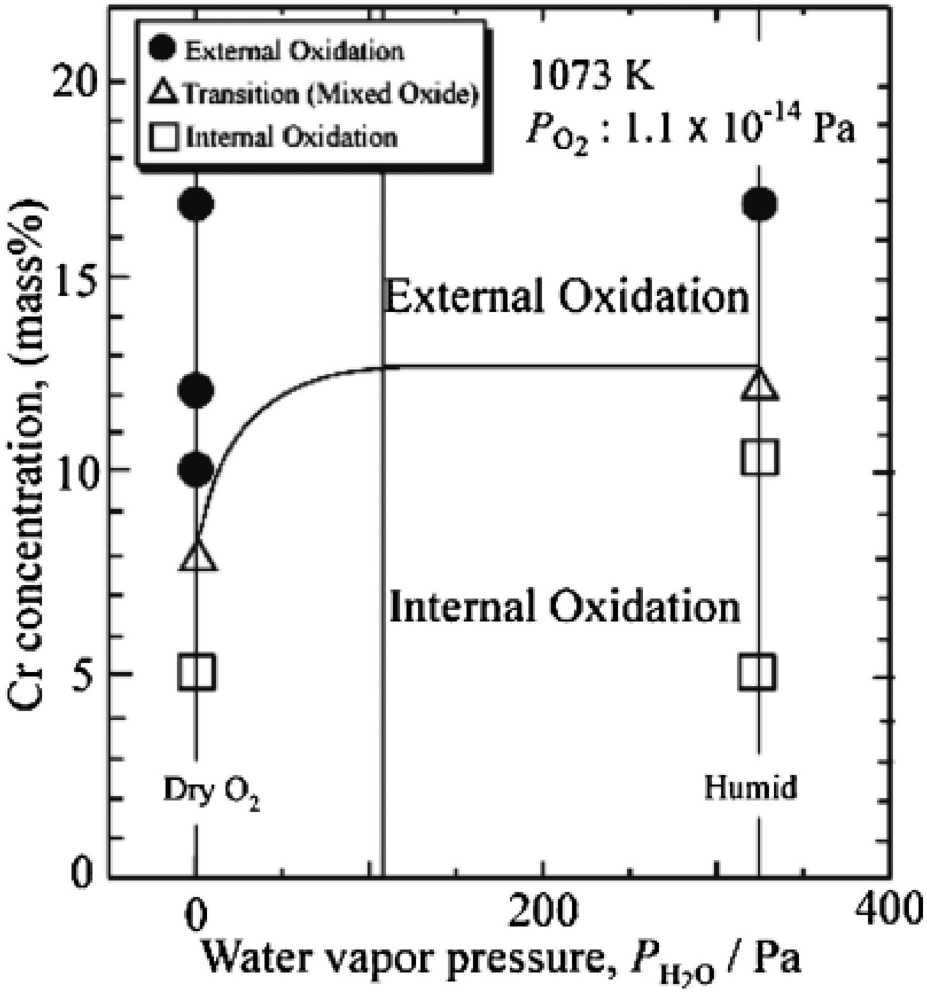

Figure 5.1 Maps for transition of external and internal oxidation of Fe-Cr alloys in dry and humid condition at 1073 K from reference [10].

Meier *et al.* [12] investigated the oxidation behavior of ferritic Fe-Cr alloys in the different atmospheres at temperatures 823 K, 923 K, and 973 K. Moreover, in the presence of water vapor, the inward flux of oxygen became larger even if the oxygen activity was lower than in the dry atmosphere [9,12]. The critical Cr concentration for forming the continuous chromia layer at 823 K shifted from 10 mass% in the dry air to 16 wt.% in the atmosphere containing water vapor [9,10].

Similar to the typical 9Cr steel, which forms a duplex scale consisting of an outer scale of iron oxides and an inner scale of Fe-Cr spinel in flowing steam at 923 K [13]. Figure 5.2 shows the Fe-9Cr alloy from a duplex scale after an oxidation test for 345.6 ks at 923 K in a 15% H_2O gas mixture environment, which is enlarged from Fig. 2.14. The formation of the chromia layer was not observed on the alloy. However, there will be a narrow area in the IOZ front where oxygen partial pressure of $\underline{Cr}/Cr_2O_3$ exists. In addition, banded structure observed in the inner scale of the duplex scale has a different Cr concentration, which was lower in the area near the IOZ [14]. It is suggested the outward diffusion of metal during oxidation. At the same time, the inward diffusion of oxygen formed and grew the spinel layer. The oxidation kinetic of this alloy follows a nearly parabolic manner with a rate-controlling step is the outward diffusion of Fe ions (Fe^{2+} and Fe^{3+}) through spinel lattice [14].

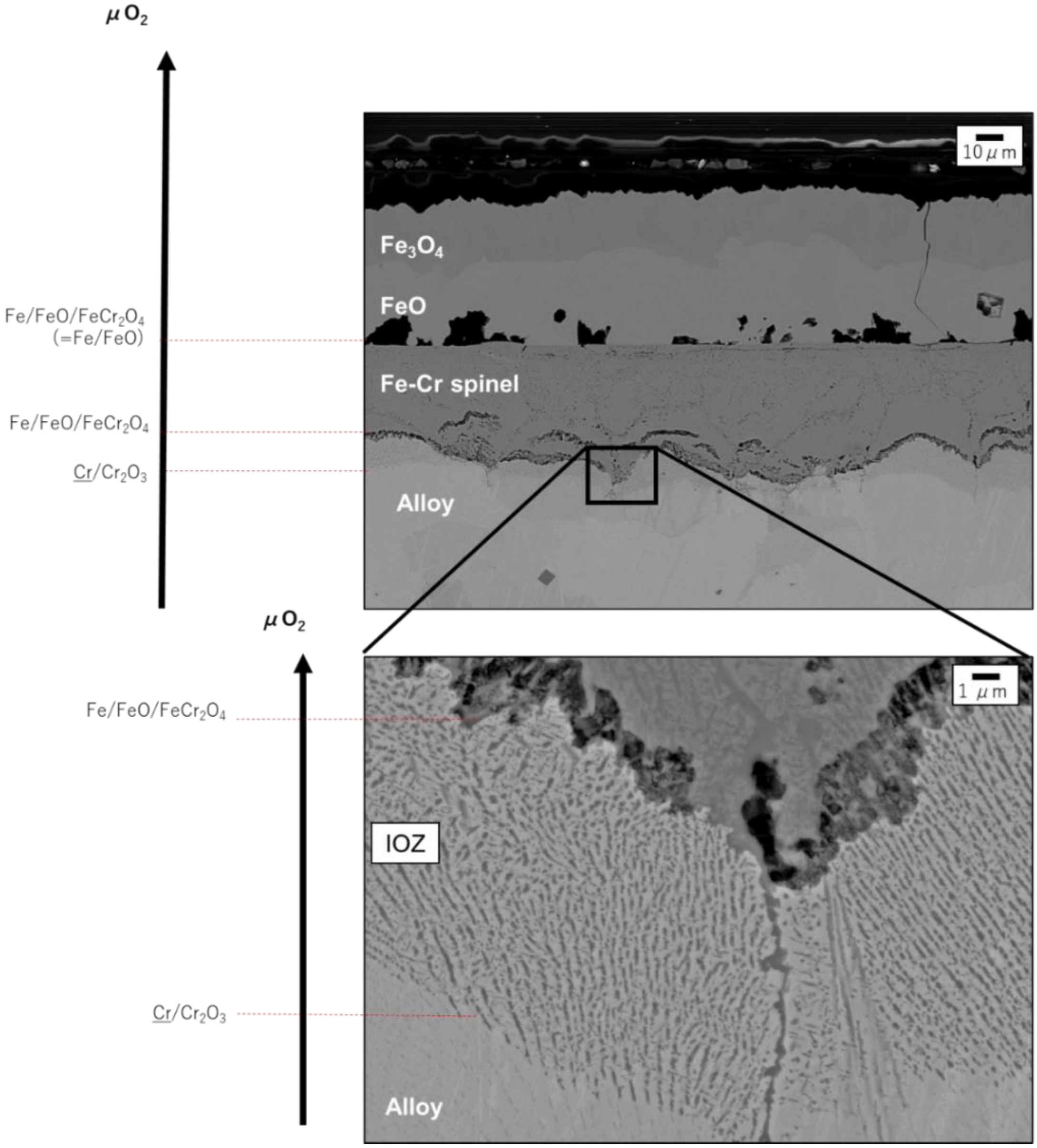

Figure 5.2 BE images of cross-sectional area of Fe-9Cr alloy after oxidation test in Ar-15% H_2O mixture at 923 K for 345.6 ks.

5.3 Guidelines for designing Fe-9Cr alloy from oxidation resistance perspective

Adding W and Nb improves the oxidation behavior of Fe-9Cr alloys but in different ways. Binary Fe-9Cr alloy performed a duplex scale consisting of the outer part (Fe_3O_4 and FeO) and inner part (inner scale and IOZ). By adding 2 mass% Nb and up to 6 mass% W, the scale thickness can be suppressed, but the formation of a continuous layer of Cr_2O_3 still cannot be achieved. Therefore, instead of forming a continuous layer of Cr_2O_3, other methods to improve the oxidation resistance of the 9Cr alloy are suggested based on the obtained results.

5.3.1 Addition of W for a better oxidation resistance

In chapter 2, a significant improvement in oxidation resistance mainly comes from the solid solution effect. It was found that W gives a unique effect by fixing the oxygen partial pressure in the IOZ to be lower than Fe/FeO equilibrium by forming Fe(W)/Fe_2W/$FeWO_4$ equilibrium. Under the Fe(W)/Fe_2W/$FeWO_4$ equilibrium, the matrix of IOZ was not oxidized, which suppressed the formation of the inner scale. This effect is unique because the phase relationship between substrate, oxide scale, and IMCs (Fe(W)/Fe_2W/$FeWO_4$) forms a small potential gradient of oxygen below the Fe/FeO equilibrium (Fig. 2.34). This useful phase relationship is not found in most typical alloying elements in 9Cr ferritic/martensitic steel, such as Mo and Nb.

In the Fe-Cr-W system, forming Fe(W)/Fe_2W/$FeWO_4$ in the IOZ is the key phenomenon to suppressing the formation of the inner scale. The unique structure was found on low content W alloy together with the presence of inner scale in some parts in the scale. It suggested that the formation of Fe(W)/Fe_2W/$FeWO_4$ can be achieved because the Cr_2O_3 particle formation induces precipitation of Fe_2W Laves phase. However, the amount of Fe_2W Laves phase cannot maintain the equilibrium of Fe(W)/Fe_2W/$FeWO_4$ for a longer time. It should be noted that adding W concentration from 3 mass% to 6 mass% was not significantly improved oxidation resistance but only sustained the Fe(W)/Fe_2W/$FeWO_4$ for a longer time. It was found that microstructure stability was an issue in maintaining the Fe(W)/Fe_2W/$FeWO_4$ equilibrium. In Fe-9Cr-3W alloy, more Fe_2W precipitates were observed in lath boundaries by conducting rapid cooling. However, the Fe_2W and lath boundaries disappear after a long time, followed by the oxidation of IOZ. It suggested that lath stability is important to keep the lath martensite structure and provide the Fe_2W phase instead of dissolving back into the matrix solubility limit.

The other benefit of solute W is found by forming a Cr and W-rich layer beneath the inner scale of low W content alloys, as shown in figures 2.23-2.25. It can be explained as chapter 4 reported the effect of W on the interdiffusion of Cr in the ferrite matrix. Although the matrix for the interdiffusion experiment is not the same as the matrix used in chapter 2, the most beneficial of W comes from the accumulation of W in the matrix during formation of IOZ. The large atom size of W creates more vacancies [15], which boosts the Cr diffusivity by a factor of 1.52 by adding 3 mass% of W into Fe-9Cr alloy at 1073 K.

Although it was found that $\widetilde{D}_{\mathrm{Cr}}^{\mathrm{Fe}}$ increased by adding W into the 9Cr alloy but the $\widetilde{D}_{\mathrm{Cr}}^{\mathrm{Fe}}$ value is not effective to develop an external chromia layer. Considering the Wagner criteria for developing and maintaining chromia layer (Eq. (5.1)), the factor 1.52 is change the N_{Cr}^{*} to be 0.8 times lower. In the case of the critical Cr concentration for forming the continuous chromia at 823 K is 16 mass% in the atmosphere containing water vapor [11], this factor of 1.52 can changed the N_{Cr}^{*} to be 13 mass%. This value is still higher than the Cr in the matrix (9 mass%). Therefore, the strategy to boost the $\widetilde{D}_{\mathrm{Cr}}^{\mathrm{Fe}}$ to form external chromia layer by adding W is not applicable. However, adding low amount of W into the alloy was found can form Cr enriched layer at the bottom part of inner scale. From the obtained result, it can be concluded that higher W content is preferred to improve oxidation properties both to sustain the Fe(W)/Fe_2W/$FeWO_4$ equilibrium for a longer time and to boost the interdiffusion of Cr without forming an external chromia layer.

As mentioned earlier, the significant improvement in oxidation resistance is by adding 3%W, and the effect becomes less significant if more W is added into alloy. This result from oxidation properties in agreement with the preferable W content for a better creep rupture strength [3] which the effect becomes saturated up to about 3 mass% as shown in figure 5.3. In the more complex system 3 mass% W is 100% tempered martensite, and the volume fraction of δ-Ferrite increases by adding more W. From these results, both the strengthening mechanism and oxidation resistance of typical 9Cr steel containing W mainly originated from the solid solution effect. Noted that in this research, pre-aged was used. Therefore, to apply the strategy of Fe(W)/Fe_2W/$FeWO_4$ equilibrium, it is suggested to perform pre-aged treatment to provide fine Fe_2W from the beginning. To ensure the precipitation of laves phase without reducing the W content in the matrix, 3-4 mass% of W is preferred. In addition, due formation of δ-Ferrite increases by adding more W, it is suggested to add more Co or other elements that can suppress the formation of δ-Ferrite.

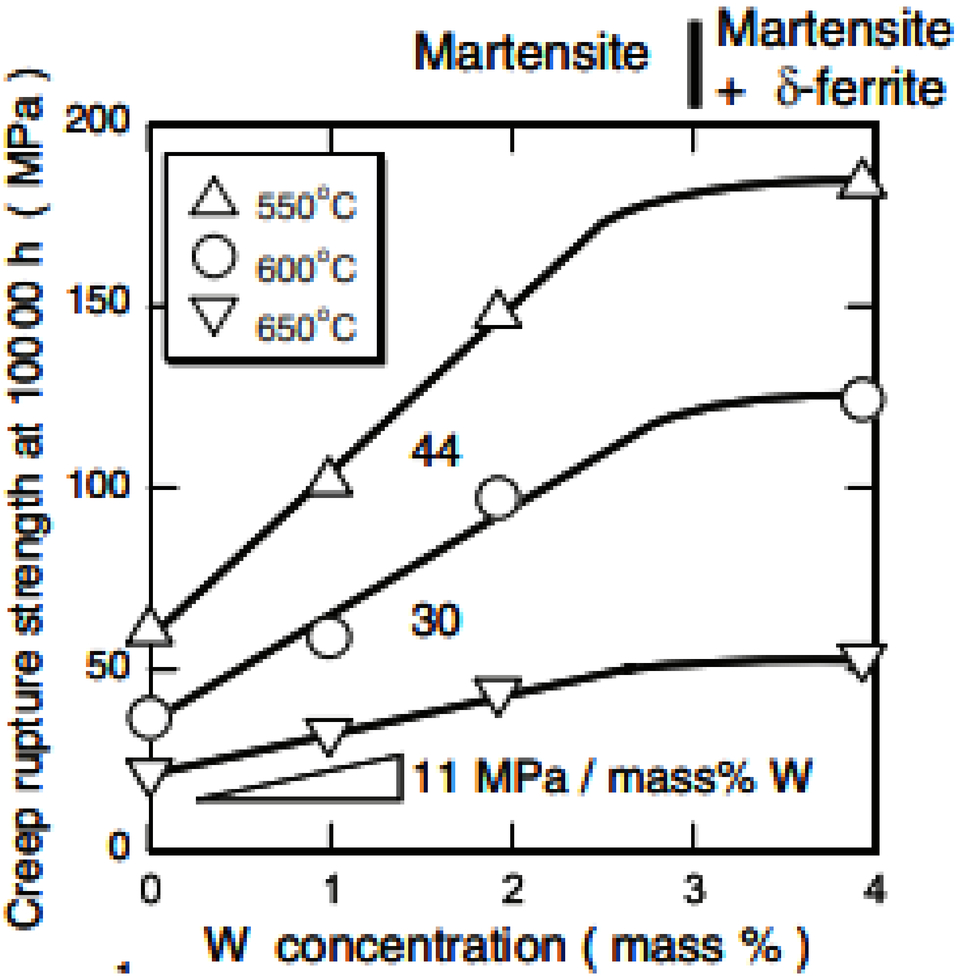

Figure 5.3 Creep rupture strength as a function of W [3].

5.3.2 Effect of Nb on the scale formation of 9Cr ferritic steels

It is well known that the solid solution strengthening mechanism in 9Cr steel originated from precipitates such as carbides ($M_{23}C_6$, M_6C), carbonitrides (MX, M_2X), and intermetallic compounds ($Fe_2(W,Mo)$ Laves phase, Fe_7W_6) [3,5]. This present work focused on the intermetallic compound (IMCs). The low solubility limit of Nb in the Fe matrix is low, and the precipitation of Nb is preferred. Adding Nb into typical 9Cr steel is meant to give a precipitation effect by forming MX-type and NbC precipitates [3,5]. However, the present work focus on the role of Nb as Laves phase Fe_2Nb on oxidation properties. In chapter 3, two types of precipitates of fine particles of Fe_2Nb and coarse intermetallic Fe-Nb were observed. Well distributed fine laves phase contributes to a better and denser Cr include internal oxide particles in the IOZ and inner scale, which led to better Cr enrichment in the inner scale. This layer retarded the outward diffusion of Fe ion through the inner scale, which resulting in more compact and thin scale. The same effect was suggested for the coarse intermetallic compound. However, the coarse compound is not distributed well in the matrix and grain boundary. Hence, the effect of the coarse intermetallic phase was smaller than the fine laves phase.

The interdiffusion experiment showed that the precipitate was not useful for boosting the Cr diffusion in the ferrite matrix. Therefore, the effect of Nb on improving the oxidation properties of Fe-9Cr alloy only relies on the two mentioned suggested mechanisms. Considering Wagner's criteria for developing and maintaining chromia layer (Eq. (5.1)), the difference between binary and ternary alloys is g^* (volume fraction of internal oxide precipitate). Kuo *et al.* [16] reported the volume fraction of Cr_2O_3 per 1 mol is 19.94 cm^3, while the volume fraction of $CrNbO_4$ is 38.96 cm^3 per mol. Adding more Nb will increase volume fraction of the $CrNbO_4$. Mentioning that the IOZ on both Fe-9Cr and Fe-9Cr-2Nb alloys are about the same, it can be concluded that adding more Nb cannot shift the N_{Cr}^* to form the external chromia layer in Fe-9Cr alloy.

Compared to the effect on the Fe-Cr-W system, the role of Nb in improving oxidation behavior is insignificant because Nb cannot increase diffusivity of Cr in the Fe matrix. It is also found that there is no useful phase relationship between the substrate, oxides, and precipitates found in the system. Although the effect is not as significant as W addition, adding Nb to form Fe_2Nb contributes to a higher volume fraction of internal oxide particles in the inner scale and IOZ, which relatively improves the oxidation resistance in duplex structure. Therefore, adding Nb into 9Cr steel can be considered as one of the ways to improve oxidation resistance of the material. Considering Nb content in the typical 9Cr steel to form MX-type and NbC is 0.05 mass% (Table 5.1), and the solubility of Nb in Fe matrix to form Fe_2Nb is around 0.1 mass%, it is needed to increase the Nb concentration in the alloy to be more than 0.15 mass%. In addition, there is a possibility that the Cr is solved into the intermetallics compounds which will consume Cr in the matrix. In that case, a longer solution treatment is preferred. In addition, because no useful phase relationship between the substrate, oxides, and precipitates was found in this system, it is not necessary to perform the pre-aged treatment to provide Fe_2Nb from the beginning.

5.4 Conclusions

The 9-12% Cr ferritic/martensitic steel is targeted to be applied in for components of the A-USC power plant at 923 K in steam condition. Considering the effects of alloying elements obtained in this thesis, some suggestions can be considered for developing future grades of 9Cr steel. A significant improvement in oxidation resistance and better creep rupture strength is given in the 3%W alloy. In terms of oxidation resistance, developing Fe(W)/$FeWO_4$/Fe_2W equilibrium is the key phenomenon to suppressing the formation of the inner scale. Therefore, it is necessary to provide fine Fe_2W from the beginning. It is suggested to add 3-4 mass% W into 9Cr steel and perform the pre-aged treatment. Higher W is meant to provide W for Fe_2W in the early stage without reducing the W content in the matrix. In addition, it should be considered to add other elements that can suppress δ-Ferrite formation. Compared to the effect on the Fe-Cr-W system, the role of Nb in improving oxidation behavior is insignificant. In this system, there was no useful phase relationship between the substrate, IMCs, and oxide scale that could suppress the formation of the inner scale was found. Adding Nb formed a higher volume fraction in the inner scale and IOZ, which relatively improves the oxidation resistance in the duplex structure. Therefore, adding Nb into 9Cr steel can be considered as one of the ways to improve oxidation resistance of the materials. Considering the low solubility of Nb in the Fe matrix to form Fe_2Nb and amount of Nb to form other strengthening phases such as carbides, the Nb content in the alloy can be increased to above 0.15 mass%.

5.5 References

[1] F. Abe, *Engineering*, **1(**2**)**, 2015, (211–224).

[2] W. Yan, W. Wang, Y. Y. Shan, and K. Yang, *Front. Mater. Sci.* **7(**1**)**, 2013, (1–27).

[3] F. Abe, *Science and Technology of advanced materials*, **9(**1**)**, 2008.

[4] P. Yan and Z. Liu, *Materials Science and Engineering: A*, **650**, 2016, (290–294).

[5] Knežević, V., Balun, J., Sauthoff, G., Inden, G., & Schneider, A. *Materials Science and Engineering: A*, **477**(1-2**)**, 2008, (334-343).

[6] Abe, Fujio. *International journal of materials research*, ***99***(4), 2008, (387-394.

[7] Toshiaki Horiuchi, Masski Igarashi, and Fujio Abe, *ISIJ International*, **42**(Supplement), 2002, (S67–S71).

[8] C. Wagner, *Zeitschrift für Elektrochemie*, *Berichte der Bunsengesellschaft für Phys. Chemie*, 63**(7)**, 1959, (772–782).

[9] G. H. Meier, K. Jung, N. Mu, and N. M. Yanar, *Oxidation of Metals*, **74(**5**)**, 2010, (319–340).

[10] Ani, Mohd Hanafi Bin and Kodama, Toshiya and Ueda, Mitsutoshi and Kawamura, Kenichi and Maruyama, Toshio, *Material Transactions*,, **50(**11**)**, 2009, (2656–2663).

[11] Wagner, Carl, *Berichte der Bunsengesellschaft für physikalische Chemie* **63(**7), 1959,(772-782)

[12] E. Essuman, G. H. Meier, J. Żurek, M. Hänsel, and W. J. Quadakkers, *Oxid. Met.*, **69(**3–4**)**, 2008, (143–162).

[13] A. Agüero, V. González, M. Gutiérrez, and R. Muelas, *Surface and coatings technology* , **237**, 2013, (30–38).

[14] B. Pujilaksono, T. Jonsson, H. Heidari, and M. Halvarsson, *Oxidation of metals*, **75(**3**)**, 2011, (183–207).

[15] S. Takemoto, H. Nitta, Y. Iijima, and Y. Yamazaki, *Philosophical Magazine*, 87**(11)**, 2007, (1619–1629).

[16] Kuo, Yen-Ling and Hayashi, Shigenari and Kakehi, Koji, *Oxidation of Metals*, **95(**1**)**, 2021, (189–202).

Chapter 6 Conclusions

High Cr ferritic/martensitic steels are being developed for A-USC power plant components performed around 923 K. This study aims to clarify the effect of alloying elements, particularly W and Nb, and microstructure on the steam oxidation behavior of 9Cr ferritic alloy at 923 K. This study aims to improve the steam oxidation behavior of 9Cr steel at 923 K by optimizing alloying elements. The conclusions from each chapter are summarized below:

Chapter 1: Introduction

The background of this study is described as one of the ways to improve power plant efficiency. Further literature review on material development and the properties of typical 9-12% Cr steel were presented. Based on the research background, the objectives and flow of this thesis are explained.

Chapter 2: The Effect of Tungsten Addition on the Steam Oxidation Behavior of Fe-9Cr Alloy at 923 K

The effect of tungsten (W) on the steam oxidation behavior of Fe-9Cr alloys under the oxygen partial pressure of $1.3\text{x}10^{-11}$ Pa in an Ar-15%H_2O gas mixture at 923 K was investigated. Fe-9Cr alloy and tungsten added Fe-9Cr alloy with three different tungsten concentrations and two different cooling rates are compared to investigate the role of tungsten as a dissolved alloying element in the substrate and precipitates. The results showed that adding W into Fe-9Cr alloy significantly improves the oxidation resistance of the alloy but without forming an external layer Cr_2O_3 layer. Formation of the inner scale was absent in the high W concentration alloys. A possible mechanism for scale formation in the W added 9Cr alloys was proposed. As a solid solution element, W promoted Cr enrichment at both the IOZ/inner scale and the IOZ/alloy interfaces, which suppress the outward diffusion of metal ions. A finer and higher fraction of the Fe_2W

phase is useful to sustain Fe(W)/Fe_2W/$FeWO_4$ equilibrium in the IOZ, which suppresses inner scale formation and contributes to the better Cr enrichment at the inner part of oxide scale.

Chapter 3: The Effect of Niobium Addition on the Steam Oxidation Behavior of Fe-9Cr Alloy at 923 K

The effect of niobium (Nb) on the steam oxidation behavior of Fe-9Cr was investigated. Fe-9Cr alloy and Nb added Fe-9Cr alloys with water quenching were prepared. The steam oxidation tests were conducted under the oxygen partial pressure of $1.3 \text{x} 10^{-11}$ Pa in an Ar-15%H_2O gas mixture at 923 K. The results show that the Fe-9Cr-2Nb alloy has a slower oxidation rate than the Fe-9Cr alloys. A duplex scale with a thinner and more compact inner scale was observed. The fine Laves phase acted as a Cr reservoir and contributed to the formation higher density of IOZ and inner scale by oxidizing Laves phase to provide a better Cr enrichment in the inner scale, which retarded the outward diffusion of Fe ion through the inner scale. The oxidation behavior of Fe-Cr-Nb system is very different from the Laves phase in the Fe-Cr-W system, which can develop the phases with a lower oxygen partial pressure of IOZ s than the Fe/ FeO equilibrium. This phenomenon suppresses the formation of the inner scale. In this system, there was no useful phase relationship between the substrate, IMCs, and oxide scale that was similar to the phases relation in the Fe-Cr-W system.

Chapter 4: The Effect of Tungsten and Niobium on the Cr Diffusivity in the Fe-9Cr Alloys with the Alloying Element

Future investigation on the effect of alloying elements, particularly W and Nb, on Cr diffusivity in the alloy is determined by analysis of the concentration profile from the diffusion couple samples. The diffusion annealing tests were carried out in an evacuated chamber at 1073 K to accelerate the atom diffusion without phase transformation. $\widetilde{D}_{\mathrm{Cr}}^{\mathrm{Fe}}$ in binary diffusion couple Fe/Fe-9Cr is calculated as $3.8 \text{ x } 10^{-16}\ \mathrm{m}^2\ \mathrm{s}^{-1}$. The ratio of $\widetilde{D}_{\mathrm{CrCr}}^{\mathrm{Fe}}$ (ternary)/$\widetilde{D}_{\mathrm{CrCr}}^{\mathrm{Fe}}$(binary) increases to be 1.52 times by adding 3 mass% of W into Fe-9Cr alloy. The ratio of $\widetilde{D}_{\mathrm{CrCr}}^{\mathrm{Fe}}$ in ternary alloy decreased with the presence of high-volume fraction of Laves phase on diffusion couple of Fe-6W/Fe-9Cr-6W. In this system, a new laves phase precipitated along the bonded interface, which suggested that reduce the effective diffusion area in the couple. In the Fe-2Nb/Fe-9Cr diffusion couple, $\widetilde{D}_{\mathrm{CrCr}}^{\mathrm{Fe}}$ (ternary)/$\widetilde{D}_{\mathrm{CrCr}}^{\mathrm{Fe}}$(binary) is 1, which suggests that the presence of Laves phase in this system has no effect on the Cr diffusivity.

Chapter 5: Engineering Design of Future 9Cr Ferritic/Martensitic Steel with a Better Steam Oxidation Resistance for Application of A-USC Power Plant

Considering the effects of alloying elements obtained in this thesis, some suggestions can be considered for developing future grades of 9Cr steel. A significant improvement in oxidation resistance and better creep rupture strength is given in the 3%W alloy. In terms of oxidation resistance, the develop the Fe(W)/Fe_2W/$FeWO_4$ equilibrium is the key phenomenon suppressing the formation of inner scale. Therefore, it is necessary to provide fine Fe_2W from the beginning. It is suggested to add 3-4 mass% W into 9Cr steel and perform the pre-aged treatment. Higher W is meant to provide W for Fe_2W in the early stage without reducing the W content in the matrix. In addition, it should be considered to add other elements that can suppress δ-Ferrite formation. Compared to the effect on the Fe-Cr-W system, the role of Nb in improving oxidation behavior is insignificant. In this system, there was no useful phase relationship between the substrate, IMCs, and oxide scale that could suppress the formation of inner scale was found. Adding Nb formed a higher volume fraction in the inner scale and IOZ, which relatively improves the oxidation resistance in the duplex structure. Therefore, adding Nb into 9Cr steel can be considered. Considering the low solubility of Nb in the Fe matrix to form Fe_2Nb (0.1 mass%) and the concentration of Nb to form precipitates such as carbide in typical 9Cr steel is 0.05 mass%, it is suggested to add Nb concentration in the alloy to be higher than 0.15 mass%.

Chapter 6: Conclusions

All conclusions from each chapter are summarized

List of Figure

List of Table

Acknowledgement

In the name of Allah, the Most Gracious and the Most Merciful. All praises to Allah, who has given me strength and encouragement throughout all the challenging moments of completing this dissertation. May Allah’s blessing goes to His final Prophet Muhammad (peace be upon him), his family, and his companions.

First and foremost, I would like to sincerely thank my supervisor, Assoc. Prof. Mitsutoshi Ueda for continuous guidance, constructive comments, precious discussions, and all the support on my work. He provided a warm spirit, sincerity, and encouragement I will never forget.

I would like to express my sincere gratitude to my Co-Supervisor, Assoc. Prof. Kenichi Kawamura for the opportunity, discussions, and comments during my work in this laboratory. Having them as my supervisors has been a great pleasure and honor.

I would like to express my gratitude to my dissertation examiners for their questions and valuable comments, which were very helpful in improving my work: Prof. Eiji Tada, Prof. Yoshisato Kimura, and Assoc. Prof. Satoru Kobayashi.

I am grateful for the opportunity to become an Outpatient Researcher in the Materials Sciences Research Center, Japan Atomic Energy Agency, Japan. My gratitude to my internship supervisor, Dr. Eriko Irisawa, and everyone who helped and assisted me during the three months internship.

I am deeply grateful to MEXT Scholarships for the financial support during my study.

Also, let me acknowledge the Open Facility Center, Materials Analysis Division, Tokyo Institute of Technology for conducting the XRF measurements.

I would also like to offer my special thanks to all my friends in Ueda and Kawamura Lab for these past five years. I am particularly thankful for the assistance given by them, especially to Yao and Takuro.

Special thanks to my beloved friends, who have always been there to support me through all ups and downs in Japan. Especially for Dini, Hani, Kak Yulia, Mba Nana, Latif, Ikki, Agung, Edgar, Rendi, Jamil, and all my Indonesian friends who cannot be mentioned one by one.

Disertasi ini Eya persembahkan untuk Bapak dan Ibu. Terima kasih untuk semua cinta, dukungan dan doanya selama ini. Terima kasih selalu mendengarkan cerita Eya setiap hari. Mas bowo dan Kak Rini, terima kasih sudah berada disebelah Bapak dan Ibu selama Eya menempuh studi. I love you all!

Tokyo, September 2022

Lidyana utami